SPATIALLY RESOLVED IONIC MEASUREMENTS WITH SCANNING ELECTROCHEMICAL MICROSCOPY

BY

ZACHARY JAMES BARTON

DISSERTATION

Submitted in partial fulfillment of the requirements
for the degree of Doctor of Philosophy in Chemistry
in the Graduate College of the
University of Illinois at Urbana–Champaign, 2017

Urbana, Illinois

Doctoral Committee:

Assistant Professor Joaquín Rodríguez-López, Chair
Professor Andrew A. Gewirth
Professor Deborah E. Leckband
Assistant Professor David W. Flaherty

ABSTRACT

Modern electrochemical energy storage systems operate by the concerted shuttling of electrons and cations between a cathode and an anode. Strategies for looking at this process do not have a direct measure of ion movement as it occurs, and thus do not provide essential mechanistic details for optimizing battery performance. This work pioneers the use of Hg-based probes to address this gap in knowledge. First, I show the collection of Li^+ over an electrified interface and characterize the linear response of Hg-based signals to changes in ion concentration. To improve the sensing strategy, I then develop a framework and model extracting position and reactivity information from cyclic voltammetry scanning electrochemical microscopy (CV-SECM) and associated methods. This maximizes spatial resolution of substrate ionic reactivity while also minimizing threats to the integrity of the probe. I then improve the sensing platform, delineating a reproducible protocol for generating Hg disc-well probes and providing side-by-side performance comparisons between the new and old probe geometries. Following this, I demonstrate the utility of CV-SECM methods and Hg disc-well probes by separating ionic activity from solid electrolyte interphase (SEI) development processes at an operating model battery anode. Ongoing and future applications for the probes and methods generated by this research include multi-ion measurements, cathode studies, and localized charge–discharge experiments to inform the rational design of the next generation of energy storage materials.

Soli Deo Gloria

ACKNOWLEDGEMENTS

I thank Prof. Joaquín Rodríguez-López for not only training me as an electrochemist but also providing me with so many opportunities to grow as an educator and author. Working through challenging experiments together has shown me the satisfaction of mitigating Murphy's Law by sheer perseverance. I am most grateful for your contagious interest in both fundamental and applied research, which has given me the same insatiable curiosity.

I thank Prof. Daniel Burden for shaping me as an analytical chemist, teaching me to hone in on experimental details and sources of noise without losing sight of the bigger picture. Thank you for devoting so much time and energy to teaching me to align more than optics.

I am indebted to all of my teachers over the years for answering my many questions and encouraging me to find new ones. I thank Prof. Deborah Leckband, Prof. Ryan Bailey, Prof. Becky Eggimann, Prof. Timothy Wilkinson, and Prof. Mark Niemczyk for allowing me to learn by teaching. I thank the entire faculty of the Chemistry and Physics departments at Wheaton College, and Prof. Daniel Burden, Prof. Becky Eggimann, and Prof. Peter Walhout in particular, for helping me to integrate faith and learning in pursuit of the sublime.

I thank the National Science Foundation for the financial support of the Graduate Research Fellowship Program. I thank the University of Illinois for financial support as well as the opportunity to learn. I thank my committee members, Prof. Andrew Gewirth, Prof. Deborah Leckband, and Prof. David Flaherty, for feedback and guidance. I thank my friends in the J.R.-L. group for sharing the many highs and lows in our pursuit of the unknown and fight against entropy. Lastly, I express my deepest gratitude to my fiancé, Erika, the Barton family, the Mock family, my family at Stratford Park Bible Chapel, and numerous friends who endured this long process with me, always offering prayers, support, and love.

TABLE OF CONTENTS

CHAPTER 1

General Introduction

Significant portions of this chapter are intended for submission as part of an invited article in *Chemistry of Materials*:

Hernández-Burgos, K.; Barton, Z. J.; Rodríguez-López, J. Finding Harmony between Ions and Electrons: New Tools and Concepts for Emerging Energy Storage Materials. *Chem. Mat.* **2017**, *In Preparation*.

1.1 Abstract

This research has produced new electrochemical methods and analytical probes for mapping ionic fluxes and electron transfer activity at operating interfaces. These tools are primarily intended to address a gap in crucial studies of energy storage systems, but they may be extended to other applications as well.

1.2 Ionic Processes in Electrochemical Energy Storage

1.2.1 Introduction

The study of charge transport mechanisms within and between materials is one of the most critical challenges facing electrochemistry since the power density and specific capacity of modern battery materials are predicated on a delicate balance between electrode structure, ion mobility, electron transport, and chemically specific interactions.[1] In order to provide a context for later chapters, what follows is a brief review of anode and cathode processes in which ionic flux plays a critical role. Then, key aspects of each chapter are highlighted to give a short overview of this research effort.

1.2.2 Anode Processes

Most modern Li-ion batteries (LIBs) utilize a graphitic anode material to accept guest Li ions during the discharge process.[2] In these materials, Li^+ inserts reversibly to form islands of ionic compounds in the galleries between graphene sheets.[3,4] This process is referred to as "intercalation," and its kinetics depend

strongly on the balance between elastic strain caused by the deformation of the graphitic planes and the strong attractive electrostatic interactions between intercalated species.[5] Enrichment of Li^+ content within the graphitic host promotes to island growth and migration between galleries. Thermodynamic and kinetic stabilization effects leads to well-defined transitions from 4, to 3, to 2, then to 1 graphitic plane(s) separating consecutive intercalant islands. This changing island plane separation is referred to as "staging," with stage IV, III, II, and I indicating the number of intermediary graphitic planes between filled galleries. Li^+ diffusion in graphitic materials is anisotropic, exhibiting much greater mobility between graphene sheets than perpendicular to them,[6] and also varies with the extent of lithiation due to attractive interactions between intercalated species.[7] The insertion and transport of Li ions is also affected by the turbostratic disorder and porosity of the host material.[8] Understanding the dynamics of ion insertion is vital for informing the design of the next generation of energy storage materials.

Although some progress may be made by tuning the architecture of the carbon-based anode, [9-11] carbon's theoretical maximum capacity (372 mA h g^{-1} or 975 mA h cm^{-3}) is a limiting factor for increasing the energy density of portable batteries. Conversion materials offer greater energy densities than those that undergo intercalation reactions, but this comes with the added cost of needing to form new structures with each charge or discharge.[12] Due to their environmental abundance and high theoretical maximum capacity (3590 mA h g^{-1} or 8365 mA h cm^{-3}), Si anodes remain an area of active research,[13,14] but pulverization and irreversible capacity loss from extreme volume changes even during initial cycles hinders their implementation in rechargeable energy storage devices.

1.2.3 Cathode Processes

Commercial LIBs typically use $LiCoO_2$ as the cathode material,[15] though olivines (*e.g.*, $LiFePO_4$), spinels (*e.g.*, $Li_4Ti_5O_{12}$ or $LiNi_{0.5}Mn_{1.5}O_4$),[16,17] and other intercalation materials have found commercial use as well.[12] In cathode intercalation materials, depletion of lithium during discharge leads to the

formation of different crystalline phases. The chemical stability of extreme phases is often lower than intermediate ones, so the width of the miscibility gap is an additional criterion for determining the usable capacity of the cathode material. On the other hand, destabilizing the crystalline lattice through the introduction of substitutions can facilitate rapid phase transformations and greater ionic mobility. The delithiation of cathode materials begins with the generation of disorder within the crystalline lattice to allow alkali ion movement, but there is not yet consensus on how this disorder propagates nor how it varies with particle size.[18] The type, domain size, and distribution of crystalline phases varies with particle size and cycling conditions, and so ongoing studies seek to maximize the accessible capacity and minimize capacity fade by investigating new crystalline structures in a variety of particle dimensions, compositions, and geometries. In addition, interfacial strain between crystalline phases can adversely impact the mobility of ions within the cathode structure, so materials and/or architectures that alleviate interfacial strain or lessen phase separation may offer higher power and longer cycle life.[19-22]

1.2.4 Solid Electrolyte Interphase (SEI) Properties

The overall performance of a LIB is strongly tied to the electrochemical and mechanical properties of the solid electrolyte interphase (SEI) resulting from decomposition reactions at the electrode–solution interface during cycling.[23-26] An ideal SEI has low electronic conductivity in order to prevent electrodeposition of lithium, which would constitute a loss of charge capacity. Such depositions may be mossy or dendritic[27] and can eventually cross the membrane separating the anode and cathode compartments with suboptimal results. Similarly, ion transport within an ideal SEI is rapid relative to the rate of discharge and follows minimally tortuous routes so as to prevent ion entrapment. An impermeable SEI leads directly to deleterious resistive heating and arcing voltage profiles during galvanostatic cycling.[28] And, an ideal SEI is sufficiently flexible to retain its structural integrity through the repeated swelling and contracting of the battery material. These volume changes may range from

10% for carbonaceous materials[29] to 300% for silicon-based anode materials,[1,30] so there is no universally applicable set of operating conditions to prevent cracking, pulverization, or loss of electrical contact. Thus, optimizing the electrical resistivity, ionic permeability, and elasticity of the stress–strain response of the SEI is vital for ensuring high-performance battery operation.[31-34]

1.3 Dissertation Outline

1.3.1 Research Motivation

The multifarious relationships between electrode structure, SEI properties, and battery performance has been investigated by a host of complementary techniques, including FTIR,[35] Raman spectroscopy,[26,36-39] spectroscopic ellipsometry,[40] X-ray techniques (XRD, XAS, and XRR),[30,41-45] TEM,[46-49] electrochemical impedance spectroscopy,[50-53] mass spectrometry,[54] and electrochemical quartz crystal microbalance (EQCMB)[55] experiments. These techniques provide access to a wealth of useful information but are unable to completely answer remaining unknown aspects of SEI growth and aging, such as spatiotemporal changes in ionic permeability during cycling. Due to the heterogeneous reactivity of energy storage materials,[56] these questions are better addressed by *in situ* scanned probe measurements, such as AFM,[57] STM,[58] SECM,[59-63] SICM,[64-66] SECCM,[67] and Hg-based SECM,[68] which access information both when and where it is needed (Figure 1.1A).[69-75] These techniques are reviewed in greater detail in Chapter 2.

Of these tools, only Hg-based SECM has access to reversible amalgamation and stripping reactions with alkali ions. Because alkali ion gradients are the motive force for alkali-ion battery operation, the ion-specific measurements obtainable by Hg-based probes offer a direct, unobscured view of localized battery material performance. This localization is increasingly important as micro- and nano-structured materials offer benefits for electrochemical energy storage.[76] Consequently, my graduate research has

involved the development of Hg-based probes and the deployment of new electroanalytical strategies by which to use them.

1.3.2 Hg-Based SECM of Alkali Ions

At first, I used Hg sphere-cap ultramicroelectrodes (UMEs) in traditional potentiostatic SECM imaging modes to collect maps of electrochemical reactivity as well as ionic gradients at battery electrode proxies (Figure 1.1B). These maps were not only the first measurements of alkali ion gradients at operating electrochemical interfaces but also the first example of co-localized electronic and ionic signals in a non-aqueous system. In addition, I calibrated the signal response of Hg sphere-caps to changes in Li-ion concentration. This constituted the first step in exploring a new way to directly correlate material defects with reactive heterogeneity in energy storage materials. These developments are discussed in Chapter 3.[68]

1.3.3 Time-Resolved SECM Strategies with Hg Sphere-Caps

Wanting to take my measurement strategy further, I looked for a way to monitor the probe–substrate gap size without an organic redox mediator. Amalgamation reactions with metal cations at Hg-based probes avoid unwanted side reactions and positive feedback mechanisms that can prove problematic for traditional SECM positioning methods, especially since the local surface reactivity is not typically known *a priori*. In order to obtain negative feedback positioning control without risking damage to the SECM probe due to saturation by collected ions, I implemented cyclic voltammetry probe approach surfaces (CV-PASs), consisting of CVs performed between incremental Z motor movements. This prevents the internal amalgam composition from reaching dangerous levels and also allows greater control of the diffusional timescale. I showed that the amalgamation current, peak stripping current, and integrated stripping charge extracted from a shared CV-PAS can be used to determine the tip–substrate gap with over 3 orders of magnitude greater accuracy and more than 20-fold

greater precision than obtained by previous potentiostatic methods.[77] Considering the timescales of diffusion and amalgam saturation, I also discovered limiting conditions for obtaining and fitting CV-PAC data (Figure 1.1C). Furthermore, I found that CV-SECM, the result of applying the same strategy as an imaging mode, can capitalize on the chemical specificity of amalgamation and stripping reactions at Hg probes to give direct measurements of ionic fluxes. The resulting hyperdimensional datasets contain kinetic, thermodynamic, temporal, and spatial information. Furthermore, this strategy of CV-SECM decouples measurements from probe movements, which all but eliminates the danger of signal distortions from forced convective transport during data collection. CV-SECM maximizes the analytical power of Hg-based SECM probes, and the mathematical models I provided allow other researchers to leverage that power for their own work. The first paper delineating CV-SECM methods is presented in Chapter 4.[78]

1.3.4 Hg Disc-Wells

Having fully capitalized on the wealth of chemical information available to Hg-based probes through CV-SECM, I shifted my attention to improving the limitations of the probes themselves. Though CV-SECM and associated strategies greatly improve the analytical capabilities of Hg-based probes, Hg sphere-caps are inherently unable to safely operate in concentrated battery environments at long enough timescales to resolve critical changes in ionic reactivity. This is a result not only of the large ratio between their surface area and internal volume but also of the radial diffusion governing their operation. Additionally, the insensitivity of side- and back-diffusion to substrate blockage makes sphere-caps susceptible to damaging collisions with the substrate and prevents the use of short working distances in SECM.

Therefore, I devised a reproducible protocol for fabricating a more robust probe geometry: the Hg disc-well, which consists of a level pool of Hg confined to a glass-walled cavity. Because these probes

offer much smaller area-to-volume ratios and exhibit smaller diffusive fluxes than equivalent sphere-cap probes, disc-wells are able to operate in approximately an order of magnitude greater analyte concentration for a given timescale and at nearly two orders of magnitude longer timescales for a given bulk analyte ion concentration. Access to such concentrated conditions allows the application of Hg-based probes to realistic alkali ion battery environments. As SECM probes, Hg disc-wells offer inherent benefits over more traditional sphere-caps. Having the electrode surface flush with the insulting basal plane of the probe increases the sensitivity, collection efficiency, and spatiotemporal resolution simply due to differences in diffusive flux lines. In addition, Hg disc-wells benefit from mechanical shielding against shear forces experienced during rapid lateral translocation. All of these factors enable Hg disc-wells to serve as superior CV-SECM probes when ionic specificity and spatial resolution are key goals (Figure 1.1D). The fabrication and electrochemical performance of Hg disc-wells are reported in Chapter 5.[79]

1.3.5 Further Applications

When combined with substrate CV measurements, Hg disc-wells can isolate the contribution of ionic fluxes to the overall substrate response (Figure 1.1E), discriminating between parasitic processes involved in SEI growth and ion staging processes involved in energy storage at graphitic anode materials, as shown in Chapter 6.[80]

Hg disc-well probes are ideal for investigating graphitic energy storage materials, where the ionic permeability of the ever-changing SEI is absolutely central to the cycling performance yet poorly understood. The ongoing application of Hg disc-wells in SECM-based studies of energy storage materials is discussed in Chapter 7 along with a presentation of the broader impact of and future outlook for the platform (Figure 1.1F).

1.4 Figure

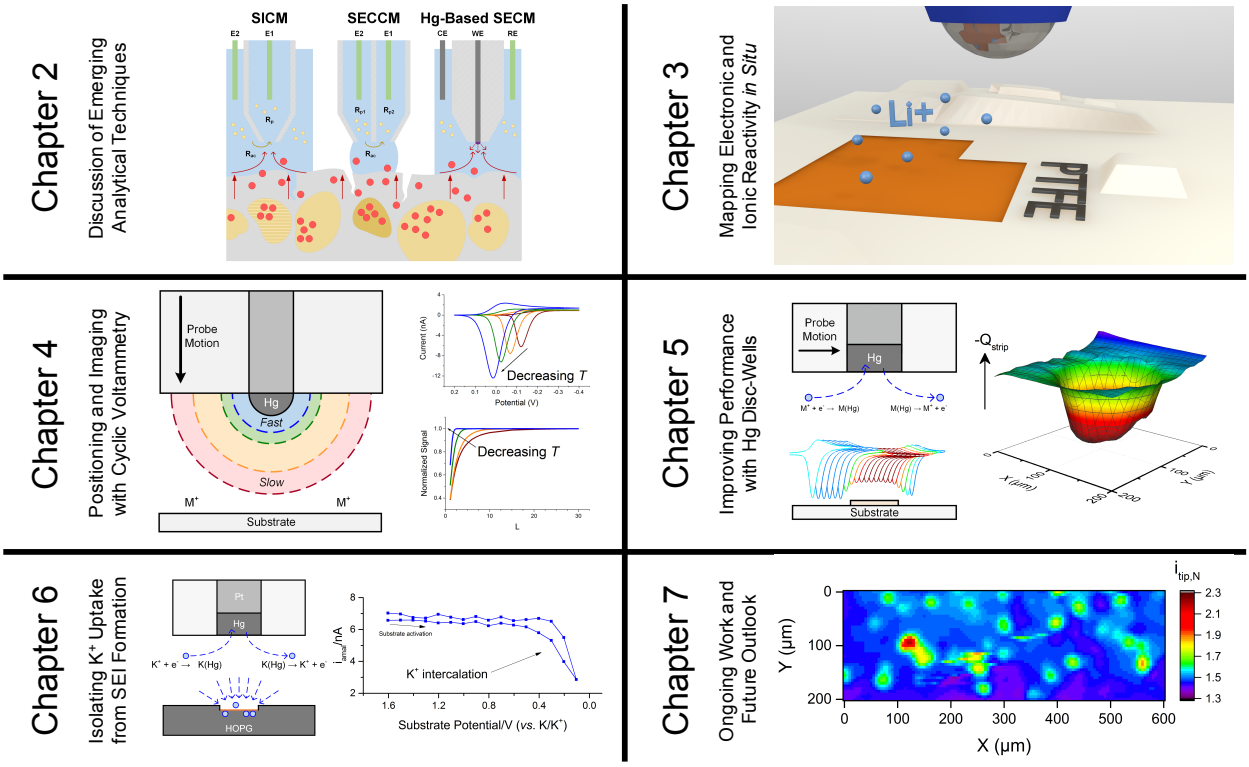

Figure 1.1. (**A**) Chapter 2 is a review article covering various scanning probe methods for investigating energy storage interfaces. Reproduced from Barton and Rodríguez-López[71] with permission. (**B**) Chapter 3 presents Hg-based SECM as a technique for mapping electronic and ionic activity *in situ*. Reproduced from Barton and Rodríguez-López[68] with permission. (**C**) Chapter 4 presents a new strategy for measuring topography and reactivity with Hg-based SECM probes. Reproduced from Barton and Rodríguez-López[78] with permission. (**D**) Chapter 5 introduces the new Hg disc-well geometry for CV-based imaging and compares its performance to that of the more traditional Hg sphere-cap geometry. Reproduced from Barton and Rodríguez-López[79] with permission. (**E**) Chapter 6 applies the techniques introduced in Chapter 4 with the probes developed in Chapter 5 to interrogate a model graphitic anode during electrochemical energy storage. Reproduced from Barton and Rodríguez-López[80] with permission. (**F**) Chapter 7 presents ongoing work and offers an outlook for Hg disc-well probes and time-resolved SECM experiments.

1.5 References

(1) Goodenough, J. B.; Kim, Y. Challenges for Rechargeable Li Batteries. *Chem. Mater.* **2010**, *22*, 587–603.

(2) Goodenough, J. B.; Park, K.-S. The Li-Ion Rechargeable Battery: a Perspective. *J. Amer. Chem. Soc.* **2013**, *135*, 1167–1176.

(3) Daumas, N.; Hérold, A. Sur Les Relations Entre La Notion De Stade Et Les Mécanismes Réactionnels Dans Les Composés D'insertion Du Graphite. *C. R. Seances Acad. Sci., Ser. C* **1969**, *268*, 373–375.

(4) Guerard, D.; Hérold, A. Intercalation of Lithium Into Graphite and Other Carbons. *Carbon* **1975**, *13*, 337–345.

(5) Dresselhaus, M. S.; Dresselhaus, G. Intercalation Compounds of Graphite. *Adv. Phys.* **2002**, *51*, 1–186.

(6) Persson, K.; Sethuraman, V. A.; Hardwick, L. J.; Hinuma, Y.; Meng, Y. S.; van der Ven, A.; Srinivasan, V.; Kostecki, R.; Ceder, G. Lithium Diffusion in Graphitic Carbon. *J. Phys. Chem. Lett.* **2010**, *1*, 1176–1180.

(7) Levi, M. D.; Aurbach, D. Diffusion Coefficients of Lithium Ions During Intercalation Into Graphite Derived From the Simultaneous Measurements and Modeling of Electrochemical Impedance and Potentiostatic Intermittent Titration Characteristics of Thin Graphite Electrodes. *J. Phys. Chem. B* **1997**, *101*, 4641–4647.

(8) Dahn, J. R.; Zheng, T.; Liu, Y.; Xue, J. S. Mechanisms for Lithium Insertion in Carbonaceous Materials. *Science* **1995**, *270*, 590–593.

(9) Wood, K. N.; O'Hayre, R.; Pylypenko, S. Recent Progress on Nitrogen/Carbon Structures Designed for Use in Energy and Sustainability Applications. *Energy Environ. Sci.* **2014**, *7*, 1212–

1238.

(10) Zhao, Y.; Wang, L. P.; Sougrati, M. T.; Feng, Z.; Leconte, Y.; Fisher, A.; Srinivasan, M.; Xu, Z. A Review on Design Strategies for Carbon Based Metal Oxides and Sulfides Nanocomposites for High Performance Li and Na Ion Battery Anodes. *Adv. Energy Mater.* **2016**, *451*, 1601424–1601470.

(11) Subramaniyam, C. M.; Deshmukh, K. A.; Tai, Z.; Mahmood, N.; Deshmukh, A. D.; Goodenough, J. B.; Dou, S. X.; Liu, H. K. 2D Layered Graphitic Carbon Nitride Sandwiched with Reduced Graphene Oxide as Nanoarchitectured Anode for Highly Stable Lithium-Ion Battery. *Electrochim. Acta* **2017**, *237*, 69–77.

(12) Cabana, J.; Monconduit, L.; Larcher, D.; Palacín, M. R. Beyond Intercalation-Based Li-Ion Batteries: the State of the Art and Challenges of Electrode Materials Reacting Through Conversion Reactions. *Adv. Mater.* **2010**, *22*, E170–E192.

(13) Favors, Z.; Wang, W.; Bay, H. H.; Mutlu, Z.; Ahmed, K.; Liu, C.; Ozkan, M.; Ozkan, C. S. Scalable Synthesis of Nano-Silicon From Beach Sand for Long Cycle Life Li-Ion Batteries. *Sci. Rep.* **2014**, *4*.

(14) Li, C.; Liu, C.; Wang, W.; Mutlu, Z.; Bell, J.; Ahmed, K.; Ye, R.; Ozkan, M.; Ozkan, C. S. Silicon Derived From Glass Bottles as Anode Materials for Lithium Ion Full Cell Batteries. *Sci. Rep.* **2017**, 1–11.

(15) Mizushima, K.; Jones, P. C.; Wiseman, P. J.; Goodenough, J. B. Li_xCoO_2 ($0<X\leq1$): a New Cathode Material for Batteries of High Energy Density. *Mater. Res. Bull.* **1980**, *15*, 783–789.

(16) Lu, X.; Zhao, L.; He, X.; Xiao, R.; Gu, L.; Hu, Y.-S.; Li, H.; Wang, Z.; Duan, X.; Chen, L.; Maier, J.; Ikuhara, Y. Lithium Storage in $Li_4Ti_5O_{12}$ Spinel: the Full Static Picture From Electron

Microscopy. *Adv. Mater.* **2012**, *24*, 3233–3238.

(17) Moorhead-Rosenberg, Z.; Huq, A.; Goodenough, J. B.; Manthiram, A. Electronic and Electrochemical Properties of $Li_{1-x}Mn_{1.5}Ni_{0.5}O_4$ Spinel Cathodes as a Function of Lithium Content and Cation Ordering. *Chem. Mater.* **2015**, *27*, 6934–6945.

(18) Whittingham, M. S. Ultimate Limits to Intercalation Reactions for Lithium Batteries. *Chem. Rev.* **2014**, *114*, 11414–11443.

(19) Cogswell, D. A.; Bazant, M. Z. Coherency Strain and the Kinetics of Phase Separation in $LiFePO_4$ Nanoparticles. *ACS Nano* **2012**, *6*, 2215–2225.

(20) Ferguson, T. R.; Bazant, M. Z. Phase Transformation Dynamics in Porous Battery Electrodes. *Electrochim. Acta* **2014**, *146*, 89–97.

(21) Lv, W.; Niu, Y.; Jian, X.; Zhang, K. H. L.; Wang, W.; Zhao, J.; Wang, Z.; Yang, W.; He, W. Space Matters: Li^+ Conduction Versus Strain Effect at $FePO_4/LiFePO_4$ Interface. *Appl. Phys. Lett.* **2016**, *108*, 083901–083905.

(22) Ravnsbæk, D. B.; Xiang, K.; Xing, W.; Borkiewicz, O. J.; Wiaderek, K. M.; Gionet, P.; Chapman, K. W.; Chupas, P. J.; Tang, M.; Chiang, Y.-M. Engineering the Transformation Strain in $LiMn_yFe_{1-y}Po_4$ Olivines for Ultrahigh Rate Battery Cathodes. *Nano Lett.* **2016**, *16*, 2375–2380.

(23) Peled, E. The Electrochemical Behavior of Alkali and Alkaline Earth Metals in Nonaqueous Battery Systems—the Solid Electrolyte Interphase Model. *J. Electrochem. Soc.* **1979**, *126*, 2047.

(24) Edström, K.; Gustafsson, T.; Thomas, J. O. The Cathode–Electrolyte Interface in the Li-Ion Battery. *Electrochim. Acta* **2004**, *50*, 397–403.

(25) Yang, L.; Ravdel, B.; Lucht, B. L. Electrolyte Reactions with the Surface of High Voltage

LiNi[Sub 0.5]Mn[Sub 1.5]O[Sub 4] Cathodes for Lithium-Ion Batteries. *Electrochem. Solid-State Lett.* **2010**, *13*, A95–3.

(26) Norberg, N. S.; Lux, S. F.; Kostecki, R. Interfacial Side-Reactions at a $LiNi_{0.5}Mn_{1.5}O_4$ Electrode in Organic Carbonate-Based Electrolytes. *Electrochem. Commun.* **2013**, *34*, 29–32.

(27) Bai, P.; Li, J.; Brushett, F. R.; Bazant, M. Z. Transition of Lithium Growth Mechanisms in Liquid Electrolytes. *Energy Environ. Sci.* **2016**, *9*, 3221–3229.

(28) Chen, K.-H.; Wood, K. N.; Kazyak, E.; LePage, W. S.; Davis, A. L.; Sanchez, A. J.; Dasgupta, N. P. Dead Lithium: Mass Transport Effects on Voltage, Capacity, and Failure of Lithium Metal Anodes. *J. Mater. Chem. A* **2017**, *00*, 1–11.

(29) Etacheri, V.; Marom, R.; Elazari, R.; Salitra, G.; Aurbach, D. Challenges in the Development of Advanced Li-Ion Batteries: a Review. *Energy Environ. Sci.* **2011**, *4*, 3243–3262.

(30) Fister, T. T.; Esbenshade, J.; Chen, X.; Long, B. R.; Shi, B.; Schlepütz, C. M.; Gewirth, A. A.; Bedzyk, M. J.; Fenter, P. Lithium Intercalation Behavior in Multilayer Silicon Electrodes. *Adv. Energy Mater.* **2014**, *4*, 1301494.

(31) Aurbach, D. Review of Selected Electrode–Solution Interactions Which Determine the Performance of Li and Li Ion Batteries. *J. Pow. Sour.* **2000**, *89*, 206–218.

(32) Verma, P.; Maire, P.; Novák, P. A Review of the Features and Analyses of the Solid Electrolyte Interphase in Li-Ion Batteries. *Electrochim. Acta* **2010**, *55*, 6332–6341.

(33) Pinson, M. B.; Bazant, M. Z. Theory of SEI Formation in Rechargeable Batteries: Capacity Fade, Accelerated Aging and Lifetime Prediction. *J. Electrochem. Soc.* **2012**, *160*, A243–A250.

(34) Tavassol, H.; Jones, E. M. C.; Sottos, N. R.; Gewirth, A. A. Electrochemical Stiffness in Lithium-Ion Batteries. *Nat. Mater.* **2016**, *15*, 1182–1187.

(35) Aurbach, D.; Daroux, M. L.; Faguy, P. W.; Yeager, E. Identification of Surface Films Formed on Lithium in Propylene Carbonate Solutions. **1987**, *134*, 1611–1620.

(36) Nanda, J.; Remillard, J.; O'Neill, A.; Bernardi, D.; Ro, T.; Nietering, K. E.; Go, J.-Y.; Miller, T. J. Local State-of-Charge Mapping of Lithium-Ion Battery Electrodes. *Adv. Funct. Mater.* **2011**, *21*, 3282–3290.

(37) Jaber-Ansari, L.; Puntambekar, K. P.; Tavassol, H.; Yildirim, H.; Kinaci, A.; Kumar, R.; Saldaña, S. J.; Gewirth, A. A.; Greeley, J. P.; Chan, M. K. Y.; Hersam, M. C. Defect Evolution in Graphene Upon Electrochemical Lithiation. *ACS Appl. Mater. Interfaces* **2014**, *6*, 17626–17636.

(38) Sole, C.; Drewett, N. E.; Hardwick, L. J. *In Situ* Raman Study of Lithium-Ion Intercalation Into Microcrystalline Graphite. *Faraday Discuss.* **2014**, *172*, 223–237.

(39) Cohn, A. P.; Muralidharan, N.; Carter, R.; Share, K.; Oakes, L.; Pint, C. L. Durable Potassium Ion Battery Electrodes From High-Rate Cointercalation Into Graphitic Carbons. *J. Mater. Chem. A* **2016**, *4*, 14954–14959.

(40) McArthur, M. A.; Trussler, S.; Dahn, J. R. In Situ Investigations of SEI Layer Growth on Electrode Materials for Lithium-Ion Batteries Using Spectroscopic Ellipsometry. *J. Electrochem. Soc.* **2012**, *159*, A198–A207.

(41) Dahn, J. R. Phase Diagram of Li_xC_6. *Phys. Rev. B* **1991**, *44*, 9170–9177.

(42) Hatchard, T. D.; Dahn, J. R. *In Situ* XRD and Electrochemical Study of the Reaction of Lithium with Amorphous Silicon. **2004**, *151*, A838–A842.

(43) Chueh, W. C.; Gabaly, El, F.; Sugar, J. D.; Bartelt, N. C.; McDaniel, A. H.; Fenton, K. R.; Zavadil, K. R.; Tyliszczak, T.; Lai, W.; McCarty, K. F. Intercalation Pathway in Many-Particle

LiFePO4 Electrode Revealed by Nanoscale State-of-Charge Mapping. *Nano Lett.* **2013**, *13*, 866–872.

(44) Xu, G.-L.; Sheng, T.; Chong, L.; Ma, T.; Sun, C.-J.; Zuo, X.; Liu, D.-J.; Ren, Y.; Zhang, X.; Liu, Y.; Heald, S. M.; Sun, S.-G.; Chen, Z.; Amine, K. Insights Into the Distinct Lithiation/Sodiation of Porous Cobalt Oxide by in Operando Synchrotron X-Ray Techniques and Ab Initio Molecular Dynamics Simulations. *Nano Lett.* **2017**, *17*, 953–962.

(45) Drüe, M.; Seyring, M.; Rettenmayr, M. Phase Formation and Microstructure in Lithium-Carbon Intercalation Compounds During Lithium Uptake and Release. *J. Pow. Sour.* **2017**, *353*, 58–66.

(46) Holtz, M. E.; Yu, Y.; Gunceler, D.; Gao, J.; Sundararaman, R.; Schwarz, K. A.; Arias, T. A.; Abercrombie, S.; Muller, D. A. Nanoscale Imaging of Lithium Ion Distribution During *In Situ* Operation of Battery Electrode and Electrolyte. *Nano Lett.* **2014**, *14*, 1453–1459.

(47) He, K.; Lin, F.; Zhu, Y.; Yu, X.; Li, J.; Lin, R.; Nordlund, D.; Weng, T.-C.; Richards, R. M.; Yang, X.-Q.; Doeff, M. M.; Stach, E. A.; Mo, Y.; Xin, H. L.; Su, D. Sodiation Kinetics of Metal Oxide Conversion Electrodes: a Comparative Study with Lithiation. *Nano Lett.* **2015**, *15*, 5755–5763.

(48) Boebinger, M. G.; Xu, M.; Ma, X.; Chen, H.; Unocic, R. R.; McDowell, M. T. Distinct Nanoscale Reaction Pathways in a Sulfide Material for Sodium and Lithium Batteries. *J. Mater. Chem. A* **2016**, *00*, 1–9.

(49) Li, J.; He, K.; Meng, Q.; Li, X.; Zhu, Y.; Hwang, S.; Sun, K.; Gan, H.; Zhu, Y.; Mo, Y.; Stach, E. A.; Su, D. Kinetic Phase Evolution of Spinel Cobalt Oxide During Lithiation. *ACS Nano* **2016**, *10*, 9577–9585.

(50) Funabiki, A.; Inaba, M.; Ogumi, Z.; Yuasa, S.-I.; Otsuji, J.; Tasaka, A. Impedance Study on the Electrochemical Lithium Intercalation Into Natural Graphite Powder. **1998**, *145*, 172–178.

(51) Mendoza-Hernandez, O. S.; Ishikawa, H.; Nishikawa, Y.; Maruyama, Y.; Sone, Y.; Umeda, M. State of Charge Dependency of Graphitized-Carbon-Based Reactions in a Lithium-Ion Secondary Cell Studied by Electrochemical Impedance Spectroscopy. *Electrochim. Acta* **2014**, *131*, 168–173.

(52) Song, J.; Bazant, M. Z. Electrochemical Impedance of a Battery Electrode with Anisotropic Active Particles. *Electrochim. Acta* **2014**, *131*, 214–227.

(53) Momma, T.; Yokoshima, T.; Nara, H.; Gima, Y.; Osaka, T. Distinction of Impedance Responses of Li-Ion Batteries for Individual Electrodes Using Symmetric Cells. *Electrochim. Acta* **2014**, *131*, 195–201.

(54) Tavassol, H.; Chan, M. K. Y.; Catarello, M. G.; Greeley, J. P.; Cahill, D. G.; Gewirth, A. A. Surface Coverage and SEI Induced Electrochemical Surface Stress Changes During Li Deposition in a Model System for Li-Ion Battery Anodes. **2013**, *160*, A888–A896.

(55) Möller, K. C.; Santner, H. J.; Kern, W.; Yamaguchi, S.; Besenhard, J. O.; Winter, M. In Situ Characterization of the SEI Formation on Graphite in the Presence of a Vinylene Group Containing Film-Forming Electrolyte Additives. *J. Pow. Sour.* **2003**, *119-121*, 561–566.

(56) Harris, S. J.; Lu, P. Effects of Inhomogeneities—Nanoscale to Mesoscale—on the Durability of Li-Ion Batteries. *J. Phys. Chem. C* **2013**, *117*, 6481–6492.

(57) Zampardi, G.; Klink, S.; Kuznetsov, V.; Erichsen, T.; Maljusch, A.; La Mantia, F.; Schuhmann, W.; Ventosa, E. Combined AFM/SECM Investigation of the Solid Electrolyte Interphase in Li-Ion Batteries. *ChemElectroChem* **2015**, *2*, 1607–1611.

(58) Seidl, L.; Martens, S.; Ma, J.; Stimming, U.; Schneider, O. In Situ Scanning Tunneling

Microscopy Studies of the SEI Formation on Graphite Electrodes for Li +-Ion Batteries. *Nanoscale* **2016**, *8*, 14004–14014.

(59) Bülter, H.; Peters, F.; Schwenzel, J.; Wittstock, G. Spatiotemporal Changes of the Solid Electrolyte Interphase in Lithium-Ion Batteries Detected by Scanning Electrochemical Microscopy. *Angew. Chem., Int. Ed.* **2014**, *53*, 10531–10535.

(60) Hui, J.; Burgess, M.; Zhang, J.; Rodríguez-López, J. Layer Number Dependence of Li^+ Intercalation on Few-Layer Graphene and Electrochemical Imaging of Its Solid–Electrolyte Interphase Evolution. *ACS Nano* **2016**, *10*, 4248–4257.

(61) Bülter, H.; Peters, F.; Wittstock, G. Scanning Electrochemical Microscopy for the in Situ Characterization of Solid-Electrolyte Interphases: Highly Oriented Pyrolytic Graphite Versus Graphite Composite. *Energy Technol.* **2016**, *4*, 1486–1494.

(62) Ventosa, E.; Madej, E.; Zampardi, G.; Mei, B.; Weide, P.; Antoni, H.; La Mantia, F.; Muhler, M.; Schuhmann, W. Solid Electrolyte Interphase (SEI) at TiO_2 Electrodes in Li-Ion Batteries: Defining Apparent and Effective SEI Based on Evidence From X-Ray Photoemission Spectroscopy and Scanning Electrochemical Microscopy. *ACS Appl. Mater. Interfaces* **2017**, *9*, 3123–3130.

(63) Ventosa, E.; Wilde, P.; Zinn, A. H.; Trautmann, M.; Ludwig, A.; Schuhmann, W. Understanding Surface Reactivity of Si Electrodes in Li-Ion Batteries by in Operando Scanning Electrochemical Microscopy. *Chem. Commun.* **2016**, *52*, 6825–6828.

(64) Lipson, A. L.; Ginder, R. S.; Hersam, M. C. Nanoscale in Situ Characterization of Li-Ion Battery Electrochemistry via Scanning Ion Conductance Microscopy. *Adv. Mater.* **2011**, *23*, 5613–5617.

(65) Lipson, A. L.; Puntambekar, K.; Comstock, D. J.; Meng, X.; Geier, M. L.; Elam, J. W.; Hersam, M. C. Nanoscale Investigation of Solid Electrolyte Interphase Inhibition on Li-Ion Battery MnO Electrodes via Atomic Layer Deposition of Al_2O_3. *Chem. Mater.* **2014**, *26*, 935–940.

(66) Momotenko, D.; McKelvey, K.; Kang, M.; Meloni, G. N.; Unwin, P. R. Simultaneous Interfacial Reactivity and Topography Mapping with Scanning Ion Conductance Microscopy. *Anal. Chem.* **2016**, *88*, 2838–2846.

(67) Takahashi, Y.; Kumatani, A.; Munakata, H.; Inomata, H.; Ito, K.; Ino, K.; Shiku, H.; Unwin, P. R.; Korchev, Y. E.; Kanamura, K.; Matsue, T. Nanoscale Visualization of Redox Activity at Lithium-Ion Battery Cathodes. *Nat. Commun.* **2014**, *5*, 5450.

(68) Barton, Z. J.; Rodríguez-López, J. Lithium Ion Quantification Using Mercury Amalgams as *In Situ* Electrochemical Probes in Nonaqueous Media. *Anal. Chem.* **2014**, *86*, 10660–10667.

(69) Lai, S. C. S.; Macpherson, J. V.; Unwin, P. R. In Situ Scanning Electrochemical Probe Microscopy for Energy Applications. *MRS Bull.* **2012**, *37*, 668–674.

(70) Ventosa, E.; Schuhmann, W. Scanning Electrochemical Microscopy of Li-Ion Batteries. *Phys. Chem. Chem. Phys.* **2015**, *17*, 28441–28450.

(71) Barton, Z. J.; Rodríguez-López, J. Emerging Scanning Probe Approaches to the Measurement of Ionic Reactivity at Energy Storage Materials. *Anal. Bioanal. Chem.* **2016**, *408*, 2707–2715.

(72) Danis, L.; Gateman, S. M.; Kuss, C.; Schougaard, S. B.; Mauzeroll, J. Nanoscale Measurements of Lithium-Ion-Battery Materials Using Scanning Probe Techniques. *ChemElectroChem* **2016**, *4*, 6–19.

(73) Schwager, P.; Bülter, H.; Plettenberg, I.; Wittstock, G. Review of Local in Situ Probing Techniques for the Interfaces of Lithium-Ion and Lithium-Oxygen Batteries. *Energy Technol.*

2016, *4*, 1472–1485.

(74) Kang, M.; Momotenko, D.; Page, A.; Perry, D.; Unwin, P. R. Frontiers in Nanoscale Electrochemical Imaging: Faster, Multifunctional, and Ultrasensitive. *Langmuir* **2016**, *32*, 7993–8008.

(75) Takahashi, Y.; Kumatani, A.; Shiku, H.; Matsue, T. Scanning Probe Microscopy for Nanoscale Electrochemical Imaging. *Anal. Chem.* **2017**, *89*, 342–357.

(76) Aricò, A. S.; Bruce, P. G.; Scrosati, B.; Tarascon, J.-M.; van Schalkwijk, W. Nanostructured Materials for Advanced Energy Conversion and Storage Devices. *Nat. Mater.* **2005**, *4*, 366–377.

(77) Lindsey, G.; Abercrombie, S.; Denuault, G.; Daniele, S.; De Faveri, E. Scanning Electrochemical Microscopy: Approach Curves for Sphere-Cap Scanning Electrochemical Microscopy Tips. *Anal. Chem.* **2007**, *79*, 2952–2956.

(78) Barton, Z. J.; Rodríguez-López, J. Cyclic Voltammetry Probe Approach Curves with Alkali Amalgams at Mercury Sphere-Cap Scanning Electrochemical Microscopy Probes. *Anal. Chem.* **2017**, *89*, 2708–2715.

(79) Barton, Z. J.; Rodríguez-López, J. Fabrication and Demonstration of Mercury Disc-Well Probes for Stripping-Based Cyclic Voltammetry Scanning Electrochemical Microscopy. *Anal. Chem.* **2017**, *89*, 2716–2723.

(80) Barton, Z. J.; Hui, J.; Schorr, N. B.; Rodríguez-López, J. Detecting Potassium Ion Gradients at a Model Graphitic Interface. *Electrochim. Acta* **2017**, *241*, 98–105.

CHAPTER 2

Emerging Scanned Probe Approaches to the Measurement of Ionic Reactivity at Energy Storage Materials

This chapter was published in *Analytical and Bioanalytical Chemistry*:

Barton, Z. J.; Rodríguez-López, J. Emerging Scanning Probe Approaches to the Measurement of Ionic Reactivity at Energy Storage Materials. *Anal. Bioanal. Chem.* **2016**, *408*, 2707–2715. DOI: 10.1007/s00216-016-9373-7

2.1 Abstract

Many modern energy storage technologies operate *via* the nominally reversible shuttling of alkali ions between an anode and a cathode capable of hosting them. The degradation process that occurs with normal usage is not yet fully understood, but emerging progress in analytical tools may help address this knowledge gap. By interrogating ionic fluxes over electrified surfaces, scanned probe methods may identify features that impact the local cyclability of a material and subsequently help inform rational electrode design for future generations of batteries. Methods developed for identifying ion fluxes for batteries show great promise for broader applications, including biological interfaces, corrosion and catalysis (Figure 2.1).

2.2 Introduction to Energy Storage Materials and Ionic Gradients

Enormous research efforts are focused on developing better battery electrode materials. Identifying connections between the concerted movement of ions and exchange of electrons is a fundamental challenge to battery technology development. This challenge is not unique to the field of energy storage, however, and methods developed for identifying ion fluxes at biological[1-4] and metallurgical interfaces (Figure 2.2) can also be applied to energy storage. For example, a scanning electrochemical microscope

(SECM) equipped with an amperometric ion-selective electrode (ISE) made from a nanopipette has been used to image K^+ channels in living kidney cells.[5] Similarly, an SECM equipped with a potentiometric ISE has been implemented to compare corrosion rates and pitting mechanisms of various Mg-containing automotive alloys.[6] Modern Li-ion batteries deliver usable current by shuttling Li^+ from an Li^+-rich anode (*e.g.*, solid Li or graphite pre-loaded with Li^+) to a Li^+-poor cathode (*e.g.*, $LiCoO_2$ or $LiFePO_4$),[7] where the insertion of Li^+ drives a change in the charge state of a transition metal.[8-10] The anode and cathode have different structures and chemical properties, but they both depend on the interfacial structures and spatially heterogeneous reactivity to cycle reversibly. Let us first consider the anode.

Graphitic materials have captured the interest of much of the scientific community looking for an inexpensive, lightweight, and comparatively stable anode. However, a number of obstacles stand in the way of accessing the full theoretical capacity of graphitic anodes (Figure 2.2). Each charge cycle causes volumetric expansion in the anode as Li^+ inserts. In fact, a full charge can produce as much as a 10% increase in volume.[9] The mechanical stress at the electrode surface associated with Li^+ insertion/deinsertion is exacerbated by the growth of the solid electrolyte interphase (SEI).[11] The SEI is a variegated mix of solvent breakdown products and trapped metal cations.[12-14] Its formation is unavoidable, so a great deal of effort has gone into controlling its thickness,[15] elasticity,[16] and electrical conductivity[17,18] so as to maintain ionic permeability[19] as well as attenuate resistive heating, electrode damage, and capacity fade.[20] When properly controlled, the SEI performs an essential role in allowing anodes to operate under conditions that would otherwise destroy them.

Likewise, the presence of defect sites in the anode material is not inherently detrimental to battery performance. A wealth of evidence suggests that specific defects not only improve battery performance but also are essential to sustained operation. The accessible power density, the long term cyclability, and

overall performance of a metal-ion battery hinges on the properties inherent to localized structural and chemical defects. Elaborate structures are costly, so striking a balance between engineered defects and fabrication price is vital to producing cost-effective energy storage solutions.[21] If we understood the relationships between various spatial heterogeneities and their activity, then we might also be able to optimize electrode materials by engineering their microstructure. An attractive goal, then, is to isolate particular defects and study their inherent properties. However, these defects begin to appear in the first few cycles of the battery and eventually reach a saturation point.[22] The story of cycling stresses and SEI formation carries the same consequences on the cathode side of Li-ion batteries. A structural evolution of the electrode occurs during operation, so the development of defects and the SEI is best observed *in situ*.

The essential common feature of all modern metal ion batteries is that their operation is fundamentally tied to the movement of ions. Unsurprisingly, ionic gradients are therefore a direct measure of the cyclability of a particular material. But accessing ionic gradients *in situ* is not something that many analytical techniques can do. Most measurements, such as spectroscopic techniques, attempt to access ionic information indirectly through its effects. Raman spectroscopy can provide qualitative reports on the presence of defects in graphitic materials as well as changes in the plane-to-plane separation in graphene caused by Li^+ intercalation/deintercalation.[22-24] However, alkali ions themselves are Raman-silent. XRD can reveal the bulk phase composition and interplanar carbon spacing in graphite and relate them to the lithiation staging mechanism.[25] This information is also available *in situ*, as has been demonstrated with amorphous silicon.[26] Together with bulk electrochemical measurements, *in situ* XRD can provide phase diagrams of cathode materials to elucidate best practices for maximizing capacity retention.[27] XPS can identify the presence of metals and map out their abundances and charge states, but only in a high vacuum ($< 10^{-8}$ mbar) sample chamber and not while the battery is operating.

Each analytical tool is useful for answering specific questions about battery operation and performance, but there are some questions that are better answered by scanned probe methods.

2.3 Introduction to Electrochemical Scanned Probe Methods

Electrochemical scanned probe methods are invaluable tools because they provide access to localized measurements of battery *activity*.[28] Information pertaining to the performance of individual defects is lost in bulk measurements, which average the impact of the entire electrode surface on battery performance. For example, the potential-dependent localization of Li^+ at grain boundaries in silicon can be visualized through AFM stress-strain measurements coupled with conductance measurements.[29] Researchers hoping to understand how the SEI impacts Li^+ diffusion[16] or how "hot spots" develop on anistropic particles[30] need to access localized ionic measurements. Bulk measurements are well suited to assessing the viability of any particular battery as a whole but are not sufficient for designing the next generation of batteries.

The SECM was introduced by Bard in 1989 for the purpose of obtaining surface maps of chemical reactivity.[31-33] An SECM consists of a potentiostat operated in conjunction with a micro- or nano-positioning system, which is used to raster a probe electrode, often a Pt, Au, or C microdisk embedded in an insulating sheath, over a substrate and coordinate reactivity to physical structures or chemically modified surface features. Over the past decade, efforts to connect surface topography to reactive heterogeneity have improved in spatial resolution as well as chemical specificity.[34-39] These emerging methods include such prominent examples as scanning ion conductance microscopy (SICM),[40,41] scanning electrochemical cell microscopy (SECCM),[42-44] and Hg-based SECM.[45-47] General schematics of each technique are included in Figure 2.3 to highlight their analytical differences as well as the rich information that can be obtained through electrochemical methods. Each technique fills its own

analytical niche, and their combined progress is helping to move the field of energy storage forward. We will now consider each in turn.

2.4 Scanning Ion Conductance Microscopy (SICM)

SICM was introduced in 1989 as a means of studying nonconducting surfaces and particularly for imaging pores in soft membranes.[48] It originally had two modes of operation: constant height and constant distance. In constant height mode, the probe was rastered through an XY plane at a preselected Z position while collecting the ionic current. On its own, constant height mode fails to decouple this ionic information from topographic effects. For example, the ionic current may decrease over a raised area of graphite even though the reactivity is unchanged. Likewise, the ionic current may decrease over a passivated area of graphite even though the substrate is flat in that area. To isolate topographic effects, SICM also had constant distance mode, wherein the probe is rastered in an XY pattern while the Z-position is modulated by a feedback loop based on the electrical conductance registered at the tip. Raised areas impinge the flow of ions through the tip's orifice, resulting in a drop in electrical conductivity and a subsequent increase in the Z-position (*i.e.*, away from the substrate).

The first application of SICM to the nanoscale study of Li-ion batteries came in 2011 from Mark Hersam's laboratory at Northwestern University.[41] This was performed using the AC mode of SICM, in which a piezo oscillates the probe vertically during the lateral raster scans. Since the resistance between the tip and the substrate is distance-dependent, this motion generates a corresponding oscillation in the probe current. The amplitude of the oscillation serves as a feedback mechanism to correct the vertical probe position. Monitoring the ionic conductance current before and after lithiation of a 60 nm thick tin film on copper revealed the development of nanoscopic spheroidal features (*via* the AC component) as well as an overall boost in the ionic conductance current (*via* the DC component) (Figure 2.4). It is worth noting that while the surface morphology changed, the contrast (relative change) in the DC

current images remained unchanged, though the absolute values in the image were almost uniformly greater. This indicated that (1) the surface activity was unchanged from what it was and (2) there were more ions present near the substrate surface than prior to lithiation. Though it is possible to speculate reasons for this, the end of the matter is that SICM needs to be coupled with supporting analytical techniques to pin down causes for the observed changes in conductivity. Hersam's group has since used SICM to confirm the success of Al_2O_3 films in preventing SEI-induced surface roughening at MnO electrodes after lithiation,[49] though no attempt was made to interpret the SICM data beyond a reference to topography inferred from the AC signal.

There are now more advanced means of acquiring topographic and electrochemical information simultaneously. With respect to methodology, the latest improvement has been to approach the probe to the substrate at each XY position rather than performing an uninterrupted raster image.[2] This method greatly improves SICM's ability to track sharp changes in surface morphology and is sufficiently different from traditional SICM to warrant its own name: hopping probe ion conductance microscopy (HPICM). The reported resolution may be slightly overestimated, since recent work indicates that the fundamental limit for the lateral resolution of SICM-based methods is approximately three times the inner radius of the pipette ($3r_i$).[50] An additional caution is the sensitivity of SICM in solutions of low ionic strength to substrate-induced charging of the nanopipette, which leads to substantial ion current rectification.[51] However, since most biological and battery environments include excess supporting electrolyte, substrate-induced ion current rectification is often easily preventable.

In addition to improvements in methodology, there have also emerged bi-functional probes made from dual-barrel theta pipettes. These use a liquid channel to control position while simultaneously performing amperometric experiments at a carbon nanoelectrode in an SECM-SICM configuration.[52,53]

SICM is superbly equipped for resolving abrupt changes in surface morphology, and its ability to provide 3-dimensional maps of ionic gradients through HPICM is an under-utilized tool that may prove useful in future investigations.

2.5 Scanning Electrochemical Cell Microscopy (SECCM)

More recently (2010), Patrick Unwin's group at the University of Warwick introduced SECCM as a tool for understanding localized heterogeneous reactivity in the context of surface features with minimal background noise.[54] The SECCM is unique in the family of scanned probe methods in that the probe contains the only electrolyte solution. Wherever the probe is brought sufficiently close to a substrate, the meniscus jumps down to contact the surface, forming a miniature electrochemical cell. Retracting and performing a jump to contact at each XY position produces a topographic map that is completely decoupled from surface electrochemical activity.

However, the true power of SECCM is revealed in studies of electroactive substrates. When connected as the working electrode, the substrate current is inherently free from much of the background noise and capacitance associated with large electrodes because only a small region is activated at any given time. This was demonstrated over a cathode material ($LiFePO_4$) for aqueous Li-ion batteries in 2014, when a collaborative effort reported by Takahashi *et al.*[43] created maps of topography combined with surface deintercalation activity (Figure 2.5). The greatly improved signal-to-noise ratio of SECCM as compared to SICM allows for the execution of localized charge and discharge curves as well as galvanostatic time-resolved potential mapping.

Unwin's group has gone on to report the development of quad-barrel SECCM-SECM probes.[55] Though these probes have yet to be applied to energy storage materials or used in organic solvents, they show great promise as aqueous probes.

Though the absence of bulk solvent contact with the substrate provides localized measurements with superb signal-to-noise ratios, a possible criticism of SECCM is that this very same absence prevents representative operating conditions. The composition of the SEI is dependent on cycling history, both for electrochemical and physical reasons. The depth to which the electrode is cycled impacts the staging mechanism for Li intercalation. For example, some Li is consumed by solvent breakdown products at the electrode surface in ways that change over time and with each cycle. Furthermore, the mechanical surface strains placed on the electrode by changes in volume may have a lateral component.[30] There may be many things worth learning from SECCM, but representative SEI behavior may be difficult to access in a traveling cell method. Nevertheless, the unprecedented signal-to-noise ratios gained from miniaturization of the electrochemical cell and the inherent separation of topography and electrochemical activity through jump-to-contact positioning of the probe ensure that SECCM will remain at the forefront of future investigations of ionic fluxes.

2.6 Hg-based Scanning Electrochemical Microscopy (SECM)

Hg-functionalized microelectrodes surfaced in the 1980s,[56] predating even the birth of SECM. However, their use as SECM probes was not reported until the early 2000s.[57,58] Hg-based SECM allows for multiple working electrodes and has been shown to operate in both aqueous[46] and non-aqueous conditions, unlike SICM, which has only been shown to operate under aqueous conditions. SECCM has been shown to operate also in an ionic liquid[59] but has yet to be employed in a typical energy storage environment. Recently, Hg-based SECM was used in the redox competition mode to differentiate between a Au electrode and PTFE on the basis of Li^+ gradients in propylene carbonate as a proxy for battery environments (Figure 2.6).[47] In this configuration, both the Hg-based probe and the conductive substrate are poised at potentials to reduce Li^+ from solution. This platform differs from SICM and

SECCM in that the current registered by the probe is a direct measure of the local Li^+ concentration and not of other ions.

In fact, a further benefit of Hg-based probes is the ability to perform stripping voltammetry. The stripping signal is useful because (1) the ability to preconcentrate ions and increase signal strength allows rapid measurements and promotes high signal-to-noise ratios, which are a distinct concern with nanoscale SICM current measurements,[4] and (2) many metal ions can be differentiated by their signature stripping potential, thereby allowing the simultaneous analysis of multiple metal ions (Figure 2.6). This may become useful in studies of cathode materials, since leaching of metals from the cathode is a known issue.[60] The stripping signal from Hg-based probes has been used for rapid, multi-ion-specific imaging of heavy metals in aqueous solutions before[45] and will soon be reported for alkali metals in non-aqueous solvents by our own laboratory. SICM and SECCM are readily able to decouple topographical and electrochemical information, but they lack the inherent chemical specificity available to Hg-based SECM.

Hg-based SECM investigations are reported with resolutions (3 μm and 10 μm)[45,47] that do not yet match those offered by SICM (30 nm)[41] or SECCM (100 nm),[43] but this does not mean that nanoscale resolution is unattainable with these probes. In fact, we have already demonstrated[47] the feasibility of miniaturization through Hg-functionalized pyrolyzed carbon-based nanopipettes.[61,62]

Though most SECM experiments are still executed in constant height mode, which does not differentiate between changes in the current caused by topography or by electrochemical activity, there are already some reported methods for operating in constant distance mode. These include shear force,[63] AC impedance,[64] and hopping intermittent contact.[65] As Hg-based SECM follows the inexorable march of scanned probe techniques towards nanoscale measurements, it may also adopt these or newer methods for separating surface morphology from reactivity.

2.7 Conclusions

Electrochemical microscopy draws from advanced concepts in charge transfer and ionic conductivity to achieve the imaging of ionic phenomena at battery interfaces. Coupling electrode surface morphology to electrochemical information reveals important relationships that are otherwise difficult to access. In this brief trends article, we've highlighted three emerging electrochemical scanned probe techniques that achieve this. SICM is able to resolve abrupt changes in surface topography, SECCM supports high signal-to-noise measurements, and Hg-based SECM permits the collection of ionic signals with chemical specificity. The story is well advanced for Li-ion batteries, but many questions remain to be answered for Na-ion and K-ion batteries.[66] Since we are just beginning to understand what happens under sodiation and desodiation,[67,68] ion-sensitive scanned probe methods have the potential to make valuable contributions to the development of the next generation of energy storage technologies. These developments will have a broad impact in our ability to address a diversity of interfaces in other fields, such as biology and corrosion science, where understanding ion transport and reactivity at the nanoscale is also essential for understanding function.

2.8 Acknowledgements and Funding Information

Z.J.B. acknowledges the support of the National Science Foundation Graduate Research Fellowship Program (DGE-1144245). Any opinions, findings, and conclusions or recommendations expressed in this material are those of the authors and do not necessarily reflect the views of the National Science Foundation. J.R.-L. acknowledges support from the Joint Center for Energy Storage Research, an Energy Innovation Hub funded by the U.S. Department of Energy, Office of Science, Basic Energy Sciences. The authors also thank UIUC for generous start-up funds.

2.9 Conflict of Interest

The authors declare no conflict of interest.

2.10 Figures

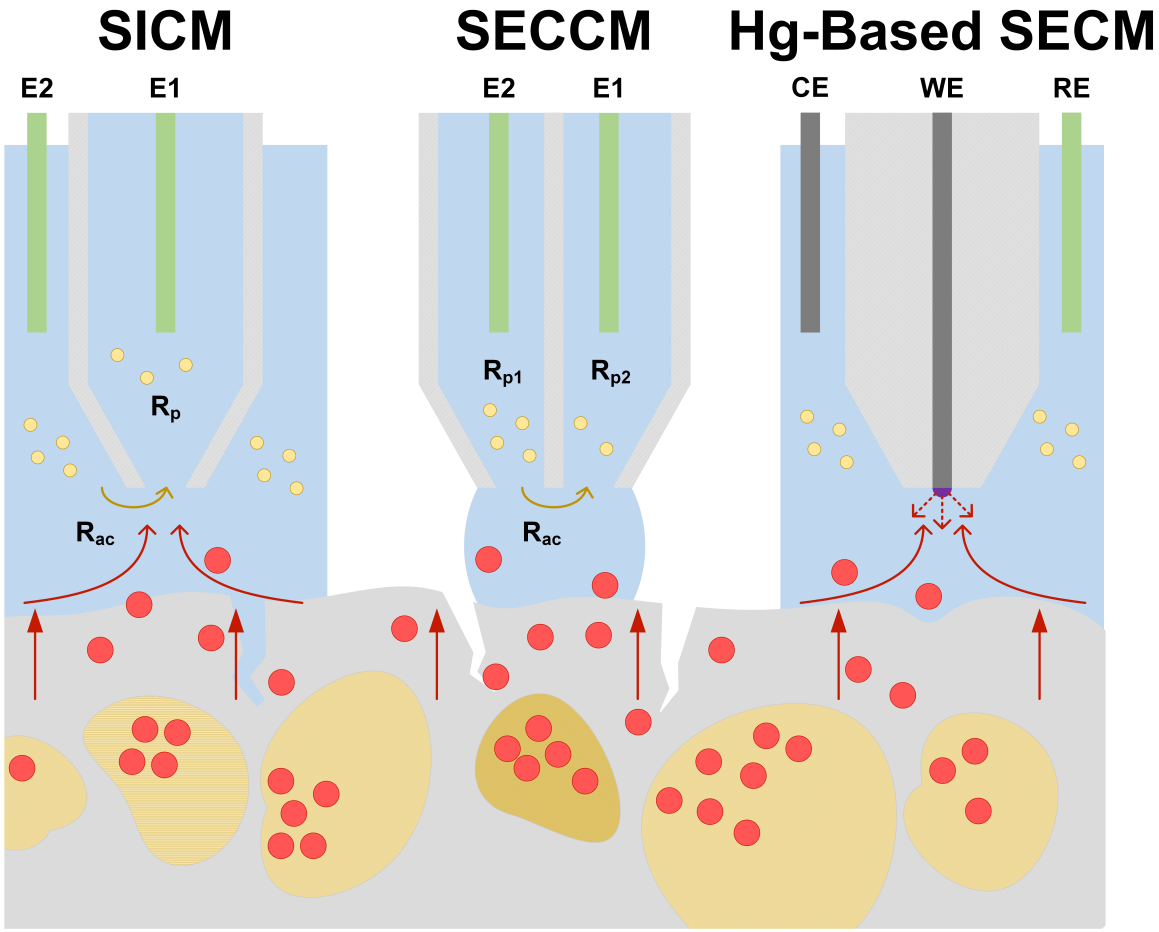

Figure 2.1. Table of contents graphic.

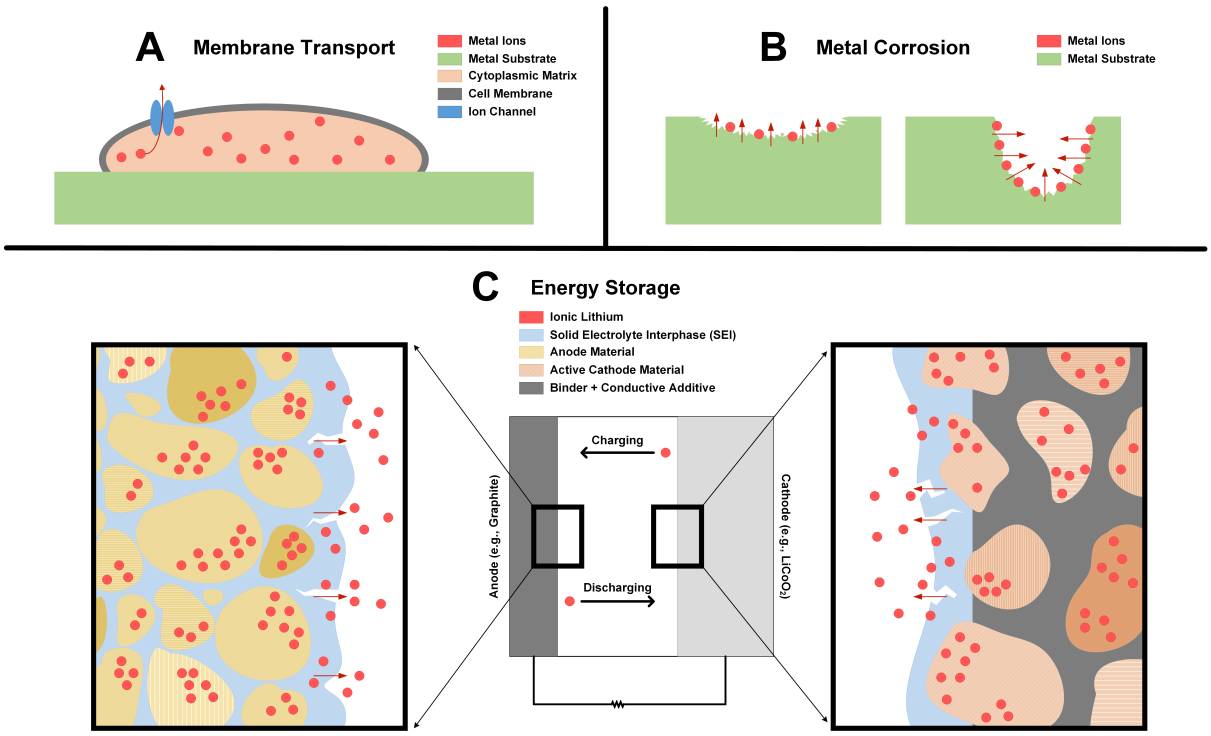

Figure 2.2. Surface-based ionic processes. (**A**) Biological systems rely on a variety of ion transport systems to respond to external stimuli. (**B**) Corrosion and pitting mechanisms are highly dependent on the properties of the metal as well as the chemical environment. (**C**) Schematic of some Li-ion battery reactive heterogeneities, including volumetric strain-induced SEI damage, trapping of Li^+ in the SEI, and the formation of "hot spots" on individual particles. Exfoliation of the graphitic anode can also occur.

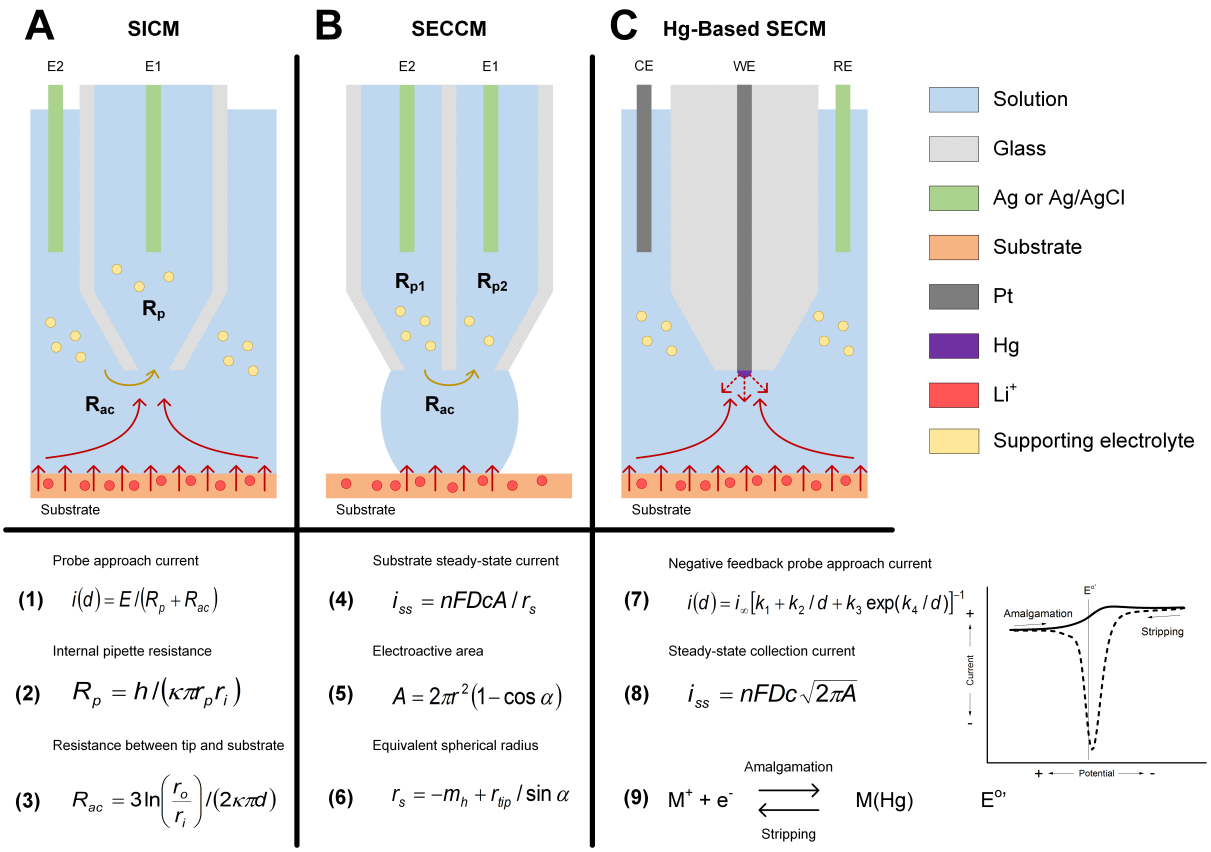

Figure 2.3. Schematics of scanned probe methods discussed in this article. (**A**) The distance-dependent ionic current (i, **equation 1**) observed at an SICM probe shares relationships with the applied potential (E), the internal resistance of pipette (R_p, **equation 2**), and the access resistance of the solution between the probe and the substrate (R_{ac}, **equation 3**). The latter two depend on the length of the tip (h), the conductivity of the solution (κ), the inner radius of the tip base (r_p), the inner (r_i) and outer (r_o) radius of the tip opening, and the tip–substrate gap (d). Topography is obtained by either hopping or oscillating the probe to pinpoint the Z-position at each XY coordinate that produces a particular preset current between the two electrodes. (**B**) After jumping to contact, the meniscus height is maintained monitoring ionic current passing from one pipette channel to the other. When maintaining a constant tip–substrate gap, the steady-state current (i_{ss}, **equation 4**) registered by the substrate working electrode depends on the number of electrons transferred (n), Faraday's constant (F), the diffusion coefficient (D) and concentration (c) of the analyte, the wetted electroactive substrate area (A, **equation 5**), and the equivalent spherical radius of the tip (r_s, **equation 6**). The electroactive substrate area is defined in terms of r_s and the half-cone angle of the tip (α), while r_s shares additional dependencies with the height of the meniscus (m_h) and the internal width of each pipette channel opening (r_{tip}). m_h is identical to the tip–substrate gap (d) only when the meniscus in contact with the both the tip and the substrate. By using a dual-channel pipette, topography can be obtained by monitoring the current flowing between the two channels in the same way used for SICM. However, a major inherent benefit of SECCM is the ability to quickly relocate the substrate surface during hopping due to the absence of current before the meniscus contacts the substrate and completes the electrical circuit. (**C**) The tip–substrate gap can be monitored through negative feedback as described by **equation 7**, where i_∞ is the steady-state current observed in bulk solution, d is the magnitude of the tip–substrate gap, and all four k_n are parameters derived from simulations. The steady-state current observed at a Hg sphere-cap SECM probe is given by **equation 8**. Hg-based SECM is distinguished from SICM and SECCM by the ability to carry out stripping reactions (**equation 9**) to isolate analyte signals and improve sensitivity (see inset).

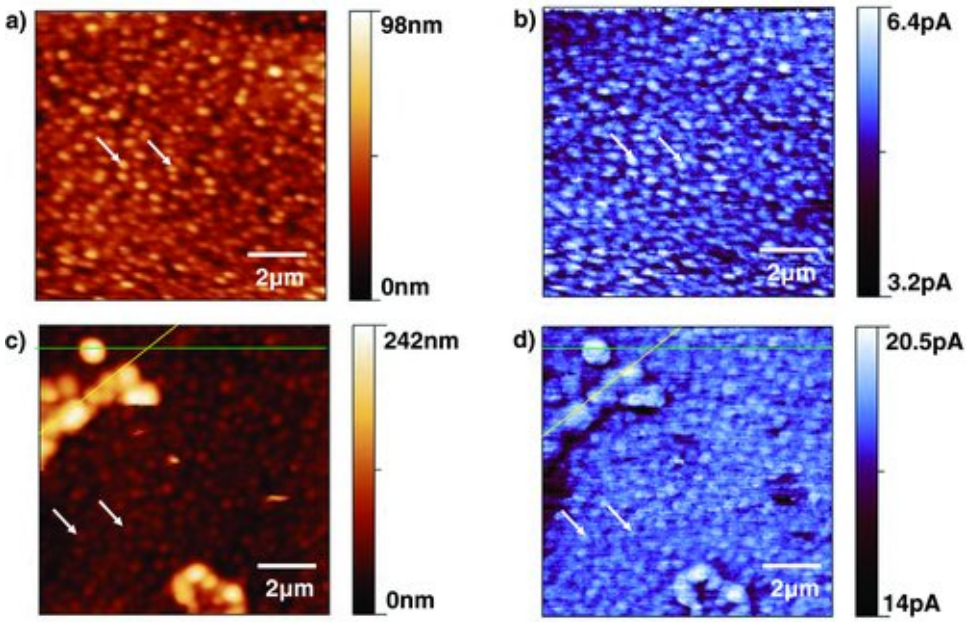

Figure 2.4. SICM (**a**, **c**) topography and (**b**, **d**) DC current images of a 60 nm thick tin thin film deposited on a 60 nm thick copper thin film on glass (**a**, **b**) before lithiation and (**c**, **d**) after 24 μAh cm^{-2} lithiation. Reproduced from Lipson *et al.*[41] with permission.

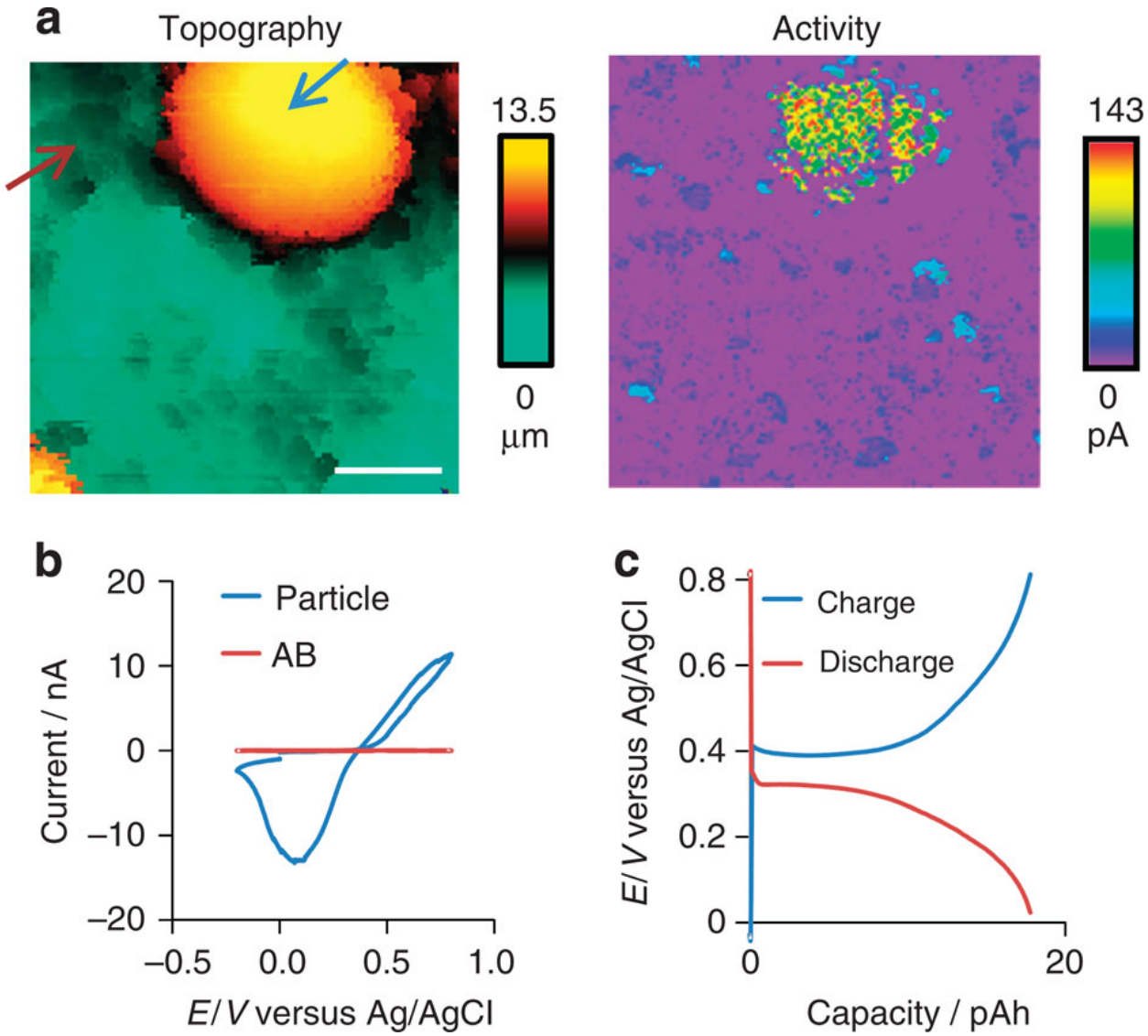

Figure 2.5. (**a**) Simultaneous SECCM topography (*left*) and current (*right*) images. Scan ranges are 20 × 20 µm. The substrate potential was +0.65 V *versus* Ag/AgCl QRCE (Li^+ deintercalation; scale bar, 5 µm). (**b**) CVs at different points on a $LiFePO_4$ electrode surface, corresponding to the blue and red arrow of **a**. Scan rate is 0.1 V s^{-1}. (**c**) Local charge (deintercalation) and discharge (intercalation) characteristics applying current magnitudes of 200 pA in each case *via* SECCM. Reproduced from Takahashi *et al.*[43] with permission.

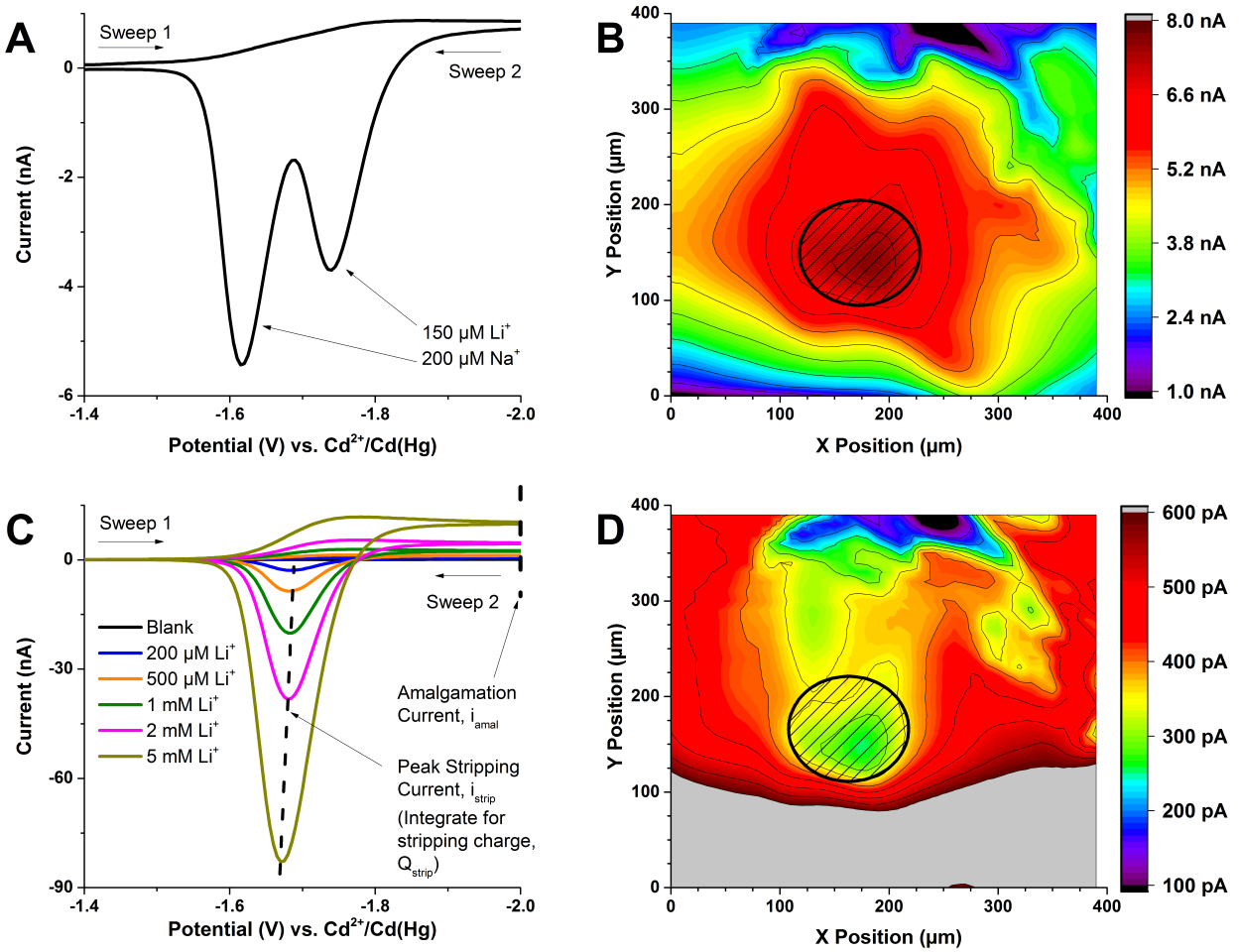

Figure 2.6. Stripping voltammetry (**A**, **C**) of alkali ions in PC by Hg-capped Pt UMEs and SECM images (**B**, **D**) over a 120 μm diameter Au electrode (outlined in black). **A**: Experimental CV of 150 μM Li^+, 200 μM Na^+, and 100 mM TBAP in PC. The current is offset by -400 pA to account for background current. **C**: Representative CVs of $LiClO_4$ and 100 mM TBAP in PC. Integration of the peak stripping current gives the stripping charge. All ν = 100 mV·s^{-1}. **B**: SECM image of ethyl viologen feedback. An increase in redness indicates an increase in substrate activity. **D**: SECM image of Li^+ consumption using redox competition mode. Lithium flux at the tip (E_{Tip} = −2.87 V) responded to activation of the substrate toward lithium reduction (E_{sub} = -3.0 V). An increase in blueness indicates a decrease in free Li^+ concentration. Adapted from Barton and Rodríguez-López.[47]

2.10 References

(1) Scott, E. R.; White, H. S.; Phipps, J. B. Iontophoretic Transport Through Porous Membranes Using Scanning Electrochemical Microscopy: Application to in Vitro Studies of Ion Fluxes Through Skin. *Anal. Chem.* **1993**, *65*, 1537–1545.

(2) Novak, P.; Li, C.; Shevchuk, A. I.; Stepanyan, R.; Caldwell, M.; Hughes, S.; Smart, T. G.; Gorelik, J.; Ostanin, V. P.; Lab, M. J.; Moss, G. W. J.; Frolenkov, G. I.; Klenerman, D.; Korchev, Y. E. Nanoscale Live-Cell Imaging Using Hopping Probe Ion Conductance Microscopy. *Nat. Methods* **2009**, *6*, 279–281.

(3) Shen, M.; Ishimatsu, R.; Kim, J.; Amemiya, S. Quantitative Imaging of Ion Transport Through Single Nanopores by High-Resolution Scanning Electrochemical Microscopy. *J. Amer. Chem. Soc.* **2012**, *134*, 9856–9859.

(4) Chen, C.-C.; Zhou, Y.; Morris, C. A.; Hou, J.; Baker, L. A. Scanning Ion Conductance Microscopy Measurement of Paracellular Channel Conductance in Tight Junctions. *Anal. Chem.* **2013**, *85*, 3621–3628.

(5) Yamada, H.; Haraguchi, D.; Yasunaga, K. Fabrication and Characterization of a K^+-Selective Nanoelectrode and Simultaneous Imaging of Topography and Local K^+ Flux Using Scanning Electrochemical Microscopy. *Anal. Chem.* **2014**, *86*, 8547–8552.

(6) Dauphin-Ducharme, P.; Asmussen, R. M.; Shoesmith, D. W.; Mauzeroll, J. *In-Situ* Mg^{2+} Release Monitored During Magnesium Alloy Corrosion. *J. Electroanal. Chem.* **2015**, *736*, 61–68.

(7) Kang, B.; Ceder, G. Battery Materials for Ultrafast Charging and Discharging. *Nature* **2009**, *458*, 190–193.

(8) Goodenough, J. B.; Kim, Y. Challenges for Rechargeable Li Batteries. *Chem. Mater.* **2010**, *22*, 587–603.

(9) Etacheri, V.; Marom, R.; Elazari, R.; Salitra, G.; Aurbach, D. Challenges in the Development of Advanced Li-Ion Batteries: a Review. *Energy Environ. Sci.* **2011**, *4*, 3243–3262.

(10) Goodenough, J. B.; Park, K.-S. The Li-Ion Rechargeable Battery: a Perspective. *J. Amer. Chem. Soc.* **2013**, *135*, 1167–1176.

(11) Tavassol, H.; Chan, M. K. Y.; Catarello, M. G.; Greeley, J. P.; Cahill, D. G.; Gewirth, A. A. Surface Coverage and SEI Induced Electrochemical Surface Stress Changes During Li Deposition in a Model System for Li-Ion Battery Anodes. **2013**, *160*, A888–A896.

(12) Aurbach, D.; Daroux, M. L.; Faguy, P. W.; Yeager, E. Identification of Surface Films Formed on Lithium in Propylene Carbonate Solutions. **1987**, *134*, 1611–1620.

(13) Verma, P.; Maire, P.; Novák, P. A Review of the Features and Analyses of the Solid Electrolyte Interphase in Li-Ion Batteries. *Electrochim. Acta* **2010**, *55*, 6332–6341.

(14) Norberg, N. S.; Lux, S. F.; Kostecki, R. Interfacial Side-Reactions at a $LiNi_{0.5}Mn_{1.5}O_4$ Electrode in Organic Carbonate-Based Electrolytes. *Electrochem. Commun.* **2013**, *34*, 29–32.

(15) Smith, A. J.; Burns, J. C.; Zhao, X.; Xiong, D.; Dahn, J. R. A High Precision Coulometry Study of the SEI Growth in Li/Graphite Cells. **2011**, *158*, A447–A452.

(16) Aurbach, D. Review of Selected Electrode–Solution Interactions Which Determine the Performance of Li and Li Ion Batteries. *J. Pow. Sour.* **2000**, *89*, 206–218.

(17) Petibon, R.; Sinha, N. N.; Burns, J. C.; Aiken, C. P.; Ye, H.; Van Elzen, C. M.; Jain, G.; Trussler, S.; Dahn, J. R. Comparative Study of Electrolyte Additives Using Electrochemical Impedance Spectroscopy on Symmetric Cells. *J. Pow. Sour.* **2014**, *251*, 187–194.

(18) Wang, D. Y.; Sinha, N. N.; Burns, J. C.; Petibon, R.; Dahn, J. R. A High Precision Study of the Electrolyte Additives Vinylene Carbonate, Vinyl Ethylene Carbonate and Lithium

Bis(Oxalate)Borate in $LiCoO_2$/Graphite Pouch Cells. *J. Pow. Sour.* **2014**, *270*, 68–78.

(19) Persson, K.; Sethuraman, V. A.; Hardwick, L. J.; Hinuma, Y.; Meng, Y. S.; van der Ven, A.; Srinivasan, V.; Kostecki, R.; Ceder, G. Lithium Diffusion in Graphitic Carbon. *J. Phys. Chem. Lett.* **2010**, *1*, 1176–1180.

(20) Zheng, J.; Gu, M.; Xiao, J.; Zuo, P.; Wang, C.; Zhang, J.-G. Corrosion/Fragmentation of Layered Composite Cathode and Related Capacity/Voltage Fading During Cycling Process. *Nano Lett.* **2013**, *13*, 3824–3830.

(21) Darling, R. M.; Gallagher, K. G.; Kowalski, J. A.; Ha, S.; Brushett, F. R. Pathways to Low-Cost Electrochemical Energy Storage: a Comparison of Aqueous and Nonaqueous Flow Batteries. *Energy Environ. Sci.* **2014**, *7*, 3459–3477.

(22) Jaber-Ansari, L.; Puntambekar, K. P.; Tavassol, H.; Yildirim, H.; Kinaci, A.; Kumar, R.; Saldaña, S. J.; Gewirth, A. A.; Greeley, J. P.; Chan, M. K. Y.; Hersam, M. C. Defect Evolution in Graphene Upon Electrochemical Lithiation. *ACS Appl. Mater. Interfaces* **2014**, *6*, 17626–17636.

(23) Inaba, M.; Yoshida, H.; Ogumi, Z.; Abe, T.; Mizutani, Y.; Asano, M. *In Situ* Raman Study on Electrochemical Li Intercalation Into Graphite. **1995**, *142*, 20–26.

(24) Sole, C.; Drewett, N. E.; Hardwick, L. J. *In Situ* Raman Study of Lithium-Ion Intercalation Into Microcrystalline Graphite. *Faraday Discuss.* **2014**, *172*, 223–237.

(25) Dahn, J. R. Phase Diagram of Li_xC_6. *Phys. Rev. B* **1991**, *44*, 9170–9177.

(26) Hatchard, T. D.; Dahn, J. R. *In Situ* XRD and Electrochemical Study of the Reaction of Lithium with Amorphous Silicon. **2004**, *151*, A838–A842.

(27) Chen, Z.; Dahn, J. R. Methods to Obtain Excellent Capacity Retention in $LiCoO_2$ Cycled to

4.5 V. *Electrochim. Acta* **2004**, *49*, 1079–1090.

(28) Lipson, A. L.; Hersam, M. C. Conductive Scanning Probe Characterization and Nanopatterning of Electronic and Energy Materials. *J. Phys. Chem. C* **2013**, *117*, 7953–7963.

(29) Balke, N.; Jesse, S.; Kim, Y.; Adamczyk, L.; Tselev, A.; Ivanov, I. N.; Dudney, N. J.; Kalinin, S. V. Real Space Mapping of Li-Ion Transport in Amorphous Si Anodes with Nanometer Resolution. *Nano Lett.* **2010**, *10*, 3420–3425.

(30) Harris, S. J.; Lu, P. Effects of Inhomogeneities—Nanoscale to Mesoscale—on the Durability of Li-Ion Batteries. *J. Phys. Chem. C* **2013**, *117*, 6481–6492.

(31) Bard, A. J.; Fan, F.-R.; Kwak, J.; Lev, O. Scanning Electrochemical Microscopy. Introduction and Principles. *Anal. Chem.* **1989**, *61*, 132–138.

(32) Bard, A. J.; Denuault, G.; Lee, C.; Mandler, D.; Wipf, D. O. Scanning Electrochemical Microscopy: a New Technique for the Characterization and Modification of Surfaces. *Acc. Chem. Res.* **1990**, *23*, 357–363.

(33) Bard, A. J.; Fan, F.-R.; Pierce, D. T.; Unwin, P. R.; Wipf, D. O.; Zhou, F. Chemical Imaging of Surfaces with the Scanning Electrochemical Microscope. *Science* **1991**, *254*, 68–74.

(34) Sun, P.; Laforge, F. O.; Mirkin, M. V. Scanning Electrochemical Microscopy in the 21st Century. *Phys. Chem. Chem. Phys.* **2007**, *9*, 802–823.

(35) Bertoncello, P. Advances on Scanning Electrochemical Microscopy (SECM) for Energy. *Energy Environ. Sci.* **2010**, *3*, 1620–1633.

(36) Mirkin, M. V.; Nogala, W.; Velmurugan, J.; Wang, Y. Scanning Electrochemical Microscopy in the 21st Century. Update 1: Five Years After. *Phys. Chem. Chem. Phys.* **2011**, *13*, 21196–21212.

(37) Kranz, C. Recent Advancements in Nanoelectrodes and Nanopipettes Used in Combined Scanning Electrochemical Microscopy Techniques. *Analyst* **2014**, *139*, 336–352.

(38) Bülter, H.; Peters, F.; Schwenzel, J.; Wittstock, G. Spatiotemporal Changes of the Solid Electrolyte Interphase in Lithium-Ion Batteries Detected by Scanning Electrochemical Microscopy. *Angew. Chem., Int. Ed.* **2014**, *53*, 10531–10535.

(39) Ventosa, E.; Schuhmann, W. Scanning Electrochemical Microscopy of Li-Ion Batteries. *Phys. Chem. Chem. Phys.* **2015**, *17*, 28441–28450.

(40) Chen, C.-C.; Zhou, Y.; Baker, L. A. Scanning Ion Conductance Microscopy. *Annu. Rev. Anal. Chem.* **2012**, *5*, 207–228.

(41) Lipson, A. L.; Ginder, R. S.; Hersam, M. C. Nanoscale in Situ Characterization of Li-Ion Battery Electrochemistry via Scanning Ion Conductance Microscopy. *Adv. Mater.* **2011**, *23*, 5613–5617.

(42) Ebejer, N.; Güell, A. G.; Lai, S. C. S.; McKelvey, K.; Snowden, M. E.; Unwin, P. R. Scanning Electrochemical Cell Microscopy: a Versatile Technique for Nanoscale Electrochemistry and Functional Imaging. *Annu. Rev. Anal. Chem.* **2013**, *6*, 329–351.

(43) Takahashi, Y.; Kumatani, A.; Munakata, H.; Inomata, H.; Ito, K.; Ino, K.; Shiku, H.; Unwin, P. R.; Korchev, Y. E.; Kanamura, K.; Matsue, T. Nanoscale Visualization of Redox Activity at Lithium-Ion Battery Cathodes. *Nat. Commun.* **2014**, *5*, 5450.

(44) Momotenko, D.; Byers, J. C.; McKelvey, K.; Kang, M.; Unwin, P. R. High-Speed Electrochemical Imaging. *ACS Nano* **2015**, *9*, 8942–8952.

(45) Alpuche-Aviles, M.; Baur, J. E.; Wipf, D. O. Imaging of Metal Ion Dissolution and Electrodeposition by Anodic Stripping Voltammetry−Scanning Electrochemical Microscopy. *Anal. Chem.* **2008**, *80*, 3612–3621.

(46) Souto, R. M.; González-García, Y.; Battistel, D.; Daniele, S. In Situ Scanning Electrochemical Microscopy (SECM) Detection of Metal Dissolution During Zinc Corrosion by Means of

Mercury Sphere-Cap Microelectrode Tips. *Chem. Eur. J.* **2011**, *18*, 230–236.

(47) Barton, Z. J.; Rodríguez-López, J. Lithium Ion Quantification Using Mercury Amalgams as *In Situ* Electrochemical Probes in Nonaqueous Media. *Anal. Chem.* **2014**, *86*, 10660–10667.

(48) Hansma, P.; Drake, B.; Marti, O.; Gould, S.; Prater, C. The Scanning Ion-Conductance Microscope. *Science* **1989**, *243*, 641–643.

(49) Lipson, A. L.; Puntambekar, K.; Comstock, D. J.; Meng, X.; Geier, M. L.; Elam, J. W.; Hersam, M. C. Nanoscale Investigation of Solid Electrolyte Interphase Inhibition on Li-Ion Battery MnO Electrodes via Atomic Layer Deposition of Al_2O_3. *Chem. Mater.* **2014**, *26*, 935–940.

(50) Rheinlaender, J.; Schäffer, T. E. Lateral Resolution and Image Formation in Scanning Ion Conductance Microscopy. *Anal. Chem.* **2015**, *87*, 7117–7124.

(51) Sa, N.; Lan, W.-J.; Shi, W.; Baker, L. A. Rectification of Ion Current in Nanopipettes by External Substrates. *ACS Nano* **2013**, *7*, 11272–11282.

(52) Takahashi, Y.; Shevchuk, A. I.; Novak, P.; Zhang, Y.; Ebejer, N.; Macpherson, J. V.; Unwin, P. R.; Pollard, A. J.; Roy, D.; Clifford, C. A.; Shiku, H.; Matsue, T.; Klenerman, D.; Korchev, Y. E. Multifunctional Nanoprobes for Nanoscale Chemical Imaging and Localized Chemical Delivery at Surfaces and Interfaces. *Angew. Chem., Int. Ed.* **2011**, *50*, 9638–9642.

(53) O'Connell, M. A.; Wain, A. J. Mapping Electroactivity at Individual Catalytic Nanostructures Using High-Resolution Scanning Electrochemical–Scanning Ion Conductance Microcopy. *Anal. Chem.* **2014**, *86*, 12100–12107.

(54) Ebejer, N.; Schnippering, M.; Colburn, A. W.; Edwards, M. A.; Unwin, P. R. Localized High Resolution Electrochemistry and Multifunctional Imaging: Scanning Electrochemical Cell Microscopy. *Anal. Chem.* **2010**, *82*, 9141–9145.

(55) Paulose Nadappuram, B.; McKelvey, K.; Byers, J. C.; Güell, A. G.; Colburn, A. W.; Lazenby, R. A.; Unwin, P. R. Quad-Barrel Multifunctional Electrochemical and Ion Conductance Probe for Voltammetric Analysis and Imaging. *Anal. Chem.* **2015**, *87*, 3566–3573.

(56) Wehmeyer, K. R.; Wightman, R. M. Cyclic Voltammetry and Anodic Stripping Voltammetry with Mercury Ultramicroelectrodes. *Anal. Chem.* **1985**, *57*, 1989–1993.

(57) Selzer, Y.; Mandler, D. Scanning Electrochemical Microscopy. Theory of the Feedback Mode for Hemispherical Ultramicroelectrodes: Steady-State and Transient Behavior. *Anal. Chem.* **2000**, *72*, 2383–2390.

(58) Mauzeroll, J.; Hueske, E. A.; Bard, A. J. Scanning Electrochemical Microscopy. 48. Hg/Pt Hemispherical Ultramicroelectrodes: Fabrication and Characterization. *Anal. Chem.* **2003**, *75*, 3880–3889.

(59) Aaronson, B. D. B.; Byers, J. C.; Colburn, A. W.; McKelvey, K.; Unwin, P. R. Scanning Electrochemical Cell Microscopy Platform for Ultrasensitive Photoelectrochemical Imaging. *Anal. Chem.* **2015**, *87*, 4129–4133.

(60) Danis, L.; Gateman, S. M.; Snowden, M. E.; Halalay, I. C.; Howe, J. Y.; Mauzeroll, J. Anodic Stripping Voltammetry at Nanoelectrodes: Trapping of Mn^{2+} By Crown Ethers. *Electrochim. Acta* **2015**, *162*, 169–175.

(61) Singhal, R.; Bhattacharyya, S.; Orynbayeva, Z.; Vitol, E.; Friedman, G.; Gogotsi, Y. Small Diameter Carbon Nanopipettes. *Nanotechnology* **2009**, *21*, 015304.

(62) Actis, P.; Tokar, S.; Clausmeyer, J.; Babakinejad, B.; Mikhaleva, S.; Cornut, R.; Takahashi, Y.; López Córdoba, A.; Novak, P.; Shevchuck, A. I.; Dougan, J. A.; Kazarian, S. G.; Gorelkin, P. V.; Erofeev, A. S.; Yaminsky, I. V.; Unwin, P. R.; Schuhmann, W.; Klenerman, D.; Rusakov, D. A.; Sviderskaya, E. V.; Korchev, Y. E. Electrochemical Nanoprobes for Single-Cell Analysis. *ACS*

Nano **2014**, *8*, 875–884.

(63) Danis, L.; Snowden, M. E.; Tefashe, U. M.; Heinemann, C. N.; Mauzeroll, J. Development of Nano-Disc Electrodes for Application as Shear Force Sensitive Electrochemical Probes. *Electrochim. Acta* **2014**, *136*, 121–129.

(64) Alpuche-Aviles, M.; Wipf, D. O. Impedance Feedback Control for Scanning Electrochemical Microscopy. *Anal. Chem.* **2001**, *73*, 4873–4881.

(65) Lazenby, R. A.; McKelvey, K.; Unwin, P. R. Hopping Intermittent Contact-Scanning Electrochemical Microscopy (HIC-SECM): Visualizing Interfacial Reactions and Fluxes From Surfaces to Bulk Solution. *Anal. Chem.* **2013**, *85*, 2937–2944.

(66) Luo, W.; Wan, J.; Ozdemir, B.; Bao, W.; Chen, Y.; Dai, J.; Lin, H.; Xu, Y.; Gu, F.; Barone, V.; Hu, L. Potassium Ion Batteries with Graphitic Materials. *Nano Lett.* **2015**, *15*, 7671–7677.

(67) Gu, M.; Kushima, A.; Shao, Y.; Zhang, J.-G.; Liu, J.; Browning, N. D.; Li, J.; Wang, C. Probing the Failure Mechanism of SnO_2 Nanowires for Sodium-Ion Batteries. *Nano Lett.* **2013**, *13*, 5203–5211.

(68) Islam, M. S.; Fisher, C. A. J. Lithium and Sodium Battery Cathode Materials: Computational Insights Into Voltage, Diffusion and Nanostructural Properties. *Chem. Soc. Rev.* **2013**, *43*, 185–204.

CHAPTER 3

Lithium Ion Quantification Using Mercury Amalgams as *in Situ* Electrochemical Probes in Non-Aqueous Media

This chapter was published as an original research article in *Analytical Chemistry*:

Barton, Z. J.; Rodríguez-López, J. Lithium Ion Quantification Using Mercury Amalgams as *in Situ* Electrochemical Probes in Nonaqueous Media. *Anal. Chem.* **2014**, *86*, 10660–10667. DOI: 10.1021/ac502517b

3.1 Abstract

We report on the quantitative, spatially resolved study of ionic processes for energy materials in non-aqueous environments by *in situ* electrochemical means at the micro- and nanoscale. Mercury-capped platinum ultra-microelectrodes (Hg/Pt UMEs) were tested as probes for alkali ions in propylene carbonate (PC) in an oxygen- and water-free environment. Anodic stripping voltammetry (ASV) performed at Hg/Pt UMEs displayed a linear response to Li^+ concentration extending from 20 μM to at least 5 mM. The sensitivities of these probes for ionic lithium are 1.93 pA μM^{-1} and -23.2 pA μM^{-1} by the steady-state amalgamation current and the peak stripping current, respectively. These values showed excellent agreement with simulated results as well as to those obtained experimentally for Cd^{2+} in H_2O. We further explored the interfacial imaging of lithium ion flux at an electrified interface. Scanning electrochemical microscopy (SECM) using Hg/Pt UMEs showed that the steady-state amalgamation of ionic lithium could be used to reliably position a probe close to a substrate. Investigations on a selectively insulated gold electrode in an organic solvent system showcased the response of Hg/Pt UMEs to lithium uptake by an electroactive material. Additionally, lithium stripping voltammetry at Hg

deposits on a 120 nm carbon nanoelectrode demonstrated the possibility of implementing the introduced imaging strategy at the nanoscale. This work opens a way to directly correlate material defects and reactive heterogeneity in energy materials with unprecedented spatial and temporal resolution (Figure 3.1).

3.2 Introduction

Charge transfer across the interface between an electrode and an electrolyte solution involves both electronic and ionic components. Although many aspects of bulk ionic transport in electrochemical cells are well understood,[1-3] the interfacial dynamics of ions in ion-batteries,[4-8] nano-porous separation membranes,[9] and supercapacitors[10]—systems that rely on *heterogeneous* ion transfer—have yet to be elucidated. Progress on this front has been hampered by the paucity of quantitative techniques for detecting interfacial ion fluxes of alkali metals such as Li^+, Na^+, and K^+ in non-aqueous environments.[4,8]

Recent interest in the imaging of electrochemical energy materials in non-aqueous media has fostered the development of different strategies for the localized detection of alkali ion fluxes. Among them are electrochemical strain microscopy (ESM),[11] scanning ion conductance microscopy (SICM),[12,13] and scanning electrochemical microscopy (SECM) approaches that employ solvent decomposition[14] or mediator competition[15] as indirect chemical probes. Alternative ion-sensitive techniques such as those based on the ion transfer across liquid–liquid interfaces[16-19] have also showed promise but seem challenging to implement for alkali ions in non-aqueous media. Most recently, lithium intercalation events have been resolved on the nanoscale in aqueous conditions by coupling an electrochemical thin layer flow cell to a transmission electron microscope (TEM).[20] Each of these approaches has much to recommend it but lacks sufficient chemical specificity or chemo-physical stability to adequately address questions presently facing energy material research.[8,10]

SECM is an emerging technique for probing the *in situ* dynamics of electrochemical energy systems.[21-26] Following our interest in electrode heterogeneity studied by SECM,[27,28] we introduce here an approach for the imaging and quantification of Li^+ flux at an electrified interface in an organic medium. By monitoring electrochemical ion-reduction and stripping reactions at Hg-capped Pt ultra-microelectrodes (UMEs), we also demonstrate the feasibility of our approach for the simultaneous analysis of multiple alkali ions and for its application at the nanoscale.

In aqueous media, Hg-based probes have demonstrated mechanical stability,[29] chemical specificity on the basis of reduction potentials and stripping traits,[30] and reliable current response to rapid changes in potential and ion flux.[31] They also have an unmatched distinction amongst analogous probes for circumventing competing processes, such as solvent decomposition reactions at highly reducing potentials.[32,33] When coupled to SECM, Hg probes facilitate metal-selective reactive imaging.[34] And, the further incorporation of fast-scan anodic stripping voltammetry (ASV) has allowed rapid, micro-resolved interrogations of the electrodeposition and surface corrosion of transition metals in aqueous media over regions measuring hundreds of micrometers on a side.[35,36] In these studies, the ability to controllably concentrate metals in the mercury phase facilitated their quantification from even the most dilute environments, such as near an ion-depleted surface. However, SECMs equipped with Hg-capped probes have never before been used to study Li^+.

Amalgams of lithium and other alkali metals have been studied in diverse media for nearly a century, and the resulting wealth of physical and chemical data[37-40] has enabled our investigation of lithium amalgams to be quantitative. For example, the solubility of alkali amalgams is high and in the case of Li^+ up to 1.33 mol. % (898 mM),[39] which allows operation of Hg/Pt UMEs in fairly concentrated solutions without risking distortion from saturation. Additionally, studies of lithium amalgam dynamics[41,42] determined that the apparent rate constant describing the formation of Li(Hg) from Li^+ in solution can

be adjusted by over seven orders of magnitude—between 9×10^{-9} cm s^{-1} and 1.5×10^{-1} cm s^{-1}—by changing the identities of the solvent and the supporting electrolyte. For solvents commonly used in battery electrodes, *e.g.*, propylene carbonate (PC), this reaction is fast. Armed with solubilities, rate constants, transfer coefficients, and diffusion coefficients, we here extend the application of Hg-capped UMEs to the imaging of alkali ion concentrations at electrified surfaces in organic media for resolving heterogeneous ion-coupled mechanisms in functional energy materials.

3.3 Materials and Methods

3.3.1 Chemicals

Cadmium (stick, ≥99.999%), phosphoric acid (85%), and potassium perchlorate (99%) were obtained from Alfa Aesar. Acetone, isopropanol, nitric acid, and water (ChromAr grade) were obtained from Avantor. Mercury (quadruple distilled, 99.9999%) was obtained from Bethlehem Apparatus Co. Potassium phosphate monobasic (99.5%) was obtained from Fisher Scientific. Agar (bacteriological grade) was obtained from Gibco. Platinum wire (25 μm and 1 mm diameter) and silver wire (1 mm diameter) were obtained from Goodfellow. Acetonitrile (MeCN), cadmium nitrate tetrahydrate, ethyl viologen diperchlorate (98%), ferrocene methanol (FcMeOH, 97%), lithium perchlorate (dry, 99.99% trace metals basis), mercury(II) nitrate monohydrate, polytetrafluoroethylene solution (PTFE, 60 wt. % in H_2O), potassium nitrate (≥99%), potassium phosphate dibasic (≥98.0%), propylene carbonate (PC, anhydrous, 99.7%), sodium perchlorate (≥98%), tetrabutylammonium hexafluorophosphate (≥99.0%), tetrabutylammonium perchlorate (TBAP, ≥99.0%), and *N*,*N*,*N*′,*N*′-tetramethyl-*p*-phenylenediamine (TMPD, 99%) were obtained from Sigma-Aldrich. Acetylene and ultra high purity argon were obtained from S. J. Smith. Undoped silicon wafers were obtained from University Wafer. All chemicals were purchased as A.C.S. reagent grade or better and used as received without further purification. The only

exception to this was the metallic mercury, which was scrubbed with concentrated nitric acid before use in order to remove adventitious impurities.

3.3.2 Electrode Fabrication and Characterization

The fabrication of metal UMEs is delineated elsewhere.[43-45] Briefly, a 25 μm diameter Pt wire was sealed inside a glass capillary with a heated metal coil, connected to a copper-tin lead with silver epoxy (Ted Pella), and then polished with 50 nm alumina particles (CHI) over a microfelt polishing pad. Before polishing, glass at the electrode's apex was removed by sharpening over silicon carbide sandpaper such that the glass-to-electrode ratio, $R_G = r_{total}/r_{Pt}$, was approximately 5. The oxidation of FcMeOH (Figure 3.2A) served as a measure of electrode size and smoothness. A Pt wire CE, agar/KNO_3-bridged KCl-saturated Ag/AgCl RE, and the Pt WE to be assessed were immersed in 0.6 mM FcMeOH with 100 mM aqueous potassium phosphate buffer (K_2HPO_4/KH_2PO_4, pH = 6.9). Then, cyclic voltammetry (CV) was performed, sweeping the applied potential between -0.05 V and +0.25 V (*vs.* Ag/AgCl) at 50 mV s^{-1}. The observed -2 nA steady-state current agreed with the predicted diffusion-limited response of a disk microelectrode,

$$i_{ss} = -4nF\mathrm{r}D_{red}C^*_{red} \quad \textbf{(1)}$$

where n = 1 electron, $F = 9.64853 \times 10^4$ C mol^{-1}, r = 12.5 μm, $D_{red} = 6.7 \times 10^{-10}$ m^2 s^{-1}, and $C_{red}^* = 0.6$ mol m^{-3} in the aforementioned system.[46,47] All working electrodes were polished until their CVs showed equally minimal capacitance.

Hg was deposited on Pt UMEs from an aqueous solution of 10 mM $Hg(NO_3)_2{\cdot}H_2O$, 0.1 M KNO_3, and 0.5 vol. % HNO_3 as described elsewhere.[31,48,49] After confirming the electrode's cleanliness *via* linear sweep voltammetry (LSV) (Figure 3.2B), the deposition process was accomplished by poising the working electrode at -0.1 V (*vs.* Ag/AgCl) for 400 s in a chronoamperometric step (Figure 3.2C). At the

95% confidence level, the mean charge deposited was 61 ± 12 μC, indicating that the mean Hg cap mass was 63 ± 13 ng. Photomicrographs of fabricated electrodes are available as Figure 3.3.

3.3.3 Nanoelectrodes

Preliminary experiments at the nanoscale were performed with Hg-capped carbon nanoelectrodes. A full description of the experimental procedure for making these nanoelectrodes will follow soon from this laboratory, building from a wealth of experimental procedures described in other works.[50-56] Briefly, quartz capillaries (O.D. = 1.0 mm, I.D. = 0.7 mm, Sutter) were pulled on a CO_2 laser-powered puller (Sutter) to yield nanopipettes. Acetylene was flowed through the pipettes at ~1000 °C to yield carbon deposits. Electrodes were then characterized in 6 mM TMPD in 0.2 M tetrabutylammonium hexafluorophosphate in MeCN. Hg deposition was carried out in a manner similar to that used for Pt UMEs.

3.3.4 Electrochemical Characterization

Hg-capped UMEs were used in a three-electrode configuration for alkali ion concentration dependence studies. All nonaqueous experiments of this type were performed in an Argon-filled drybox (UNILab, MBraun) with a Pt wire CE placed in the same compartment as the WE and using a separate compartment for a cadmium amalgam reference (Cd^{2+}/Cd(Hg), CAR, -0.3515 V *vs.* NHE[3]) electrode. The construction and stability of the CAR in organic solvent systems are well documented.[57-60] Though the CAR typically employs $CdCl_2$ and NaCl in conjunction, the present study instead used the nitrate salt of cadmium for its high solubility in PC. Unless otherwise stated, the supporting electrolyte consisted of 100 mM TBAP in PC. Alkali ion spikes were added from 1000× concentrated solutions of the appropriate perchlorate salt dissolved in PC. Full calibration curves using separately prepared Hg-capped UMEs were repeated independently 6 times. The amalgamation and stripping currents were averaged and fit by a linear model to assess the sensitivity and limit of detection (LoD) of the probes.

For the purpose of comparison, the same W-cell was constructed in ambient conditions with 10 mM KNO_3 dissolved in H_2O, and Cd^{2+} stripping experiments were carried out using concentrations between 1 nM and 0.1 mM. Ambient ASV work and electrode fabrication was carried out with a CHI 660 potentiostat. All experiments involving lithium were performed with a CHI 920D workstation.

Nanoscale Hg electrodes were tested in a solution of PC containing 1 mM $LiClO_4$ without additional supporting electrolyte. CV was performed with the potential paused at -3.2 V (*vs.* Pt QRE) at the end of the cathodic sweep for 20 seconds before continuing with the anodic return sweep.

3.3.5 Fitting of SECM Probe Approach Curves

Probe approach curves made with sphere-cap electrodes were fit in accordance with the method reported by Lindsey *et al.*,[61] which was in part derived from the use of shape factors to treat steady-state currents at sphere-cap microelectrodes by Myland *et al.*[62] Originally, the current (i_{tip}) registered at the probe was expressed as

$$\frac{i_{\mathrm{tip}}(d)}{i_{\mathrm{tip},\infty}} = \frac{1}{k_1 + k_2 \cdot a/d + k_3 \cdot \exp\left(k_4 \cdot a/d\right)} \tag{2}$$

or

$$\frac{i_{\mathrm{tip}}(d)}{i_{\mathrm{tip},\infty}} = \frac{1}{k_1 + k_2/L + k_3 \cdot \exp\left(k_4/L\right)} \tag{3}$$

where $i_{\mathrm{tip},\infty} = i_{\mathrm{tip}}(d \to +\infty)$, L is the tip–substrate separation, d, expressed in terms of the basal cap radius, a, and all four k_n values are analytically determined constants and only valid for specific values of L and H, which is the cap height, h, expressed in terms of the basal cap radius.

Because the particular software used to control the approach to the substrate reports the tip–substrate separation as a relative value, the above equation had to be adjusted to account for mismatch between the recorded distances reflected in the abscissa and the true distances in the experiment. This

was accomplished by the inclusion of a fudge factor (s) that is equivalent to the difference between the input final value of d and the true final value of d. Recall that d is a variable, not a constant parameter.

$$i_{\text{tip}}(d) = \frac{i_{\text{tip},\infty}}{k_1 + k_2 \cdot a/(s+d) + k_3 \cdot \exp\left(k_4 \cdot a/(s+d)\right)} \quad \textbf{(4)}$$

Using equation **(4)**, all parameters were held as fixed except for $i_{\text{tip},\infty}$ and s, and the resulting fudge factor was applied to a copy of the original dataset to rectify the tip–substrate distance. The transposed dataset was then fit as before but with the fudge factor held fixed as zero to obtain the true ending tip–substrate separation.

3.3.6 SECM in Redox Competition Mode

A Au-sputtered silicon wafer was selectively insulated with a thin PTFE coat (Figure 3.4), the procedure for which is described elsewhere.[63] The initial approach of a Hg/Pt UME to a PTFE-coated area of the substrate was performed in the feedback mode in PC containing 5.00 mM ethyl viologen diperchlorate as the redox mediator. After locating an electroactive region of bare Au by imaging in positive feedback mode, the cell was thoroughly rinsed and then filled with 1 mM $LiClO_4$ in PC. All SECM approach curves and images were collected with a Ag QRE to minimize crowding in the electrochemical cell. All associated potentials have been reported *vs.* CAR for consistency by matching Li stripping potentials. With the tip poised at -2.7 V (*vs.* CAR), the collection of Li^+ by the probe was used as the feedback mechanism to facilitate its approach to the substrate.

When near the substrate, a CV was run at the substrate with the tip held at -2.7 V (*vs.* CAR) to verify that the amalgamation current (i_{amal}) was sensitive to Li^+ uptake at the substrate. To better visualize the competition between the substrate and the tip, CVs were also run at the tip with the substrate biased at different potentials.

3.3.7 Digital Simulations

Simulations of binary Li amalgams were performed with a COMSOL Multiphysics model, which is described in detail in Appendix A. In short, we simulated a Hg droplet suspended at an SECM tip with dimensions representative of experimental values. Electrode reactions were modeled on Butler–Volmer kinetics, and a triangular potential waveform was applied as is done in cyclic voltammetry. The currents resulting from the amalgamation and stripping processes, as well as the charge passed during stripping were compared to those obtained experimentally. All of the parameters required for simulating the studied systems were taken from the literature and are reported in Table 3.1.[39,42,64-69]

3.4 Results and Discussion

3.4.1 Chemical Selectivity

Although the simultaneous reduction of alkali ions in PC requires a cathodic excursion to very reducing potentials, Hg/Pt UMEs do not sacrifice the chemical specificity that typifies stripping voltammetry. For example, Li^+ and Na^+ can be simultaneously quantified from the stripping current each produces. A CV experiment at 100 $mV \cdot s^{-1}$ in PC containing 150 μM Li^+, 200 μM Na^+, and 100 mM TBAP demonstrates clear stripping peak separation (Figure 3.5A). While the cathodic current corresponding to the amalgamation of the two alkali ions (Figure 3.5A) cannot easily distinguish their relative contributions, the stripping portion of the CV is better able to resolve them. Thus, while the steady-state amalgamation of ions can be used for the total quantification of alkali ions, the stripping signal can be used to provide chemical specificity. This makes it also possible to analyze for K^+ in the presence of either Li^+ or Na^+ (Figure 3.6). We now focus on the ability of Hg-capped electrodes to quantitatively detect the most reducing metal in the alkali family: Li.

3.4.2 Sensitivity

Pursuant to characterizing the sensitivity and LoD of Hg/Pt UMEs for Li, CV was performed in solutions of 100 mM TBAP in PC spiked with $LiClO_4$ over the range of 1 nM to 5 mM. The resulting voltammograms (Figure 3.5B) display a monotonic increase of both i_{amal} (Figure 3.7A) and i_{strip} (Figure 3.7B) as the solution ion concentration increases. The averaged results of six independent calibration curve measurements carried out with different Hg deposits in individually prepared W-cells are shown in Figure 3.7. A similar plot for the stripping charge is provided as Figure 3.8. The linear relationships (Table 3.2) derived from these concentration studies over a range of 20 μM to 5 mM allow the extrapolation of ion fluxes from measurements of current in SECM images. As expected, the preconcentration of analyte by amalgamation gives i_{strip} a substantially higher sensitivity to changes in concentration than otherwise obtainable. The experimental i_{amal} obeys the behavior described by Myland and Oldham[62] (see equation 13 therein) for a mass-transport limited process at a sphere-cap type electrode. Furthermore, results extracted from COMSOL simulations agree with the experimental i_{amal} and i_{strip}. Also, it is noteworthy that despite the possibility of forming diverse Li(Hg) phases,[40] the CV can be explained by a single reduction and stripping process occurring at approximately -1.67 V (*vs.* CAR) over a wide concentration range.

The sensitivity of Hg/Pt UMEs to Li^+ in PC was compared to their sensitivity to Cd^{2+} in water, since the latter system is commonly used and well characterized.[38,70-72] Typical cadmium stripping voltammograms are provided in Figure 3.9. Assuming that the solvated radius of Li^+ is essentially the same in water as it is in PC and that the same is true of Cd^{2+}, then Walden's rule, $D_1 \cdot \eta_1 = D_2 \cdot \eta_2 = constant$, holds true.[73] This is not an insignificant assumption, given the kinetic importance of the solvent and supporting electrolyte as reported by Baranski and Fawcett,[41] but it appears to be justifiable by its

efficacy. Differences in ionic charges and in the kinematic viscosities of H_2O (0.890 mPa s) and PC (2.516 mPa s) are therefore corrected by the calculation:

$$i_{\mathrm{Cd,corr}} = \frac{1}{2} \cdot \frac{0.890}{2.516} \cdot i_{\mathrm{Cd,raw}} \qquad (5)$$

Cadmium stripping experiments yielded viscosity-corrected sensitivities of 1811 pA μM^{-1} and 25791 pA μM^{-1} (Figure 3.10). These are only 12.1% and 5.7% different from those obtained from i_{amal} and i_{strip}, respectively, for lithium. Therefore, the sensitivity of Hg/Pt UMEs for the model system of Cd^{2+} in H_2O is not significantly different from that for Li^+ in PC. The agreement between experimental Li and Cd sensitivities as well as the linearity of i_{amal} and i_{strip} in a practical concentration range encouraged us to use this system for quantitative analysis.

3.4.3 Limit of Detection

The LoD for a method resulting in a linear calibration model of the form $y(x) = m \cdot x + b$ can be approximated by LoD = $3 \cdot s_b/m$, where s_b is the standard error in the ordinate-intercept and m is the slope of the fit. The LoDs based on this calculation are reported in Table 3.2. These results demonstrate that the detection of Li^+ can be performed over at least two orders of magnitude of concentration in PC and that good linearity is observed at concentrations below 5 mM. In individual concentration studies, Li^+ was detected down to 20 μM with a LoD as low as 19 μM by i_{amal} and 28 μM by i_{strip}. In comparison, the LoD from COMSOL simulations was 0.53 μM by i_{amal} and 3.1 μM by i_{strip}. This concentration range (19 μM to 5 mM) is well suited for recreating the main features of Li^+ intercalation and deposition processes.

3.4.4 Imaging of Reactivity

In order to test the *in situ* capabilities of Hg/Pt UMEs, competitive lithium stripping was performed in a battery-like environment, where lithium was electrodeposited on Au to mimic the uptake of lithium

by battery electrodes during operation. To locate an electroactive area, a Hg sphere-cap UME was first approached to a distance of 26.2 μm ($2.3 \cdot r_{Pt}$) over an insulating substrate region in PC containing 5.00 mM ethyl viologen diperchlorate (Figure 3.11). The fitting parameters are provided in Table 3.3. The identification of an electroactive region (Figure 3.12) was then facilitated by ethyl viologen's reduction at the Au substrate (E_{sub} = -0.5 V) and regeneration at the Hg/Pt UME tip (E_{tip} = +0.0 V). Once the SECM tip was aligned with an active portion of the Au substrate, the PTFE cell was rinsed twice with clean PC and then filled with 1 mM $LiClO_4$ in PC so that local changes in Li^+ concentration in response to substrate activation could be studied.

The amalgamation current at the Hg/Pt tip responded to electrochemical activity at the substrate. While positioned near the center of the 120 μm diameter electroactive Au spot (bold circle in Figure 3.3 and Figure 3.5) and poised at -2.7 V (*vs.* CAR), the Hg-capped probe reported i_{amal} to be 1.18 nA, 0.50 nA, and -0.03 nA when the substrate CV reached +0.7 V, -0.8 V, and -3.0 V (*vs.* CAR), respectively (Figure 3.13B). Thus, as the substrate was swept to greater overpotentials for lithium reduction, the tip collection current decreased in response. This relationship became the foundation of the imaging technique presented in this work.

Redox competition was exhibited not only in the tip collection current but also in the tip stripping current. A tip CV gave i_{strip} as -2.79 nA, -1.51 nA, and -0.47 nA when the substrate was poised at +1.0 V, -0.8 V, and -3.0 V (*vs.* CAR), respectively (Figure 3.13C). The stripping current provides solid confirmation that the electrochemical changes observe are due to the decrease in the local Li^+ concentration rather than presence of other additive cathodic processes, such as solvent decomposition.

Since the present system contained only one amalgam-forming species and because competing chemical processes did not constitute a significant portion of i_{amal}, the chemical specificity afforded by

fast scan CV or chronoamperometry was not necessary for this particular case. Therefore, the more accessible of the two parameters—the amalgamation current—was selected to investigate Li^+ flux.

The amalgamation of lithium served as a reliable electrochemical process for monitoring the tip–substrate distance *via* negative feedback. An approach curve performed in 1 mM $LiClO_4$ in PC (Figure 3.13A) showed the characteristic decrease in Li^+ flux at the probe on nearing the substrate surface. The probe was positioned at a tip–substrate separation of 23.8 μm ($1.9 \cdot r_{Pt}$) based on fitting to an established mathematical model[61] for sphere-cap electrodes. Specific approach curve fitting parameters can be found in Table 3.3. The ability to monitor the probe's position through the amalgamation of lithium makes Hg-capped electrodes practical for SECM in non-aqueous environments.

Spatial differences in Li^+ concentration are detectable by the Hg/Pt UME as differences in i_{amal}. The central region of exposed electroactive Au substrate is not spatially resolved when biased at +1.0 V (*vs.* CAR) (Figure 3.14A). Decreases in the tip current caused by impingement of the Hg cap by physically elevated features on the substrate revealed some PTFE debris, and overall the image shows only the effects of negative feedback. With the substrate biased at -0.8 V (*vs.* CAR) (Figure 3.14B), the electroactive Au region remained indistinguishable from the surrounding PTFE-coated regions. However, the local Li^+ concentration decreased in response to the activation of the substrate electrode, thus establishing the sensitivity of the probe to the consumption of Li^+ by Au. Lastly, with the substrate biased at -3.0 V (*vs.* CAR) (Figure 3.14C), the electroactive Au region became apparent as a circular region of low Li^+ concentration centered near [X, Y] = [175 μm, 150 μm]. The conditions in Figure 3.14C were repeated with a slower tip velocity to emphasize the spatial heterogeneity in the Li^+ concentration gradient due to competition with the electroactive portion of the substrate. The resulting electrochemical map (Figure 3.14D) clearly indicates a Li^+-depleted region localized at the electroactive

Au spot. The arc of low tip current from PTFE debris near [X, Y] = [200 μm, 380 μm] continued to provide assurance that the substrate and Hg/Pt UME were in good alignment.

The tip current when passing over the electroactive spot was 1.84 nA, 0.81 nA, and 0.50 nA when the substrate was poised at +1.0 V, -0.8 V, and -3.0 V (*vs.* CAR). Therefore, the substrate behaved as expected from substrate CVs (Figure 3.13B) when either fully deactivated or fully activated. Since the stationary and mobile currents agree, the mercury probe appears to be mechanically stable during lateral movement.

One possible shortcoming of continuously monitoring the i_{amal} is that there is no way for lithium to leave the mercury phase during the imaging process. Chronoamperometric simulations in COMSOL (Figure 3.15) indicated that the 3.1 pL Hg sphere-cap used in Figure 3.14 reaches saturation within 193 s when biased at -2.7 V (*vs.* CAR) in 1 mM $LiClO_4$. Since the data in Figure 3.14ABC were collected by rastering in 20 μm steps at 100 ms intervals (200 μm s^{-1}), the total Li^+ collection times were 82 s (accounting for the return scans). This translates into an internal lithium concentration of 396 mM, or 44% of the solubility limit. This supports the notion that decreases in i_{amal} used to create the electrochemical maps in Figure 3.14ABC were truly caused by depletion of surface-localized Li^+ due to uptake by the substrate and not merely spurious associations caused by saturation of the probe.

The high-resolution SECM image of Li^+ flux (Figure 3.14D) also suggests that the Hg-capped probe did not cause any surface corrosion. Dilute Li(Hg) amalgams have been shown to corrode and penetrate PTFE surfaces,[74] such as the insulating coating on the Au substrate or the body of the electrochemical cell. Additionally, Au electrodes have been shown to reduce PTFE when poised at -2.2 V (*vs.* Ag/AgCl) in DMF.[75] However, comparing the initial substrate surface in ethyl viologen diperchlorate (Figure 3.12) to its state after several rounds of Li^+-based imaging (Figure 3.14D) suggests that the surface topography and electrode size were unaltered over the course of imaging. Thus, any corrosion of PTFE into LiF by

either lithium amalgam or the Au electrode was negligible, and future work with energy materials should be similarly free from this contamination.

Interestingly, the high-resolution dataset presented in Figure 3.14D was taken with v_{tip} = 50 μm s^{-1} (10 μm per 200 ms). The collection time then was 642 s, which corresponds to 2.81 M lithium in the amalgam and exceeds the 898 mM lithium solubility limit. One possible explanation for the continued operation of the probe under such long collection times may be the formation of lithium-rich phases in the amalgam.[40] If so, this could help account for small shifts in the reduction potential and stripping peak shape under concentrated conditions (> 2 mM $LiClO_4$) and slow scan rates (< 50 mV s^{-1}). The probe's stability, then, is maximized under internally dilute conditions—achievable through fast scan rates and low bulk analyte concentrations. In order to facilitate high resolution, large area investigations, future work will aim to replace the constant potential imaging conditions with a fast-scan CV approach, such as the one demonstrated by Alpuche-Aviles *et al.*[35] This will allow access to the selectivity information afforded by the stripping current and also prevent the saturation of the amalgam by lithium.

3.4.5 Nanostripping Experiments

It is desirable to increase the spatial resolution of the Hg-capped electrodes presented here. Ongoing work in the authors' laboratory aims to identify ideal conditions for reliably fabricating carbon-based nanoelectrodes (Figure 3.16). An example of Li^+ stripping at an Hg deposit on a 120 nm C electrode is shown in Figure 3.17. Integration of the Li stripping peak gives 5.48 pC, which corresponds to 52.9 amol Li in a 9 fL Hg drop (on the basis of the integration of the Hg deposition current). This amounts to 5.9 mM Li in the amalgam prior to stripping. This result demonstrates the feasibility of ASV at the nanoscale and suggests that amalgam saturation will not hamper SECM investigations based on the redox competition mode. We will soon employ these SECM probes to interrogate materials more recognizably applicable to energy storage and do so with reduced complications from diffusional broadening.

3.5 Conclusions

We have shown here for the first time the ability to electrochemically quantify lithium and other alkali ions in a non-aqueous medium for spatially resolved studies using SECM. Individual Hg/Pt UMEs have exhibited responses to as low as 20 μM Li^+ in PC with no additional time required to concentrate the amalgam beyond the ~6 s spent sweeping the potential in CVs run at 100 mV s^{-1}. The linear range of the probes, which extends over at least 2 orders of magnitude (20 μM Li^+ to 5 mM Li^+), permits their reliable operation in highly dynamic environments. And, the 1.93 pA μM^{-1} sensitivity of their amalgamation current to Li^+ concentration ensures good resolution of differences in Li^+ flux. This is even more the case by the peak stripping current, which boasts a 23.2 pA μM^{-1} sensitivity to ionic lithium. Furthermore, because of the chemical specificity of ASV, the possibility of quantifying Li^+ and other alkali ions simultaneously is well within reach.

Using PTFE-coated Au in PC as a proxy for electrode materials, Hg/Pt UMEs have identified surface features at the microscale by differences in the local Li^+ flux. Probe-substrate distance was monitored by the amalgamation of lithium at the tip and approaches to the substrate were fit with an existing model for negative feedback at sphere-cap UMEs.[61] The agreement between stationary and mobile probe currents attests to their mechanical stability. The absence of substrate corrosion and the continued operation of the probe beyond the reported saturation concentration for lithium amalgams together confirm the chemical stability of the Hg-capped UMEs.

Hg-based probes afford rapid, reliable, and robust quantification of alkali ions in conditions that are inaccessible to alternative approaches. A characterization of the sensitivity, useful range, and LoD for other s-block metals in organic media is forthcoming. Additionally, efforts to extend the application of Hg-capped probes to the nanoscale were introduced here and are an ongoing subject of study in our laboratory for a variety of energy material investigations.

3.6 Acknowledgements

This material is based upon work supported by the National Science Foundation Graduate Research Fellowship Program under Grant No. DGE-1144245. Any opinions, findings, and conclusions or recommendations expressed in this material are those of the authors and do not necessarily reflect the views of the National Science Foundation. This work was also supported as part of the Joint Center for Energy Storage Research, an Energy Innovation Hub funded by the U.S. Department of Energy, Office of Science, Basic Energy Sciences. The authors also thank UIUC for generous start-up funds. The authors are grateful to Teresa C. Cristarella for assistance with preparing the insulated gold substrate, Dr. Mei Shen for valuable discussion, and Burton H. Simpson for the use of several carbon-based nanoelectrodes.

3.7 Figures and Tables

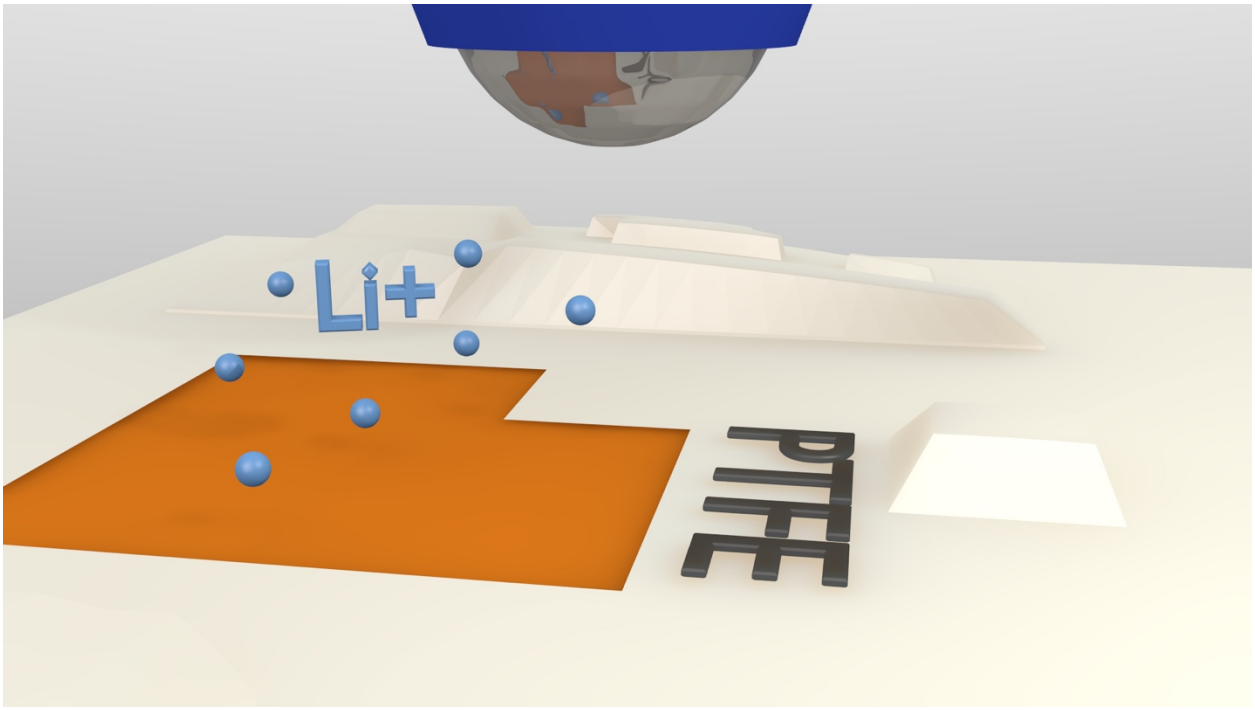

Figure 3.1. Table of contents graphic.

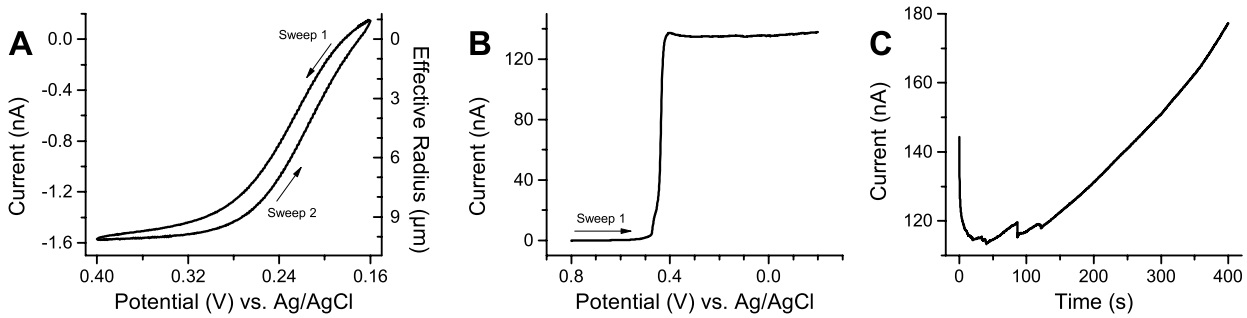

Figure 3.2. (**A**): The magnitude of the steady-state oxidation current (1.55 nA) at a Pt UME in an aqueous solution of 600 μM FcMeOH (D_{red} = 6.7 × 10^{-6} cm^2 s^{-1}) and 100 mM potassium phosphate buffer (K_2HPO_4/KH_2PO_4, pH = 6.9) corresponds to an electroactive disk having a radius of 10 μm. (**B**): LSV run at 50 $mV{\cdot}s^{-1}$ showing that Hg deposition begins around +0.45 V (*vs.* Ag/AgCl). (**C**): The current response to a constant potential of -0.1 V (*vs.* Ag/AgCl) over the course of 400 s illustrates the nucleation of discrete Hg drops (0 s to 10 s), the agglomeration of small Hg droplets into larger, unified drops (10 s to 130 s), and the steady vertical growth (increasing *h* with nearly constant *r*) of a single, combined Hg drop (130 s to 400 s). The value of 400 s was selected over the previously reported value[49] of 300 s in order to obtain a height-to-radius ratio approximating unity, which is characteristic of truly hemispherical caps. Integration of the *i*-t curves indicated an average mass of 63 ± 13 ng per Hg cap. This agreed well with the optically determined value of 66 ± 23 ng per Hg cap (Figure 3.3).

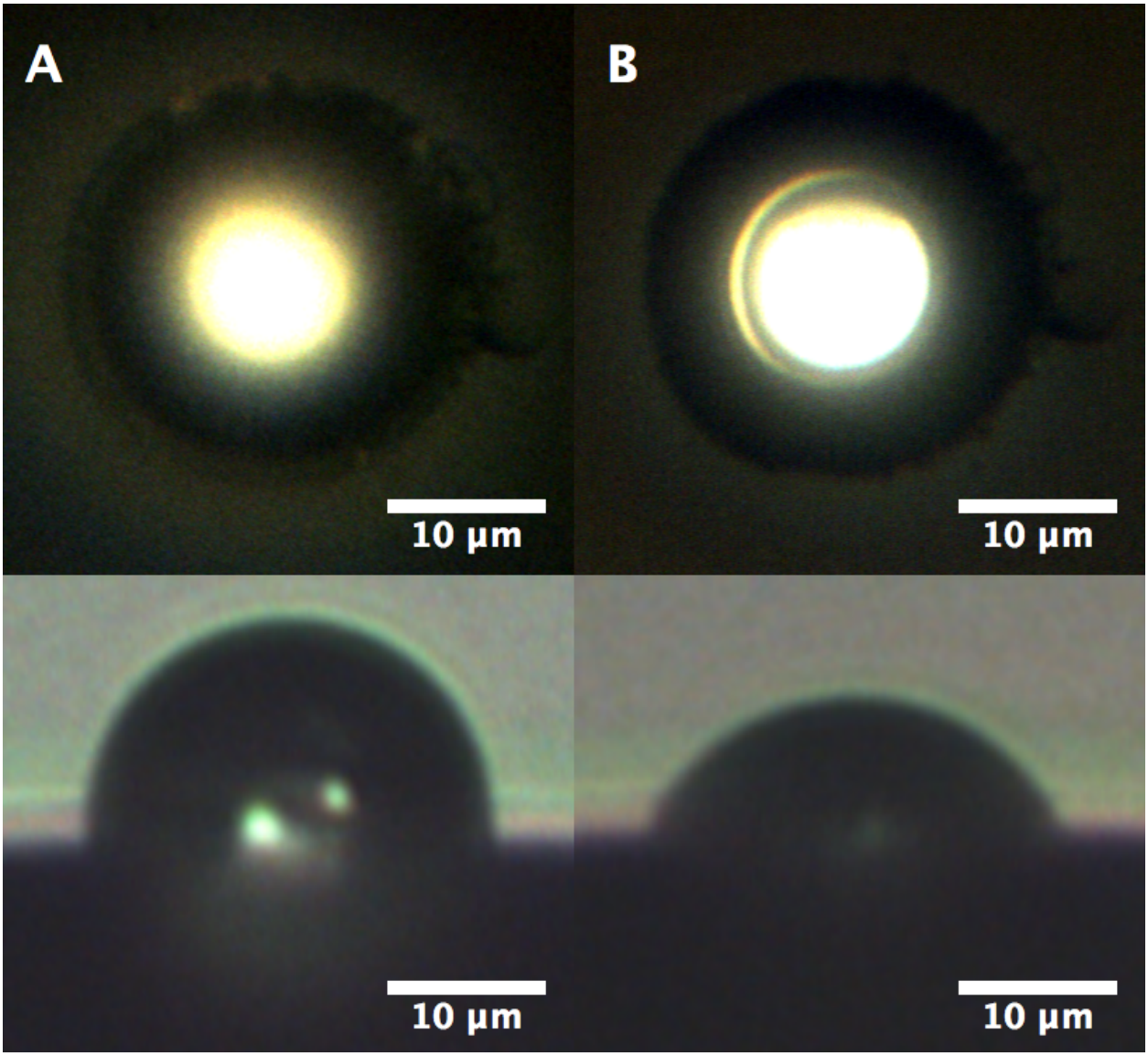

Figure 3.3. Optical micrographs of a Hg/Pt UME before (**A**) and after (**B**) many hours of electrochemical experimentation. The cap height decreased (38% change), but the basal radius remained relatively unchanged (5% change). This demonstrates the mechanical stability of the Hg-capped probes. The cap was deposited by a 400 s chronoamperogram with the Pt UME (nominally 25 µm across) poised at -0.1 V (*vs.* Ag/AgCl) in 13.9 mM $Hg(NO_3)_2{\cdot}H_2O$ + 0.12 M KNO_3 + 0.5 vol. % HNO_3 in H_2O.

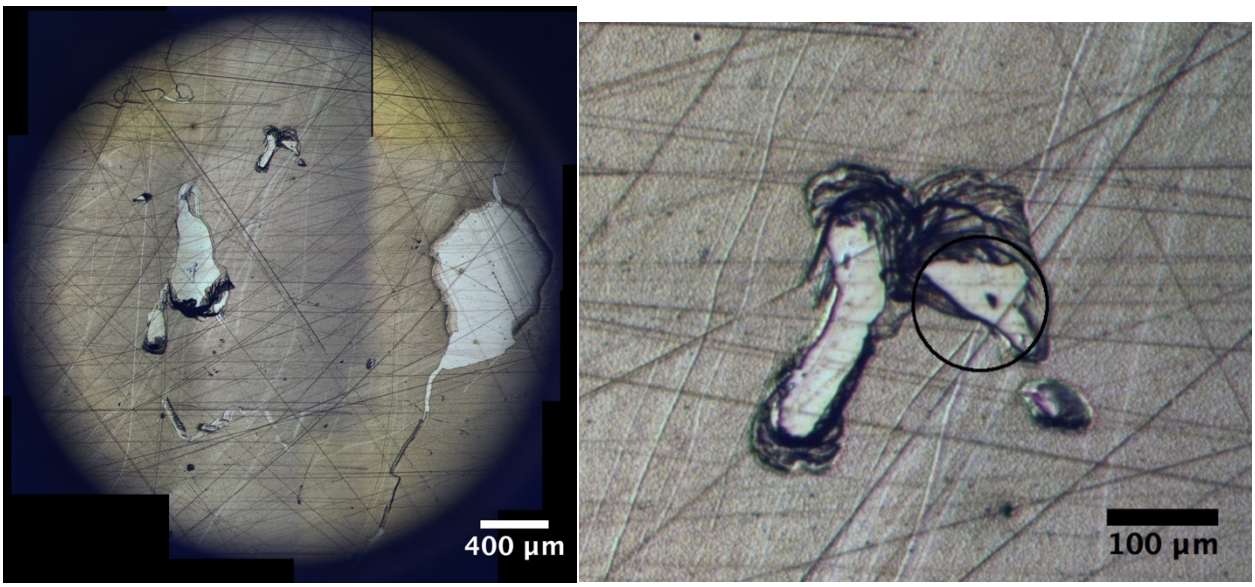

Figure 3.4. Image of combined photomicrograph tiles of the Au/PTFE substrate taken immediately prior to the electrochemical studies presented in Figure 3.11, Figure 3.12, Figure 3.13, and Figure 3.14. The underlying gold substrate (blue tinted regions) is considerably scratched. The PTFE (grey regions) did not break away from the surface perfectly, which resulted in some areas of insulating debris. Though not executed perfectly in the present study, the technique for creating insulated microelectrode arrays has been successfully employed in the past.[63] The quality of the exposed electrode spots is not a topic of particular interest to the present work. The most likely site of interrogation discussed in this work is shown in greater detail (though with the same magnification) on the right.

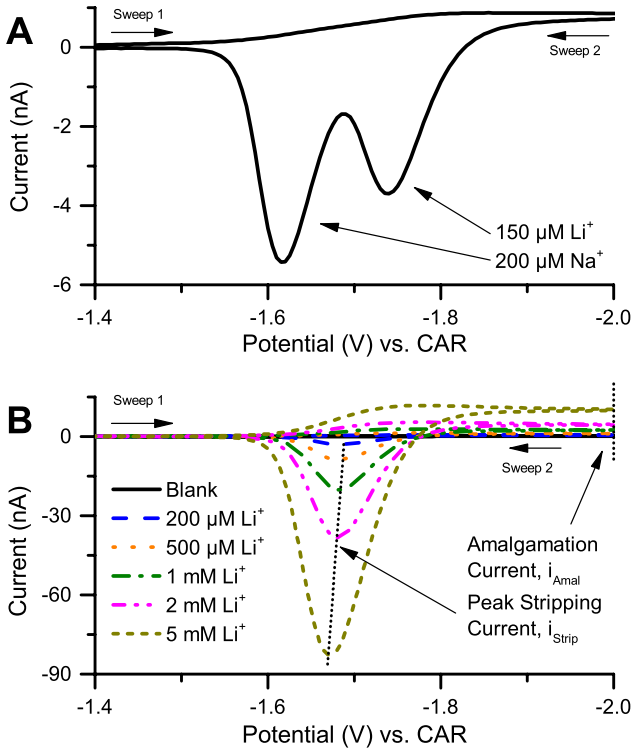

Figure 3.5. Stripping voltammetry of alkali ions in PC by Hg-capped Pt UMEs. (**A**) Experimental CV of 150 μM Li^+, 200 μM Na^+, and 100 mM TBAP in PC. The current is offset by −400 pA to account for background current. (**B**) Representative CVs of $LiClO_4$ and 100 mM TBAP in PC. All ν = 100 mV s^{-1}.

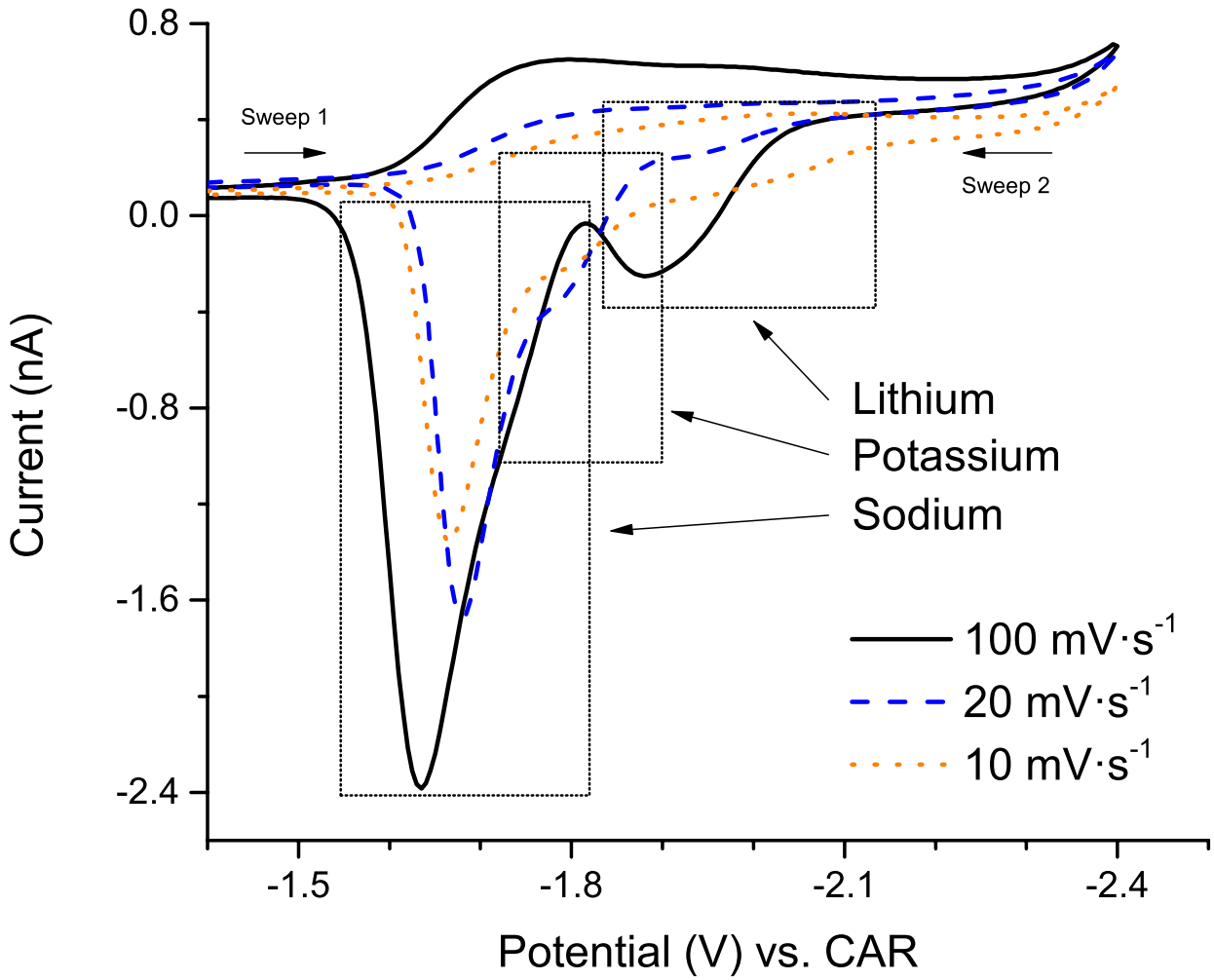

Figure 3.6. Stripping voltammograms of 0.1 mM $LiClO_4$, 0.1 mM $NaClO_4$, and 0.1 mM $KClO_4$ in PC containing 100 mM TBAP as supporting electrolyte. The broadening of the stripping peaks and their small separation makes the simultaneous analysis of Li, Na, and K untenable except at impractical voltage sweep rates ($\nu \leq 20$ mV s^{-1}). However, detection of any two of these species in the absence of additional amalgam-forming moieties is eminently feasible (see Figure 3.5).

	Li^+	Na^+
E^o in H_2O (mV, *vs.* SHE) [66]	-2195.1 ± 0.3	-1958.92 ± 0.23
E^o in PC (mV, *vs.* CAR) †	-1630 (-1710 ‡)	-1580
$D_{M+(PC)}$ (10^{-6} cm^2 s^{-1}) [64]	2.4 §	2.0 ◊
$D_{M(Hg)}$ (10^{-6} cm^2 s^{-1}) [65,69]	9.2	8.4
k_{PC}^o (cm s^{-1}) [42,64]	0.01 §	(>1) ◊
α [42,64]	0.7 §	(0.5) ◊
Solubility Limit (mol. %) [39,68]	1.33	5.40
Hg Cap Basal Radius (μm) †	12.1 (Li + Hg)	12.9 (Li + Na + Hg)
Hg Cap Volume (pL) †	4.6 (Li + Hg)	2.5 (Li + Na + Hg)
Hg Cap Mass (ng) †	61.9 (Li + Hg)	33 (Li + Na + Hg)

† Experimentally determined

‡ For the tertiary amalgam presented in Figure 3.5A, where Li^+ is reduced into a preexisting amalgam of Na and Hg

§ Cronnolly *et al.*[67] report that $D_{PC} = 1.7 \times 10^{-6}$ cm^2 s^{-1}, $k_{PC}^o = 7.7 \times$ 10-3 cm s^{-1} and $\alpha = 0.72$ for Li^+ in 0.2 M TBAP in PC.

◊ Hills and Peter[64] report data for Na^+ in 0.5 M TBAP in PC. This work, however, was done in 0.1 M TBAP in PC. Also, Hills and Peter were unable to report exact values for the rate constant and transfer coefficient because the peak potential did not vary with the voltage sweep rate in CVs, even at 1000 V s^{-1}. Therefore, digital simulations in this work have assumed that $k_{PC}^o = 1$ cm s^{-1} and $\alpha = 0.5$.

Table 3.1. Relevant amalgam kinetic parameters for digital simulations performed in COMSOL.

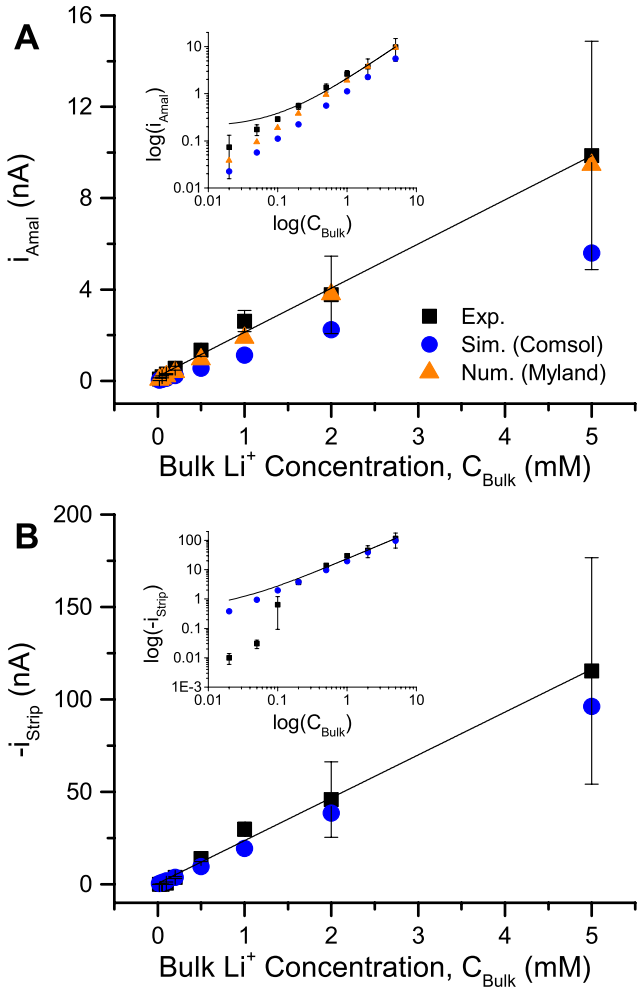

Figure 3.7. Calibration curves for the detection of Li^+ by the amalgamation current (**A**) and stripping peak current (**B**) at Hg/Pt UMEs. The error bars represent the standard deviation about the mean of six independent data sets and do not account for the 21% variance in the Hg cap volume.

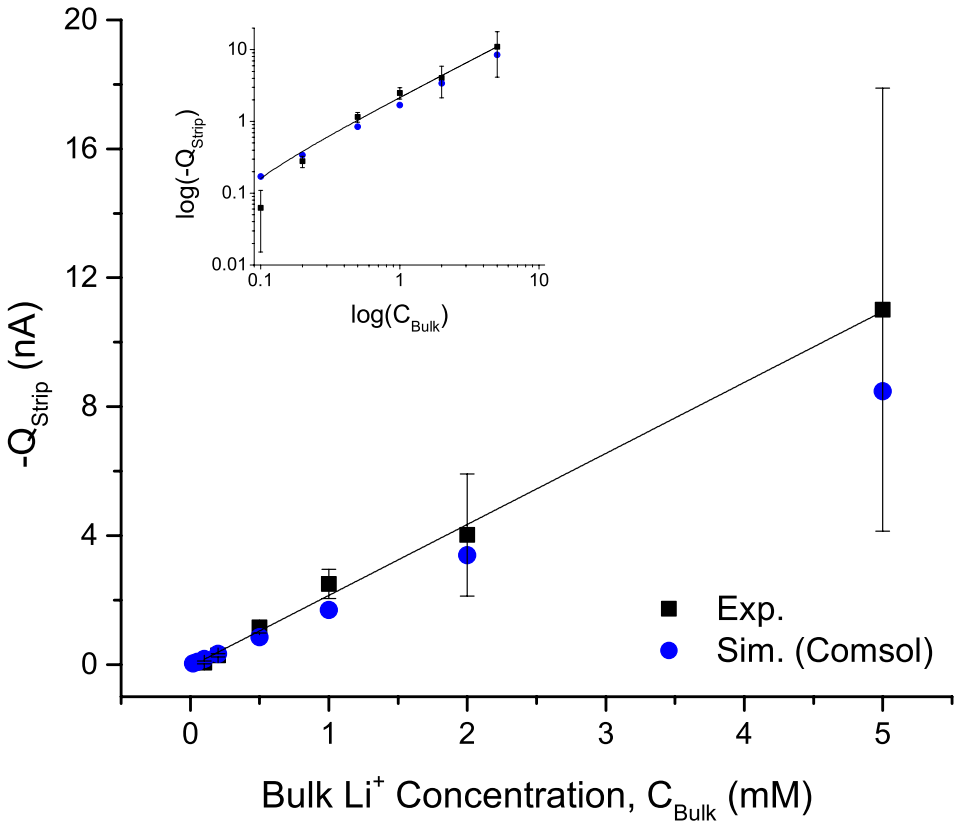

Figure 3.8. Calibration curves for integrated stripping charge response to Li^+ concentration using $LiClO_4$ in PC containing 100 mM TBAP as supporting electrolyte. Experimental: slope = 2.20 pC μM^{-1}, intercept = -59 pC, R_{adj}^2 = 0.99597, LoD = 192 µM. COMSOL: slope = 1.6990 pC μM^{-1}, intercept = -0.55 pC, R_{adj}^2 = 1, LoD = 3.0 µM.

Signal, y	m (pA μM^{-1})	s_m	b (pA)	s_b	R_{adj}^2	LoD (μM), 6 Exps.	LoD (μM), 1 Exp.
$i_{amal, exp.}$	1.93	0.058	191	112	0.9938	174.2	19 †
$i_{amal, sim. (COMSOL)}$	1.11744	5.3e-5	0.1	0.2	1	--	0.53
$i_{amal, num. (Myland)}$	1.89	--	0	--	--	--	--
$-i_{strip, exp.}$	23.2	0.65	465	1272	0.9946	164.7	28 †
$-i_{strip, sim. (COMSOL)}$	19.295	5.3e-3	-2	20	1	--	3.1

† Extrapolated from an analyte concentration range of 20 μM to 100 μM.

Table 3.2. Linear fits of experimental and simulated Li^+ amalgamation and stripping behavior.

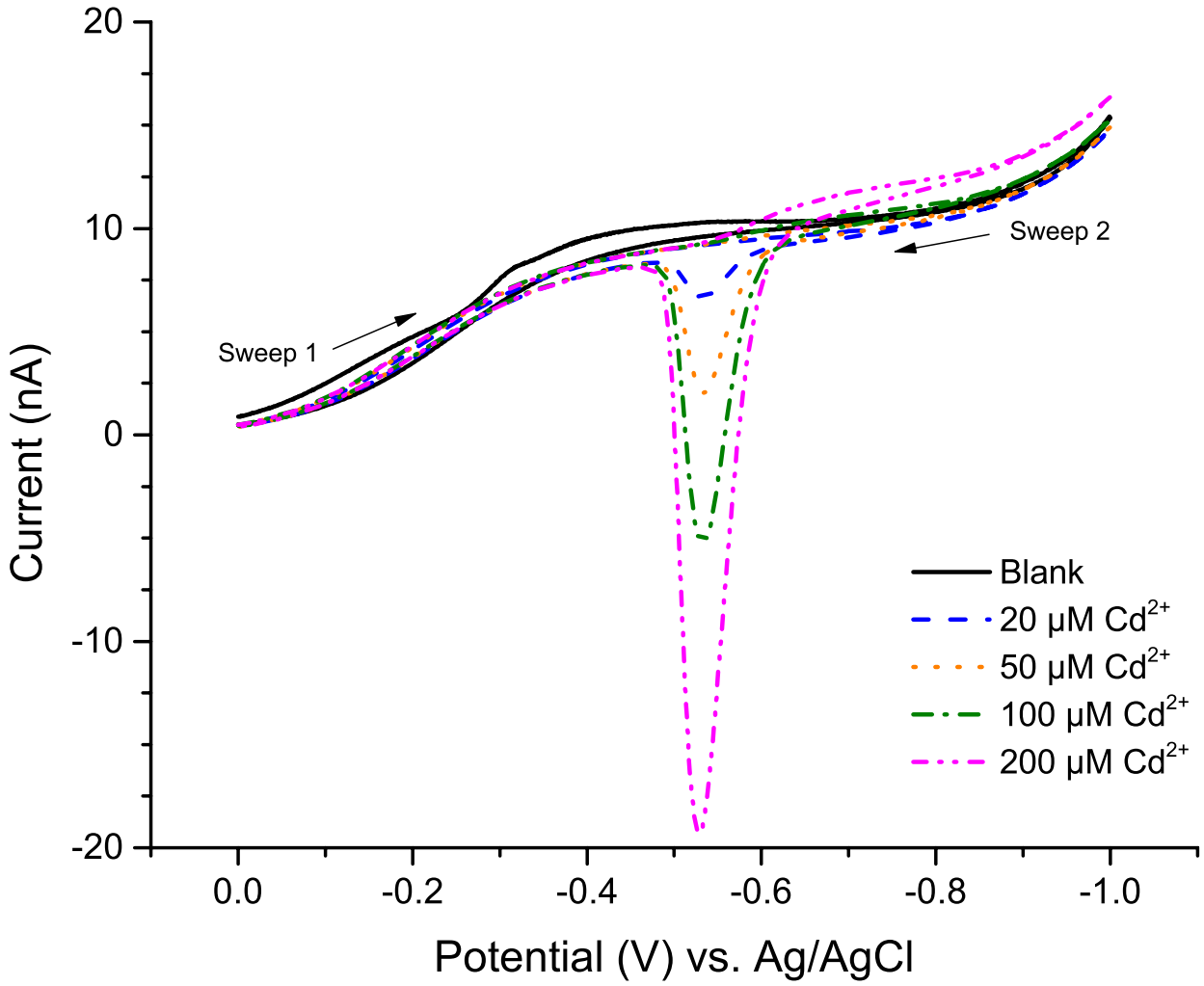

Figure 3.9. Stripping voltammetry of $Cd(NO_3)_2{\cdot}4H_2O$ in H_2O containing 10 mM KNO_3 as supporting electrolyte.

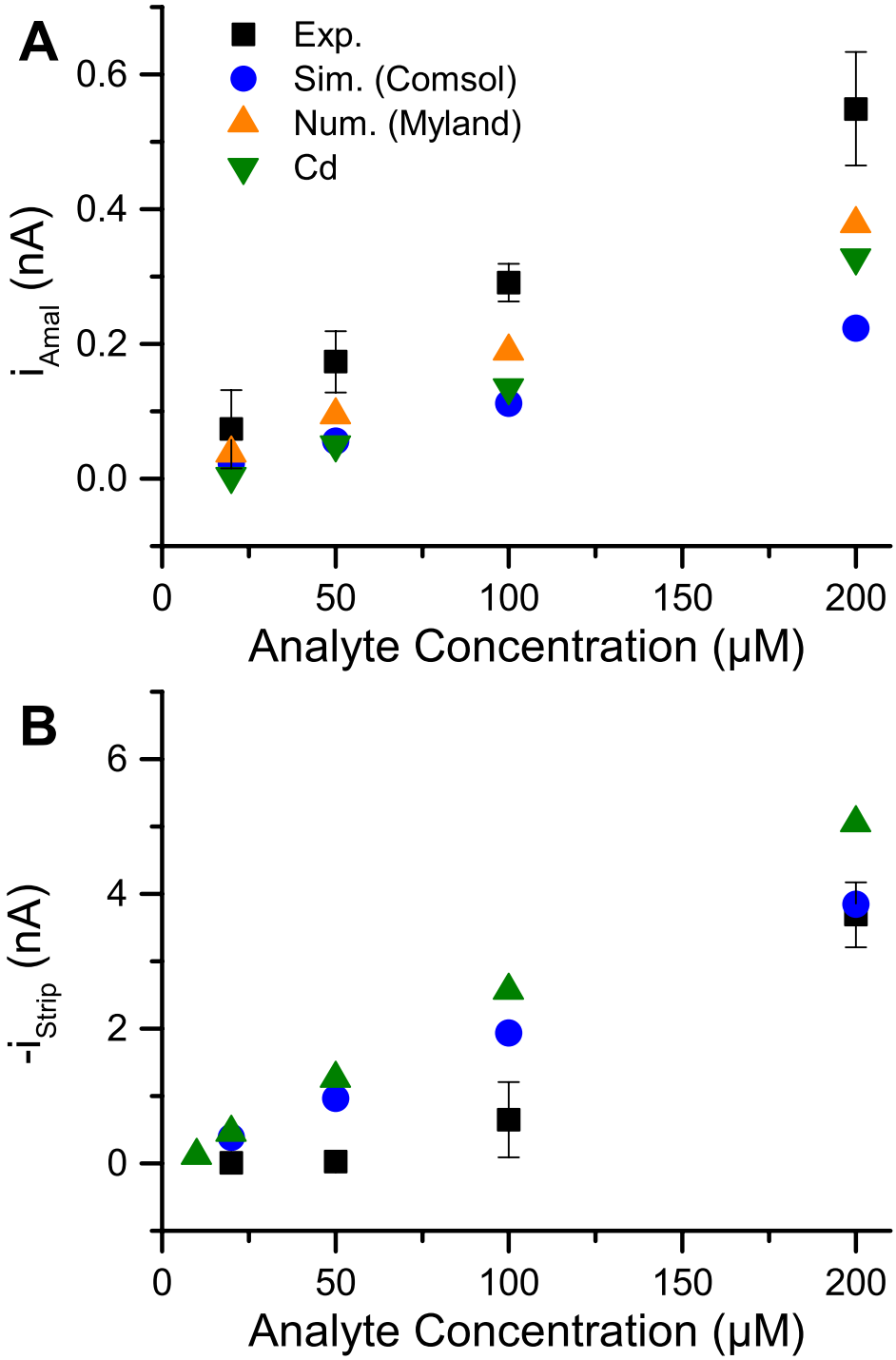

Figure 3.10. Calibration curves for viscosity-corrected Cd^{2+} stripping data. For i_{amal}, slope = 1811 pA μM^{-1}, intercept = -38 pA, and R_{adj}^2 = 0.9973. For i_{strip}, slope = 25791 pA μM^{-1}, intercept = -70 pA, and R_{adj}^2 = 0.99902.

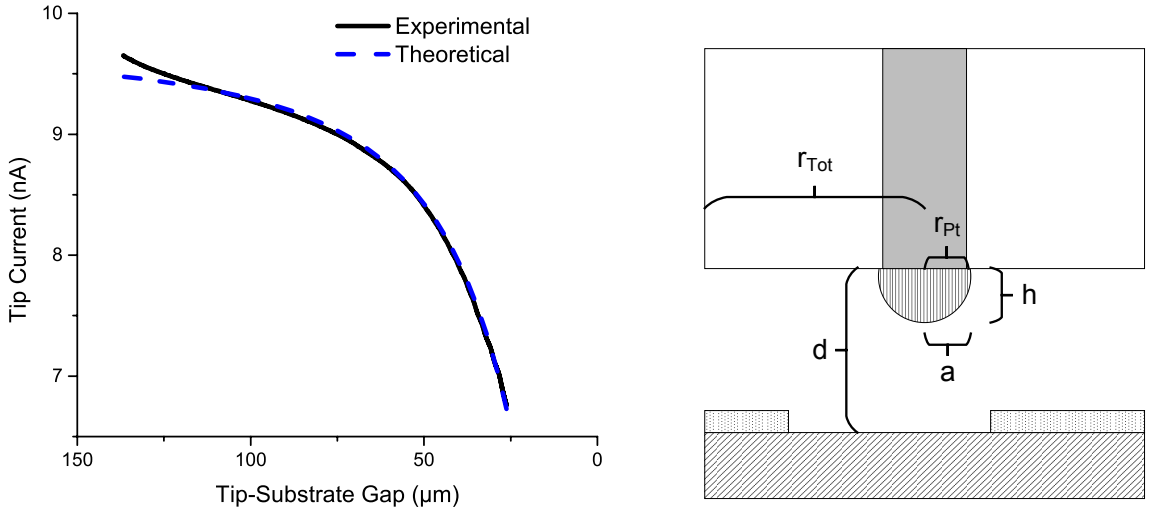

Figure 3.11. Probe approach curve in PC containing 5 mM ethyl viologen diperchlorate (*at left,* **A**). Salient parameters are indicated in the accompanying diagram (*at right,* **B**). Parameter values can be found in Table 3.3.

	Figure 3.11A, $(EV)^{2+}$	Figure 3.13A, Li^{+}
Concentration (mM)	5	1
Step Size (nm)	100	200
Step Rate (ms)	100	100
Approach Speed (μm s^{-1})	1	2
Cap Basal Radius, *a* (μm)	11.5	12.7
Cap Height, *h* (μm)	9.9	9.5
Cap Volume, *V* (pL)	2.9	3.1
Cap Mass, *m* (ng)	39.7	42.1
H, Experimental	0.76	0.73
H, Model (R_G = 10)	0.78	0.78
L_{max}, Experimental	11.89	11.31
L_{min}, Experimental	2.28	1.87
k_1	0.3081	0.3081
k_2	2.1772	2.1772
k_3	0.6931	0.6931
k_4	-2.9374	-2.9374
$i_{tip,\infty}$	9.786	1.578
Final Distance, d_{final} (μm)	26.2	23.8

Table 3.3. Probe approach curve parameters used for the hindered diffusion model described by Lindsey *et al.*[61] $H = h/a$ and $L = d/a$.

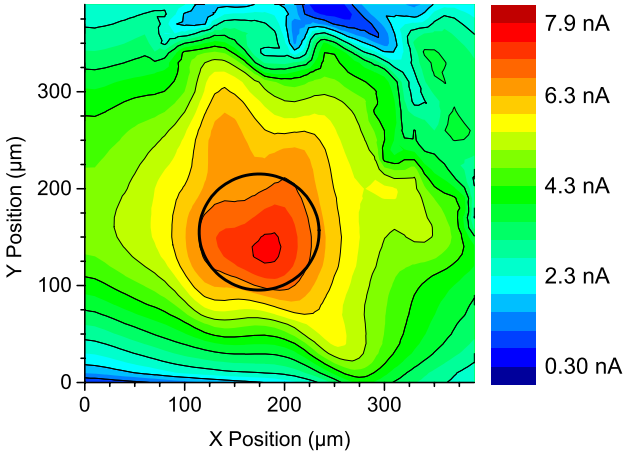

Figure 3.12. SECM image of a 120 µm diameter Au electrode (outlined in black) taken in SG-TC mode with ethyl viologen acting as the mediator. v_{tip} = 100 µm s^{-1} (10 µm per 100 ms) and d_{final} = 26.2 µm (2.3·r_{Pt}) from Figure 3.11A. An increase in redness indicates increased electrochemical activity at the substrate surface.

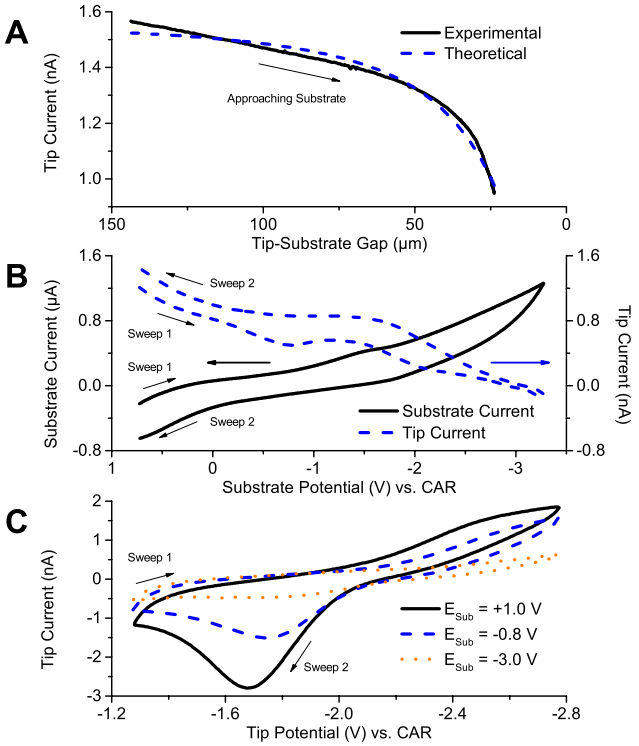

Figure 3.13. Detection of Li^+ fluxes in proximity to a 120 μm diameter Au electrode. (**A**) Probe approach curve at 2 μm s^{-1} (200 nm per 100 ms). E_{tip} = −2.7 V, E_{sub} = off, and d_{final} = 23.8 μm (1.9·r_{Pt}). (**B**) Substrate CV taken at ν = 50 mV s^{-1} with E_{tip} = −2.7 V. (**C**) Tip CVs taken at ν = 100 mV s^{-1}. All work was performed in PC containing 1 mM $LiClO_4$.

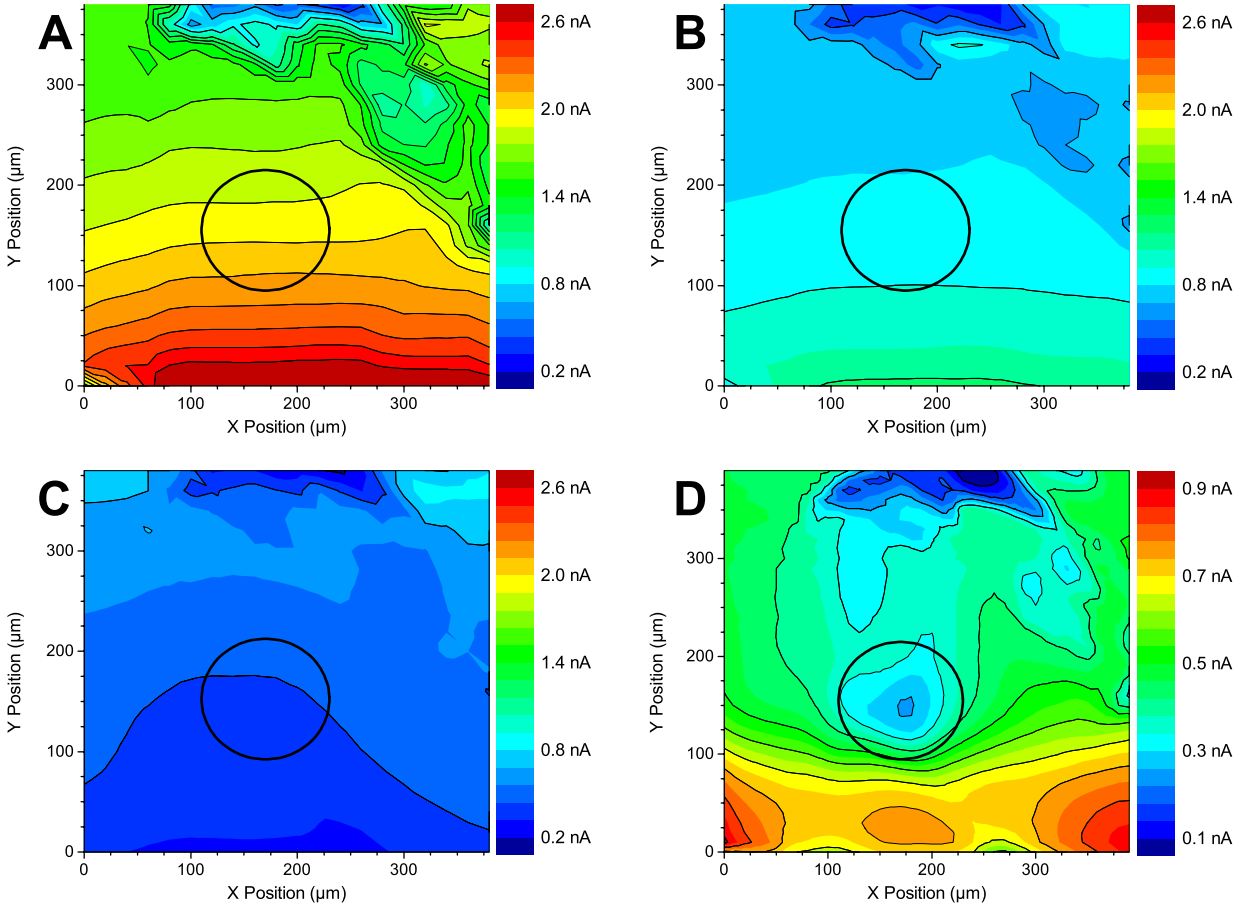

Figure 3.14. SECM images of Li^+ consumption using redox competition mode by an operating 120 µm diameter Au electrode (outlined in black). Lithium flux at the tip (E_{tip} = −2.87 V) responded to differences in the substrate's activity toward lithium reduction when poised at +1.0 V (**A**), −0.8 V (**B**), and −3.0 V (**C** and **D**). Images **A**, **B**, and **C** were each acquired in 82 s with v_{tip} = 200 µm s^{-1} (20 µm per 100 ms) and d_{final} = 23.8 µm (1.9·r_{Pt}) from Figure 3.13A. Image **D** represents a higher resolution version of image **C** and was acquired in 642 s with v_{tip} = 50 µm s^{-1} (10 µm per 200 ms). The probe was rastered in the +X direction. An increase in blueness indicates a decrease in free Li^+ concentration.

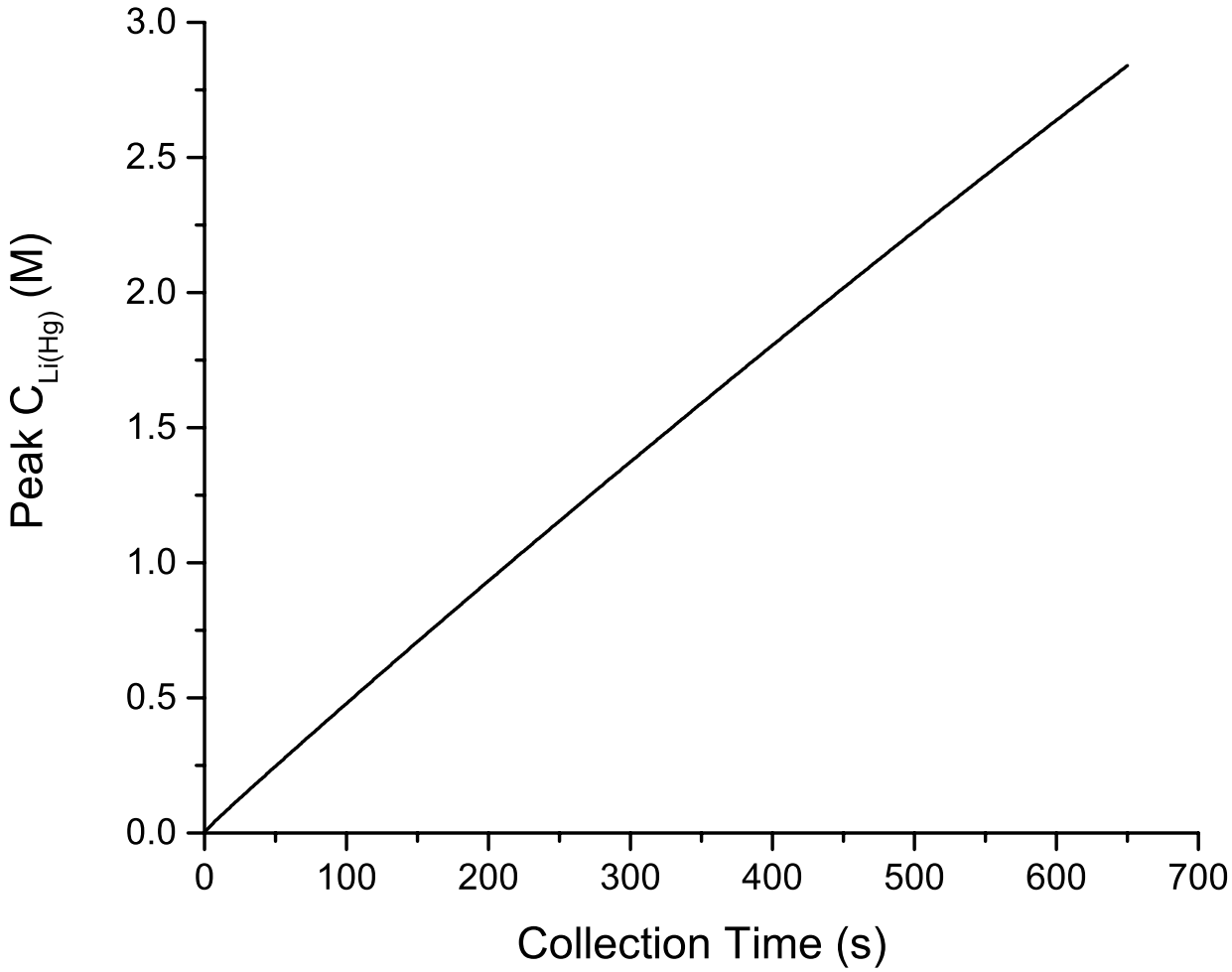

Figure 3.15. To check that the amalgam was not becoming saturated with lithium, simulations of chronoamperograms taken in 1, 2, 5, and 10 mM $LiClO_4$ in PC were used to predict the concentration of lithium in the WE amalgam. The internal lithium concentration was found to be a linear function of both external lithium concentration and preconcentration time. When poised at a constant potential of -2.4 V *vs.* CAR (which appears to be equivalent to the -2.7 V *vs.* CAR applied at the probe in Figure 3.14), the simulated amalgam reaches saturation within 16 seconds in 10 mM $LiClO_4$ and within 184 seconds in 1 mM $LiClO_4$.

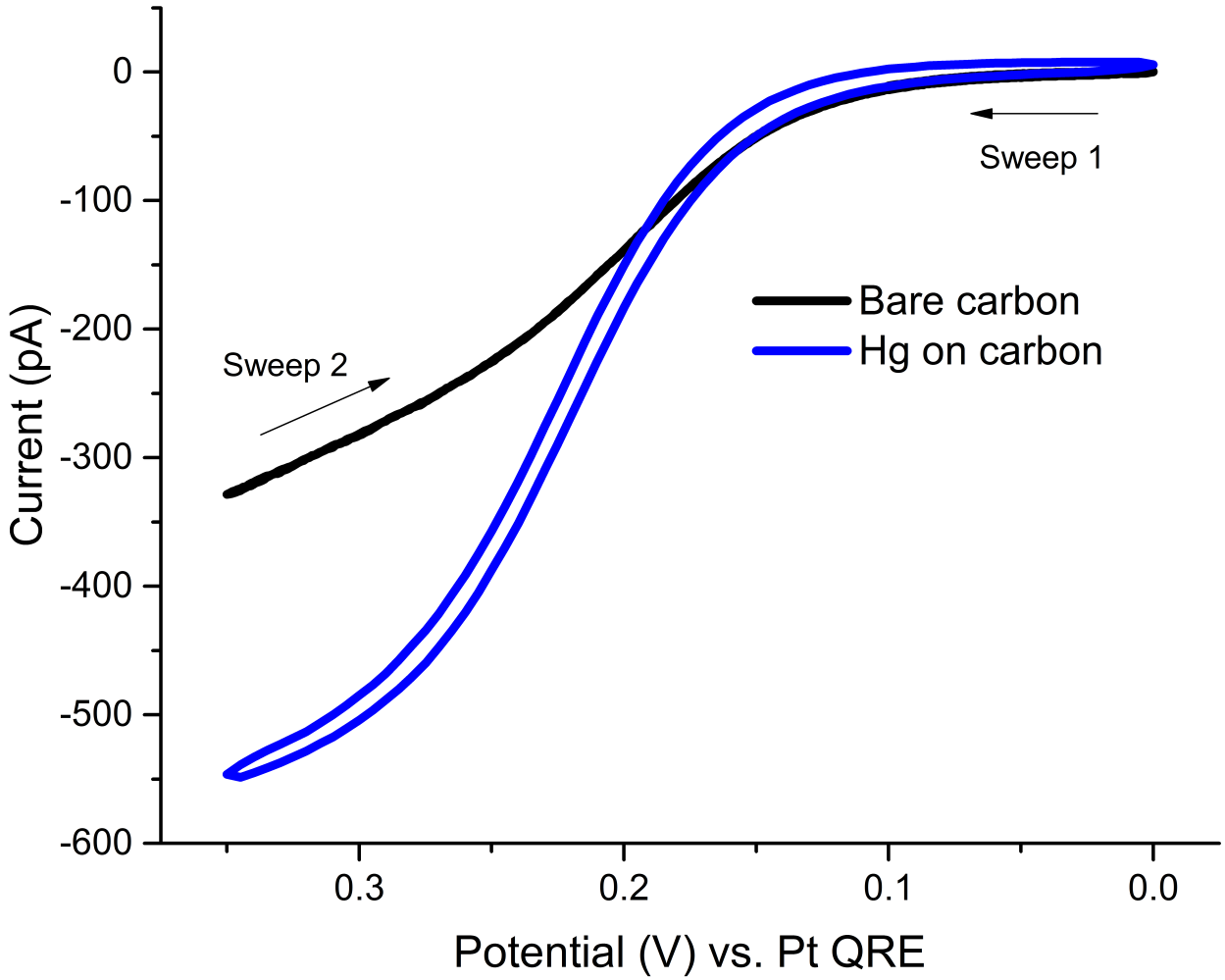

Figure 3.16. The oxidation of TMPD indicated that the bare carbon electrode had an electroactive surface area equivalent to that of a planar disc having a 120 nm radius.

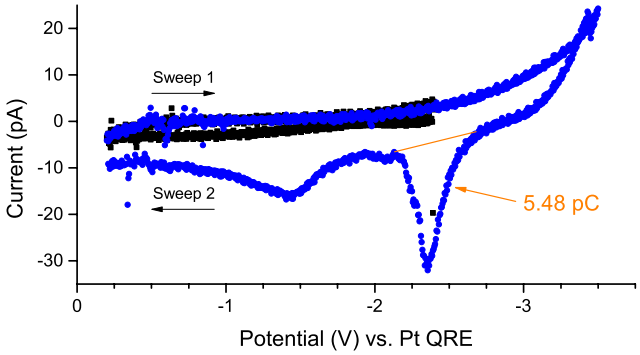

Figure 3.17. Lithium stripping at a mercury-capped carbon nano-electrode with an effective basal radius of 120 nm. Integration of the stripping peak marked by the orange baseline gives 5.48 pC. The potential was held at −3.2 V for 20 s in PC containing 1 mM $LiClO_4$.

3.8 References

(1) Bockris, J. O.; Reddy, A. K. N. Chapter 1. In *Modern Electrochemistry 1: Ionics*; Electrochemistry; 1998; pp. 1–34.

(2) Bockris, J. O.; Reddy, A. K. N. Chapter 4. In *Modern Electrochemistry 1: Ionics*; Ion Transport in Solutions; 1998; pp. 361–600.

(3) Bard, A. J.; Faulkner, L. R. *Electrochemical Methods: Fundamentals and Applications*; 2nd ed.; Wiley: New York, 2001.

(4) Aurbach, D. Review of Selected Electrode–Solution Interactions Which Determine the Performance of Li and Li Ion Batteries. *J. Pow. Sour.* **2000**, *89*, 206–218.

(5) Verbrugge, M. W.; Koch, B. J. Electrochemical Analysis of Lithiated Graphite Anodes. *J. Electrochem. Soc.* **2003**, *150*, A374–A384.

(6) Srinivasan, V.; Newman, J. Discharge Model for the Lithium Iron-Phosphate Electrode. *J. Electrochem. Soc.* **2004**, *151*, A1517–A1529.

(7) Goodenough, J. B.; Kim, Y. Challenges for Rechargeable Li Batteries. *Chem. Mater.* **2010**, *22*, 587–603.

(8) Harris, S. J.; Lu, P. Effects of Inhomogeneities—Nanoscale to Mesoscale—on the Durability of Li-Ion Batteries. *J. Phys. Chem. C* **2013**, *117*, 6481–6492.

(9) Wang, Y.; He, P.; Zhou, H. Li-Redox Flow Batteries Based on Hybrid Electrolytes: at the Cross Road Between Li-Ion and Redox Flow Batteries. *Adv. Energy Mater.* **2012**, *2*, 770–779.

(10) Liu, J.; Zhang, J.-G.; Yang, Z.; Lemmon, J. P.; Imhoff, C.; Graff, G. L.; Li, L.; Hu, J.; Wang, C.; Xiao, J.; Xia, G.; Viswanathan, V. V.; Baskaran, S.; Sprenkle, V.; Li, X.; Shao, Y.; Schwenzer, B. Materials Science and Materials Chemistry for Large Scale Electrochemical Energy Storage: From Transportation to Electrical Grid. *Adv. Funct. Mater.* **2012**, *23*, 929–946.

(11) Balke, N.; Jesse, S.; Kim, Y.; Adamczyk, L.; Tselev, A.; Ivanov, I. N.; Dudney, N. J.; Kalinin, S. V. Real Space Mapping of Li-Ion Transport in Amorphous Si Anodes with Nanometer Resolution. *Nano Lett.* **2010**, *10*, 3420–3425.

(12) Lipson, A. L.; Ginder, R. S.; Hersam, M. C. Nanoscale in Situ Characterization of Li-Ion Battery Electrochemistry via Scanning Ion Conductance Microscopy. *Adv. Mater.* **2011**, *23*, 5613–5617.

(13) Lipson, A. L.; Hersam, M. C. Conductive Scanning Probe Characterization and Nanopatterning of Electronic and Energy Materials. *J. Phys. Chem. C* **2013**, *117*, 7953–7963.

(14) Xu, F.; Beak, B.; Jung, C. In Situ Electrochemical Studies for Li^+ Ions Dissociation From the $LiCoO_2$ Electrode by the Substrate-Generation/Tip-Collection Mode in SECM. *J. Solid State Electrochem.* **2011**, *16*, 305–311.

(15) Zampardi, G.; Ventosa, E.; La Mantia, F.; Schuhmann, W. *In Situ* Visualization of Li-Ion Intercalation and Formation of the Solid Electrolyte Interphase on TiO_2 Based Paste Electrodes Using Scanning Electrochemical Microscopy. *Chem. Commun.* **2013**, *49*, 9347–9349.

(16) Shao, Y.; Mirkin, M. V. Voltammetry at Micropipet Electrodes. *Anal. Chem.* **1998**, *70*, 3155–3161.

(17) Reymond, F.; Fermín, D.; Lee, H. J.; Girault, H. H. Electrochemistry at Liquid/Liquid Interfaces: Methodology and Potential Applications. *Electrochim. Acta* **2000**, *45*, 2647–2662.

(18) Cousens, N. E. A.; Kucernak, A. R. Increasing the Potential Window of the Interface Between Two Immiscible Electrolyte Solutions to More Than 1.2 V. *Electrochem. Commun.* **2011**, *13*, 1539–1541.

(19) Shen, M.; Ishimatsu, R.; Kim, J.; Amemiya, S. Quantitative Imaging of Ion Transport Through Single Nanopores by High-Resolution Scanning Electrochemical Microscopy. *J. Amer. Chem. Soc.* **2012**, *134*, 9856–9859.

(20) Holtz, M. E.; Yu, Y.; Gunceler, D.; Gao, J.; Sundararaman, R.; Schwarz, K. A.; Arias, T. A.; Abercrombie, S.; Muller, D. A. Nanoscale Imaging of Lithium Ion Distribution During *In Situ* Operation of Battery Electrode and Electrolyte. *Nano Lett.* **2014**, *14*, 1453–1459.

(21) Bard, A. J.; Denuault, G.; Lee, C.; Mandler, D.; Wipf, D. O. Scanning Electrochemical Microscopy: a New Technique for the Characterization and Modification of Surfaces. *Acc. Chem. Res.* **1990**, *23*, 357–363.

(22) Eckhard, K.; Chen, X.; Turcu, F.; Schuhmann, W. Redox Competition Mode of Scanning Electrochemical Microscopy (RC-SECM) for Visualisation of Local Catalytic Activity. *Phys. Chem. Chem. Phys.* **2006**, *8*, 5359–5365.

(23) Pust, S. E.; Maier, W.; Wittstock, G. Investigation of Localized Catalytic and Electrocatalytic Processes and Corrosion Reactions with Scanning Electrochemical Microscopy (SECM). *Z. Phys. Chem.* **2008**, *222*, 1463–1517.

(24) Bertoncello, P. Advances on Scanning Electrochemical Microscopy (SECM) for Energy. *Energy Environ. Sci.* **2010**, *3*, 1620–1633.

(25) Mirkin, M. V.; Nogala, W.; Velmurugan, J.; Wang, Y. Scanning Electrochemical Microscopy in the 21st Century. Update 1: Five Years After. *Phys. Chem. Chem. Phys.* **2011**, *13*, 21196–21212.

(26) Rodríguez-López, J.; Zoski, C.; Bard, A. J. Application to Electrocatalysis and Photocatalysis and Surface Interrogation. In *Scanning Electrochemical Microscopy*; Bard, A. J.; Mirkin, M. V., Eds.; CRC Press, 2012; pp. 525–568.

(27) Rodríguez-López, J.; Minguzzi, A.; Bard, A. J. Reaction of Various Reductants with Oxide Films

on Pt Electrodes as Studied by the Surface Interrogation Mode of Scanning Electrochemical Microscopy (SI-SECM): Possible Validity of a Marcus Relationship. *J. Phys. Chem. C* **2010**, *114*, 18645–18655.

(28) Tan, C.; Rodríguez-López, J.; Parks, J. J.; Ritzert, N. L.; Ralph, D. C.; Abercrombie, S. Reactivity of Monolayer Chemical Vapor Deposited Graphene Imperfections Studied Using Scanning Electrochemical Microscopy. *ACS Nano* **2012**, *6*, 3070–3079.

(29) Ciani, I.; Daniele, S.; Bragato, C.; Baldo, M.-A. Stability of Mercury-Coated Platinum Microelectrodes Upon Touching a Solid Surface in Scanning Electrochemical Microscopy (SECM) Experiments. *Electrochem. Commun.* **2003**, *5*, 354–358.

(30) Daniele, S.; Baldo, M.-A.; Ugo, P.; Mazzocchin, G. A. Determination of Heavy Metals in Real Samples by Anodic Stripping Voltammetry with Mercury Microelectrodes. *Anal. Chim. Acta* **1989**, *219*, 19–26.

(31) Nepomnyashchii, A. B.; Alpuche-Aviles, M.; Pan, S.; Zhan, D.; Fan, F.-R.; Bard, A. J. Cyclic Voltammetry Studies of Cd^{2+} And Zn^{2+} Complexation with Hydroxyl-Terminated Polyamidoamine Generation 2 Dendrimer at a Mercury Microelectrode. *J. Electroanal. Chem.* **2008**, *621*, 286–296.

(32) Selzer, Y.; Turyan, I.; Mandler, D. Studying Heterogeneous Catalysis by the Scanning Electrochemical Microscope (SECM): the Reduction of Protons by Methyl Viologen Catalyzed by a Platinum Surface. *J. Phys. Chem. B* **1999**, *103*, 1509–1517.

(33) Fernández, J. L.; Hurth, C.; Bard, A. J. Scanning Electrochemical Microscopy #54. Application to the Study of Heterogeneous Catalytic Reactions—Hydrogen Peroxide Decomposition. *J. Phys. Chem. B* **2005**, *109*, 9532–9539.

(34) Souto, R. M.; González-García, Y.; Battistel, D.; Daniele, S. In Situ Scanning Electrochemical

Microscopy (SECM) Detection of Metal Dissolution During Zinc Corrosion by Means of Mercury Sphere-Cap Microelectrode Tips. *Chem. Eur. J.* **2011**, *18*, 230–236.

(35) Alpuche-Aviles, M.; Baur, J. E.; Wipf, D. O. Imaging of Metal Ion Dissolution and Electrodeposition by Anodic Stripping Voltammetry–Scanning Electrochemical Microscopy. *Anal. Chem.* **2008**, *80*, 3612–3621.

(36) Munteanu, G.; Munteanu, S.; Wipf, D. O. Rapid Determination of Zeptomole Quantities of Pb^{2+} With the Mercury Monolayer Carbon Fiber Electrode. *J. Electroanal. Chem.* **2009**, *632*, 177–183.

(37) Hine, T. B. The Electrical Conductivities of Dilute Sodium, Potassium and Lithium Amalgams. *J. Amer. Chem. Soc.* **1917**, *39*, 882–895.

(38) Stevens, W. G.; Shain, I. Electrolysis with Constant Potential. Diffusion Currents of Metal Species Dissolved in Spherical Mercury Electrodes. *J. Phys. Chem.* **1966**, *70*, 2276–2280.

(39) Cogley, D. R.; Butler, J. N. The Activity of Lithium in Lithium Amalgams. *J. Phys. Chem.* **1968**, *72*, 1017–1020.

(40) Deiseroth, H.-J. Alkali Metal Amalgams, a Group of Unusual Alloys. *Prog. Solid State Chem.* **1997**, *25*, 73–123.

(41) Baranski, A.; Fawcett, W. R. Electroreduction of Alkali Metal Cations. Part 1.—Effects of Solution Composition. *J. Chem. Soc., Faraday Trans. 1* **1980**, *76*, 1962–1977.

(42) Baranski, A.; Drogowska, M. A.; Fawcett, W. R. The Kinetics of Electroreduction of Lithium Ions in Tetrahydrofuran at Mercury and Mercury Amalgam Electrodes. *J. Electroanal. Chem. Interfacial Electrochem.* **1986**, *215*, 237–247.

(43) Kwak, J.; Bard, A. J. Scanning Electrochemical Microscopy. Theory of the Feedback Mode. *Anal. Chem.* **1989**, *61*, 1221–1227.

(44) Wipf, D. O.; Bard, A. J. Scanning Electrochemical Microscopy: VII. Effect of Heterogeneous Electron-Transfer Rate at the Substrate on the Tip Feedback Current. **1991**, *138*, 469–474.

(45) Fan, F.-R.; Demaille, C. Preparation of Tips for Scanning Electrochemical Microscopy. In *Scanning Electrochemical Microscopy*; Bard, A. J.; Mirkin, M. V., Eds.; CRC Press, 2012; pp. 25–52.

(46) Liljeroth, P.; Johans, C.; Slevin, C. J.; Quinn, B. M.; Kontturi, K. Micro Ring–Disk Electrode Probes for Scanning Electrochemical Microscopy. *Electrochem. Commun.* **2002**, *4*, 67–71.

(47) Miao, W.; Ding, Z.; Bard, A. J. Solution Viscosity Effects on the Heterogeneous Electron Transfer Kinetics of Ferrocenemethanol in Dimethyl Sulfoxide–Water Mixtures. *J. Phys. Chem. B* **2002**, *106*, 1392–1398.

(48) Baldo, M.-A.; Daniele, S.; Mazzocchin, G. A. Cyclic Voltammetry at Mercury Microelectrodes. Effects of Mercury Thickness and Scan Rate. *Electrochim. Acta* **1996**, *41*, 811–818.

(49) Mauzeroll, J.; Hueske, E. A.; Bard, A. J. Scanning Electrochemical Microscopy. 48. Hg/Pt Hemispherical Ultramicroelectrodes: Fabrication and Characterization. *Anal. Chem.* **2003**, *75*, 3880–3889.

(50) McNally, M.; Wong, D. K. Y. An in Vivo Probe Based on Mechanically Strong but Structurally Small Carbon Electrodes with an Appreciable Surface Area. *Anal. Chem.* **2001**, *73*, 4793–4800.

(51) Singhal, R.; Bhattacharyya, S.; Orynbayeva, Z.; Vitol, E.; Friedman, G.; Gogotsi, Y. Small Diameter Carbon Nanopipettes. *Nanotechnology* **2009**, *21*, 015304.

(52) Velmurugan, J.; Mirkin, M. V. Fabrication of Nanoelectrodes and Metal Clusters by Electrodeposition. *ChemPhysChem* **2010**, *11*, 3011–3017.

(53) Morton, K. C.; Morris, C. A.; Derylo, M. A.; Thakar, R.; Baker, L. A. Carbon Electrode Fabrication From Pyrolyzed Parylene C. *Anal. Chem.* **2011**, *83*, 5447–5452.

(54) Takahashi, Y.; Shevchuk, A. I.; Novak, P.; Zhang, Y.; Ebejer, N.; Macpherson, J. V.; Unwin, P. R.; Pollard, A. J.; Roy, D.; Clifford, C. A.; Shiku, H.; Matsue, T.; Klenerman, D.; Korchev, Y. E. Multifunctional Nanoprobes for Nanoscale Chemical Imaging and Localized Chemical Delivery at Surfaces and Interfaces. *Angew. Chem., Int. Ed.* **2011**, *50*, 9638–9642.

(55) Hu, K.; Gao, Y.; Wang, Y.; Yu, Y.; Zhao, X.; Rotenberg, S. A.; Gökmeşe, E.; Mirkin, M. V.; Friedman, G.; Gogotsi, Y. Platinized Carbon Nanoelectrodes as Potentiometric and Amperometric SECM Probes. *J. Solid State Electrochem.* **2013**, *17*, 2971–2977.

(56) McKelvey, K.; Nadappuram, B. P.; Actis, P.; Takahashi, Y.; Korchev, Y. E.; Matsue, T.; Robinson, C.; Unwin, P. R. Fabrication, Characterization, and Functionalization of Dual Carbon Electrodes as Probes for Scanning Electrochemical Microscopy (SECM). *Anal. Chem.* **2013**, *85*, 7519–7526.

(57) Marple, L. W. Reference Electrode for Anhydrous Dimethylformamide. *Anal. Chem.* **1967**, *39*, 844–846.

(58) Manning, C. W.; Purdy, W. C. Reference Electrode for Electrochemical Studies in Dimethylformamide. *Anal. Chim. Acta* **1970**, *51*, 124–126.

(59) Hall, J. L.; Jennings, P. W. Modification of the Preparation of a Cadmium Amalgam Reference Electrode for Use in *N*,*N*-Dimethylformamide. *Anal. Chem.* **1976**, *48*, 2026–2027.

(60) Vieira, K. L.; Peters, D. G. Voltammetric Behavior of Tertiary Butyl Bromide at Mercury Electrodes in Dimethylformamide. *J. Electroanal. Chem. Interfacial Electrochem.* **1985**, *196*, 93–104.

(61) Lindsey, G.; Abercrombie, S.; Denuault, G.; Daniele, S.; De Faveri, E. Scanning Electrochemical Microscopy: Approach Curves for Sphere-Cap Scanning Electrochemical Microscopy Tips. *Anal. Chem.* **2007**, *79*, 2952–2956.

(62) Myland, J. C.; Oldham, K. B. Diffusion-Limited Currents at Hemispheroidal Microelectrodes. *J. Electroanal. Chem. Interfacial Electrochem.* **1990**, *288*, 1–14.

(63) Rodríguez-López, J.; Alpuche-Aviles, M.; Bard, A. J. Selective Insulation with Poly(Tetrafluoroethylene) of Substrate Electrodes for Electrochemical Background Reduction in Scanning Electrochemical Microscopy. *Anal. Chem.* **2008**, *80*, 1813–1818.

(64) Hills, G. J.; Peter, L. M. Electrode Kinetics in Aprotic Media. *J. Electroanal. Chem. Interfacial Electrochem.* **1974**, *50*, 175–185.

(65) Galus, Z. Diffusion Coefficients of Metals in Mercury. *Pure Appl. Chem.* **1984**, *56*, 635–644.

(66) Mussini, T.; Longhi, P.; Rondinini, S. Standard Potentials of Amalgam Electrodes in Aqueous Solutions, Temperature Coefficients and Activity Coefficients of Metals in Mercury. *Pure Appl. Chem.* **1985**, *57*, 169–179.

(67) Cronnolly, C.; Pillai, K. C.; Waghorne, W. E. Electrode Kinetic Studies of the Zn^{2+}/Zn(Hg) and Li^{+}/Li(Hg) Couples in Dimethylsulphoxide + Propylene Carbonate Solvent Systems. *J. Electroanal. Chem. Interfacial Electrochem.* **1986**, *207*, 177–187.

(68) Guminski, C. Selected Properties of Simple Amalgams. *J. Mater. Sci.* **1989**, *24*, 2661–2676.

(69) Kozin, L. F.; Hansen, S. C. Chapter 3. Diffusion of Metals in Mercury. In *Mercury Handbook*; Royal Society of Chemistry: Cambridge, 2013; pp. 50–60.

(70) Nicholson, R. S. Theory and Application of Cyclic Voltammetry for Measurement of Electrode Reaction Kinetics. *Anal. Chem.* **1965**, *37*, 1351–1355.

(71) Schiewe, J.; Oldham, K. B.; Myland, J. C.; Bond, A. M.; Vicente-Beckett, V. A.; Fletcher, S. Linear-Scan Anodic Stripping Voltammetry with Thin-Film Electrodes: Theory of the Stripping Stage and Experimental Tests. *Anal. Chem.* **1997**, *69*, 2673–2681.

(72) Limon-Petersen, J. G.; Rees, N. V.; Dickinson, E. J. F.; Compton, R. G. Quantitative

Voltammetry in Weakly Supported Media. Two Electron Transfer, Chronoamperometry of Electrodeposition and Stripping for Cadmium at Microhemispherical Mercury Electrodes. *J. Phys. Chem. C* **2009**, *113*, 15320–15325.

(73) Izutsu, K. Polarography and Voltammetry in Nonaqueous Solutions. In *Electrochemistry in Nonaqueous Solutions*; Wiley-VCH Verlag GmbH & Co. KGaA: Weinheim, Germany, 2009; pp. 233–285.

(74) Jansta, J.; Dousek, F. P. Electrochemical Corrosion of Polytetrafluorethylene Contacting Lithium Amalgam. *Electrochim. Acta* **1973**, *18*, 673–674.

(75) Deiss, F.; Combellas, C.; Fretigny, C.; Sojic, N.; Kanoufi, F. Lithography by Scanning Electrochemical Microscopy with a Multiscaled Electrode. *Anal. Chem.* **2010**, *82*, 5169–5175.

CHAPTER 4

Cyclic Voltammetry Probe Approach Curves (CV-PACs) with Alkali Amalgams at Mercury Sphere-Cap Scanning Electrochemical Microscopy (SECM) Probes

This chapter was published as an original research article in *Analytical Chemistry*:

Barton, Z. J.; Rodríguez-López, J. Cyclic Voltammetry Probe Approach Curves with Alkali Amalgams at Mercury Sphere-Cap Scanning Electrochemical Microscopy Probes. *Anal. Chem.* **2017**, *89*, 2708–2715. DOI: 10.1021/acs.analchem.6b04093

4.1 Abstract

We report a method of precisely positioning a Hg-based ultramicroelectrode (UME) for scanning electrochemical microscopy (SECM) investigations of any substrate. Hg-based probes are capable of performing amalgamation reactions with metal cations, which avoid unwanted side reactions and positive feedback mechanisms that can prove problematic for traditional probe positioning methods. However, prolonged collection of ions eventually leads to saturation of the amalgam accompanied by irreversible loss of Hg. In order to obtain negative feedback positioning control without risking damage to the SECM probe, we implement cyclic voltammetry probe approach surfaces (CV-PASs), consisting of CVs performed between incremental motor movements. The amalgamation current, peak stripping current, and integrated stripping charge extracted from a shared CV-PAS give three distinct probe approach curves (CV-PACs), which can be used to determine the tip-substrate gap to within 1% of the probe radius. Using finite element simulations, we establish a new protocol for fitting any CV-PAC and demonstrate its validity with experimental results for sodium and potassium ions in propylene carbonate by obtaining over 3 orders of magnitude greater accuracy and more than 20-fold greater precision than

existing methods. Considering the timescales of diffusion and amalgam saturation, we also present limiting conditions for obtaining and fitting CV-PAC data. The ion-specific signals isolated in CV-PACs allow precise and accurate positioning of Hg-based SECM probes over any sample and enable the deployment of CV-PAS SECM as an analytical tool for traditionally challenging conditions (Figure 4.1).

4.2 Introduction

4.2.1 Background

Scanning electrochemical microscopy (SECM) is a powerful analytical tool for examining heterogeneous surface reactivity.[1-3] Because the probe signal is sensitive to changes in surface reactivity as well as topography, precise knowledge of the tip-substrate gap is essential for quantitative SECM studies. Coupled techniques relying on conductance, impedance, or shear force have been used to support SECM probe positioning.[4] However, challenges associated with their implementation in viscous solutions of high ionic strength or with "non-traditional" probe geometries (*e.g.*, liquid-based probes rather than solid microdiscs) make the use of more traditional Faradaic methods desirable. Expressions describing the current at microelectrodes of various geometries under negative feedback conditions have been very successful for positioning SECM probes.[5-9] This is preferable to positive feedback, which convolves substrate kinetics with mass transport. However, negative feedback positioning can be difficult to implement with various reactive substrates or chemical environments that regenerate or degrade redox mediators.

Hg sphere-cap ultramicroelectrodes (UMEs) are uniquely suited for use in otherwise challenging chemical environments since they may form reversible amalgams with various metal cations, yielding a quantitative signal that may be used for probe positioning. For example, we have previously used these probes in the detection of ion fluxes during the electrodeposition of Li^+ on Au and the insertion of Li^+ at multi-layer graphene.[10,11] Our continued interest in imaging alkali ion fluxes at operating battery

interfaces and other reactive environments has led us to find a means of accurately positioning SECM probes in the absence of a redox mediator.

Monitoring the anodic stripping voltammetry of solution-phase alkali ions by Hg-based SECM probes is convenient, since the amalgam is not soluble in solution and therefore cannot give positive feedback. Additionally, the reaction, though reversible, occurs at potentials sufficiently displaced from open circuit that competitive consumption or generation of alkali ions is avoided. Recently, the potentiostatic amalgamation of Li^+ at a Hg sphere-cap UME was fit by an established PAC model,[8,10] but the risk of saturating the amalgam by prolonged collection of ions makes this difficult to implement over large distances or in concentrated solutions, even though the solubilities of alkali metals in Hg are in the molar range.

We now resolve this issue by performing CVs between incremental motor movements to create probe approach surfaces (PASs). The amalgamation current (i_{amal}), peak stripping current (i_{strip}), and integrated stripping charge (Q_{strip}) can each be extracted as cross-sections of a single CV-PAS to give three separate CV-PACs, each of which can be used to determine the tip-substrate distance. We develop an expression for quickly estimating the tip-substrate gap from the onset of negative feedback and demonstrate a universally applicable method for calculating the gap precisely with assistance from finite element simulations.

After discussing limiting conditions that allow the successful application of the PAC fitting parameters provided in the literature,[8] we establish a protocol for fitting any CV-PAC on a case-by-case basis and demonstrate its validity with experimental CV-PAS data for Na^+ and K^+ in propylene carbonate. The only previous report of CV-PASs taken with Hg-based probes was performed under aqueous conditions with heavy metal ions and did not include fitting of PAS-derived data.[12] Therefore, this is the first report of alkali ion CV-PASs as well as the first time CV-PAC data of any kind has been

used to accurately determine the tip-substrate gap, thus expanding the SECM toolkit for non-traditional electrochemical probes.

4.2.2 Diffusive Timescale

Negative feedback refers to the decrease in flux caused when the presence of a substrate hinders the radial expansion of the concentration gradient originating at the SECM probe. This phenomenon is governed by relationships between the length and time of diffusive mass transport, which are simplified by first defining normalized time (T):

$$T = \frac{Dt}{a_1^2} = \frac{D\Delta E_t}{a_1^2 \nu} \quad \textbf{(1)}$$

where D is the diffusion coefficient of the reactant in solution, a_1 is the basal radius of the Hg sphere-cap, and t is the time allowed for depletion of reactants from solution to occur. In this context, t refers to the passage of time in the normal sense and not to some characteristic timescale or crossing time. For CVs, this time can be approximated as $t = \Delta E_t/\nu$, where ΔE_t is the cumulative potential range traversed up to the considered point in time under activated conditions and ν is the potential sweep rate. For amalgamation signals, the time is given by $t_{amal} = (E_{1/2} - E_{sw})/\nu$, where E_{sw} is the potential marking the switch from the cathodic potential excursion to the anodic return sweep and $E_{1/2}$ is the half-wave potential.

4.2.3 Geometric Terms

Hg sphere-caps probes consist of an electrodeposited Hg drop with basal radius a_1 and central height h supported on a Pt UME with total tip radius a_2. The probe position is measured as the distance d from the basal plane of the sphere-cap (not its apex) to the surface of the substrate. In order to compare diffusive mass transport effects for probes of various sizes, it is useful to introduce normalized versions of each parameter: $H = h/a_1$, $R_G = a_2/a_1$, and $L = d/a_1$. To facilitate comparisons between negative feedback

behavior and diffusional transport, we also define $G = L\text{-}H = (d\text{-}h)/a_1$, where G is the normalized distance from the apex of the Hg sphere-cap to the substrate plane. For clarity, these terms are also indicated schematically in Figure 4.2.

The distance at closest approach to a substrate is indicated with a subscript "f", resulting in $G_f = L_f - H$. Similarly, the distance at which negative feedback begins is indicated with a subscript "o", giving $G_o = L_o - H$. In this paper, we define the onset of negative feedback, G_o, as the tip-substrate gap for which the probe signal is decreased by 10% of the maximum signal difference achievable without crashing (approximated by $G = 0.1$):

$$G_o = \left\{ G \left| \frac{i_G - i_{G=0.1}}{i_{inf} - i_{G=0.1}} = 0.9 \right. \right\} \quad (2)$$

This definition rescales the current to range from unity to zero, thereby accounting for the decrease in total achievable negative feedback response for shorter timescales. Defining a feedback threshold without rescaling the signal can result in G_o occurring well into the steep portion of CV-PACs for short timescales.

Because the following discussion is framed in terms of T, H, R_G, and L (or G), it is valid across a wide range of probe dimensions and experimental conditions.

4.2.4 Diffusive Transport Lengths

The concentration gradient that develops due to the depletion of M^+ from solution is sometimes estimated by the Nernstian diffusion layer thickness (δ_1), which is the fictional radial distance from the electrode surface at which bulk concentration would be observed if the gradient were linear. Under mass-transport control, the normalized Nernstian diffusion layer thickness (w_1) at a hemispherical microelectrode under potentiodynamic conditions for $T >> \pi^{-1}$ (~0.32) is given by[13]

$$w_1 = \frac{\delta_1}{a_1} = \left(1 + \frac{1}{\sqrt{\pi T}}\right)^{-1} \quad (3)$$

which is identical to the result obtained following a large potential step without kinetic complications.[14,15] w_1 tends towards unity as T increases towards $+\infty$, but for small T, diffusion can be taken as nearly planar during potentiodynamic studies.[16] The Nernstian diffusion layer is confined to a region much closer to the electrode surface than G_o for all values of T, so it is not a clear predictor of G_o. Nevertheless, w_1 is useful as a lower boundary describing the initially rapid growth of the depletion region.

Unlike the theoretical Nernstian diffusion layer, the real depletion layer continuously expands without approaching some limiting behavior. The thickness of the depletion region is approximately equal to the radial distance (δ_2) from the electrode surface at which ($\partial C_{ox}/\partial t$) is maximized. The normalized depletion layer thickness (w_2) is approximated by[17]

$$w_2 = \frac{\delta_2}{a_1} = (2T)^{1/3} \qquad (4)$$

In contrast to w_1, w_2 extends farther into solution than the onset of negative feedback for all values of T. Thus, w_1 and w_2 constitute lower and upper boundaries, respectively, for G_o.

4.3 Experimental Section

4.3.1 Chemicals

Cadmium (stick, ≥99.999%) and potassium perchlorate (99%) were obtained from Alfa Aesar. Nitric acid and water (ChromAr grade) were obtained from Avantor. Cadmium sulfate was obtained from J. T. Baker Chemical Company. Mercury (quadruple distilled, 99.9999%) was obtained from Bethlehem Apparatus Company. Platinum wire (25 μm and 0.5 mm diameter) and silver wire (1 mm diameter) were obtained from Goodfellow. Sulfuric acid (AR grade) was obtained from Macron Fine Chemicals. Cadmium nitrate tetrahydrate (99.999% trace metals basis), dimethylformamide (DMF, anhydrous, 99.8%), lithium perchlorate (battery grade, dry, 99.99% trace metals basis), mercury(II)

nitrate monohydrate (≥99.99% trace metals basis), propylene carbonate (PC, anhydrous, 99.7%), sodium perchlorate (≥98%), tetrabutylammonium perchlorate (TBAP, ≥99.0%), and *N*,*N*,*N*′,*N*′-tetramethyl-*p*-phenylenediamine (TMPD, 99%) were obtained from Sigma-Aldrich. Tetramethylammonium nitrate was obtained from Southwestern Analytical Chemicals. Ultra high purity (UHP) argon was obtained from S. J. Smith. All purchased chemicals were of A.C.S. reagent grade or better and used as received without further purification.

4.3.2 Working Electode Fabrication

Hg was electrodeposited on Pt UMEs (a_1 = 12.5 μm, $2 < R_G < 5$) similarly to previously described methods[10,18,19] from an aqueous solution of 10 mM $Hg(NO_3)_2{\cdot}H_2O$, 0.1 M tetramethylammonium nitrate, and 0.5 vol. % HNO_3 at a constant potential of -0.24 V *vs.* $E_{1/2}$ (Figure 4.3). The change in the supporting electrolyte from KNO_3 to a tetraalkylammonium salt was implemented in order to prevent contamination by trace amounts of amalgam-forming potassium. The deposition was manually terminated on the passage of 53 μC of charge ($n = 2$) to give a hemispherical Hg cap ($h = a_1$ = 12.5 μm, $H = 1$) (Figure 4.4). Relationships between Q, a_1, h, V and A are described elsewhere.[20] After Hg deposition, the probe was promptly removed from solution and sequentially rinsed with H_2O, acetone, and isopropanol to prevent changes in the Hg volume[21] and remove adsorbed species. Visual confirmation of the Hg sphere-cap probe dimensions was obtained with a Zeiss AxioLab.A1 microscope or an Olympus BX51TRF microscope. Probes were used shortly after preparation and not stored for later use.

4.3.3 Fabrication of a Cadmium Amalgam Reference

Previously,[10] we prepared a CAR by immersing a cadmium rod in a Hg pool while applying heat as originally reported by Marple in 1967.[22] This reference electrode was demonstrably stable over several months of use in PC. Nevertheless, the pooling of mercury beneath the saturated cadmium amalgam

suggested that the amalgam might have been oversaturated and undergone phase changes, preventing it from maintaining equilibrium with the filling solution. Considering this as well as the health risks concomitant with heating up metallic Cd and Hg, we have since adopted a modified version of the electrolytic amalgamation method catalogued in 1965 for the production of Weston Cells[23] and reported in detail for non-aqueous reference electrode construction by Hall and Jennings[24] in 1976.

Specifically, a 1.27 cm diameter Cd rod (CE and RE) was immersed in a solution of 1 M $CdSO_4$ in acidified H_2O (pH ~0.5). Electrical connection to the Hg pool (WE) was made with a coiled Pt wire (~1 mm diameter) inserted through the bottom of the cell, or by placing the Pt wire in an insulating polymeric sleeve to prevent exposure to solution. After applying -4.0 V (*vs.* Cd rod) for ~24 hours, the Hg pool (WE) was converted to Cd(Hg). Since the goal is saturate the Hg pool with Cd, any charge lost to hydrolysis and oxygen reduction is inconsequential, and the solution need not by purged with inert gas. Excess liquid Hg was siphoned away from the saturated amalgam, which takes on a granular consistency. The Cd(Hg) was washed multiple times with H_2O to remove excess $CdSO_4$ and H_2SO_4. It was then washed repeatedly with DMF until the decanted solution appeared clear and not cloudy. This clean, saturated cadmium amalgam was ground together with $Cd(NO_3)_2{\cdot}4H_2O$ with a mortar and pestle in an Argon-filled glovebox to give the slurry used in the reference electrode. The reference electrode itself was then assembled in the manner reported by Manning and Purdy.[25] That is, 1 mL of 1 M $Cd(NO_3)_2{\cdot}4H_2O$ in PC was dispensed into the contact well to prevent the entrapment of pockets of Ar before scooping in a column of Cd(Hg) 1.5 cm tall. This was then stirred with a length of glass to liberate pockets of gas and solvent and ensure full contact between the amalgam and the Pt contact. The amalgam was then topped with a ~0.3 cm layer of finely ground $Cd(NO_3)_2{\cdot}4H_2O$ salt to ensure continued Cd^{2+} saturation. The cell was then filled the rest of the way with 1 M $Cd(NO_3)_2{\cdot}4H_2O$ in PC.

It is worth noting that nearly all previously reported instances of a cadmium amalgam reference electrode have used chloride salts, presumably because of their excellent stability in DMF and the added benefit of being stable in an anhydrous state. However, the $Cd(Hg)/CdCl_2$ reference is irreversible in PC, possibly due to chloride adsorption on the amalgam.[26] In the absence of chloride, $Cd(Hg)/Cd^{2+}$ has a reasonable electron transfer coefficient ($\alpha = 0.34$).[27] This is why we have elected to use the nitrate salt of cadmium instead of the chloride. The nitrate salt is approximately ten times more soluble than the chloride is in PC (limiting solubilities of 0.161 M $CdCl_2$[26] and ~1 M $Cd(NO_3)_2{\cdot}4H_2O$) and has proven to be stable over the course of several months.

4.3.4 Construction of Electrochemical Cell

CV-PASs were conducted in a standard Teflon SECM cell over a glass substrate with a three-electrode configuration consisting of a Hg-capped Pt UME as the working electrode (WE), a cadmium amalgam (CAR) as the reference electrode (RE), and a flame-polished Pt wire as the counter electrode (CE). Electrochemical control and WE positioning was provided by a CHI 920D Scanning Electrochemical Microscope. All SECM experiments were carried out in a H_2O- and O_2-free MBRAUN UNIlab glove box filled with UHP argon.

4.3.5 Approaching a Surface

The initial approach of a Hg/Pt UME to an insulating glass substrate (Figure 4.5) was performed in the negative feedback mode in PC containing 500 μM TMPD as the redox mediator, 500 μM $MClO_4$ (M = Na or K) as the alkali analyte source, and 500 mM TBAP as the supporting electrolyte. After reaching the substrate with negative feedback ($i/i_{inf} \sim 70\%$) from the first single-electron oxidation of TMPD, the probe was retracted at least 400 μm from the point of closest approach. The probe was then approached to the surface in preselected increments with stripping CVs taken between motor movements to produce a CV-PAS. i_{amal} CV-PACs were created by sampling the current at the switching potential

between the cathodic and anodic potential sweep segments. i_{strip} CV-PACs were created by sampling the minimum current value in the anodic potential sweep. Q_{strip} CV-PACs were created by integrating the peak in the anodic potential sweep.

4.3.6 Fitting Negative Feedback

CV-PACs made with sphere-cap electrodes were fit in accordance with an analytical approximation developed for pure negative feedback at disc UMEs[5,6] and later extended to sphere-cap UMEs:[8]

$$\frac{i(L)}{i_{\mathrm{inf}}} = \left[k_1 + \frac{k_2}{L+s} + k_3 \exp\left(\frac{k_4}{L+s}\right)\right]^{-1} \quad (5)$$

where i is the current at some particular L, i_{inf} is the current recorded in the absence of hindered diffusion (*i.e.*, at large L), and s is freely adjustable and determines the abscissa. All data was handled in terms of L and only presented in terms of G after the application of equation **(5)**. If the input L values agree with those expected by the model, then s approaches zero. If the model fits the data well, then the uncertainty in the probe position, u_L, also approaches zero. Initially, the k_i values provided in the literature[8] were used, since they are tailored to sphere-cap UME geometries. Since these are based on fits of single-step chronoamperograms (CA), they are hereafter referred to as *ca*-k_i coefficients for the sake of brevity. Similarly, our own k_i coefficients based on simulated CV-PAC data are referred to as *cv*-k_i coefficients.

4.3.7 Digital Simulations

An updated version of our previously published COMSOL model[10] was used to generate CV-PAS data corresponding to a wide range of conditions, including our own particular experimental parameters.

Previously, we used a single "transport of diluted species" physics node to describe the behavior of two species (*ox* and *red*) in two phases (solution and Hg). We defined a flux discontinuity describing Butler-Volmer kinetics at the phase boundary and set the diffusion coefficient of the out-of-phase species to 1×10^{-32} m^2 s^{-1} to prevent movement of *ox* into the Hg phase or *red* into the solution phase.

However, the accumulation of *ox* in the Hg phase within a few mesh elements of the phase boundary led to approximately two-fold smaller current than observed experimentally. Therefore, we switched to using two "transport of diluted species" physics nodes, each one describing the behavior of a single species in a single phase (*ox* in solution or *red* in Hg). This allowed us to define a flux where we had previously defined a flux discontinuity and thus resolved the issue of *ox* buildup within the Hg phase. The normalized currents (i/i_{inf}) were nearly unaffected by the change, but the raw currents increased nearly two-fold with the change, bringing them much closer to the experimentally observed values. We flipped the probe orientation to limit the computational time spent re-meshing during PASs. We also changed the geometry of the sphere-cap from a Bezier curve to a truncated sphere to give a closer approximation of the Hg cap. Lastly, the time stepper was changed to "generalized alpha" to improve convergence during stripping processes, which produce large fluxes.

Besides generating data to characterize the working limits of the CA-PAC coefficients, the COMSOL model was used to generate CV-PAS data mimicking our experimental conditions. These data served as learning sets for tailoring the coefficients as follows. For each simulated PAS, the associated CV-PACs were extracted and fit with k_1, k_2, k_3, and k_4 allowed to vary freely with the originally reported CA-PAC k_i values for the nearest combination of *H* and *RG* serving as the initial estimates. For the training step, *s* was fixed at zero since the true tip-substrate gap was known. Then, setting the new coefficients as fixed parameters and allowing *s* to vary freely, the tailored models were applied to experimental data generated under matching conditions. The resulting *s* was applied to a copy of the original experimental dataset to rectify the tip-substrate distance. The transposed experimental dataset was then fit as before. This process was repeated until *s* was minimized in order to obtain the true final tip-substrate gap, L_f.

4.4 Results and Discussion

4.4.1 Experimental Amalgamation/Stripping CV-PACs

CV-PACs were obtained by monitoring the three main signals (*i.e.*, i_{amal}, i_{strip}, and Q_{strip}) generated by tip stripping voltammograms at different heights with respect to an insulating substrate. We show in Figure 4.6 the evolution of the CVs and their signals derived from the detection of Na^+ or K^+ in PC. After demonstrating the added accuracy of our fitting model, we then develop the model and describe conditions for its use in subsequent sections.

The initial rough approach to the substrate was based on monitoring the first single-electron oxidation of TMPD at the probe (Figure 4.5) and exhibits negative feedback in qualitative agreement with the current decrease expected from diffusional blocking within one tip radius of tip-substrate collision ($G_f < 1$). We deliberately did not crash the probe in our experiments, and the agreement between the initial TMPD PAC and one performed directly after the CV-PAS demonstrates that the probe was undamaged from physical contact, PC breakdown,[28] amalgam saturation, or the formation of quaternary ammonium amalgams.[29,30] Thus, the signal response in Figure 4.6 is due entirely to negative feedback, not parasitic processes. Though we use an organic mediator to corroborate our findings here, our data show that amalgamation or stripping signals are sufficient in of themselves to facilitate an approach to a substrate.

The subsequent CV-PAS with $NaClO_4$ (Figure 4.6AC) ending at the same distance from the substrate only shows appreciable negative feedback for $L < 3$ ($G < 2$). From equations **(1)**, **(4)**, and **(6)**, this observation is consistent with the calculated T_{amal} of 3.5, for which $w_2 = 1.9$ and $G_o = 1.8$. Since the expanding depletion region only begins to reach the substrate for $L \leq L_o$, the probe response at large L is not a function of L. Therefore, experimental CV-PACs based on i_{amal}, i_{strip}, and Q_{strip} were fit for $L \leq 3.48$ ($G \leq 2.48$) to maximize the fitting accuracy near the substrate. The literature *ca-k*$_i$ coefficients fit poorly

($\chi_{red}^2 = 3.25 \times 10^{-3}$ and $R_{adj}^2 = 0.68856$) and overestimate the final tip-substrate gap for i_{amal} by $s = 0.3$ with $u_L = 0.1$, giving $L_f = 1.7 \pm 0.1$ ($G_f = 0.7 \pm 0.1$). For an ideal fit, s and u_L converge to zero. We therefore developed situation-specific *cv*-k_i coefficients for fitting our experimental CV-PAC data (Figure 4.7) by fitting simulated data with s fixed at zero and the *cv*-k_i values allowed to freely vary. These situation-specific coefficients fit the experimental data well ($\chi_{red}^2 = 4.2 \times 10^{-5}$ and $R_{adj}^2 = 0.99683$) and report $s = 4 \times 10^{-5}$ with $u_L = 4 \times 10^{-3}$, giving $L_f = 1.396 \pm 0.004$ ($G_f = 0.396 \pm 0.004$). The distance reported by our fitting method is more than 4 orders of magnitude more accurate ($s = 4 \times 10^{-5}$ compared with $s = 0.3$) and over 20-fold more precise ($u_L = 4 \times 10^{-3}$ compared with $u_L = 0.1$) than the results obtained with the literature *ca*-k_i coefficients.

This strategy yields a similar improvement with CV-PAC data for $KClO_4$ in PC (Figure 4.6BD). As before, negative feedback is only observed for $L < 3$ ($G < 2$). This is consistent with the calculated T_{amal} of 4.1, for which $w_2 = 2.0$ and $G_o = 1.9$. Experimental CV-PACs were fit for $L \leq 3.99$. As expected, literature *ca*-k_i coefficients[8] fit the data poorly ($\chi_{red}^2 = 3.3 \times 10^{-3}$ and $R_{adj}^2 = 0.61317$) and overestimate the final tip-substrate gap for i_{amal} by $s = 0.6$ with $u_L = 0.1$, giving $L_f = 2.0 \pm 0.1$ ($G_f = 1.0 \pm 0.1$). However, *cv*-k_i coefficients trained on simulated data closely mimicking the experimental conditions fit the experimental data well ($\chi_{red}^2 = 4.33 \times 10^{-4}$ and $R_{adj}^2 = 0.99492$) and report $s = 4 \times 10^{-4}$ with $u_L = 6 \times 10^{-3}$, giving $L_f = 1.352 \pm 0.006$ ($G_f = 0.352 \pm 0.006$). The distance reported by our fitting method is more than 3 orders of magnitude more accurate ($s = 4 \times 10^{-4}$ compared with $s = 0.6$) and over 20-fold more precise ($u_L = 6 \times 10^{-3}$ compared with $u_L = 0.1$) than the results obtained with the literature *ca*-k_i coefficients.

These results demonstrate the importance of fitting CV-PACs with parameters that take into account not only the probe dimensions (R_G and H) but also the experimental timescale (T). If fit with the correct *cv*-k_i coefficients, amalgamation or stripping signals from a variety of ions can be used to

position a Hg-based SECM probe. The agreement between signal types permits a selective use of signals, as i_{strip} and Q_{strip} are viable measurements even when overlapping processes interfere with i_{amal}. Furthermore, since this technique always gives negative feedback (Figure 4.8), it enables probe positioning over any substrate, regardless of electronic conductivity.

4.4.2 Predicting Negative Feedback Onset

In arriving to a practical approach to detect the presence of the substrate by fitting negative feedback approach curves extracted from stripping voltammetry, one must consider relationships between space, time, and mass transport. For any sphere-cap probe dimensions, decreasing T causes G_o to decrease and the steepness of the response $(\partial i/\partial G)$ for $G < G_o$ to increase. For example, the simulated i_{amal} CV-PACs in Figure 4.9 cover combinations of four v values (0.001, 0.01, 0.1, and 1 V s^{-1}) and two D_{ox} values (4×10^{-10} and 2×10^{-10} m^2 s^{-1}) selected to give a number of similar T values for nine different electrode dimensions. CV-PACs exhibit negative feedback over a smaller range and with increased slope for smaller T. Small R_G gives a smaller change in current with respect to distance than obtained with large R_G, but the effect of R_G is negligible for small T, since the depletion region does not extend beyond the bounds of the insulating sheath. A comparison of G_o values of two different electrode radii and two different R_G values is available as Figure 4.10. And, for any particular combination of R_G and H, curves with a common T value share a common curvature and exhibit negative feedback at the same distance from the substrate (Figure 4.11).

This leads to a key difference between CV-PACs and potentiostatic PACs. Sustained electrochemical activity continuously depletes reactant from solution at all times, and it is the disturbance of this expanding depletion region by the presence of a substrate that causes negative feedback, regardless of how closely the measured current approximates the ideal steady-state response.

In traditional potentiostatic PACs, the probe is moved while applying a potential. T continuously increases since there is no break in activity, and the current as the probe approaches a substrate has some dependence on the motor travel distance, step size, and translation speed. However, each CV in a CV-PAS is a discrete event, so T is identical for each position in the approach. Therefore, the onset of negative feedback (G_o) for CV-PACs (and CA-PACs) does not depend on motion control and can be expressed as a function of T by considering the time-dependence of mass transport.

Rather than distinguishing between two approximate diffusion regimes or making assumptions regarding electrode accessibility, we fit the G_o datasets in Figure 4.11 with a freely-varying reciprocal power function of the form

$$G_o = \frac{1}{A+(BT)^{-C}} \quad \textbf{(6)}$$

where A, B, and C are positive real numbers.

This function is a generalized form of w_1 and w_2, since $G_o = w_1$ is given by $A = 1$, $B = \pi$, and $C = (1/2)$ and $G_o = w_2$ is given by $A = 0$, $B = 2$, and $C = (1/3)$. Similarly, pure semi-infinite planar diffusion is given by $A = 0$, $B = \pi$, and $C = (1/2)$. The fit results for the data in Figure 4.11 are given in Table 4.1.

The onset of negative feedback (G_o) at long timescales is dominated by A, which increases with decreasing H and exhibits greater sensitivity to H at smaller R_G values. G_o converges to A^{-1} at large T, though the precise limiting behavior may not necessarily hold true for T values greater than those shown here since the depletion region is always expanding for all T. Nevertheless, this means that a tall sphere-cap exhibits negative feedback farther from the substrate than does a more oblate sphere-cap. Even for a hemispherical cap ($H = 1.0$), the range of A values found here (0.145 to 0.08) leads to limiting G_o of 6.9 to 12.9. This sensitivity to R_G helps explain why existing approximations[31] of the time-dependent depletion region thickness, *e.g.*, w_1 and w_2, do not predict the onset of negative feedback well (Figure

4.11). Both of these boundaries assume that the electrode is uniformly accessible (*i.e.*, R_G is infinitely large), but this is not accurate for UMEs with a finite R_G in bulk solution,[32,33] much less under hindered diffusion.[8]

At short timescales, the onset of negative feedback (G_o) is dominated by *B* and *C*. *B* increases with decreasing *H* or R_G and, like *A*, shows greater sensitivity to changes in *H* at smaller R_G values. Thus, tall sphere-caps have a smaller sensitivity to changes in *T* than do more oblate sphere-caps. The sensitivity to differences in *T* increases with shrinking insulating sheath width, but increases more for squat sphere-caps than for tall ones. This can be understood as a consequence of differential access to back-diffusion. *C* is generally ~0.5, but deviates to smaller values for small R_G and large *H*. *B* and *C* are less sensitive than *A* to changes in the probe geometry in part because they dominate at short timescales, when species beyond the bounds of the insulating electrode sheath are not given sufficient time to reach the electrode surface.

These results allow experimentalists to either estimate the distance at which feedback will occur (G_o) and select a SECM motor step size to avoid crashing or, having reached a resolution limit for motion control, to select E_{sw} and *v* such that G_o is large enough to avoid an undesirable collision between the probe and substrate. Typical SECM working distances are less than the length of one probe radius ($G_f < 1$) to mitigate diffusional broadening and increase signal collection efficiency, so we strongly recommend using conditions giving $G_o \geq 1$. The alternative ($G_o < 1$) not only carries a high risk of crashing the probe into the substrate but also is difficult to fit accurately since so few data points exhibit feedback behavior. Therefore, the smallest usable time, T_{min}, satisfies $G_o = 1$ (Table 4.1).

For example, the lower temporal limit for a sphere-cap with $H = 1.0$ and $R_G = 10$ is $T_{min} = 0.89 \pm 0.04$. For the particular case of Li^+, Na^+, or K^+ in PC, diffusion coefficients are typically $D_{ox} = 2 \times 10^{-10}$ m^2

s^{-1} and the maximum overpotential is ~0.4 V (limited by solvent breakdown),[34] which gives ΔE_t ~ 0.45 V for small T. See Table 4.2 for physical data. From equation **(2)**, the maximum usable sweep rate (ν_{max}) under these conditions is 0.65 V s^{-1} for a 12.5 μm radius tip or 97 V s^{-1} for a a_1 = 1.0 μm (Figure 4.10). At sweep rates faster than these, negative feedback only occurs for $G \leq 1$, quantitative fitting of CV-PAC data is difficult at best, and the probe is likely to crash. Based on the temporal limit for H = 1.0 and R_G = 10, which is the largest of those tested here, T_{min} = 0.9 constitutes the approximate limit for quantitative CV-PACs.

Setting the lower limit of T_{min} = 0.9 also guarantees that kinetic complications do not occur over the experimentally relevant range of heterogeneous rate constants (k^o), electron transfer coefficients (α), and diffusion coefficients (D_{ox}) for alkali amalgams in PC, DMSO, and other common solvents (Figure 4.12). This simplification is a prerequisite for making generalized claims, since these parameters may be strongly affected for alkali amalgams by changes in the supporting electrolyte identity and concentration.[35-37]

4.4.3 CV-PAC Model Coefficients

In addition to the onset of negative feedback (G_o), the curvature of CV-PACs is time-dependent. Because *ca*-k_i and *cv*-k_i coefficients are specific not only to a particular combination of R_G and H but also to a specific value of T, coefficients tailored to "steady-state conditions" are in fact only applicable over a narrow set of conditions. For any combination of R_G and H, literature *ca*-k_i coefficients derived for "steady-state conditions" lead to overestimation of L_f ($s > 0$) for small T and underestimation of L_f ($s < 0$) for large T (Figure 4.13). Setting the reasonable requirement that L_f be accurate to within 10% of the basal radius ($|s| < 0.1$), the absolute error from the application of literature *ca*-k_i values falls within acceptable levels for $40 < T < 960$ for R_G = 10. For a 12.5 μm radius hemispherical cap UME working in

typical conditions for Na^+ or K^+ amalgamation in PC, this restricts the sweep rate to roughly 10 mV s^{-1} > v > 0.4 mV s^{-1}. Within this range, literature *ca*-k_i coefficients may be applied confidently.

CV-PACs at other timescales, however, must be fit by parameters tailored to the particular conditions. Fitting simulated CV-PACs with k_i allowed to vary freely and s fixed at zero gives a much better fit ($\chi_{red}^2 < 1 \times 10^{-4}$) than using the literature *ca*-k_i coefficients over all tested values of T (Figure 4.13) and generates the *cv*-k_i coefficients shown in Figure 4.14. Though freely-varying *cv*-k_i models fit simulated CV-PACs well over a wide range of conditions, the resulting *cv*-k_i coefficients converge with orders of magnitude greater uncertainty for short timescales (approximately $T < 1$). This compromises the accuracy of their application to experimental data and is further support for the recommended lower temporal limit of $T_{min} = 0.9$. This demonstrates that the poor fits associated with the original *ca*-k_i coefficients are at least partially due to disagreement between the assumed and actual T values.

4.4.4 Solubility Limitations

Large T values can be impossible to implement experimentally since irreversible phase changes occur if the amalgam is saturated,[38] leading to Hg loss in the following anodic sweep. The temporal saturation limit (T_{sat}) under diffusion-limited conditions depends primarily on the bulk metal ion concentration (C_{ox}^*) and the amalgam solubility limit (C_{lim}), which varies from ion to ion. For example, the mole fraction solubilities of Li, K, and Na in Hg are 1.33%, 2.53%, and 5.40%, respectively.[39-41] Ignoring small changes in amalgam volume, this gives solubility limits of 0.90 M Li(Hg), 1.7 M K(Hg), and 3.6 M Na(Hg). Because amalgamation is not reversible for $T > T_{sat}$, the range of physically usable T values is limited to $T_{min} < T < T_{sat}$. Similarly, the usable range of analyte concentrations is limited to $C_{ox}^* < C_{ox,sat}$. These relationships are presented in Figure 4.15 along with the temporal limits imposed for detecting negative feedback onset without crashing and for using literature *ca*-k_i coefficients.

In addition, the saturation conditions depend on the probe geometry. As already mentioned, decreasing the thickness of the insulating probe sheath (R_G) increases the contribution of back-diffusion to the flux, particularly at large T, where the depletion region extends past the edge of the insulating sheath. However, changing from $R_G = 10$ to $R_G = 2$ produces less than 10% change in $C_{ox,sat}$ or T_{sat}. If C_{ox}^* and T are selected so as to avoid operation near the saturation boundary demarking zone (**I**), the impact of R_G on T_{sat} is negligible. Though R_G has little impact on saturation conditions, decreasing the height (H) of the Hg sphere-cap drastically decreases $C_{ox,sat}$ or T_{sat}. For any given combination of R_G and T, changing from $H = 1.0$ to $H = 0.5$ drops $C_{ox,sat}$ by ~40%. And $C_{ox,sat}$ for $H = 0.2$ is ~70% smaller than for a hemispherical cap. Thus, shorter sphere-caps saturate more readily than taller ones do.

4.4.5 Future Work: Ionic CV-SECM Imaging

CV-PAS experiments can also be performed laterally over a substrate to interrogate ionic gradients caused by an activated substrate. This has been reported for Pb^{2+} and Cd^{2+} in aqueous conditions[12] but never for alkali ions. Probe scan curves (CV-PSCs) of TMPD and $LiClO_4$ in PC with a Hg-based SECM probe operating in redox competition mode over an activated Au interdigitated array on Si wafer are shown in Figure 4.17. The cyclic voltammetry probe scan surface (CV-PSS) data from which the CV-PSCs are extracted are available as Figure 4.16, and a similar substrate can be seen in Figure 4.8. The TMPD oxidation current at the SECM probe is increased over 330 μm < X < 1150 μm by the regeneration of TMPD from $(TMPD\bullet)^+$ at the Au substrate. Then, without substrate activation towards Li ion uptake, the Li stripping signal at the Hg probe shows no topographic variations but for a slight substrate tilt. However, with the substrate activated to compete for Li ions, the probe stripping signal shows a marked decrease over the same region that produced positive feedback for TMPD. The spatial agreement between TMPD feedback and Li^+ competition signals show that ion-specific information about substrate reactivity can be obtained reliably and with spatial contrast from stripping signals.

The difference in signals again highlights the relationship between time and distance in diffusional transport. We use $T = 13.7$ for the TMPD CV-PSS but $T = 0.72$ for the Li CV-PSSs so as to avoid saturating the Hg probe. These conditions correspond to zone **V** in Figure 4.15, which would be unsuitable for approaching a substrate, but are not an issue for lateral movement. When the substrate is activated for redox competition, the probe need only expand far enough to interact with the concentration gradient established by the substrate. Due to the disparity in timescales, the reactant depletion layer as estimated by equation **(4)** reaches farther into solution for the TMPD CVs ($w_2 = 3.0$) than for the Li stripping CVs ($w_2 = 1.1$). Consequently, substrate topography and tilt are less evident in the Li stripping data than in the TMPD data under these conditions, even though L_f is unchanged.

This also suggests the possibility of probing reactivity and topography simultaneously through mixed redox mediator feedback and constant negative ionic feedback. Given the importance of ionic reactivity to biological systems and energy storage platforms, the ability to selectively isolate ionic signals with Hg-based probes while also conducting traditional SECM investigations with an organic mediator holds great promise for future investigations.

4.5 Conclusions

We have approached Hg sphere-cap UMEs to a surface in a non-aqueous medium using only the amalgamation/stripping signals of an alkali ion from CVs. Using experimental data for $NaClO_4$ and $KClO_4$ in PC, we demonstrated that i_{amal}, i_{strip}, and Q_{strip} CV-PACs extracted as cross-sections of a shared CV-PAS can all be fit well with *cv*-k_i coefficients tailored to the correct R_G, H, and T values.

We introduced approximations of the time-dependent depletion layer thickness, w_1 and w_2, as boundaries for the onset of negative feedback (G_o) and defined equation **(6)** to fit G_o for $R_G = \{10, 5, 2\}$ and $H = \{1.0, 0.5, 0.2\}$ over a wide range of T values. From this expression, we defined the approximate

practical limit of $T_{min} = 0.9$ for sphere-cap UMEs for all values of R_G, H, and a_1. This expression is useful for selecting instrumental parameters in advance to optimize the SECM approach curve response.

Since the coefficients used to fit CV-PACs depend on R_G, H, and T, the best practice is to generate situation-specific coefficients from simulations matching the particular experimental details as closely as possible. Though time-consuming, this ensures the best accuracy and precision while also preventing possible overfitting of data, especially at small T.

The ability to extract a CV-PAC from the amalgamation or stripping signal of an ion not involved in substrate chemistry allows definitive probe positioning without prior knowledge of local surface properties. When coupled with an organic mediator such as TMPD, it is possible to obtain height information from negative feedback while also carrying out complementary studies in the substrate generation, tip collection (SG-TC) mode. This may be useful for SECM studies of energy storage materials with ever-changing solid electrolyte interphase (SEI) properties, polymer films with selective conductivity, or fibrous membranes with ion-selective permeability.[11,42]

4.6 Acknowledgements

This material is based upon work supported by the National Science Foundation Graduate Research Fellowship Program under Grant No. DGE-1144245. Any opinions, findings, and conclusions or recommendations expressed in this material are those of the authors and do not necessarily reflect the views of the National Science Foundation. J.R.-L. acknowledges support from an Alfred P. Sloan Foundation Fellowship. The authors also thank UIUC for generous start-up funds. Z.J.B. is grateful to J. Hui for supplying Au interdigitated arrays and thanks B. H. Simpson and M. Burgess for fruitful discussions.

4.7 Figures and Tables

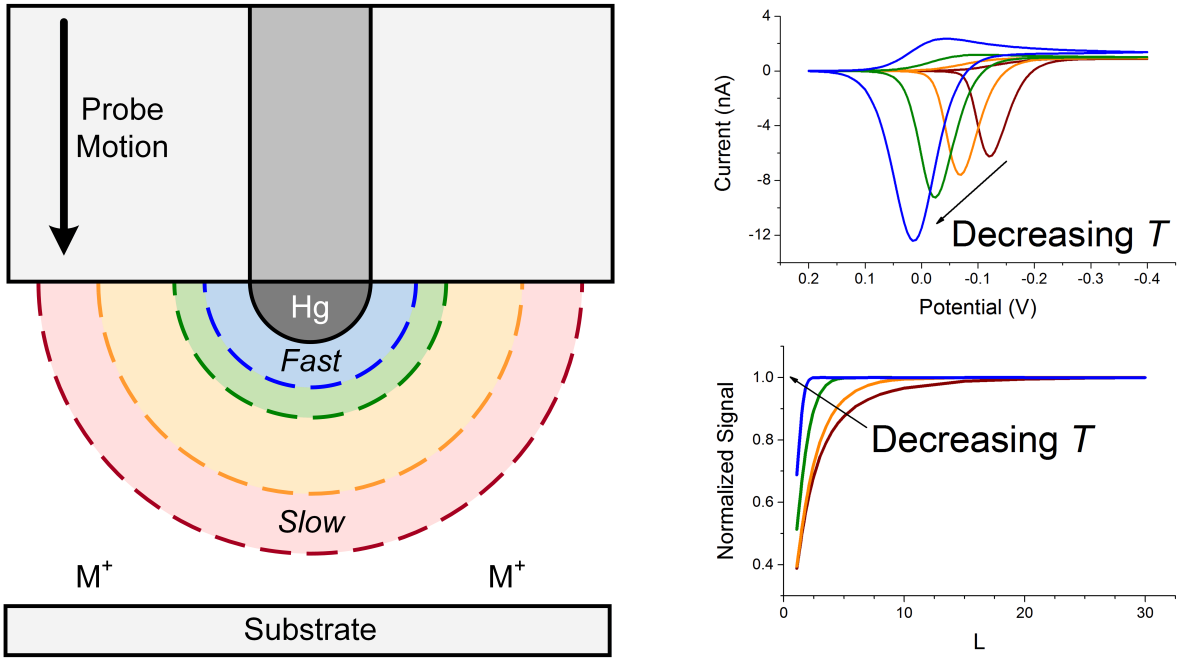

Figure 4.1. Table of contents graphic.

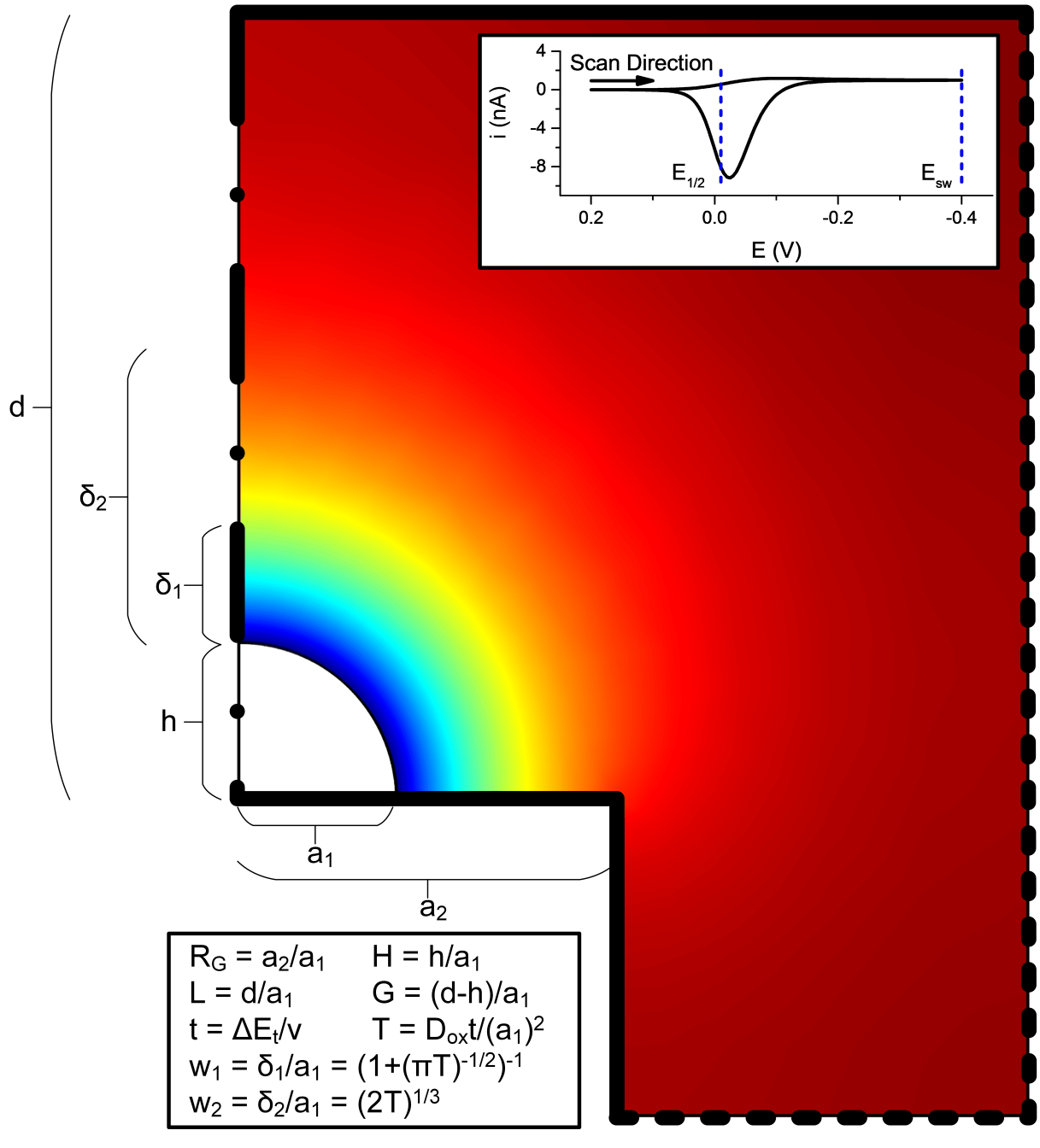

Figure 4.2. Schematic of Hg sphere-cap probe collecting Na^+ in the amalgam phase. Solid lines indicate zero-flux boundaries, dashed lines indicate open boundaries, and the dash-dot line indicates the axis of rotational symmetry. The concentration gradient shown here corresponds to T_{amal}, or E_{sw} as indicated in the associated CV (**inset**). a_1 = 12.5 μm, R_G = 2.4, H = 1, L = 5, G = 4. For the concentration gradient shown here, T_{amal} = 3.5, so w_1 = 0.77, w_2 = 1.9, and G_o = 1.75.

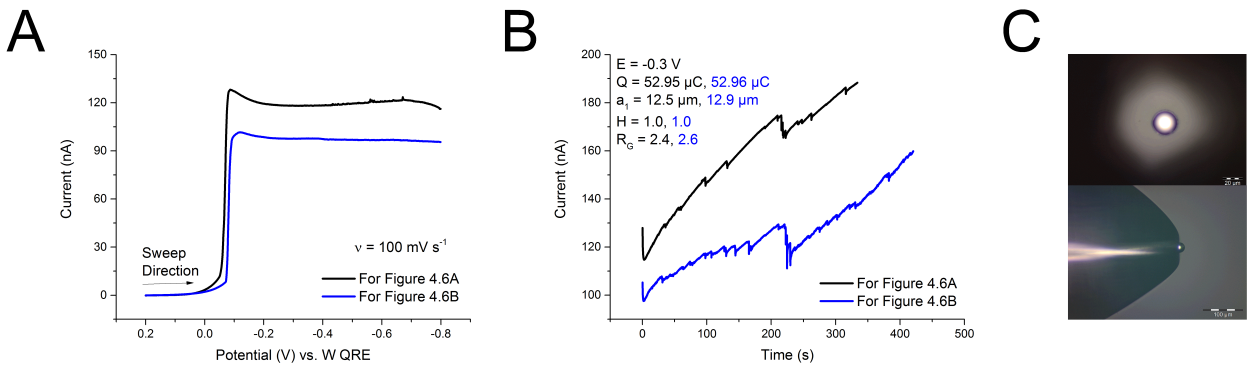

Figure 4.3. (**A**): Linear sweep voltammogram (LSV) run at 100 mV s^{-1} showing that Hg deposition begins around -0.06 V (*vs.* W QRE). (**B**): The electrodeposition of Hg at a constant potential of -0.3 V (*vs.* W QRE; -0.24 V *vs.* $E_{1/2}$) was terminated when ~53 µC had been passed so that H = 1.0. (**C**): Photomicrographs of the probe used in Figure 4.6B. The Pt UME is fully covered by Hg. The scale bars indicate 20 µm in the end view image and 100 µm in the side view image.

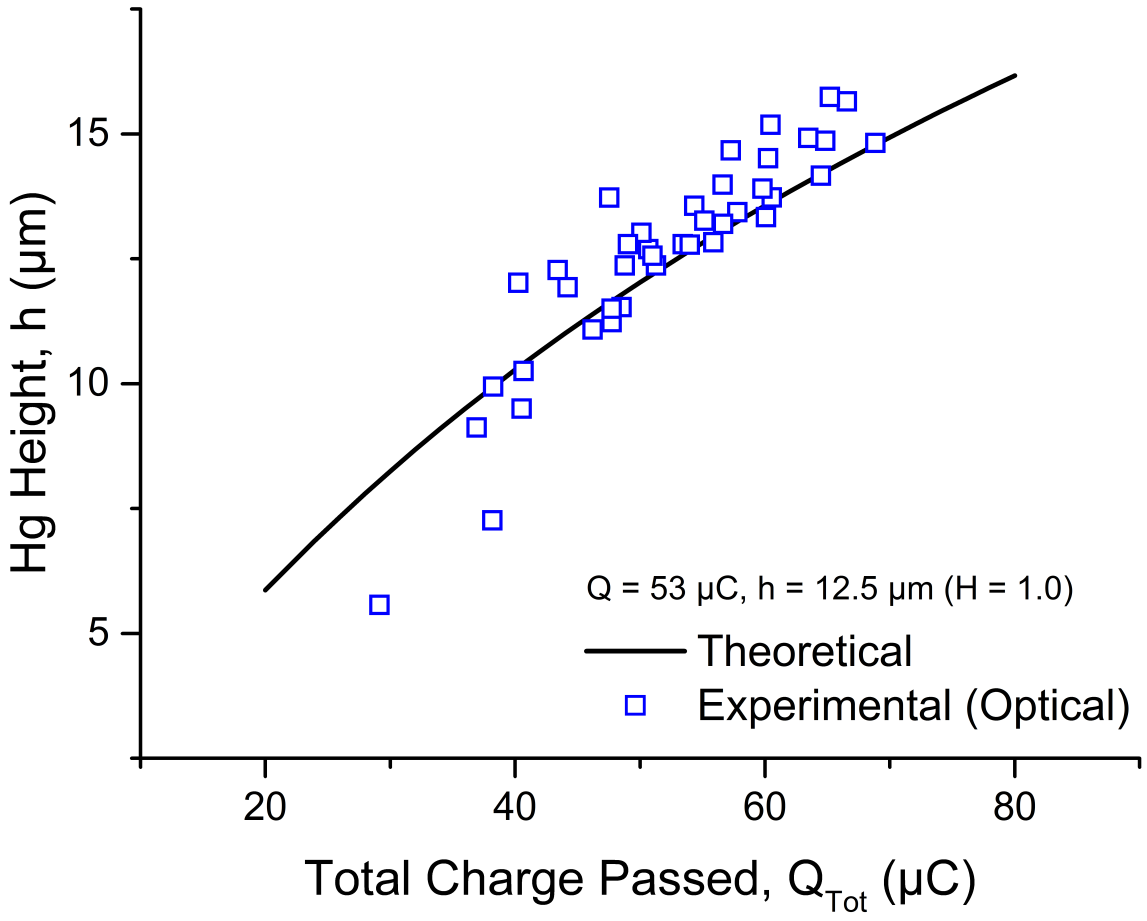

Figure 4.4. Optically measured heights (blue symbols) generally agree with the heights predicted from the measured charge assuming 100% Coulombic efficiency. Errors due to experimental imprecision include misalignment between the basal plane of the probe and the optical axis of observation.

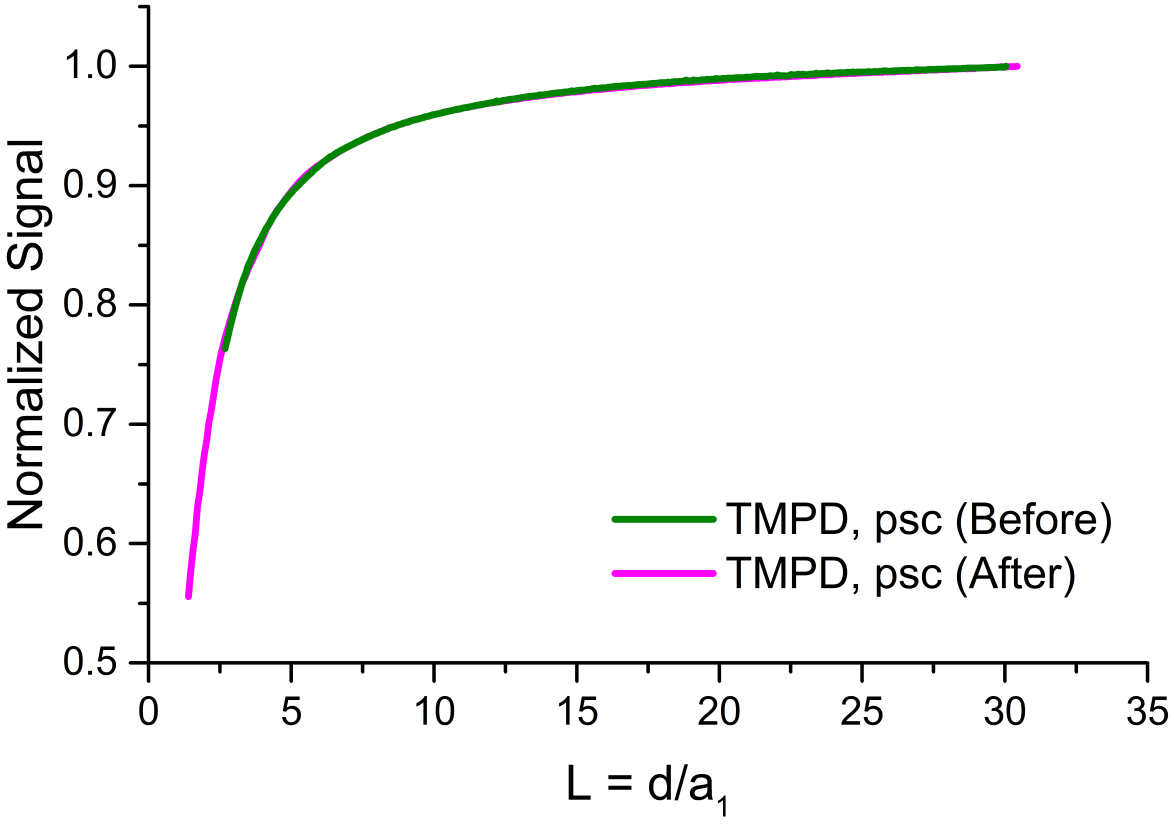

Figure 4.5. Probe scan curves (PSCs) based on TMPD oxidation taken immediately before and after the Na(Hg) CV-PAS experiment reported in Figure 4.6A. The second TMPD PSC terminates at the same tip-substrate gap as the Na(Hg) CV-PACs, *i.e.*, $L_f = 1.396$ (± 0.004). Comparison of the two curves demonstrates that the probe was not damaged during the course of the experiment, neither by collision with the glass substrate, saturation of the amalgam, nor activation of corrosive side-reactions.

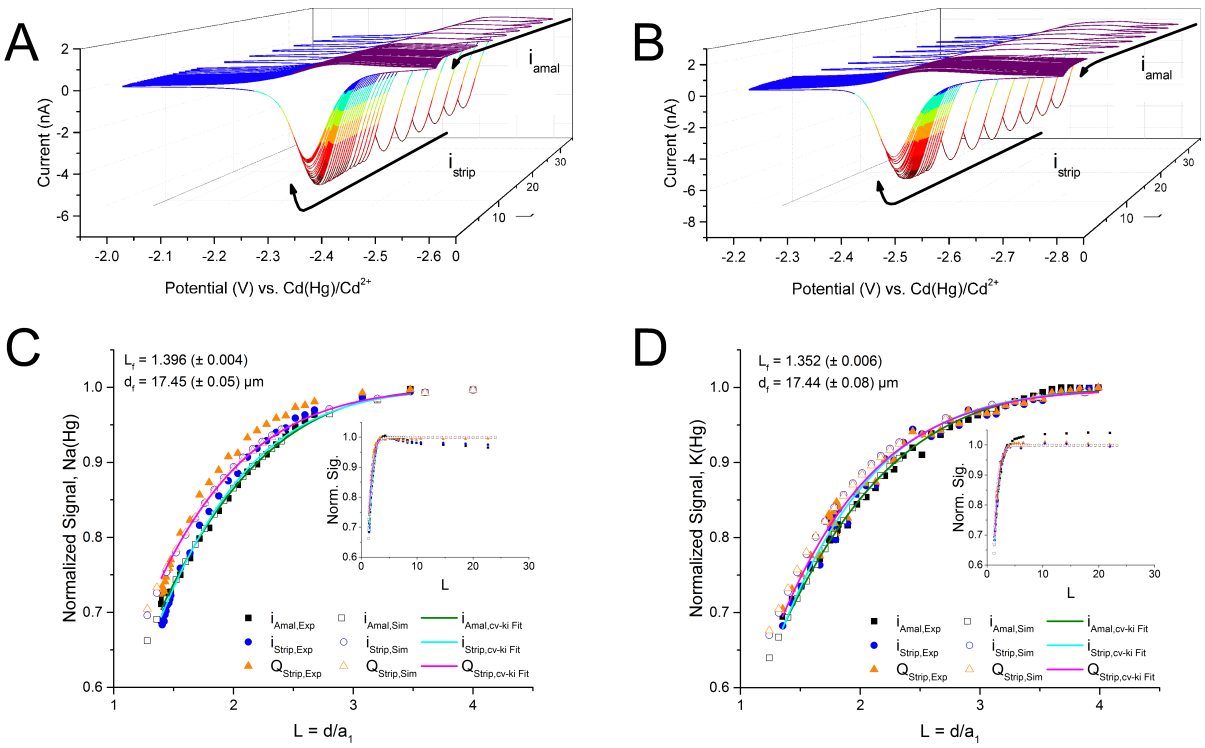

Figure 4.6. Experimental CV-PAS and CV-PAC data over a glass substrate for 0.5 mM $NaClO_4$ (**A**, **C**) and 0.5 mM $KClO_4$ (**B**, **D**) in PC with 0.5 M TBAP as supporting electrolyte. The initial increase in signal as L decreases in the Na(Hg) data may be attributed to conditioning of the Hg probe. A non-amalgam-forming reaction (*e.g.*, oxygen reduction) slightly affects the amalgamation signal in the K(Hg) data but does not distort the stripping current or charge. For $NaClO_4$ (**A**, **C**), a_1 = 12.5 µm, H = 1.0, R_G = 2.4, ν = 100 mV s^{-1}, T_{amal} = 3.5, and L_f = 1.396 ± 0.004. For $KClO_4$ (**B**, **D**), a_1 = 12.9 µm, H = 1.0, R_G = 2.6, ν = 100 mV s^{-1}, T_{amal} = 4.1, and L_f = 1.352 ± 0.006.

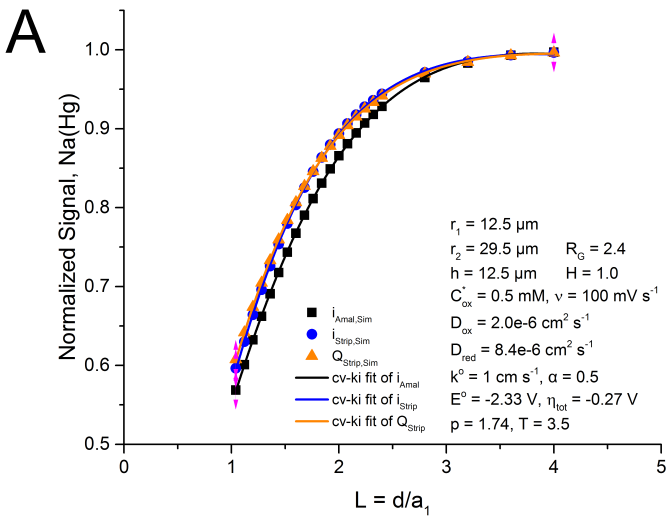

B

Equation	iinf/(k1+(k2/(L+sL))+k3*exp(k4/(L+sL)))		
Red. Chi-Sqr.	1.30383E-6	2.46892E-6	6.8865E-7
Adj. R-Sqr.	0.99992	0.99983	0.99995
		Value	Standard Error
Normalized Amalgamation Current	k1	0.32834	0.0169
	k2	1.48428	0.01801
	k3	1.09043	0.01866
	k4	-5.08804	0.20926
	iinf	1	0
	sL	0	0
Normalized Peak Stripping Current	k1	0.01532	0.07088
	k2	1.66486	0.05792
	k3	1.20998	0.05029
	k4	-2.98041	0.22776
	iinf	1	0
	sL	0	0
Normalized Stripping Charge	k1	0.15607	0.03234
	k2	1.50092	0.02718
	k3	1.04149	0.02112
	k4	-3.15126	0.13563
	iinf	1	0
	sL	0	0

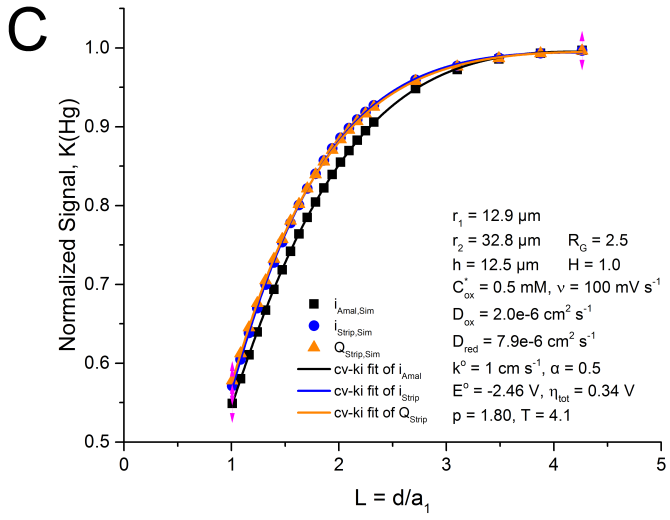

D

Equation	iinf/(k1+(k2/(L+sL))+k3*exp(k4/(L+sL)))		
Red. Chi-Sqr.	8.14533E-7	2.63569E-6	7.36066E-7
Adj. R-Sqr.	0.99996	0.99984	0.99995
		Value	Standard Error
Normalized Amalgamation Current	k1	0.35838	0.01196
	k2	1.4721	0.01266
	k3	0.97331	0.01106
	k4	-5.00184	0.15534
	iinf	1	0
	sL	0	0
Normalized Peak Stripping Current	k1	-0.06898	0.08101
	k2	1.75667	0.06245
	k3	1.24658	0.06461
	k4	-2.69174	0.20579
	iinf	1	0
	sL	0	0
Normalized Stripping Charge	k1	0.02715	0.04027
	k2	1.64641	0.03138
	k3	1.12808	0.03152
	k4	-2.74934	0.11799
	iinf	1	0
	sL	0	0

Figure 4.7. Generation of *cv-k*$_i$ fitting parameters (**B**, **D**) for Figure 4.6 from freely varying fits of CV-PACs (**A**, **C**) extracted from simulated CV-PAS data. Relevant simulation parameters are indicated in **A** and **C**.

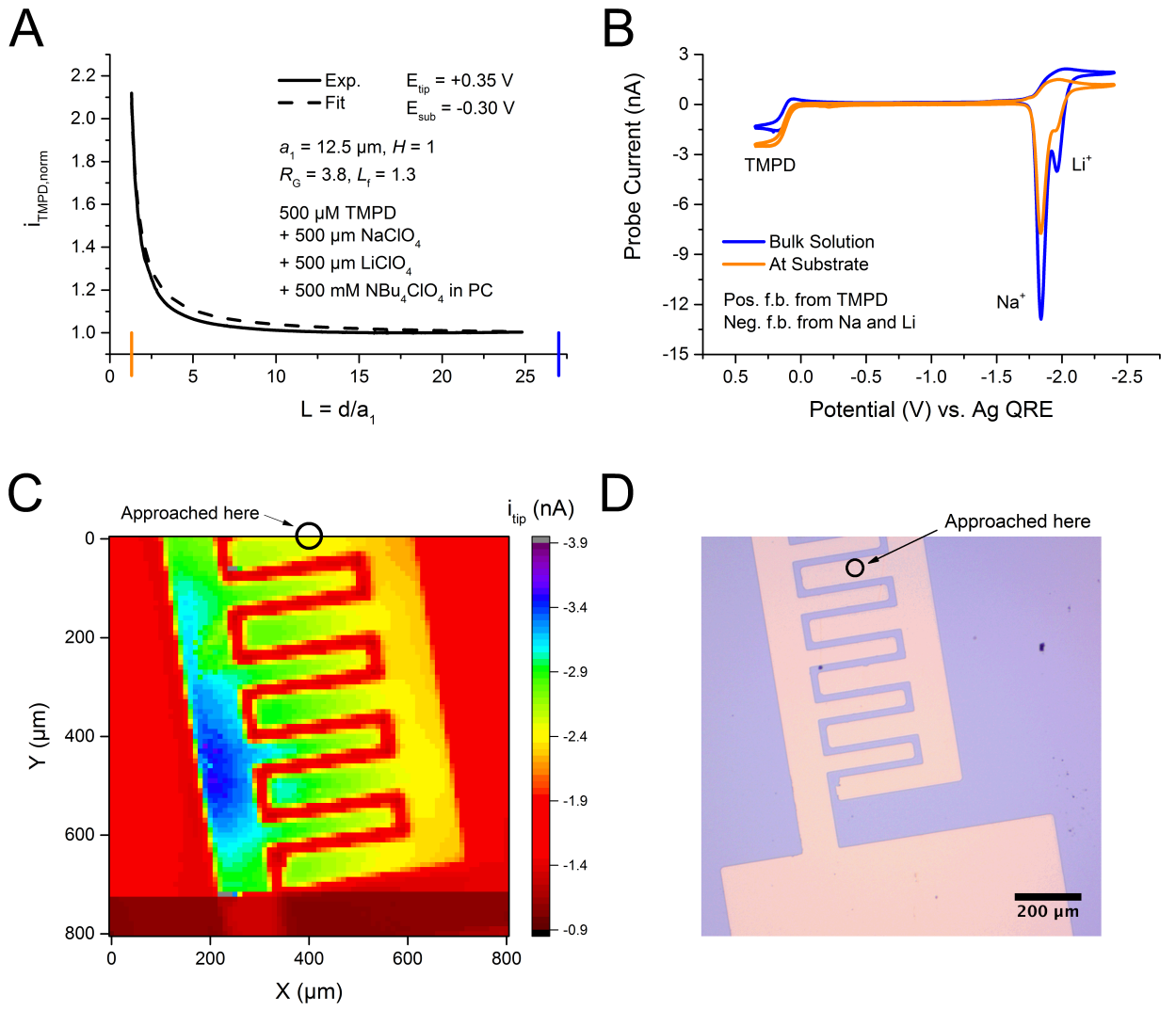

Figure 4.8. (**A**) A PAC based on TMPD oxidation taken with a Hg sphere-cap UME (a_1 = 12.5 µm, R_G = 3.8, H = 1.0) over a Au interdigitated array (IDA) on a Si wafer shows positive feedback. According to literature fitting parameters[8] for R_G = 5, H = 1.0 (dashed line), the final distance is L_f = 1.3 (G_f = 0.3). (**B**) CVs taken in bulk solution and at the substrate (L = 1.3) demonstrate positive feedback for TMPD oxidation but negative feedback for Na(Hg) and Li(Hg) amalgamation and stripping. (**C**) An SECM image taken in the direct mode proves the probe approached directly over a Au finger. (**D**) A photomicrograph of the Au IDA taken prior to electrochemical experiments confirms the approach location. The black circle in panels **C** and **D** has diameter of 50 µm and is approximately the same cross-sectional size as the SECM probe.

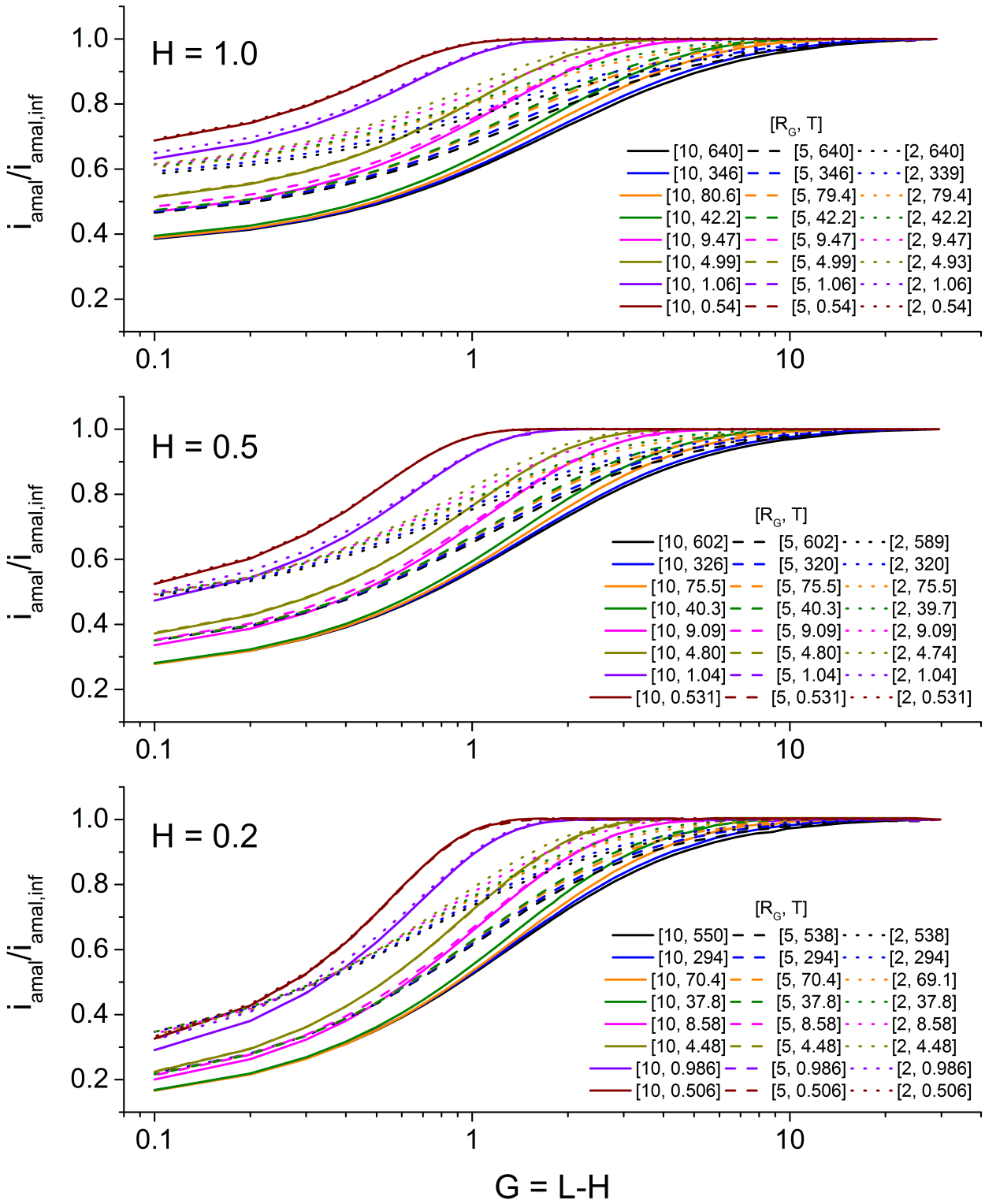

Figure 4.9. Simulated i_{amal} CV-PACs monitoring $M^+ + e^- \rightarrow M(Hg)$ (M = Li, Na, or K). Collision between the probe and the substrate would occur at $G = 0$.

A

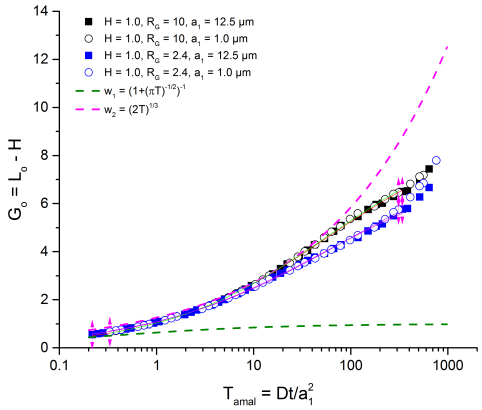

B

Equation	(A+(B*x)^-C)^-1			
Red. Chi-Sqr.	0.0031	0.00309	0.0021	0.00265
Adj. R-Sqr.	0.99884	0.9988	0.99946	0.99929
		Value	Standard Error	
(L-H) | i(L)[0,1] = 0.90	A	0.12539	0.00334	
(L-H) | i(L)[0,1] = 0.90	B	1.63564	0.06204	
(L-H) | i(L)[0,1] = 0.90	C	0.46445	0.00967	
(L-H) | i(L)[1,0] = 0.90	A	0.11276	0.0039	
(L-H) | i(L)[1,0] = 0.90	B	1.66258	0.06736	
(L-H) | i(L)[1,0] = 0.90	C	0.43955	0.00999	
(L-H) | i(L)[0,1] = 0.90	A	0.10832	0.00195	
(L-H) | i(L)[0,1] = 0.90	B	1.36292	0.03723	
(L-H) | i(L)[0,1] = 0.90	C	0.50846	0.00719	
(L-H) | i(L)[1,0] = 0.90	A	0.10685	0.00226	
(L-H) | i(L)[1,0] = 0.90	B	1.33974	0.04255	
(L-H) | i(L)[1,0] = 0.90	C	0.51083	0.00843	

Figure 4.10. (**A**) Normalized negative feedback onset distance (G_o) at various timescales for two different electrode radii (a_1 = 12.5 μm and 1.0 μm) and insulating sheath radii (R_G = 10 and 2.4). (**B**) Freely varying fits of negative feedback onset by equation **(6)**. G_o is independent of probe radius for small T but increases with decreasing radius (a_1) for large T, when the reactant depletion layer extends beyond the edge of the probe's insulating sheath (*i.e.*, approximately when $w_2 > a_2 - a_1$).

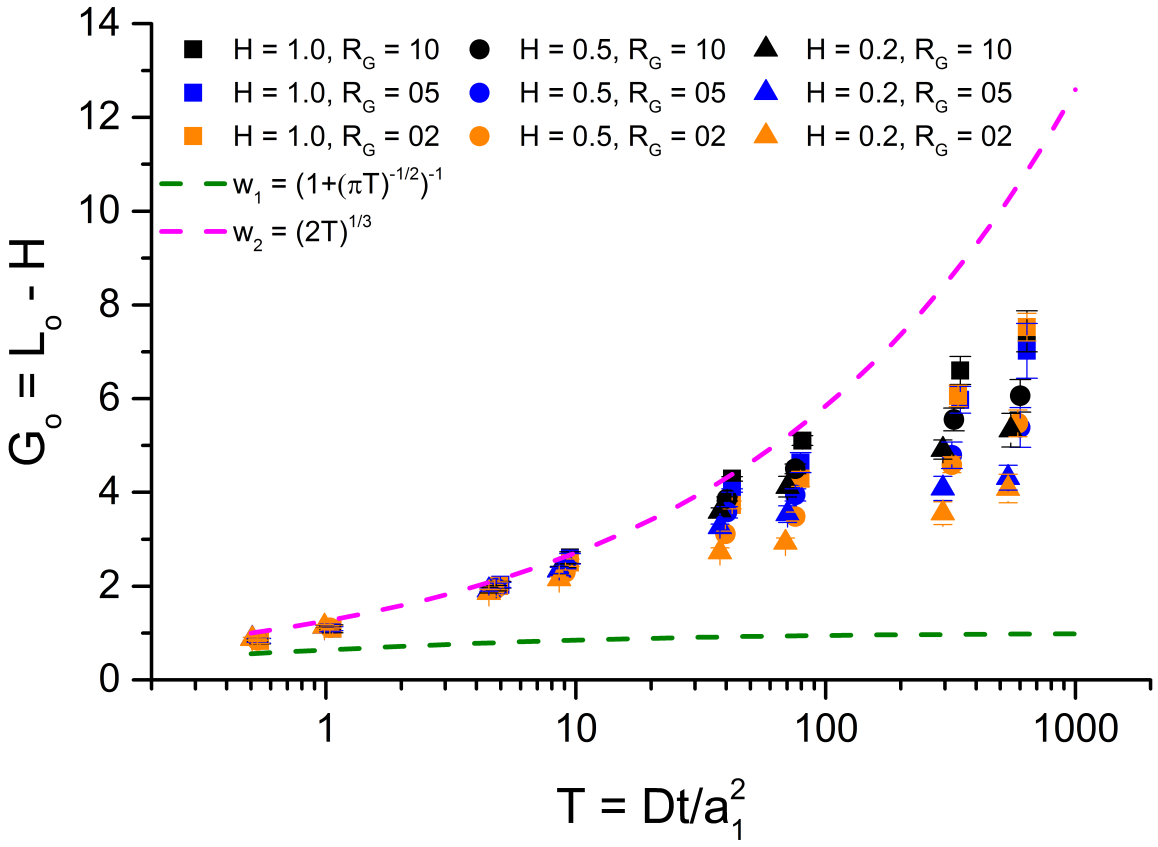

Figure 4.11. Simulated negative feedback onset distances for various sphere-cap UME probe dimensions. w_1 (green dashed line) and w_2 (pink dashed line) constitute diffusional transport limits predicted for $H = 1.0$ and infinitely large R_G.

H	R_G	A	$\pm u_A$	B	$\pm u_B$	C	$\pm u_C$	R_{adj}^2	T_{min}	$\pm u_{T,min}$
1.0	10	0.100	0.004	1.39	0.06	0.50	0.01	0.99956	0.89	0.04
1.0	5	0.116	0.005	1.50	0.05	0.49	0.01	0.99968	0.86	0.03
1.0	2	0.08	0.02	1.6	0.2	0.40	0.03	0.99448	0.78	0.1
0.5	10	0.121	0.008	1.59	0.07	0.47	0.02	0.99897	0.83	0.04
0.5	5	0.163	0.005	1.81	0.06	0.50	0.01	0.99928	0.79	0.03
0.5	2	0.16	0.02	2.0	0.3	0.43	0.04	0.99125	0.76	0.1
0.2	10	0.145	0.008	1.96	0.07	0.46	0.02	0.99863	0.72	0.03
0.2	5	0.199	0.005	2.19	0.06	0.50	0.01	0.99942	0.71	0.02
0.2	2	0.25	0.02	2.6	0.2	0.49	0.04	0.99366	0.69	0.07

All parameters are derived from application of equation **(6)**, $G_o = (A+(B \cdot T)^{-C})^{-1}$, to the simulated data presented in Figure 4.11. T_{min} corresponds to the condition $G_o = 1$.

Table 4.1. Negative feedback onset parameters and smallest usable normalized time.

Species	Solvent	Electrolyte, Conc.	D_{ox} ($cm^2\ s^{-1}$)	k^o ($cm\ s^{-1}$)	α
Na	AN	TEAP, 0.1 M	n.r.	5.70×10^{-1}	0.52
Na	DMF	TBAP, 0.1 M	n.r.	3.20×10^{-1}	0.63
Na	DMSO	TEAP, 0.1 M	n.r.	5.40×10^{-2}	0.55
Na	PC	TBAP, 0.5 M	2.00×10^{-6}	>1	~0.5
K	AN	TEAP, 0.1 M	n.r.	~2	0.5
K	DMF	TBAP, 0.1 M	n.r.	1.33	0.62
K	DMSO	TEAP, 1.0 M	2.80×10^{-6}	>1	n.r.
K	PC	TBAP, 1.0 M	n.r.	>1	~0.5
Li	AN	TEAP, 0.1 M	n.r.	2.30×10^{-2}	0.63
Li	DMF	TBAP, 0.1 M	n.r.	4.70×10^{-4}	0.82
Li	DMSO	TBAP, 0.1 M	n.r.	1.30×10^{-4}	0.7
Li	DMSO	TBAP, 0.2 M	3.50×10^{-6}	3.00×10^{-4}	0.73
Li	DMSO	TBAP, 1.0 M	1.80×10^{-6}	1.30×10^{-4}	0.7
Li	PC	TBAP, 0.1 M	2.40×10^{-6}	1.00×10^{-2}	0.7
Li	PC	TBAP, 0.2 M	1.70×10^{-6}	2.20×10^{-2}	0.72

Table 4.2. Collection of physical data relevant to stripping voltammetry.[35,43-45] The diffusion coefficients for Na, K and Li in Hg are 9.2×10^{-6} $cm^2\ s^{-1}$, 8.4×10^{-6} $cm^2\ s^{-1}$, and 7.9×10^{-6} $cm^2\ s^{-1}$, respectively.[46] Parameters not reported in the literature are indicated as n.r.

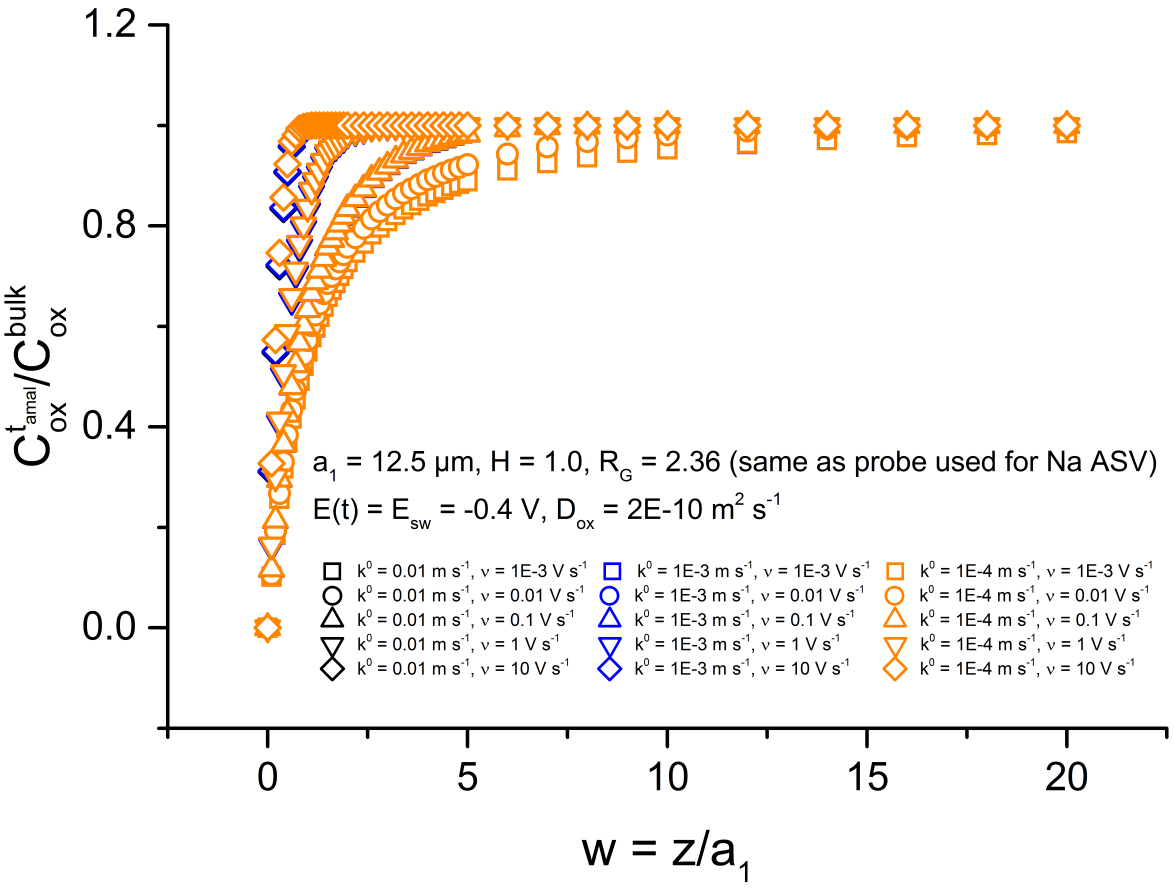

Figure 4.12. Normalized concentration profiles extending into solution some distance (z) from the sphere-cap's apex and normal to the basal plane of the sphere-cap. For a given potential scan rate (ν), the concentration profile is unaffected by changes in the heterogeneous rate constant (k^o). Therefore, k^o is not small enough under physically relevant conditions to cause kinetic complications and invalidate the assumption of mass-transport control.

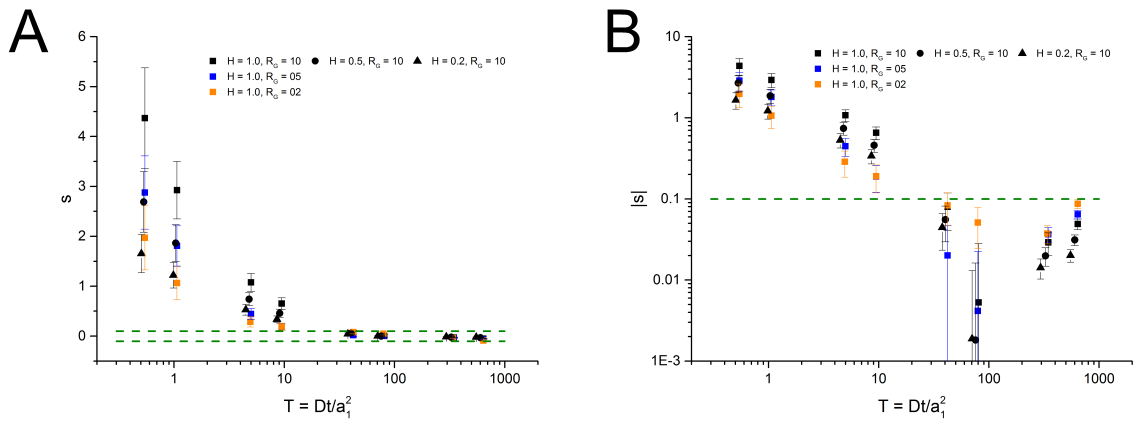

Figure 4.13. The tip-substrate gap offset (s) determined from applying literature ca-k_i coefficients to CV-PACs is positive at short timescales and negative at long timescales (**A**). The absolute value s does not converge to zero as T increases (**B**). The green dashed lines indicate the limits of acceptable error.

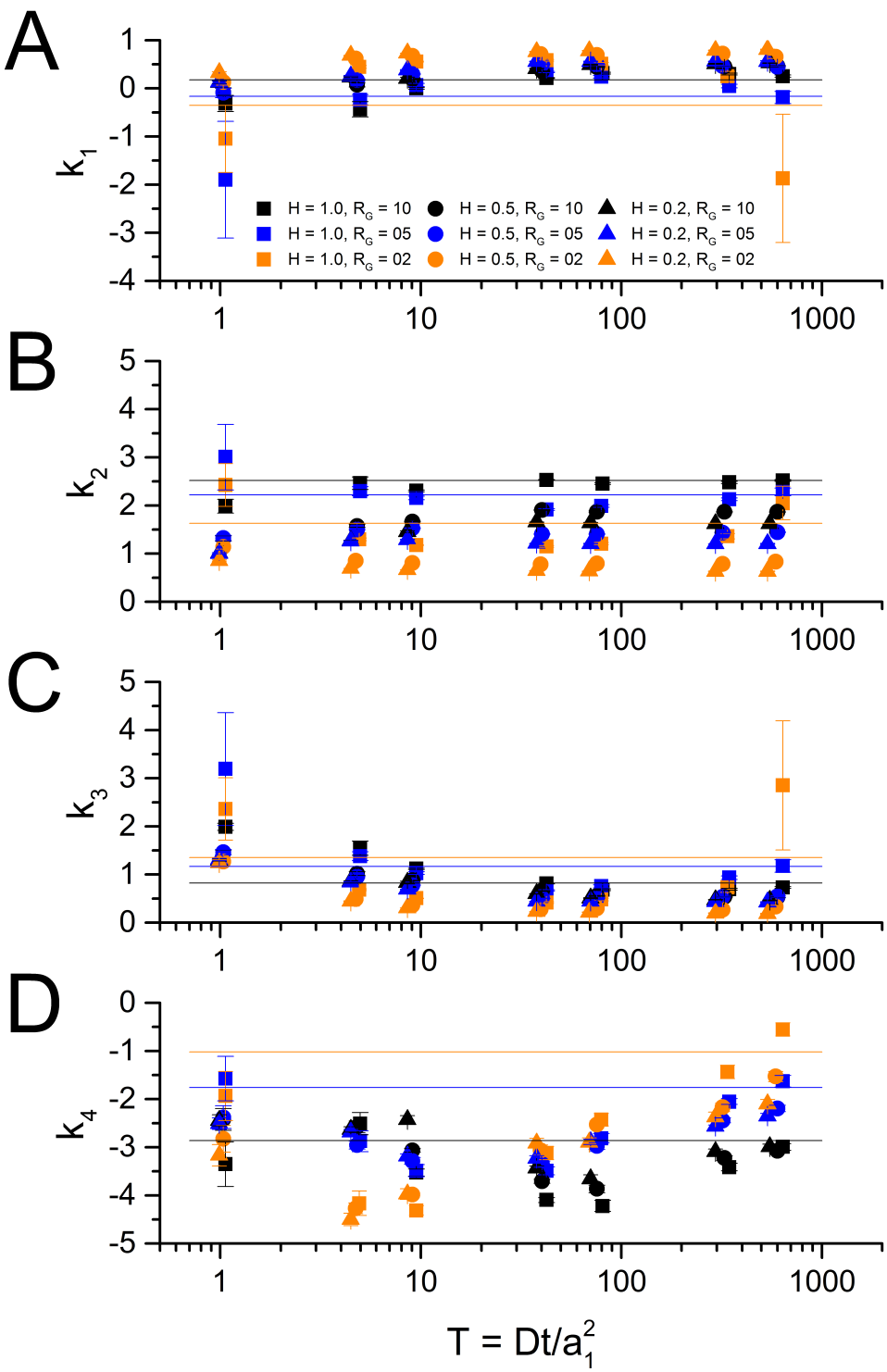

Figure 4.14. Optimized *cv*-k_1 (**A**), *cv*-k_2 (**B**), *cv*-k_3 (**C**), and *cv*-k_4 (**D**) coefficients across all physically useful T values. The literature *ca*-k_i coefficients corresponding to $H = 1.0$ are presented as T-independent lines and color-coded by R_G. The legend in **A** applies to all panels.

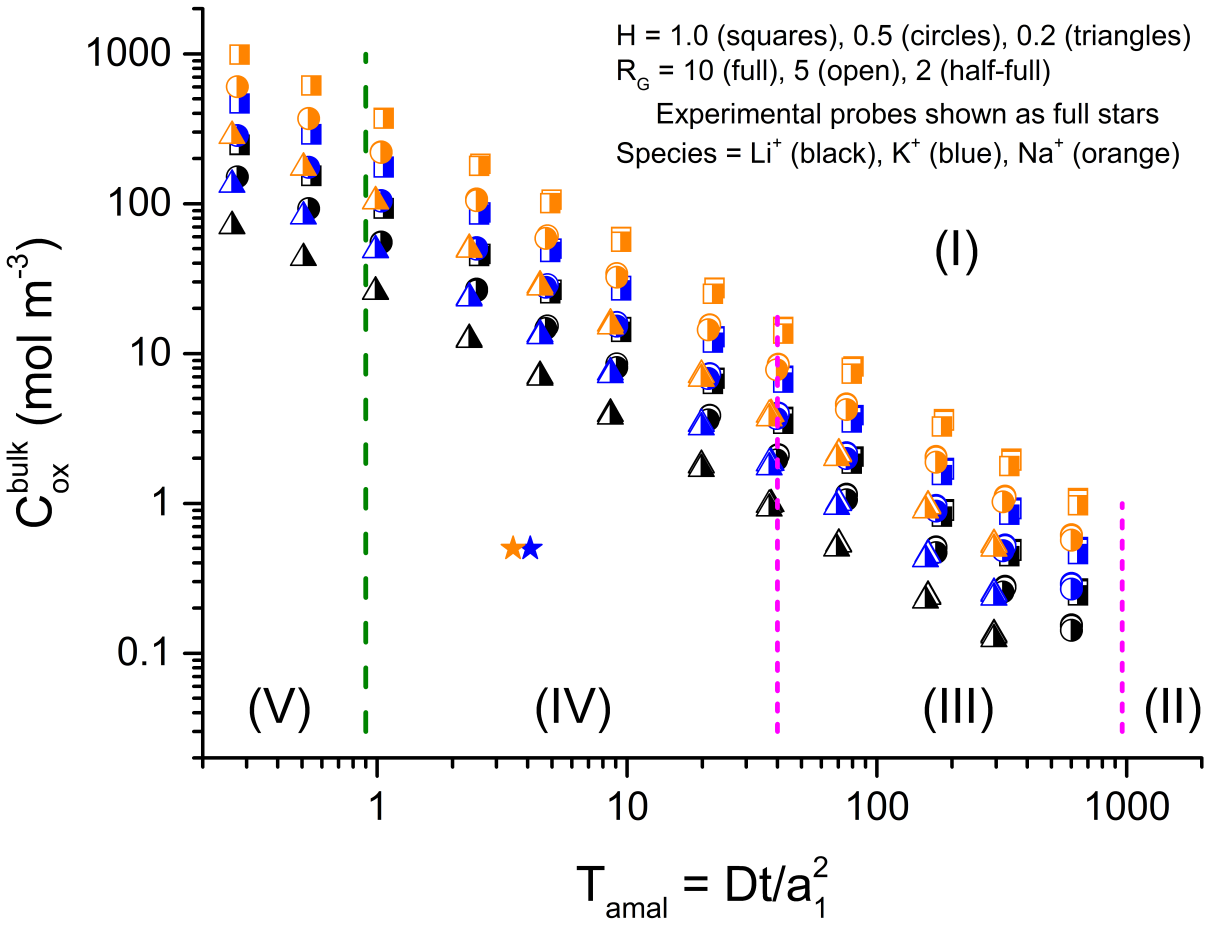

Figure 4.15. Zone diagram summarizing experimental limitations for amalgamation-/stripping-based CV-PACs. Saturation of the amalgam prevents operation in zone **I**. Tailored *cv*-k_i coefficients fit CV-PACs well for $T > 0.9$ (*i.e.*, zones **II**, **III**, and **IV**), indicated by the green gashed line. The short timescales in zone **V** do not fit well and increase the risk of a probe-substrate collision. Literature values for *ca*-k_i coefficients report L_f correctly to within 10% of the tip radius ($|s| \leq 0.1$) for $40 < T < 960$ (zone **III**), which is bracketed by pink dashed lines. The literature values underestimate L_f in zone **II** and overestimate L_f in zones **IV** and **V**.

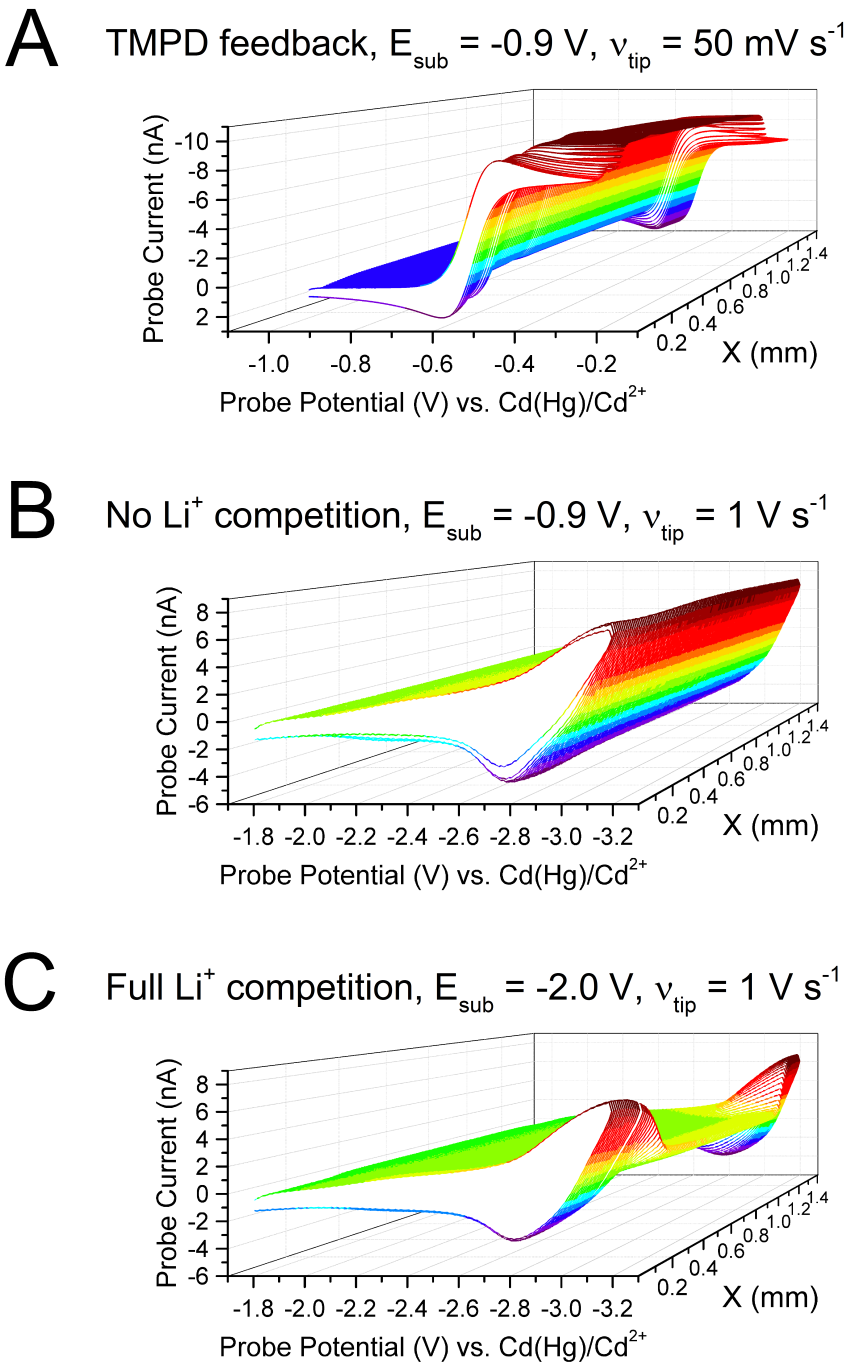

Figure 4.16. Experimental CV-PSSs from which the CV-PSCs in Figure 4.17 are extracted. (**A**) TMPD oxidation at the probe (v = 50 mV s^{-1}, T = 13.7) with the substrate poised to regenerate TMPD from (TMPD•)$^+$ shows the location of the Au band on the insulating Si wafer substrate. Li amalgamation/stripping at the probe (v = 1 V s^{-1}, T_{amal} = 0.72) with the substrate poised at an inactive potential (**B**) and then at an active potential (**C**) for Li uptake indicates an even surface and confirms the electrode location. The cell contains 5 mm TMPD, 5 mM $LiClO_4$, and 0.5 M TBAP in PC. The SECM motor step size is 10 μm. The potential and current axes in (**A**) are both reversed to better display the current from the oxidation of TMPD.

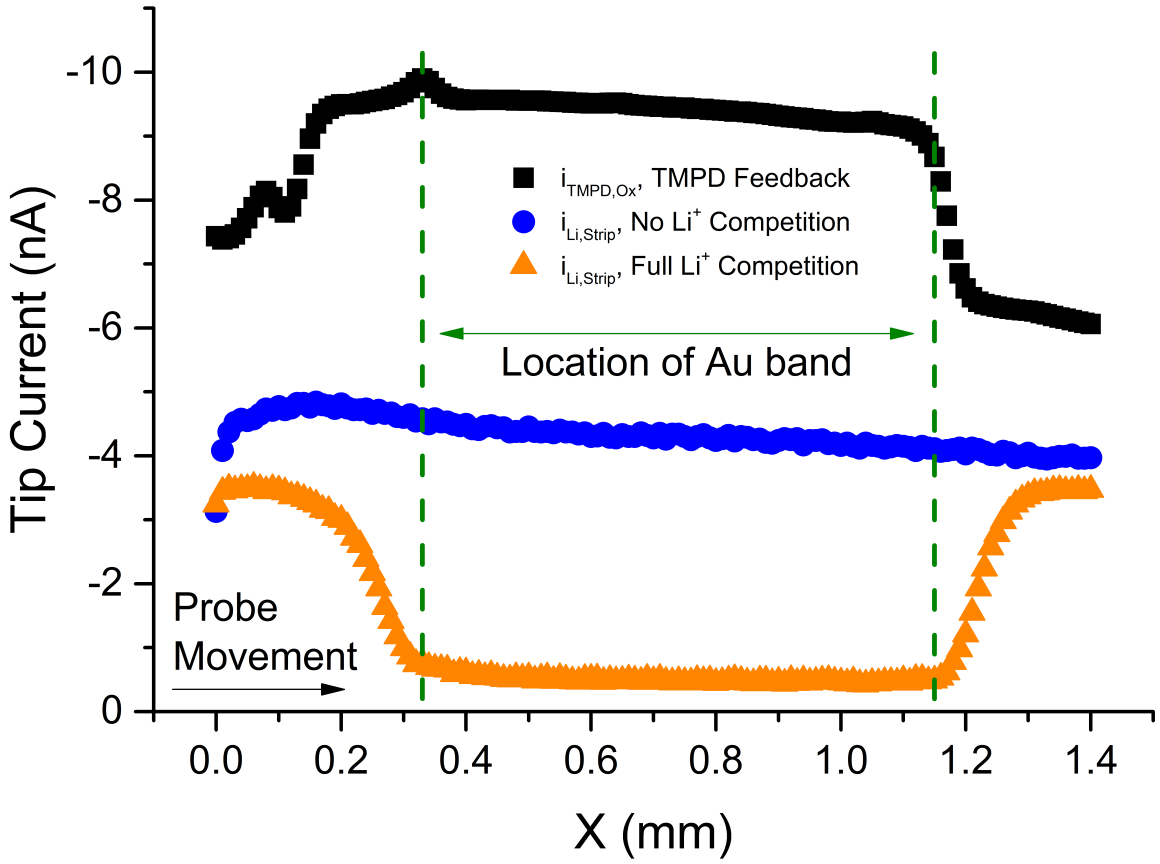

Figure 4.17. Experimental CV-PSCs extracted from CV-PSSs performed laterally over a Au band electrode on an insulating Si wafer. Each data point is derived from its own CV. The cell contains 5 mM TMPD, 5 mM $LiClO_4$, and 0.5 M TBAP in PC. The TMPD CV-PSC is executed at ν = 50 mV s^{-1} (T = 13.7). The Li^+ CV-PSCs are executed at ν = 1 V s^{-1} (T_{amal} = 0.72). The SECM motor step size is 10 μm.

4.8 References

(1) Bard, A. J.; Fan, F.-R.; Kwak, J.; Lev, O. Scanning Electrochemical Microscopy. Introduction and Principles. *Anal. Chem.* **1989**, *61*, 132–138.

(2) Amemiya, S.; Bard, A. J.; Fan, F.-R.; Mirkin, M. V.; Unwin, P. R. Scanning Electrochemical Microscopy. *Annu. Rev. Anal. Chem.* **2008**, *1*, 95–131.

(3) Polcari, D.; Dauphin-Ducharme, P.; Mauzeroll, J. Scanning Electrochemical Microscopy: a Comprehensive Review of Experimental Parameters From 1989 to 2015. *Chem. Rev.* **2016**, *116*, 13234–13278.

(4) O'Connell, M. A.; Wain, A. J. Combined Electrochemical-Topographical Imaging: a Critical Review. *Anal. Methods* **2015**, *7*, 6983–6999.

(5) Mirkin, M. V.; Fan, F.-R.; Bard, A. J. Scanning Electrochemical Microscopy Part 13. Evaluation of the Tip Shapes of Nanometer Size Microelectrodes. *J. Electroanal. Chem.* **1992**, *328*, 47–62.

(6) Amphlett, J. L.; Denuault, G. Scanning Electrochemical Microscopy (SECM): an Investigation of the Effects of Tip Geometry on Amperometric Tip Response. *J. Phys. Chem. B* **1998**, *102*, 9946–9951.

(7) Selzer, Y.; Mandler, D. Scanning Electrochemical Microscopy. Theory of the Feedback Mode for Hemispherical Ultramicroelectrodes: Steady-State and Transient Behavior. *Anal. Chem.* **2000**, *72*, 2383–2390.

(8) Lindsey, G.; Abercrombie, S.; Denuault, G.; Daniele, S.; De Faveri, E. Scanning Electrochemical Microscopy: Approach Curves for Sphere-Cap Scanning Electrochemical Microscopy Tips. *Anal. Chem.* **2007**, *79*, 2952–2956.

(9) Lefrou, C.; Cornut, R. Analytical Expressions for Quantitative Scanning Electrochemical Microscopy (SECM). *ChemPhysChem* **2010**, *11*, 547–556.

(10) Barton, Z. J.; Rodríguez-López, J. Lithium Ion Quantification Using Mercury Amalgams as *In Situ* Electrochemical Probes in Nonaqueous Media. *Anal. Chem.* **2014**, *86*, 10660–10667.

(11) Hui, J.; Burgess, M.; Zhang, J.; Rodríguez-López, J. Layer Number Dependence of Li^+ Intercalation on Few-Layer Graphene and Electrochemical Imaging of Its Solid–Electrolyte Interphase Evolution. *ACS Nano* **2016**, *10*, 4248–4257.

(12) Alpuche-Aviles, M.; Baur, J. E.; Wipf, D. O. Imaging of Metal Ion Dissolution and Electrodeposition by Anodic Stripping Voltammetry–Scanning Electrochemical Microscopy. *Anal. Chem.* **2008**, *80*, 3612–3621.

(13) Molina, Á.; Gonzalez, J.; Martínez-Ortiz, F.; Compton, R. G. Geometrical Insights of Transient Diffusion Layers. *J. Phys. Chem. C* **2010**, *114*, 4093–4099.

(14) Diard, J. P.; Le Gorrec, B.; Montella, C. Diffusion Layer Approximation Under Transient Conditions. *J. Electroanal. Chem.* **2005**, *584*, 182–191.

(15) Molina, A.; Laborda, E.; González, J.; Compton, R. G. Effects of Convergent Diffusion and Charge Transfer Kinetics on the Diffusion Layer Thickness of Spherical Micro- and Nanoelectrodes. *Phys. Chem. Chem. Phys.* **2013**, *15*, 7106–7108.

(16) Molina, A.; González, J.; Henstridge, M. C.; Compton, R. G. Voltammetry of Electrochemically Reversible Systems at Electrodes of Any Geometry: a General, Explicit Analytical Characterization. *J. Phys. Chem. C* **2011**, *115*, 4054–4062.

(17) Bond, A. M.; Oldham, K. B.; Zoski, C. G. Steady-State Voltammetry. *Anal. Chim. Acta* **1989**, *216*, 177–230.

(18) Wehmeyer, K. R.; Wightman, R. M. Cyclic Voltammetry and Anodic Stripping Voltammetry with Mercury Ultramicroelectrodes. *Anal. Chem.* **1985**, *57*, 1989–1993.

(19) Mauzeroll, J.; Hueske, E. A.; Bard, A. J. Scanning Electrochemical Microscopy. 48. Hg/Pt

Hemispherical Ultramicroelectrodes: Fabrication and Characterization. *Anal. Chem.* **2003**, *75*, 3880–3889.

(20) Stojek, Z.; Osteryoung, J. Experimental Determination of the Coefficient in the Steady State Current Equation for Spherical Segment Microelectrodes. *Anal. Chem.* **1989**, *61*, 1305–1308.

(21) Nyholm, L.; Björefors, F. Stability of Preplated Mercury Coated Platinum and Carbon Fibre Microelectrodes. *Anal. Chim. Acta* **1996**, *327*, 211–222.

(22) Marple, L. W. Reference Electrode for Anhydrous Dimethylformamide. *Anal. Chem.* **1967**, *39*, 844–846.

(23) Hamer, W. J. *Standard Cells: Their Construction, Maintenance, and Characteristics*; Washington, D.C., 1965; pp. 1–41.

(24) Hall, J. L.; Jennings, P. W. Modification of the Preparation of a Cadmium Amalgam Reference Electrode for Use in *N,N*-Dimethylformamide. *Anal. Chem.* **1976**, *48*, 2026–2027.

(25) Manning, C. W.; Purdy, W. C. Reference Electrode for Electrochemical Studies in Dimethylformamide. *Anal. Chim. Acta* **1970**, *51*, 124–126.

(26) Synnott, J. C.; Butler, J. N. Chloride Reversible Electrodes for Use in Aprotic Organic Solvents. *Anal. Chem.* **1969**, *41*, 1890–1894.

(27) Brisard, G. M.; Lasia, A. Study of Solvent Effects on the Kinetics of the Cd(II)/Cd(Hg) Reaction. *J. Electroanal. Chem. Interfacial Electrochem.* **1991**, *314*, 103–116.

(28) Dousek, F. P.; Jansta, J.; Říha, J. Electrochemical Systems for Galvanic Cells in Organic Aprotic Solvents. *J. Electroanal. Chem. Interfacial Electrochem.* **1973**, *46*, 281–287.

(29) Littlehailes, J. D.; Woodhall, B. J. Quaternary Ammonium Amalgams. *Discuss. Faraday Soc.* **1968**, *45*, 187–192.

(30) Garcia, E.; Cowley, A. H.; Bard, A. J. Quaternary Ammonium Amalgams as Zintl Ion Salts and

Their Use in the Synthesis of Novel Quaternary Ammonium Salts. *J. Amer. Chem. Soc.* **1986**, *108*, 6082–6083.

(31) Phillips, C. G. The Long-Time Transient of Two- and Three-Dimensional Diffusion in Microelectrode Chronoamperometry. *J. Electroanal. Chem.* **1992**, *333*, 11–32.

(32) Daniele, S.; Ciani, I.; Battistel, D. Effect of the Insulating Shield Thickness on the Steady-State Diffusion-Limiting Current of Sphere Cap Microelectrodes. *Anal. Chem.* **2008**, *80*, 253–259.

(33) Ellison, J.; Eloul, S.; Batchelor-McAuley, C.; Tschulik, K.; Salter, C.; Compton, R. G. The Effect of Insulator Nano-Sheath Thickness on the Steady State Current at a Micro-Disc Electrode. *J. Electroanal. Chem.* **2015**, *745*, 66–71.

(34) Moshkovich, M.; Gofer, Y.; Aurbach, D. Investigation of the Electrochemical Windows of Aprotic Alkali Metal (Li, Na, K) Salt Solutions. *J. Electrochem. Soc.* **2001**, *148*, E155–E167.

(35) Baranski, A.; Fawcett, W. R. Electroreduction of Alkali Metal Cations. Part 1.—Effects of Solution Composition. *J. Chem. Soc., Faraday Trans. 1* **1980**, *76*, 1962–1977.

(36) Fawcett, W. R. Comparison of Solvent Effects in the Kinetics of Simple Electron-Transfer and Amalgam Formation Reactions. *Langmuir* **1989**, *5*, 661–671.

(37) Koper, M. T. M.; Schmickler, W. A Theory for Amalgam Forming Electrode Reactions. *J. Electroanal. Chem.* **1998**, *450*, 83–94.

(38) Deiseroth, H.-J. Alkali Metal Amalgams, a Group of Unusual Alloys. *Prog. Solid State Chem.* **1997**, *25*, 73–123.

(39) Bent, H. E.; Swift, E., Jr. The Activity of Sodium in Dilute Sodium Amalgams. *J. Amer. Chem. Soc.* **1936**, *58*, 2216–2220.

(40) Cogley, D. R.; Butler, J. N. The Activity of Lithium in Lithium Amalgams. *J. Phys. Chem.* **1968**, *72*, 1017–1020.

(41) Guminski, C. Selected Properties of Simple Amalgams. *J. Mater. Sci.* **1989**, *24*, 2661–2676.

(42) Burgess, M.; Hernández-Burgos, K.; Cheng, K. J.; Moore, J. S.; Rodríguez-López, J. Impact of Electrolyte Composition on the Reactivity of a Redox Active Polymer Studied Through Surface Interrogation and Ion-Sensitive Scanning Electrochemical Microscopy. *Analyst* **2016**, *141*, 3842–3850.

(43) Hills, G. J.; Peter, L. M. Electrode Kinetics in Aprotic Media. *J. Electroanal. Chem. Interfacial Electrochem.* **1974**, *50*, 175–185.

(44) Cronnolly, C.; Pillai, K. C.; Waghorne, W. E. Electrode Kinetic Studies of the Zn^{2+}/Zn(Hg) and Li^{+}/Li(Hg) Couples in Dimethylsulphoxide + Propylene Carbonate Solvent Systems. *J. Electroanal. Chem. Interfacial Electrochem.* **1986**, *207*, 177–187.

(45) Baranski, A.; Drogowska, M. A.; Fawcett, W. R. The Kinetics of Electroreduction of Lithium Ions in Tetrahydrofuran at Mercury and Mercury Amalgam Electrodes. *J. Electroanal. Chem. Interfacial Electrochem.* **1986**, *215*, 237–247.

(46) Kozin, L. F.; Hansen, S. C. Chapter 3. Diffusion of Metals in Mercury. In *Mercury Handbook*; Royal Society of Chemistry: Cambridge, 2013; pp. 50–60.

CHAPTER 5

Fabrication and Demonstration of Mercury Disc-Well Probes for Stripping-Based Cyclic Voltammetry Scanning Electrochemical Microscopy (CV-SECM)

This chapter was published as an original research article in *Analytical Chemistry*:

Barton, Z. J.; Rodríguez-López, J. Fabrication and Demonstration of Mercury Disc-Well Probes for Stripping-Based Cyclic Voltammetry Scanning Electrochemical Microscopy. *Anal. Chem.* **2017**, *89*, 2716–2723. DOI: 10.1021/acs.analchem.6b04022

5.1 Abstract

Scanning electrochemical microscopy (SECM) is a rising technique for the study of energy storage materials. Hg-based probes allow the extension of SECM investigations to ionic processes, but the risk of irreversible Hg amalgam saturation limits their operation to rapid timescales and dilute analyte solutions. Here, we report a novel fabrication protocol for Hg disc-well ultramicroelectrodes (UMEs), which retain access to stripping information but are less susceptible to amalgam saturation than traditional Hg sphere-caps or thin-films. The amalgamation and stripping behaviors of Hg disc-well UMEs are compared to those of traditional Hg sphere-cap UMEs and corroborated with data from finite element simulations. The improved protection against amalgam saturation allows Hg disc-wells to operate safely in highly concentrated environments at long timescales. The utility of the probes for bulk measurements extends also to SECM studies, where the disc geometry facilitates small tip-substrate gaps and improves both spatial and temporal resolution. Because they can carry out slow, high-resolution anodic stripping voltammetry approaches and imaging in concentrated solutions, Hg disc-well

electrodes fill a new analytical niche for studies of ionic reactivity and are a valuable addition to the electrochemical toolbox (Figure 5.1).

5.2 Introduction

There is an emerging interest in understanding the mechanisms underlying alkali ion insertion and plating at materials for energy storage. Scanning electrochemical microscopy (SECM) is often used to study electrochemical redox activity with spatial resolution,[1-5] but ions such as K^+, Li^+ and Na^+ are not reliably detectable with traditional solid electrodes. Instead, techniques such as ITIES,[6-8] SICM,[9-11] SECCM,[12,13] and Hg-based SECM[14,15] have been used in a number of modes to explore various interfaces with these ions.[16] Because of their ability to assess redox and ionic reactivity simultaneously, ease of fabrication, and electrochemical versatility, Hg-based probes are ideally suited for experiments in complex, real-world systems, such as those posed by ion battery electrode operation. Historically, these electrodes have been implemented as sphere-caps[14,15,17-26] or thin films.[27-30] Sphere-caps provide quantitative measurements even at short timescales since diffusion is spherical both inside and outside the Hg phase. However, the insensitivity of side- and back-diffusion to substrate blockage makes sphere-caps susceptible to damaging collisions with the substrate and prevents the use of short working distances in SECM. This is compounded by the height of the Hg sphere-cap above the basal plane, since collision occurs on contact with the Hg before contact with the probe's basal plane. Thin films offer much greater sensitivity to changes in substrate topography and reactivity but are highly susceptible to amalgam saturation and subsequent Hg loss owing to their large surface area and small volume. This restricts their operation to dilute solutions and rapid sweep rates, limiting their versatility and ability to resolve stripping signals from various alkali ions.

To facilitate ion-specific amperometric measurements at higher analyte concentrations than physically accessible to Hg sphere-caps or thin films, we here report on the fabrication, characterization,

and analytical performance of Hg disc-well ultramicroelectrodes (UMEs). Though recent works have described alternative fabrications of Hg disc-wells as UMEs[31] and nanoelectrodes,[32] to the best of our knowledge there has been no report of their performance as stripping probes. We compare the amalgamation and stripping behavior of sphere-caps and disc-wells in non-aqueous alkali ion solutions and corroborate our findings with finite element simulations. Following our interest in cyclic voltammetry probe approach surfaces (CV-PASs) based on alkali amalgamation and stripping,[33] we demonstrate good fits of experimental and simulated Na(Hg) CV-PACs data with an adapted analytical model.[34] We also showcase the versatility and ruggedness of Hg disc-wells as dual sensors for redox and ionic activity through cyclic voltammetry scanning electrochemical microscopy (CV-SECM) imaging. We conclude that Hg disc-wells offer high substrate sensitivity while also providing greater protection against saturation than sphere-caps, enabling them to serve as superior SECM probes when ionic specificity and spatial resolution are key goals.

5.3 Experimental Section

5.3.1 Chemicals

Nitric acid and water (ChromAr grade) were obtained from Avantor. Platinum wire (25 μm and 0.5 mm diameter) and silver wire (1 mm diameter) were obtained from Goodfellow. Lithium perchlorate (battery grade, dry, 99.99% trace metals basis), mercury(II) nitrate monohydrate (≥99.99% trace metals basis), propylene carbonate (PC, anhydrous, 99.7%), sodium perchlorate (≥98%), tetrabutylammonium perchlorate (TBAP, ≥99.0%), and *N*,*N*,*N*′,*N*′-tetramethyl-*p*-phenylenediamine (TMPD, 99%) were obtained from Sigma-Aldrich. Tetramethylammonium nitrate (NMe_4NO_3) was obtained from Southwestern Analytical Chemicals. Ultra high purity (UHP) argon was obtained from Airgas. All purchased chemicals were of A.C.S. reagent grade or better and used as received without further purification.

5.3.2 Working Electrode Fabrication

Pt disc UMEs were made in the usual way by sealing a Pt wire of radius (a_1) 12.5 μm in a borosilicate glass capillary, shaping the insulating glass sheath with a beveller to give a small total probe radius (a_2), and polishing with aqueous alumina slurries over felt polishing pads. Creating a glass ratio ($R_G = a_2/a_1$) smaller than 4 is beneficial not only for improving surface sensitivity and spatial resolution in SECM studies but also for determining the etch depth (h_2) optically. Following electrode polishing, a cavity was etched electrochemically, filled with Hg, and then leveled to give a Hg disc-well UME (Figure 5.2). Accompanying photographs of a probe throughout the fabrication process and following experimental work are presented in Figure 5.3.

In keeping with established methods,[35-37] Pt disc UMEs (a_1 = 12.5 μm, $1 < R_G < 4$) were etched electrochemically by applying an AC waveform of 2.70 $V_{p\text{-}p}$ at 60 Hz with a variac between a Pt UME and a carbon rod submerged in 30 v. % sat. $CaCl_2$ + 10 v. % HCl in H_2O. The etched cavity depth grows approximately linearly with time until its normalized value ($H_2 = h_2/a_1$) reaches unity, which occurs around 30 s under the present conditions (Figure 5.4A). We typically etch for 50 s. It is also possible to chemically etch the Pt UME by exposure to aqua regia,[31,38] but this takes ~20 minutes per UME and can create a conically etched surface, which is undesirable for stripping analysis. Unlike existing protocols, etching was carried out under ultrasonic agitation in order to (1) facilitate mass transport in the cavity, (2) maintain electrical contact by dislodging and/or imploding trapped bubbles, and (3) promote uniform progression of the etch front.[39,40] Photographs of the etching setup are available as Figure 5.5.

Mercury was deposited potentiostatically at +0.2 V (*vs.* Ag/AgCl) in 10 mM $Hg(NO_3)_2{\cdot}H_2O$ + 0.1 M NMe_4NO_3 and 0.5 v. % HNO_3 in H_2O until the deposition current reached 160 nA, the value observed at the completion of a Hg hemispherical cap on a Pt UME of equal basal radius and R_G (Figure 5.4B). Deposition takes much longer in the cavity than at an inlaid disc, but accelerating the process in

deep cavities by increasing either the Hg^{2+} concentration or the overpotential can create unstable Hg deposits that detach and break electrical contact with the Pt (Figure 5.6).

Excess mercury was removed by placing the overfilled Hg probe in an inverted position under a benchtop microscope (Zeiss AxioLab.A1) and bringing a clean, flexible glass coverslip into contact with the basal plane of the electrode. Contact between the Hg and the glass coverslip was monitored by focusing on the basal plane of the overfilled Hg well probe through the transparent coverslip. On contacting the Hg, the glass coverslip was moved slowly closer and sideways to force excess Hg laterally to the edges of the UME sheath. The coverslip must be clean so that it is not wet by the Hg, as this would create an under-filled Hg well. We obtained good results by washing coverslips with high purity H_2O, acetone, and isopropanol, followed by drying with compressed air. Besides ensuring that no additional Hg is removed from the well, the high surface energy between the glass coverslip and the Hg ensures that excess Hg is forced to the edges of the glass sheath to minimize contact area and surface energy as the probe is brought into the plane of the coverslip. This method stands in contrast to a previously reported protocol calling for mechanical polishing of the liquid mercury deposit.[31] Displacing the excess Hg with a non-wetting coverslip may also improve reproducibility and decrease contamination compared with other strategies.

5.3.3 Electrochemical Experiments

With the exception of probe fabrication, all work was completed under H_2O- and O_2-free conditions in an MBRAUN UNIlab glove box filled with UHP argon. Electrochemical experiments were performed in a standard Teflon SECM cell over a glass substrate in a three-electrode configuration consisting of a Hg-based UME as the working electrode (WE), a Ag wire as the quasi-reference electrode (QRE), and a flame-polished Pt wire as the counter electrode (CE). Electrochemical control and WE positioning was achieved with a CHI 920D Scanning Electrochemical Microscope. Unless otherwise specified, the

analyte solution consisted of 0.5 mM TMPD and 0.5 mM $NaClO_4$ in PC with 0.5 M TBAP as supporting electrolyte.

5.3.4 Fitting Negative Feedback

Traditional potentiostatic probe approach curves (PACs) were carried out over $0 < L < 40$ (where $L = d/a_1$ and d is the width of the tip-substrate gap) with 30 seconds of quiet time and fit with established models.[41,42] The maximum step size was 100 nm and the duration of each step was 100 ms.

Cyclic voltammetry probe approach curves (CV-PACs) were extracted from cyclic voltammetry probe approach surfaces (CV-PASs), each of which is series of CVs recorded between sequential SECM probe motor movements. These were fit as described[33] by an adapted analytical model:[34]

$$\frac{i(L)}{i_{\mathrm{inf}}} = \left[k_1 + \frac{k_2}{L+s} + k_3 \exp\left(\frac{k_4}{L+s}\right)\right]^{-1} \quad \textbf{(1)}$$

where i is the current at some particular L, i_{inf} is the current recorded at effectively infinitely large L, and s is freely adjustable and determines the abscissa. If the model fits the data well, then s and the uncertainty in the probe position, u_L, approach zero. All four k_i values are tabulated constants specific to some combination R_G and T, where $T = Dt/a_1^2$. A range of solutions for $R_G = 3$ is provided as Table 5.1.

5.3.5 Digital Simulations

Our sphere-cap COMSOL model was adapted to address disc-well geometries with no fundamental changes. A full description of the COMSOL model is available as Appendix A.

5.4 Results and Discussion

5.4.1 Scan Rate Dependence

The peak cathodic amalgamation current for Na(Hg) formation at sphere-cap and disc-well UMEs increases with the square-root of the potential scan rate (*i.e.*, $|i_p| \propto \nu^{0.5}$) as expected for mass-transport limited conditions (Figure 5.7).[43] However, the peak anodic stripping current for Na^+ does not behave in

the same way. At sphere-cap UMEs, the peak Na(Hg) stripping current does not demonstrate monotonic behavior, though it does still increase in response to increases in scan rate. However, the peak stripping current observed at disc-well UMEs decreases with increasing scan rate. This trend is also corroborated by simulated data. At sufficiently small scan rates, the peak stripping current at disc-wells stops increasing with decreasing scan rate and reverses, decreasing in response to decreases in scan rate. This is even more pronounced at slower scan rates, as shown in Figure 5.8. This behavior is a consequence of disc-wells having different internal and external diffusion regimes while sphere-caps exhibit spherical diffusion both inside and outside the Hg phase.[44,45]

The deviation of experimental disc-well stripping peak intensity from simulated behavior at fast scan rates (Figure 5.7D) coincides with pronounced broadening of the stripping peak and the appearance of a preceding anodic shoulder (Figure 5.7B). A full set of experimental and simulated CVs is available as Figure 5.9. Alkali amalgamation and stripping kinetics are known to depend heavily on solution and amalgam solvation energies as well as the double layer structure and composition. It has been suggested that the rate-limiting step may change based on the applied potential since this changes the nature of the electrical double-layer.[46,47] We therefore suggest that the appearance of the pre-peak may be caused not only by mass transport effects but also by differences in the differential capacitance at sphere-cap and disc-well electrodes.

Generally speaking, stripping peaks are diffusion-limited for shallow disc-wells under slow conditions ($(T_{strip} - T_{amal}) > H_2^2$). Stripping peaks are broadened and distorted at short timescales, and the transition from ideal to distorted behavior is more sharply defined for deeper disc-wells (larger H_2).[48]

Because the alkali stripping signal at a disc-well UME is diminished, broadened, and distorted by a preceding anodic shoulder at fast scan rates, rapid stripping analysis may not be suitable for quantitative work. However, signals from amalgamation or solution-phase redox processes remain reliable. This

enables rapid CV-PAS and CV-SECM studies[30] without the risk of saturating the amalgam in concentrated solutions.

At slow scan rates, the diffusion-limited Na amalgamation current observed at a disc-well is smaller than that observed at a hemispherical cap of equal basal radius and R_G by a factor of ~0.6 (Figure 5.7C), which is consistent with the factor of $2/\pi$ (~0.64) predicted from theory.[21,49,50] Interestingly, the stripping currents also approach this ratio at slow scan rates (Figure 5.7D), further supporting the suitability of disc-well stripping signals for analytical SECM work, particularly at large T.

5.4.2 Saturation Limits

Stripping signals are well resolved at low scan rates both for sphere-cap UMEs and disc-well UMEs, but disc-well UMEs do not saturate as quickly. Since the etch depth is controllable (Figure 5.4), disc-well UMEs can be made to have much greater volume than sphere-caps having the same basal radius, so a disc-well may hold more moles of analyte before approaching the saturation limit. For a given basal radius, a disc-well has greater volume than a hemispherical cap ($H_1 = 1$) for $H_2 > 2/3$. Additionally, the ratio of the exposed surface area to the volume is smaller for a disc-well ($A_{dw}/V_{dw} = 1/h_2$) than for a hemispherical cap ($A_{hs}/V_{hs} = 3/a_1$) of equal radius for $H_2 > 1/3$. Thus, a disc-well may have a smaller volume than a sphere-cap yet still take a longer time to reach saturation. This is demonstrated by the comparison of simulated data for a hemispherical cap ($a_1 = 12.5$ μm, $H_1 = 1$, $R_G = 10$) and a shallow disc-well ($a_1 = 12.5$ μm, $H_2 = 0.5$, $R_G = 10$) in Figure 5.10. The increased volume, decreased area-to-volume ratio, and decreased steady-state flux of disc-wells as compared to sphere-caps extends their operation to approximately an order of magnitude larger C_{ox}^* for a given T or to nearly two orders of magnitude longer T for a given C_{ox}^*. In fact, the sphere-cap used in Figure 5.7A eventually ceased stripping activity after 2.5 hours whereas the disc-well used in Figure 5.7B remained operational for the entirety of the 6

hours of stripping experiments (and at a variety of larger T values) and showed no sign of Hg loss through electrochemical or visual examination (Figure 5.3).

As with sphere-caps, R_G has little impact on the saturation limits for disc-wells. For this reason, the symbols indicating data sets from R_G =10 and R_G = 3 in Figure 5.10 overlap almost completely.

5.4.3 Approaching a Substrate

Our initial approach with a Hg disc-well UME (Figure 5.7B, insets) to a glass substrate was a traditional potentiostatic probe approach curve (PAC) based on the first single-electron oxidation of TMPD and terminated at 50% negative feedback. For comparison, a sphere-cap UME (Figure 5.7A, insets) was approached to 70% negative feedback under the same experimental conditions (Figure 5.11). The regular oscillations in experimental data are related to differences in the applied sampling rate and the integral sampling rate of the CHI 920D hardware and have a period beginning at 10 μm (0.01 Hz) and decreasing to 2.5 μm (0.3 Hz). The disc-well TMPD PAC is fit well ($\chi_{red}^2 = 9.4891 \times 10^{-5}$, R_{adj}^2 = 0.99091) by an established analytical model for disc UMEs,[42,51] which gives the final tip-substrate gap as L_f = 0.5912 (± 0.0013). The analogous PAC data for a sphere-cap is fit by a model originally intended for disc UMEs but later adapted to the sphere-cap geometry. This model fits well ($\chi_{red}^2 = 3.4375 \times 10^{-5}$, R_{adj}^2 = 0.99484) with the closest reported conditions (ca-k_i coefficients for H_1 = 1, R_G = 2 rather than H_1 = 1, R_G = 3) and reports the final tip-substrate gap as L_f = 1.4830 (± 0.0013). Since the sphere-cap has H_1 = 1, crashing occurs at L_f = 1 and the final distance between the apex of the sphere-cap and the substrate is G_f = 0.4830 (± 0.0013). Though both probes are positioned accurately within one tip length of an insulating substrate and with acceptable precision, the PAC sensitivity (slope) is greater for a disc-well than a sphere-cap. As has been previously observed,[21] the negative feedback response at disc UMEs is sharper than at sphere-cap UMEs since a greater fraction of the total flux at disc UMEs is normal to the

plane of the insulating sheath. Consequently, disc-wells may approach closer to substrates than sphere-caps not only because they do not crash until the basal plane contacts the substrate but because the sensitivity to changes in the tip-substrate gap is greater. This facilitates high-resolution SECM work, since the shorter working distance curtails diffusional broadening and improves collection efficiency.[52]

Neither the sphere-cap nor the disc-well UME exhibits forced convective transport. Since TMPD has a diffusion coefficient of $D_{red} = 3.1 \times 10^{-10}$ m^2 s^{-1},[53] moving the disc-well UME ($a_1 = 12.5$ μm, $H_2 = 1.2$, $R_G = 3$) faster than 0.25 μm s^{-1} should give appreciable deviations (≥ 2%) from steady-state conditions due to forced convective transport,[54] which in turn frustrates accurate fitting of PACs. The initial speed (100 nm steps taken as 100 ms increments) exceeds this but automated modulation of the step size on the detection of negative feedback brings the speed within acceptable limits (100 nm/s at 10 nm / 100 ms). The absence of convective distortions in the potentiostatic TMPD PACs is corroborated by quasi-steady-state CV currents (Figure 5.12), which show the same decrease in current as the PAC. So forced convection does not contribute to the difference in PAC shapes, and both datasets are reliable.

5.4.4 Cyclic Voltammetry Probe Approach Surfaces (CV-PASs)

Traditional PACs allow the reactant depletion region to expand continuously with time, so the experimental timescale and length of influence increase as the probe approaches a substrate. As observed at Hg sphere-caps,[33] constructing CV-PACs from CV-PASs keeps T uniform over the course of the approach and increases spatial resolution. This phenomenon is also observed for CV-PASs at disc-well UMEs (Figure 5.13). A CV-PAS based on Na amalgamation/stripping and terminating at the same L_f presented in Figure 5.11 shows clear dependence on L (Figure 5.13A). Its simulated analog agrees well (Figure 5.13B). The experimental distances in Figure 5.13A and Figure 5.13C are those determined by fitting of the TMPD PAC in Figure 5.11.

The simulated CV-PAS distances, which are inherently correct, nearly overlap the experimental distances determined from fitting the TMPD PAC. Freely varying *cv*-k_i models fit the simulated CV-PACs well ($\chi_{red}^2 \leq 8.36 \times 10^{-7}$, $R_{adj}^2 \geq 0.99995$). The resulting tailored *cv*-k_i coefficients (Table 5.1) fit the experimental data well ($\chi_{red}^2 \leq 5.47 \times 10^{-5}$, $R_{adj}^2 \geq 0.99698$) but report $s = 0.1782$ ($\pm$ 0.0056). That is, the distance determined from CV-PAS data is greater than that determined from traditional PAC data by $0.18 \cdot a_1$, or 2.25 μm. Considering the slightly less pronounced curvature of the experimental CV-PAC curves as compared with their simulated counterparts, we suspect that the difference in distances may be attributable to substrate tilt.[55,56] Substrate tilt impacts both PACs and CV-PACs, but the effects are amplified at the shorter timescale used for these CV-PACs. In the absence of secondary confirmation of probe position, we trust more the distance obtained by fitting the CV-PAC data, since it agrees with the simulated response.

Scanning over a wider potential range, CV-PASs can emphasize differences in topography and reactivity by simultaneously probing for positive feedback with a redox mediator and pure negative feedback with an alkali ion. An example of this is available as Figure 5.14.

5.4.5 Cyclic Voltammetry Scanning Electrochemical Microscopy (CV-SECM)

The superior spatial sensitivity of Hg disc-wells extends also to movement parallel to a substrate. To demonstrate this, a Hg disc-well UME ($a_1 = 12.5$ μm, $R_G = 2.8$, $H_2 = 1.4$) was used to collect Na(Hg) CV-SECM data over an insulating substrate consisting of a glass slide decorated with a repeating array of SU-8 2002.5 polymer pillars. Additional experimental details are available in Figure 5.16. Having identified a single polymer pillar (Figure 5.15A) by negative feedback of TMPD oxidation in a traditional SECM image (Figure 5.15B), we then executed a CV-SECM image. This involved recording a full CV of Na amalgamation and stripping at each probe position (Figure 5.15C). Extraction of the

amalgamation current (Figure 5.15D), stripping current (Figure 5.15E), and stripping charge (Figure 5.15F) gives three complementary CV-SECM images.

The CV-SECM data were collected at $L = 0.462$ ($\pm$ 0.002) with $T_{amal} = 7.0$, which is neither so short as to diminish surface sensitivity nor so long as to risk saturation damage to the Hg. At this distance and timescale, the 2.5 μm tall substrate pillar (over which $L = 0.262$) decreases i_{amal} by 55%, i_{strip} by 38%, and Q_{strip} by 37%. Ideally, these signals are in agreement. However, i_{amal} may have been obscured by the presence of trace oxygen. i_{strip} and Q_{strip} are insensitive to side reactions such as oxygen reduction, so their response is more reliable in this case. These responses are slightly greater than the 34% decrease predicted for a traditional PAC over the same change in L. This is to be expected because the reactant depletion layer is thinner at T_{amal} =7.0 than at the long timescales ($40 < T < 1000$) typically assumed in feedback SECM studies.

Besides accessing ionic information without probe saturation, Hg-based CV-SECM is distinct from traditional potentiostatic SECM imaging in that probe movement and data acquisition are not simultaneous. Consequently, traditional probe speed limits designed to minimize signal distortions from convective mass transport[57,58] may be relaxed. This is qualitatively evident in comparing the potentiostatic SECM image (Figure 5.15B) to the CV-SECM i_{amal} image (Figure 5.15D). The probe movement speed for the CV-SECM data was 50 μm s^{-1}, which is 5-fold greater than that used for the SECM data (10 μm s^{-1}), but the CV-SECM image exhibits greater radial symmetry around the pillar. Thus, CV-SECM at disc-wells can mitigate convective distortions from rapid probe translation speeds. Disc-wells are better able to capitalize on the availability of rapid movement speeds in CV-SECM than are sphere-caps, since disc-wells may operate safely (Figure 5.16) at speeds that can dislodge sphere-caps (Figure 5.17) due to shear forces. The capabilities of CV-SECM compliment the chemical and mechanical stability of Hg disc-wells.

5.5 Conclusions

We have described a novel Hg disc-well SECM probe fabrication protocol involving ultrasonic-assisted electrochemical etching of Pt disc UMEs and displacement of excess Hg by the imposition of a non-wetting, flexible glass coverslip. Fabrication of Hg disc-well UMEs is rapid, tunable, and reliable. These electrodes are suitable for anodic stripping voltammetry of alkali ions in non-aqueous solvents and perform well in SECM studies.

The increased volume, decreased area-to-volume ratio, and decreased steady-state flux of disc-wells as compared to sphere-caps extends Hg disc-well operation to approximately an order of magnitude larger concentrations for a given timescale and to nearly two orders of magnitude longer timescales for a given bulk ion concentration. Access to such concentrated solutions allows the application of Hg-based probes to realistic alkali ion battery environments. Though differences in external and internal diffusional transport distort stripping signals at disc-well UMEs at the fast scan rates (short timescales) necessary for concentrated analytes, amalgamation signals remain unperturbed and are suitable for rapid CV-SECM work. At the other extreme, access to long timescales in less concentrated alkali solutions facilitates multi-ion stripping analysis with previously unobtainable resolution without incurring probe damage due to amalgam saturation. Because Hg disc-wells may operate safely in highly concentrated environments at long timescales, they may address unstudied systems for the first time and known systems with greater depth.

As SECM probes, Hg disc-wells offer advantages over their sphere-cap counterparts. Having the electrode surface flush with the insulating basal plane of the probe increases substrate sensitivity and enables smaller tip-substrate gaps, which in turn increase collection efficiency and spatiotemporal resolution. Disc-wells also remain intact at probe speeds that dislodge sphere-caps. CV-SECM

capitalizes on these benefits to enable new investigations under conditions previously inaccessible to anodic stripping voltammetry.

Planned future work includes investigations of SEI electrical conductivity over an operating Na-ion battery cathode or anode material while simultaneously measuring Na^+ uptake or release at the substrate and monitoring changes in the tip-substrate gap through Li(Hg) or K(Hg) signals. We foresee that these probes may also be used in biological systems involving the transport of Na and K ions.

5.6 Acknowledgements

This material is based upon work supported by the National Science Foundation Graduate Research Fellowship Program under Grant No. DGE-1144245. Any opinions, findings, and conclusions or recommendations expressed in this material are those of the authors and do not necessarily reflect the views of the National Science Foundation. J.R.-L. acknowledges support from an Alfred P. Sloan Foundation Fellowship. The authors also thank UIUC for generous start-up funds. Z.J.B. thanks J. Hui for sharing SECM substrates and M. Burgess and B. H. Simpson for fruitful discussions.

5.7 Figures and Table

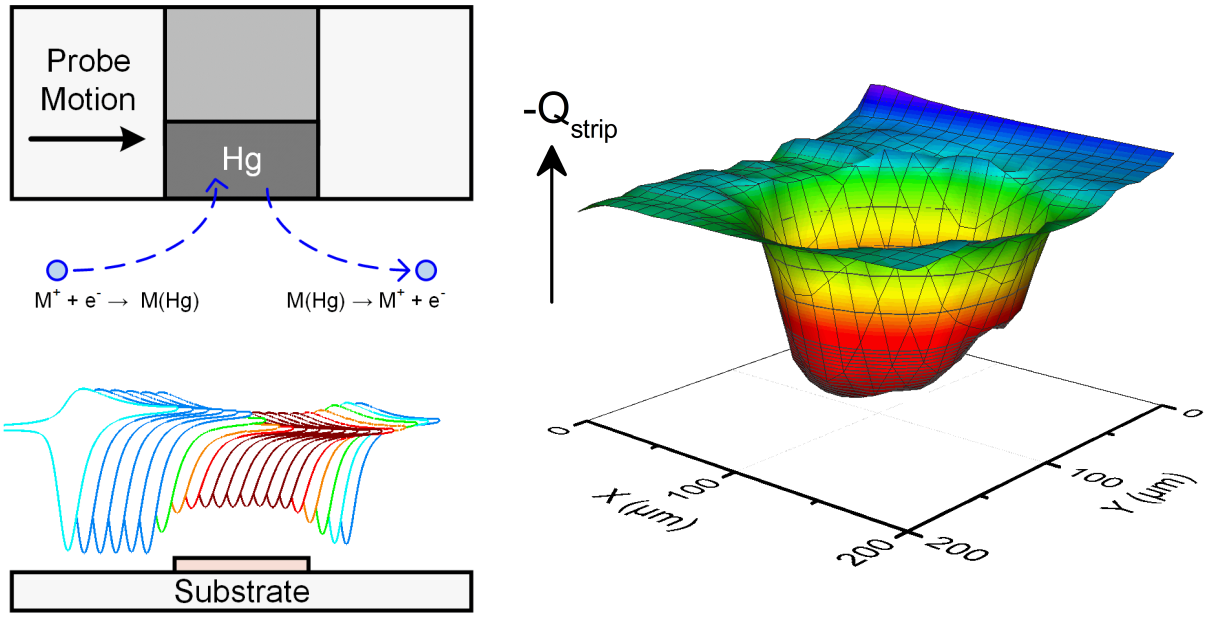

Figure 5.1. Table of contents graphic.

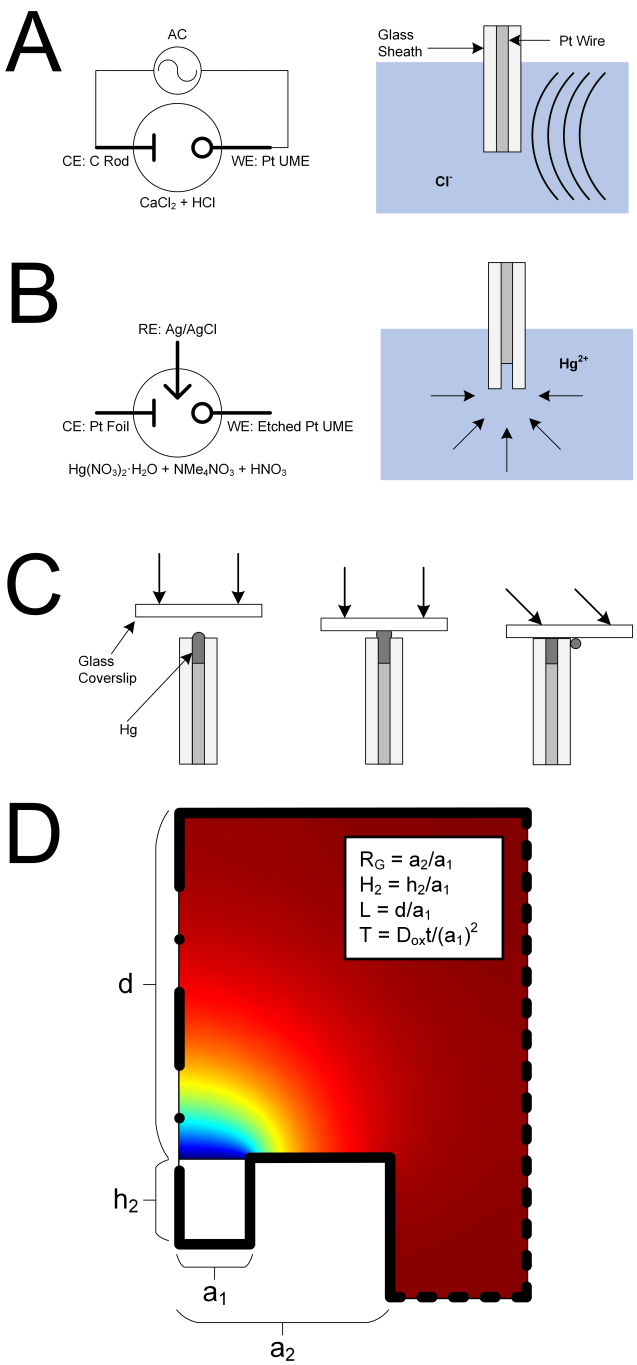

Figure 5.2. Schematic representation of a Hg disc-well UME and its fabrication. (**A**) Ultrasonic-assisted electrochemical etching of a Pt UME. (**B**) Potentiostatic over-deposition of Hg in the etched cavity. (**C**) Leveling by non-wetting displacement of Hg. (**D**) Schematic of a Hg disc-well UME performing an amalgamation reaction indicating geometric terms. Solid lines indicate zero-flux boundaries, dashed lines indicate open boundaries, and the dash-dot line indicates the axis of rotational symmetry. The concentration gradient for M^+ is shown with blue color indicating low concentration. The height of the Hg sphere-cap prior to leveling is h_1, giving $H_1 = h_1/a_1$.

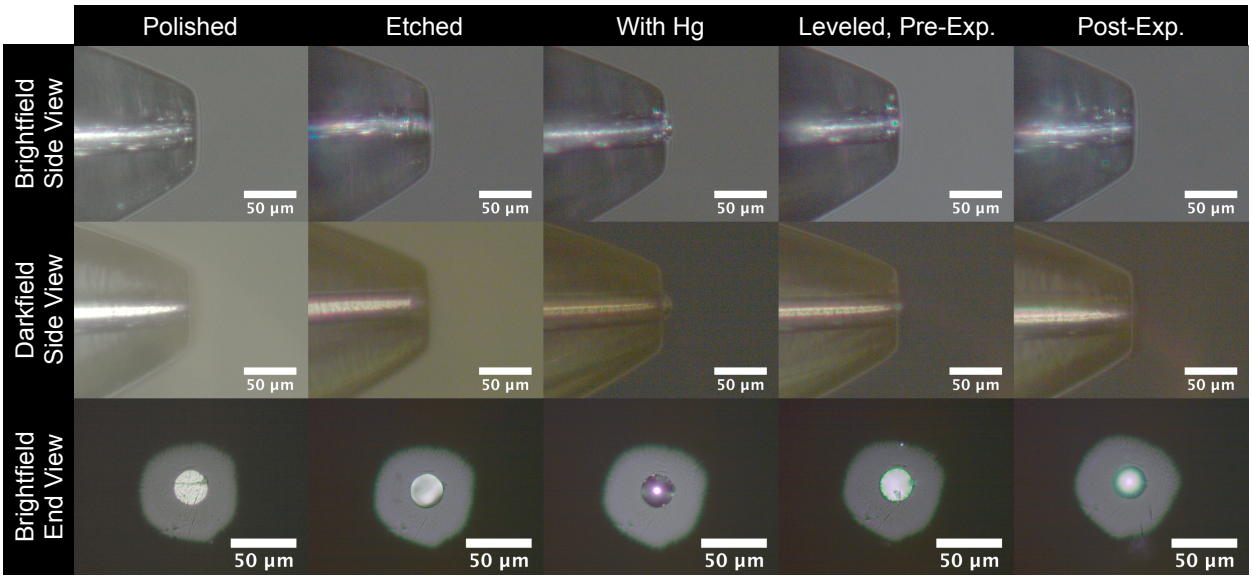

Figure 5.3. Photomicrographs of the disc-well UME used in the generation of data for Figure 5.7C. The scale bars are 50 µm wide. a_1 = 12.5 µm, H_2 = 1.2, R_G = 3. The out-of-focus sphere visible near the center of the probe in the side "leveled" views is the small Hg drop located at the top edge of the glass in the end "leveled" view. The mercury deposit is preserved between the pre-experiment (abbreviated as "Pre-Exp.") and post-experiment (abbreviated as "Post-Exp.") images.

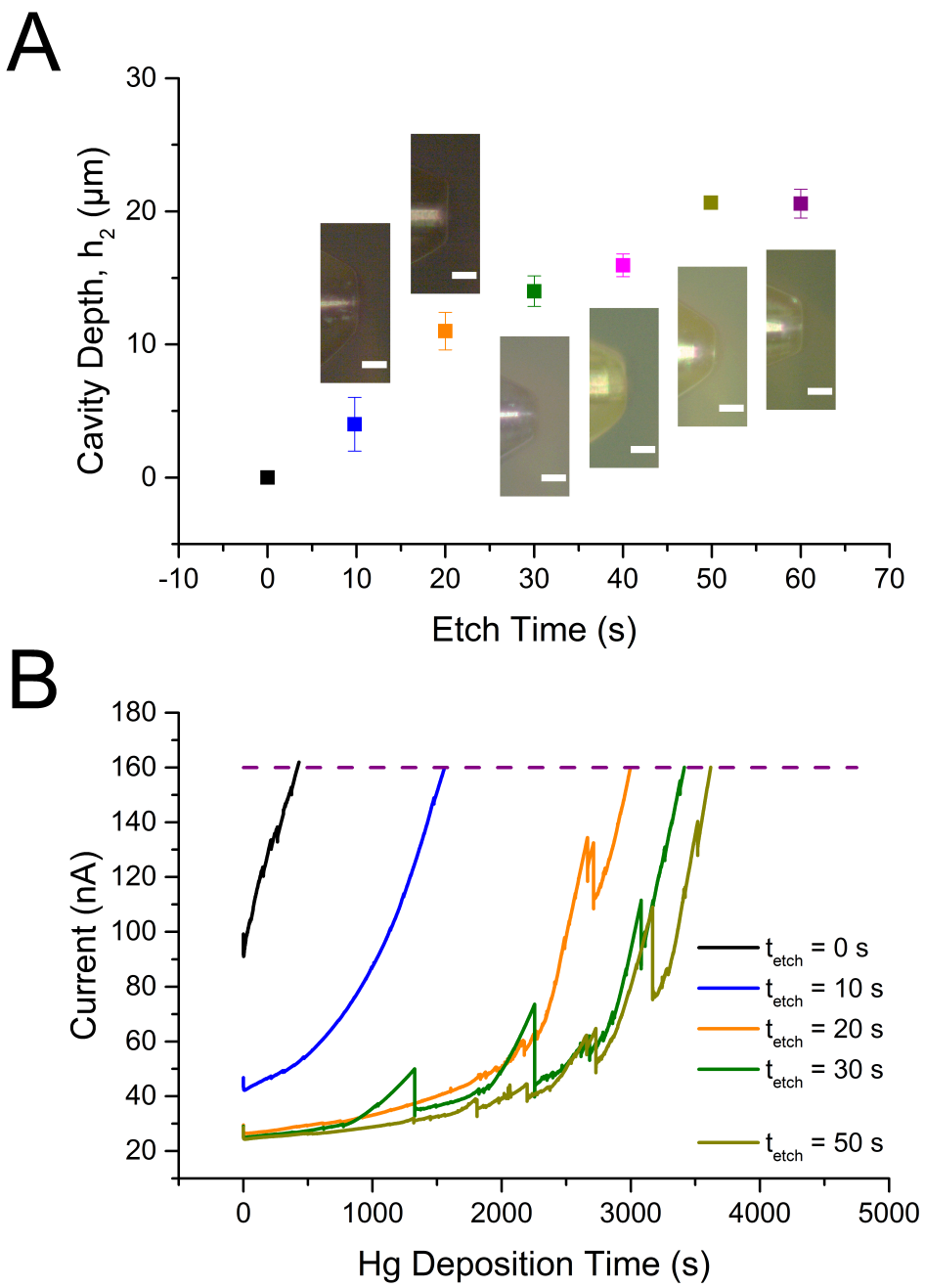

Figure 5.4. Electrochemical etching of Pt and subsequent overfilling with Hg. (**A**) Cavity depth of Pt UMEs etched for 0 s, 10 s, 20 s, 30 s, 40 s, 50 s, and 60 s. Error bars indicate the 90% confidence interval. The scale bars are 25 μm wide. (**B**) Subsequent deposition of Hg sphere-caps with E = +0.2 V (*vs.* Ag/AgCl). Deposition of 56 μC on a Pt disc of radius 12.5 μm corresponds to the formation of a hemispherical cap (H_1 = 1.0) (**B**, black line). Hg deposition was terminated when the current exceeded 160 nA (purple dashed line) so that the Hg surface area was at least as large as that of a hemispherical cap.

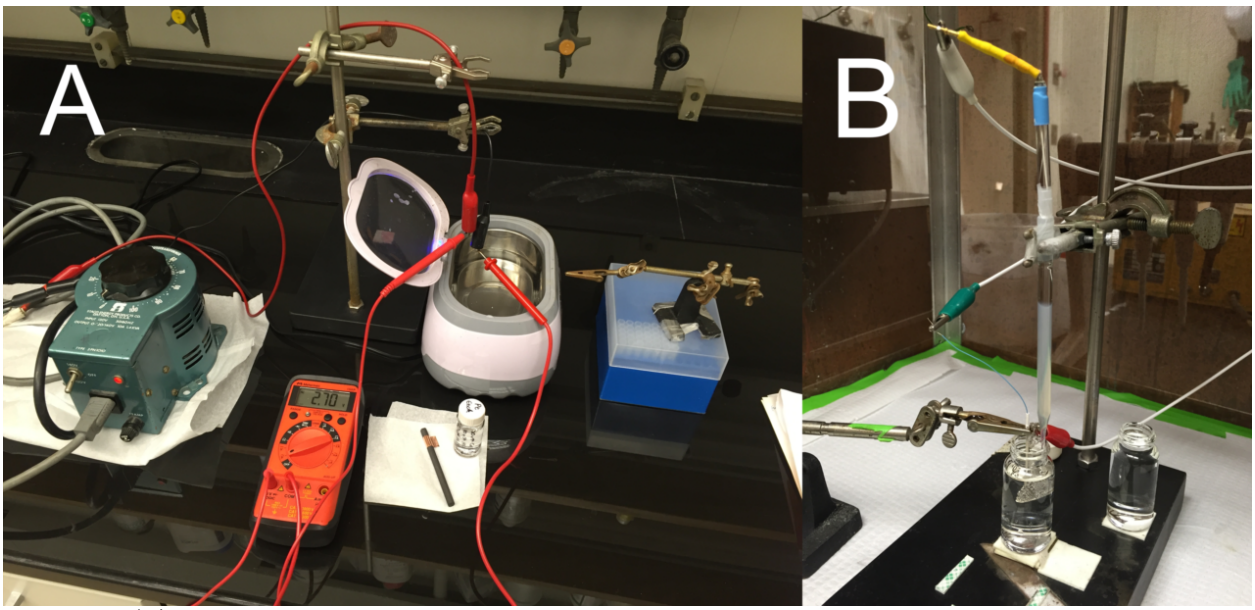

Figure 5.5. (**A**) Photograph of typical Pt etching setup. The variac potential supply is set to deliver 2.70 $V_{p\text{-}p}$ at 60 Hz. After confirming the variac settings, the 20 mL glass vial containing the etchant solution is secured to the bottom of the sonicator bath with a piece of double-sided foam tape to prevent the sidewalls from contacting the Pt UME. (**B**) Photograph of typical Hg deposition setup. Etched Pt UMEs are briefly sonicated while submerged in the deposition solution to eliminate any trapped air pockets from the etched cavity, and the tall sidewalls of a 20 mL glass vial are convenient for this purpose.

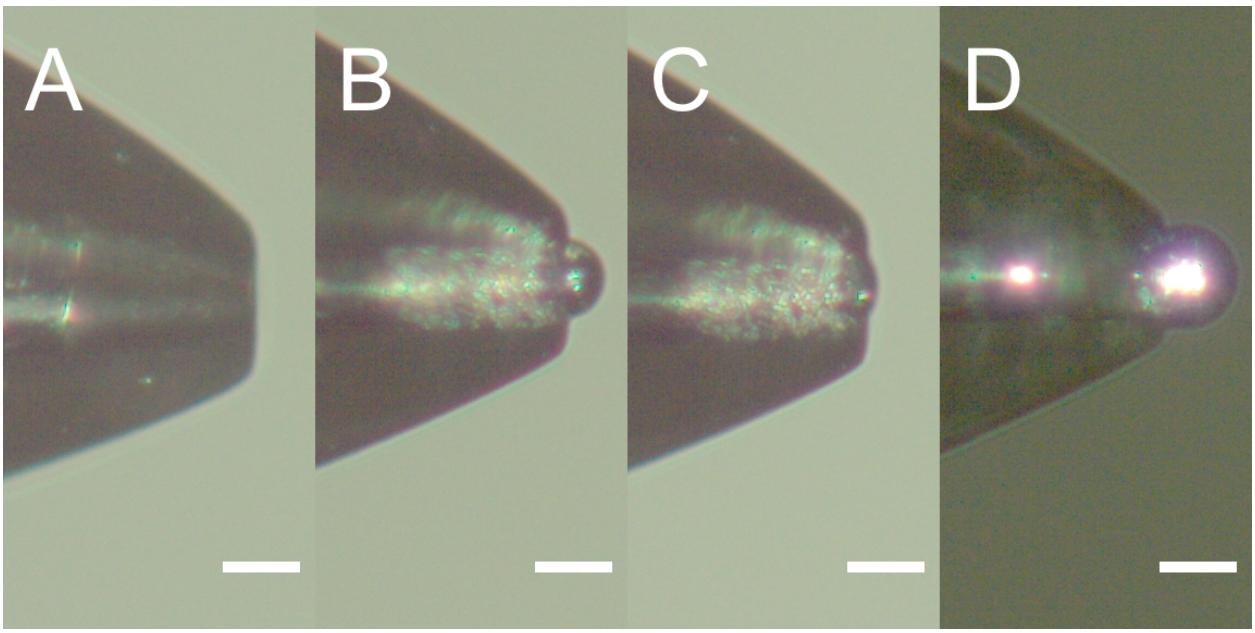

Figure 5.6. Photomicrographs of a Hg disc-well probe made with deep Pt etching from 240 seconds treatment (**A**), rapid Hg deposition from 50 mM Hg^{2+} solution (**B**), and mechanical polishing with a Kimwipe (**C**). On cathodic polarization, the electrical connection was lost (**D**). The apparent secondary etch channel is an artifact caused by reflections in the polished insulating glass sheath. The scale bars are 25 μm wide.

T	k_1	$\pm u_{k1}$	k_2	$\pm u_{k2}$	k_3	$\pm u_{k3}$	k_4	$\pm u_{k4}$	χ_{red}^2	R_{adj}^2
16.90	0.656	0.004	0.830	0.003	0.352	0.004	-3.08	0.06	1.31E-06	0.99998
8.83	0.627	0.004	0.853	0.003	0.420	0.003	-3.53	0.06	1.07E-06	0.99998
6.82	0.595	0.004	0.871	0.003	0.471	0.003	-3.54	0.06	1.36E-06	0.99998
4.61	0.52	0.01	0.909	0.006	0.569	0.006	-3.2	0.1	4.76E-06	0.99993
3.55	0.44	0.02	0.94	0.01	0.65	0.01	-2.8	0.1	9.85E-06	0.99986
1.89	0.15	0.05	1.01	0.03	0.93	0.05	-1.8	0.1	4.14E-05	0.9994
0.99	-0.3	0.2	1.04	0.06	1.3	0.2	-1.2	0.1	1.06E-04	0.99837
0.96	-0.3	0.2	1.04	0.06	1.4	0.2	-1.1	0.1	1.10E-04	0.99831
0.75	-0.5	0.3	1.06	0.08	1.6	0.3	-0.9	0.1	1.52E-04	0.99758
0.50	-1.2	0.6	1.1	0.2	2.3	0.6	-0.7	0.1	2.35E-04	0.99599
0.37	-2	1	1.2	0.2	3	1	-0.5	0.1	2.95E-04	0.99471

Table 5.1. Tailored *cv*-k_i coefficients from simulated CV-PACs. a_1 = 12.5 μm, R_G = 3, H_1 = 0, H_2 = 1.2. T = 6.82 corresponds to the conditions in Figure 5.13.

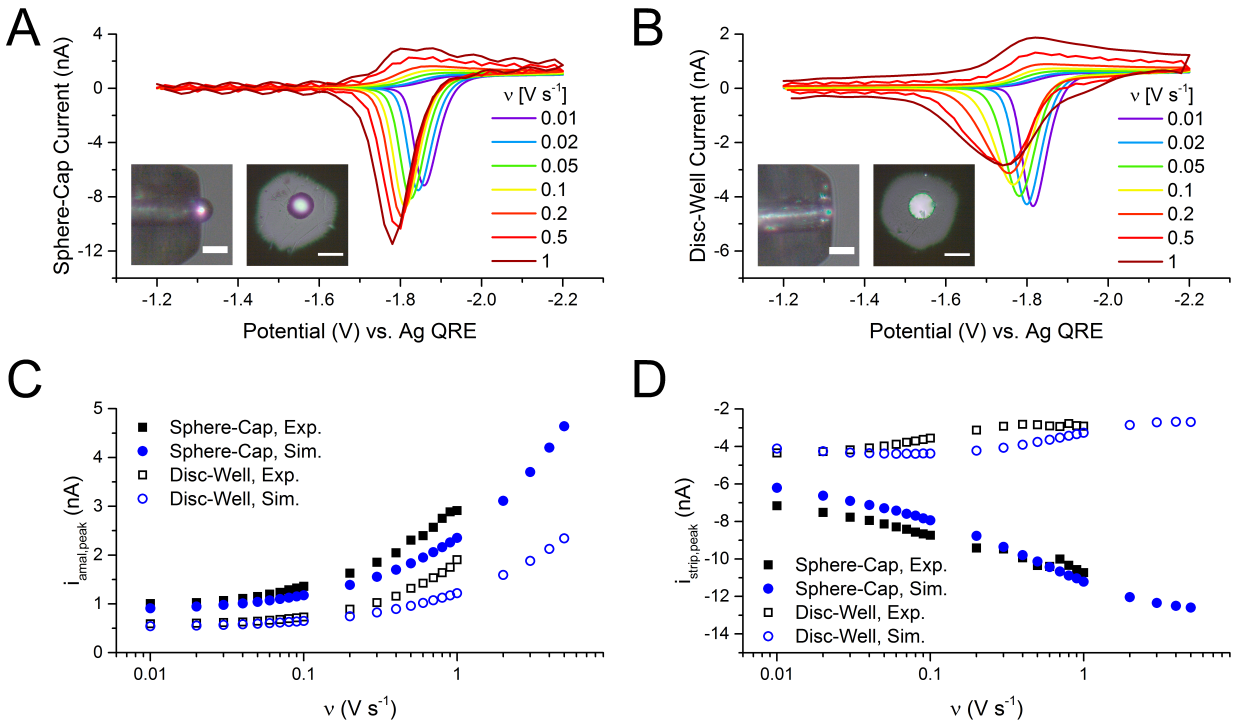

Figure 5.7. Scan rate dependence for $Na^+ + e^- \rightleftarrows Na(Hg)$ at a sphere-cap UME (**A**) and a disc-well UME (**B**). Peak amalgamation current (**C**) increases with ν for both geometries but peak stripping current (**D**) decreases with ν for disc-well UMEs. An artifact (period = 5 samples, amplitude = 0.3 nA) associated with low sampling frequencies is evident at 1.0 V s^{-1} for both probes. For clarity, it has been removed from the disc-well data in **B** with a 5-point fast-Fourier transform filter. Simulation conditions are: $C_{ox}^* = 0.5$ mol m^{-3}, $D_{ox} = 2.0 \times 10^{-10}$ m^2 s^{-1}, $D_{red} = 8.4 \times 10^{-10}$ m^2 s^{-1}, $k^o = 0.01$ m s^{-1}, $\alpha = 0.5$, $E^o = -1.85$ V. Photomicrographs show the similar scale of the sphere-cap (**A**, insets) and disc-well (**B**, insets). The scale bars are 25 μm wide.

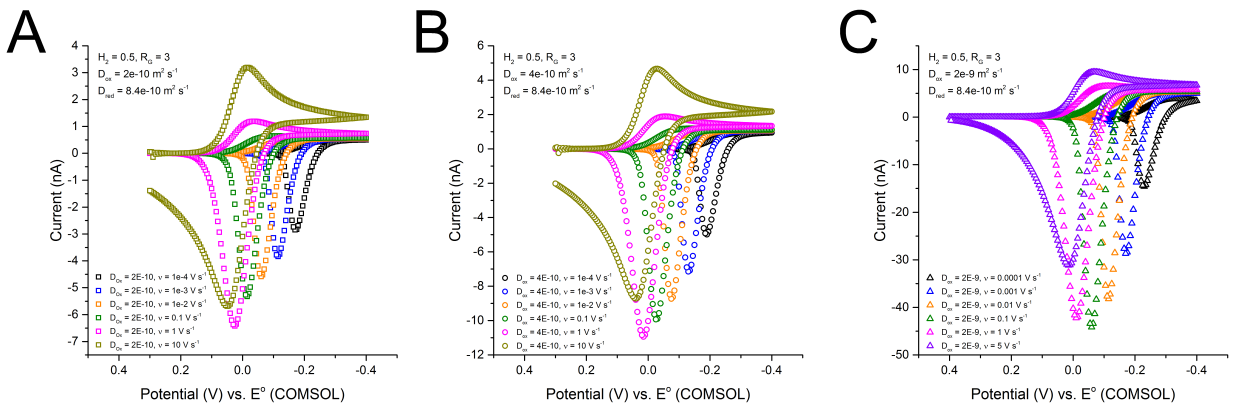

Figure 5.8. Simulated stripping voltammetry at a disc-well UME at various potential sweep rates with $D_{ox} = 2 \times 10^{-10}$ $m^2\ s^{-1}$ (**A**), 4×10^{-10} $m^2\ s^{-1}$ (**B**), and 2×10^{-9} $m^2\ s^{-1}$ (**C**). The critical scan rate, ν_{crit}, marking the transition from positive $(\delta i_p/\delta \nu)$ at small ν to negative $(\delta i_p/\delta \nu)$ at large ν decreases as D_{ox} increases. In other words, rapid external diffusion coefficients support undistorted stripping behavior for Hg disc-wells at rapid scan rates.

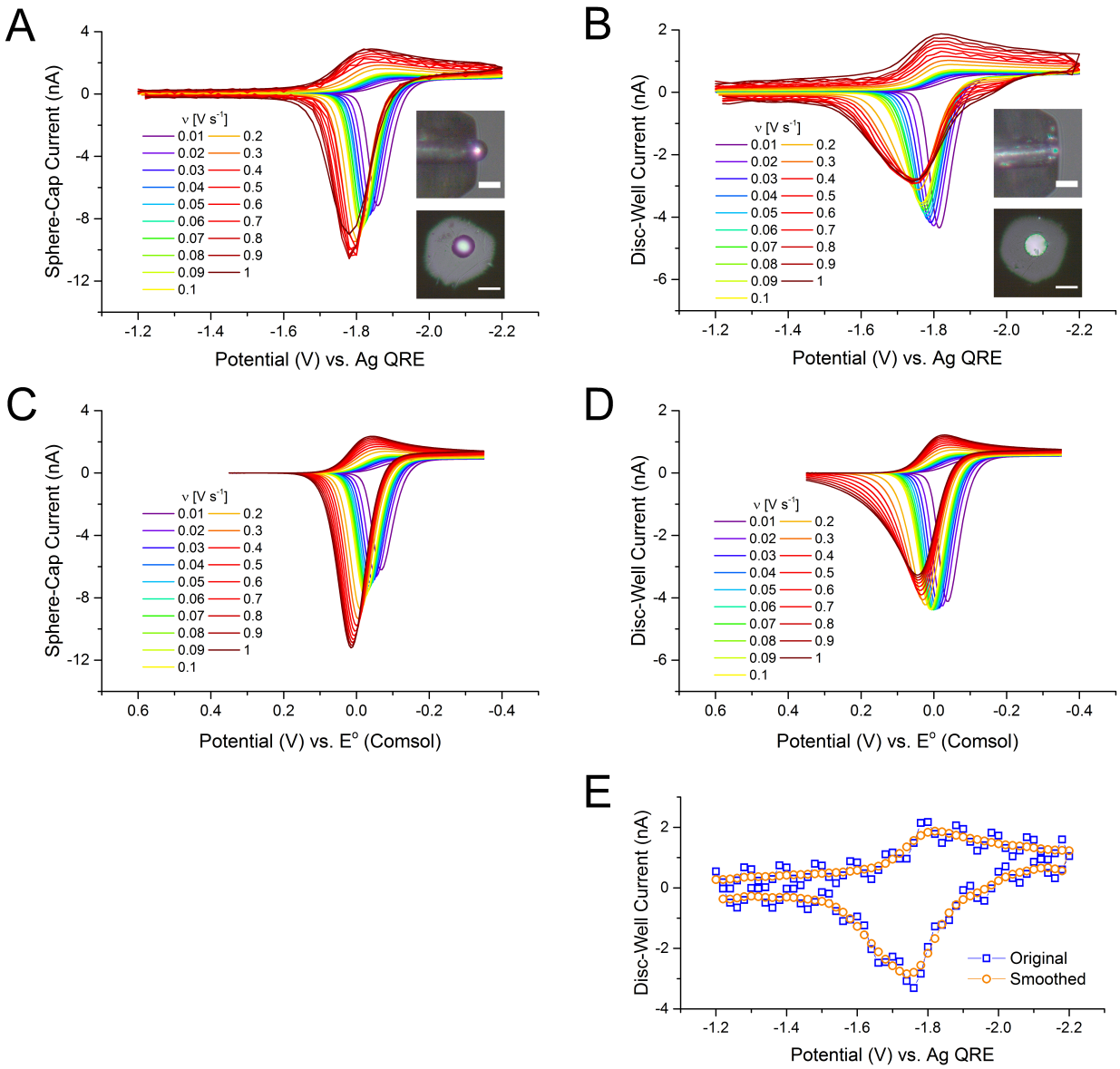

Figure 5.9. Experimental (**A**, **B**) and simulated (**C**, **D**) CVs used to generate the data in Figure 5.7C and Figure 5.7D. (**E**) CV data corresponding to $\nu = 1$ V s^{-1} in Figure 5.7B (and panel **B** here) with and without a Fourier filter to remove an instrument artifact.

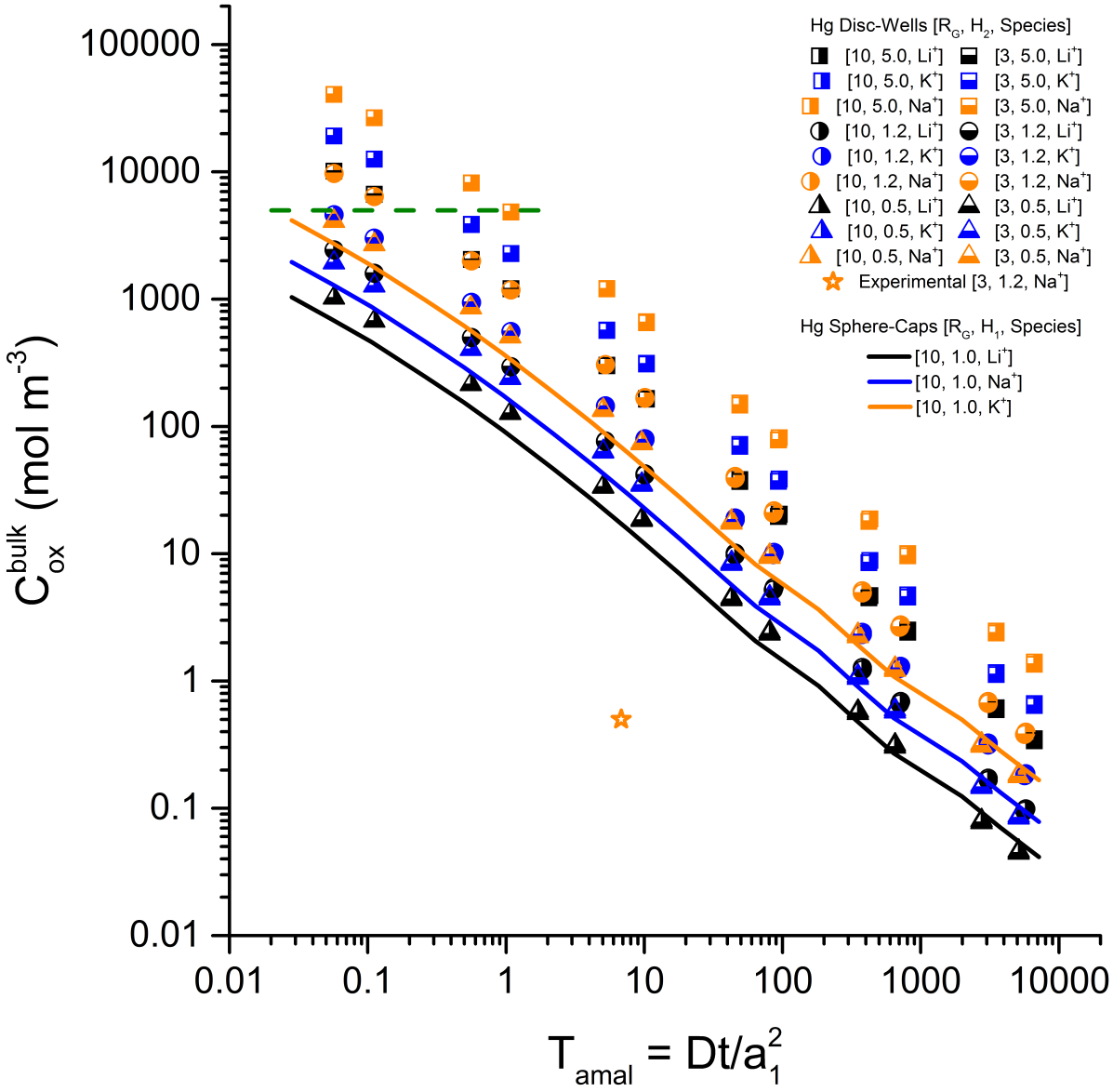

Figure 5.10. Simulated saturation conditions for sphere-cap and disc-well UMEs. The dashed green line indicates the saturation limit for $LiClO_4$ in PC at standard temperature and pressure. Open orange circles correspond to saturation conditions for the disc-well probe used in Figure 5.7B. The open orange star indicates the experimental conditions used in Figure 5.13, namely 0.5 mM Na^+ and $T_{amal} = 6.82$. Because R_G has little impact on saturation conditions, right-filled symbols and bottom-filled symbols overlap almost completely.

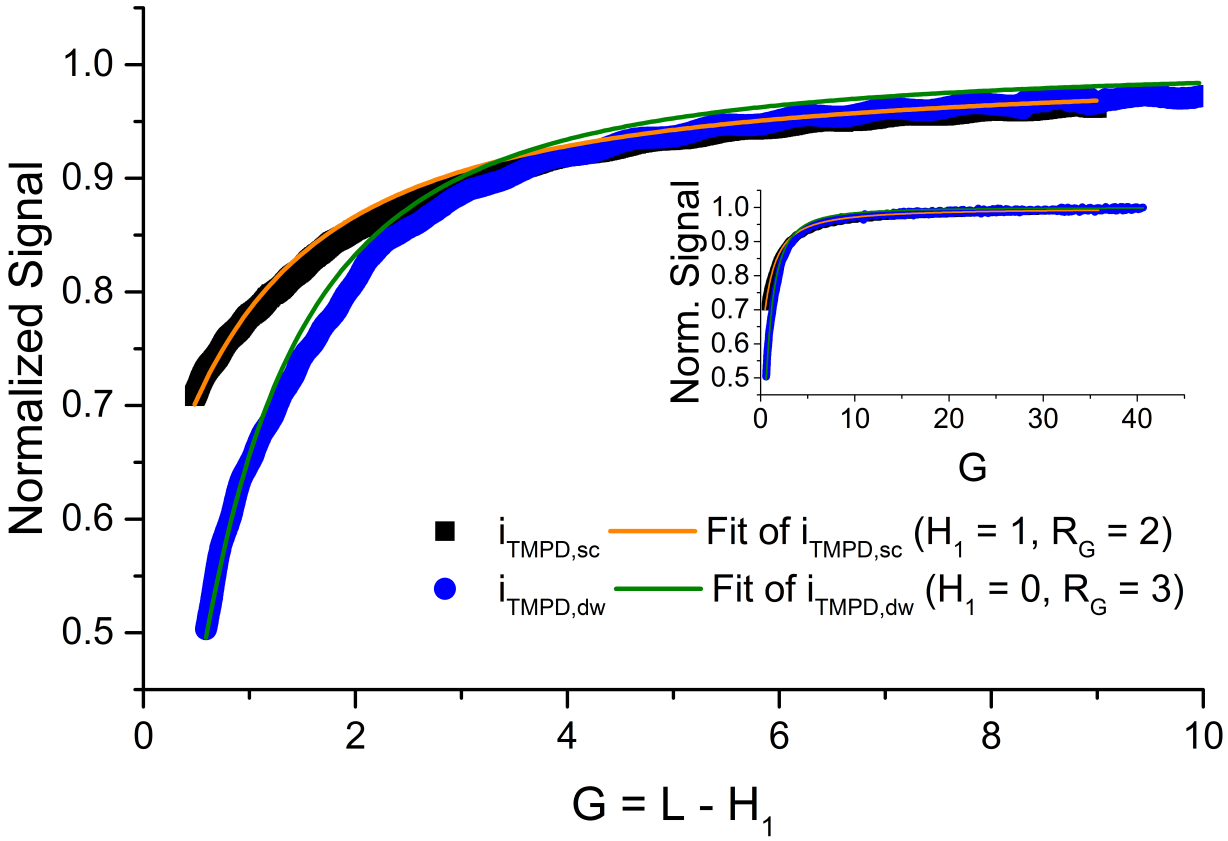

Figure 5.11. Potentiostatic probe approach curves made with sphere-cap and disc-well UMEs over an insulator. The sphere-cap is approached to 70% negative feedback ($L_f = 1.4830$, $H_1 = 1.0$, $G_f = 0.4830$) while the disc-well is approached to 50% negative feedback ($L_f = G_f = 0.5912$). The currents are normalized by their initial value at $G \sim 40$ (see **inset**). Probe speed varies from 1.0 μm s^{-1} to 0.1 μm s^{-1}.

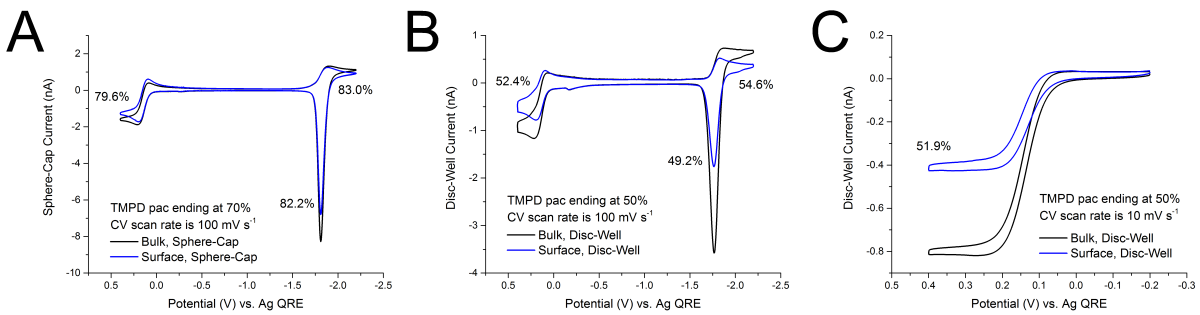

Figure 5.12. CVs taken with a sphere-cap UME (**A**) and a disc-well UME (**B, C**) before and after TMPD PACs presented in Figure 5.11. The decrease in current confirms the PAC response and demonstrates that forced convection did not have a significant effect.

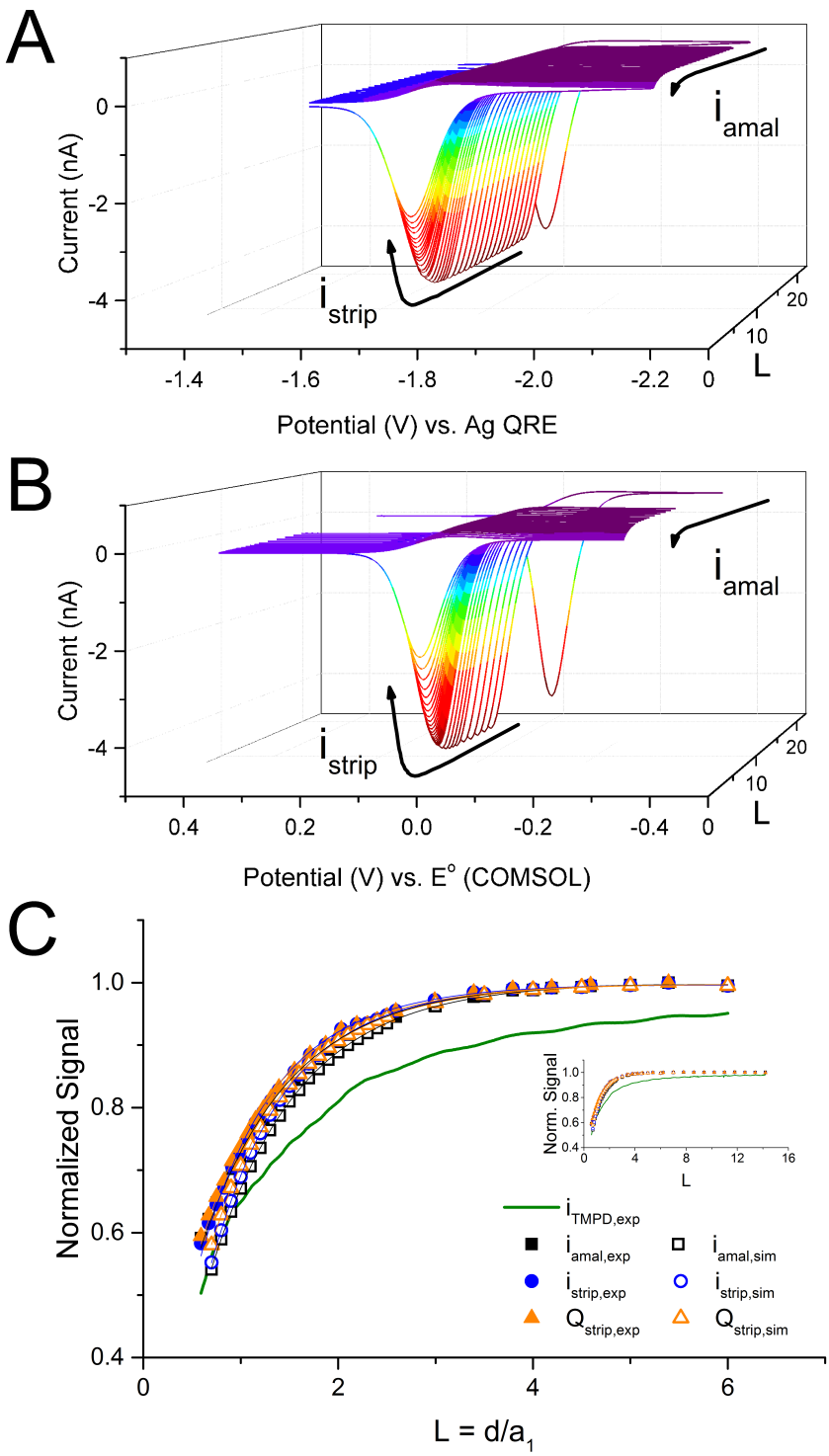

Figure 5.13. CV-PACs (**C**) extracted from experimental (**A**) and simulated (**B**) CV-PAS data for $Na^+ + e^- \rightleftarrows Na(Hg)$ in 0.5 mM TMPD + 0.5 mM $NaClO_4$ + 0.5 M TBAP in PC at a Hg disc-well UME. Simulation conditions are: a_1 = 12.5 μm, H_1 = 0, H_2 = 1.2, R_G = 3, ΔE_t = 0.35 V, D_{Na+} = 2.0 × 10^{-10} m^2 s^{-1}, $D_{Na(Hg)}$ = 8.4 × 10^{-10} m^2 s^{-1}, ν = 50 mV s^{-1}, T_{amal} = 6.82, k^o = 0.01 m s^{-1}, α = 0.5.

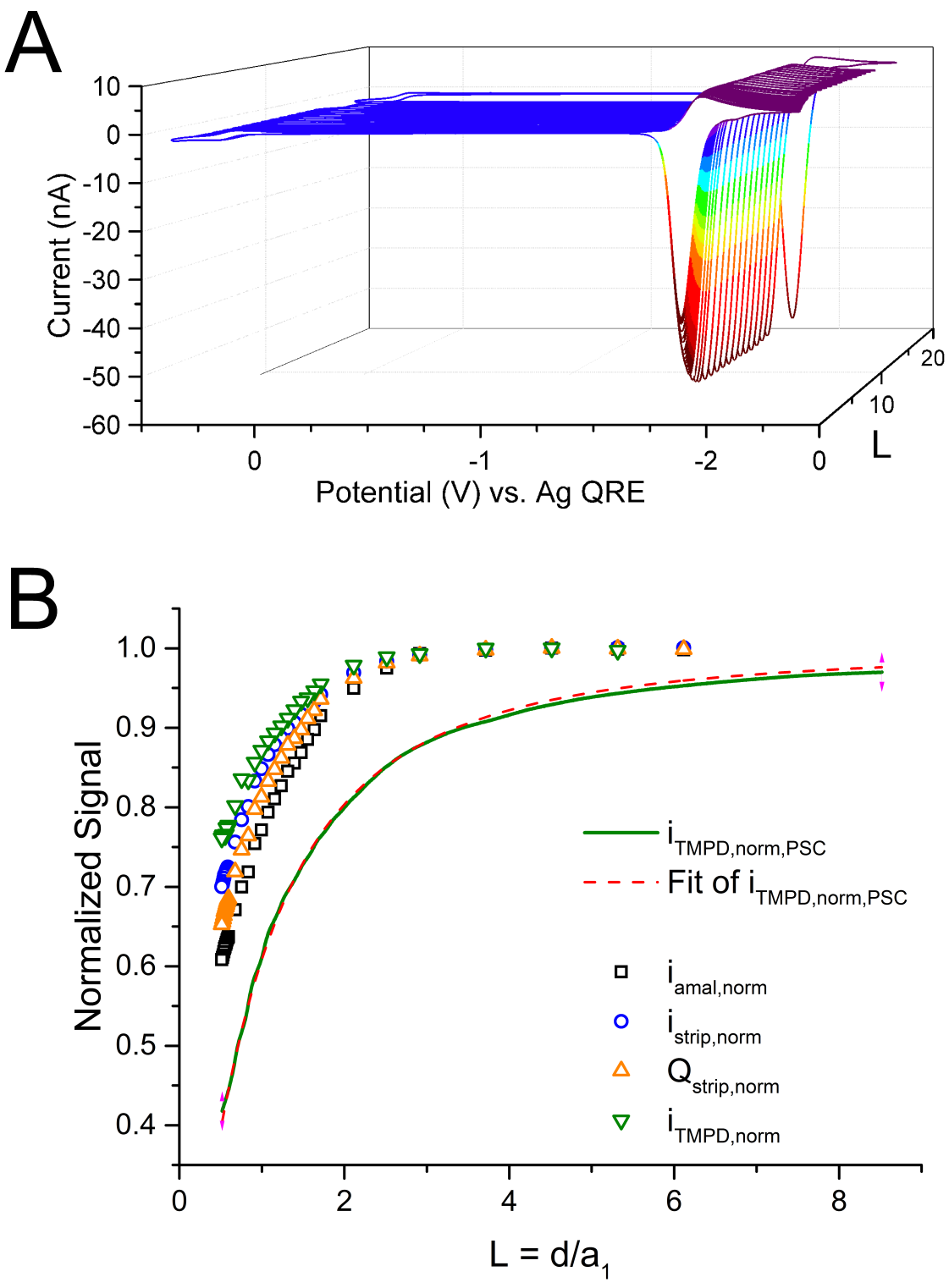

Figure 5.14. CV-PAS (**A**) and resulting CV-PACs (**B**) taken with a Hg disc-well UME (a_1 = 12.5 μm, R_G = 4, H_2 = 1.3) at ν =100 mV s^{-1} ($T_{Li,amal}$ = 11.5 ± 0.4 , $T_{TMPD,ox}$ = 5.2 ± 0.2) over an inactive TiO_2 substrate in a solution of 1 mM TMPD + 10 mM $LiClO_4$ + 0.5 M TBAP in PC. The potentiostatic PSC data in **B** gives the final tip-substrate gap as L_f = G_f = 0.520 ± 0.001.

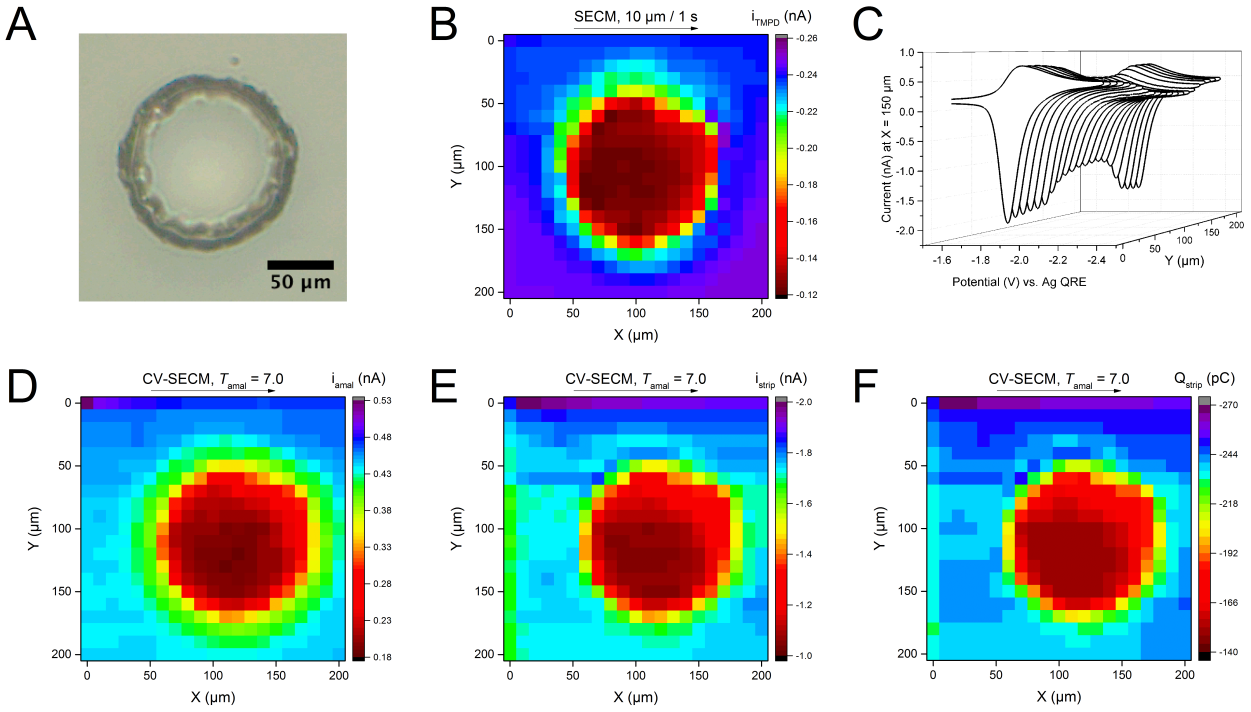

Figure 5.15. CV-SECM data collected with a Hg disc-well UME (a_1 = 12.5 µm, R_G = 2.8, H_2 = 1.4) in 0.5 mM TMPD + 0.5 mM $NaClO_4$ + 0.1 M TBAP in PC. (**A**) The region of interest contains a pillar of insulating polymer (SU-8 2002.5) measuring 2.5 µm in height and 50 µm in radius supported on glass. (**B**) A potentiostatic SECM image of TMPD oxidation with negative feedback taken at L = 0.462 ± 0.002 (d = 5.78 ± 0.03 µm). The probe was rastered in the +X direction at 10 µm s^{-1}. (**C**) Cross section of CV-SECM data at X = 150 µm with ν = 0.1 V s^{-1} (T_{amal} = 7.0). Images of the amalgamation current (**D**), peak stripping current (**E**), and integrated stripping charge (**F**) extracted from CV-SECM data. The probe was rastered in the +X direction between CV measurements at 50 µm s^{-1}.

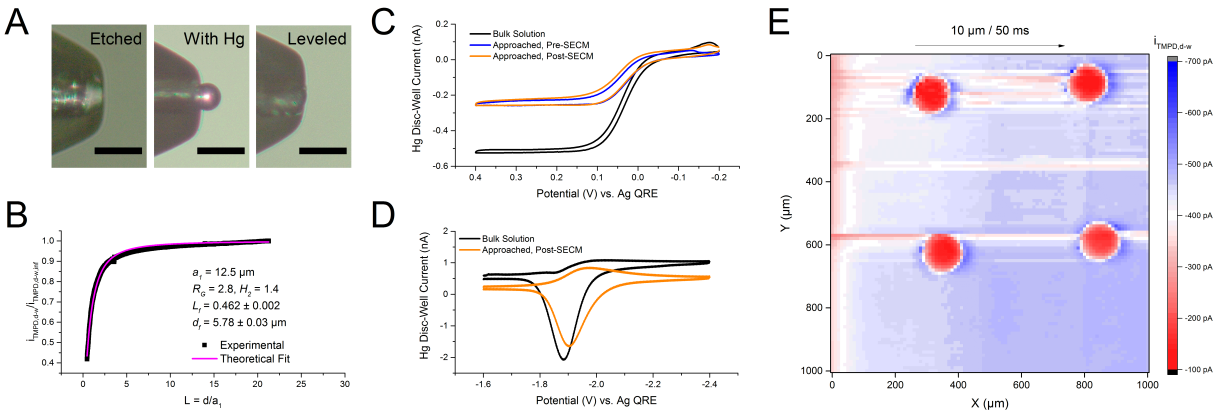

Figure 5.16. Demonstration of the chemical and mechanical stability of a Hg disc-well UME (**A**) over a glass slide decorated with a matrix of insulating pillars (SU-8 2002.5) measuring 100 µm in diameter and 2.5 µm in height. Neighboring pillars are separated by 500 µm, measured from their centers. The scale bars indicate 50 µm. (**B**) The disc-well was positioned near the glass substrate with a potentiostatic probe approach curve (PAC) based on TMPD oxidation. The probe moved with a speed of 1 µm s^{-1} (100 nm per 100 ms) and halted at L_f = 0.462 ± 0.002. CVs of TMPD oxidation (**C**) at 10 mV s^{-1} and Na amalgamation/stripping (**D**) at 100 mV s^{-1} suggest no change in the disc-well surface area and demonstrate the persistence of Hg following a rapid SECM image (**E**) based on TMPD oxidation. To acquire the SECM image, the probe was rastered in the +X direction at 200 µm s^{-1} (10 µm per 50 ms). The pillar centered at X = 810 µm and Y = 90 µm is featured in Figure 5.15. The solution consisted of 0.5 mM TMPD + 0.5 mM $NaClO_4$ + 0.1 M NBu_4ClO_4 in PC.

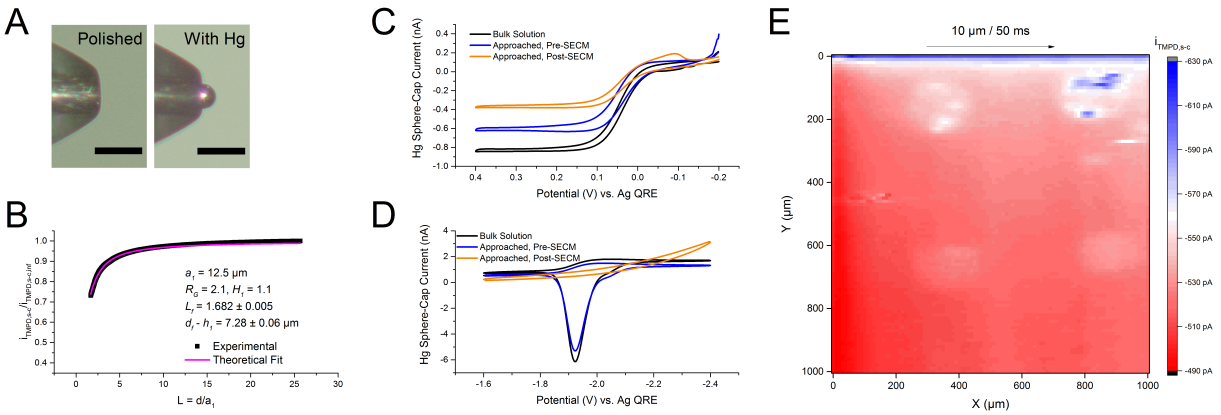

Figure 5.17. Demonstration of the comparative mechanical instability of a Hg sphere-cap UME (**A**) under rapid lateral movement. The scale bars indicate 50 µm. (**B**) The sphere-cap was positioned near the glass substrate with a potentiostatic probe approach curve (PAC) based on TMPD oxidation. The probe moved with a speed of 1 µm s^{-1} (100 nm per 100 ms) and halted at L_f = 1.682 ± 0.005 (G_f = 0.582 ± 0.005). CVs of TMPD oxidation (**C**) at 10 mV s^{-1} and Na amalgamation/stripping (**D**) at 100 mV s^{-1} suggest that the Hg deposit is intact after approaching the surface but completely absent following a rapid SECM image (**E**) based on TMPD oxidation. The solution, scanned area, and probe velocity in panel **E** are the same as in Figure 5.16E, but the sphere-cap does not survive the process. The probe is too far from the substrate for abrasion to occur, and the timescale of the Na amalgamation/stripping CVs in **D** is too short to incur saturation damage. This suggests that the Hg sphere-cap was dislodged by shear forces during lateral movement.

5.8 References

(1) Sun, P.; Laforge, F. O.; Mirkin, M. V. Scanning Electrochemical Microscopy in the 21st Century. *Phys. Chem. Chem. Phys.* **2007**, *9*, 802–823.

(2) Amemiya, S.; Bard, A. J.; Fan, F.-R.; Mirkin, M. V.; Unwin, P. R. Scanning Electrochemical Microscopy. *Annu. Rev. Anal. Chem.* **2008**, *1*, 95–131.

(3) Mirkin, M. V.; Nogala, W.; Velmurugan, J.; Wang, Y. Scanning Electrochemical Microscopy in the 21st Century. Update 1: Five Years After. *Phys. Chem. Chem. Phys.* **2011**, *13*, 21196–21212.

(4) *Scanning Electrochemical Microscopy*; Bard, A. J.; Mirkin, M. V., Eds.; 2nd ed.; CRC Press, 2012.

(5) Kranz, C. Recent Advancements in Nanoelectrodes and Nanopipettes Used in Combined Scanning Electrochemical Microscopy Techniques. *Analyst* **2014**, *139*, 336–352.

(6) Lee, H. J.; Beriet, C.; Girault, H. H. Amperometric Detection of Alkali Metal Ions on Micro-Fabricated Composite Polymer Membranes. *J. Electroanal. Chem.* **1998**, *453*, 211–219.

(7) Amemiya, S.; Bard, A. J. Scanning Electrochemical Microscopy. 40. Voltammetric Ion-Selective Micropipet Electrodes for Probing Ion Transfer at Bilayer Lipid Membranes. *Anal. Chem.* **2000**, *72*, 4940–4948.

(8) Cai, C.; Tong, Y.; Mirkin, M. V. Probing Rapid Ion Transfer Across a Nanoscopic Liquid–Liquid Interface. *J. Phys. Chem. B* **2004**, *108*, 17872–17878.

(9) Lipson, A. L.; Ginder, R. S.; Hersam, M. C. Nanoscale in Situ Characterization of Li-Ion Battery Electrochemistry via Scanning Ion Conductance Microscopy. *Adv. Mater.* **2011**, *23*, 5613–5617.

(10) Chen, C.-C.; Zhou, Y.; Baker, L. A. Scanning Ion Conductance Microscopy. *Annu. Rev. Anal. Chem.* **2012**, *5*, 207–228.

(11) Lipson, A. L.; Puntambekar, K.; Comstock, D. J.; Meng, X.; Geier, M. L.; Elam, J. W.; Hersam,

M. C. Nanoscale Investigation of Solid Electrolyte Interphase Inhibition on Li-Ion Battery MnO Electrodes via Atomic Layer Deposition of Al_2O_3. *Chem. Mater.* **2014**, *26*, 935–940.

(12) Ebejer, N.; Güell, A. G.; Lai, S. C. S.; McKelvey, K.; Snowden, M. E.; Unwin, P. R. Scanning Electrochemical Cell Microscopy: a Versatile Technique for Nanoscale Electrochemistry and Functional Imaging. *Annu. Rev. Anal. Chem.* **2013**, *6*, 329–351.

(13) Takahashi, Y.; Kumatani, A.; Munakata, H.; Inomata, H.; Ito, K.; Ino, K.; Shiku, H.; Unwin, P. R.; Korchev, Y. E.; Kanamura, K.; Matsue, T. Nanoscale Visualization of Redox Activity at Lithium-Ion Battery Cathodes. *Nat. Commun.* **2014**, *5*, 5450.

(14) Barton, Z. J.; Rodríguez-López, J. Lithium Ion Quantification Using Mercury Amalgams as *In Situ* Electrochemical Probes in Nonaqueous Media. *Anal. Chem.* **2014**, *86*, 10660–10667.

(15) Hui, J.; Burgess, M.; Zhang, J.; Rodríguez-López, J. Layer Number Dependence of Li^+ Intercalation on Few-Layer Graphene and Electrochemical Imaging of Its Solid–Electrolyte Interphase Evolution. *ACS Nano* **2016**, *10*, 4248–4257.

(16) Barton, Z. J.; Rodríguez-López, J. Emerging Scanning Probe Approaches to the Measurement of Ionic Reactivity at Energy Storage Materials. *Anal. Bioanal. Chem.* **2016**, *408*, 2707–2715.

(17) Wehmeyer, K. R.; Wightman, R. M. Cyclic Voltammetry and Anodic Stripping Voltammetry with Mercury Ultramicroelectrodes. *Anal. Chem.* **1985**, *57*, 1989–1993.

(18) Penczek, M.; Stojek, Z. Anodic Stripping Voltammetry at a Micro-Disc Mercury Film Electrode. *J. Electroanal. Chem. Interfacial Electrochem.* **1985**, *191*, 91–100.

(19) Stojek, Z.; Osteryoung, J. Experimental Determination of the Coefficient in the Steady State Current Equation for Spherical Segment Microelectrodes. *Anal. Chem.* **1989**, *61*, 1305–1308.

(20) Colyer, C. L.; Oldham, K. B.; Fletcher, S. Growth of Mercury Electrodeposits on an Inlaid Disc

: Thermodynamic Theory. *J. Electroanal. Chem. Interfacial Electrochem.* **1990**, *290*, 33–48.

(21) Mauzeroll, J.; Hueske, E. A.; Bard, A. J. Scanning Electrochemical Microscopy. 48. Hg/Pt Hemispherical Ultramicroelectrodes: Fabrication and Characterization. *Anal. Chem.* **2003**, *75*, 3880–3889.

(22) Limon-Petersen, J. G.; Rees, N. V.; Streeter, I.; Molina, Á.; Compton, R. G. Potential Step Chronoamperometry at Hemispherical Mercury Electrodes: the Formation of Thallium Amalgams and the Measurement of the Diffusion Coefficient of Thallium in Mercury. *J. Electroanal. Chem.* **2008**, *623*, 165–169.

(23) Souto, R. M.; González-García, Y.; Battistel, D.; Daniele, S. In Situ Scanning Electrochemical Microscopy (SECM) Detection of Metal Dissolution During Zinc Corrosion by Means of Mercury Sphere-Cap Microelectrode Tips. *Chem. Eur. J.* **2011**, *18*, 230–236.

(24) Danis, L.; Gateman, S. M.; Snowden, M. E.; Halalay, I. C.; Howe, J. Y.; Mauzeroll, J. Anodic Stripping Voltammetry at Nanoelectrodes: Trapping of Mn^{2+} By Crown Ethers. *Electrochim. Acta* **2015**, *162*, 169–175.

(25) Velmurugan, J.; Noël, J.-M.; Mirkin, M. V. Nucleation and Growth of Mercury on Pt Nanoelectrodes at Different Overpotentials. *Chem. Sci.* **2013**, *5*, 189–194.

(26) Burgess, M.; Hernández-Burgos, K.; Cheng, K. J.; Moore, J. S.; Rodríguez-López, J. Impact of Electrolyte Composition on the Reactivity of a Redox Active Polymer Studied Through Surface Interrogation and Ion-Sensitive Scanning Electrochemical Microscopy. *Analyst* **2016**, *141*, 3842–3850.

(27) Baranski, A. Rapid Anodic Stripping Analysis with Ultramicroelectrodes. *Anal. Chem.* **1987**, *59*, 662–666.

(28) Coetzee, J. F.; Ecoff, M. J. Potentiometric Stripping Analysis at Microelectrodes in Various

Solvents and Some Comparisons with Voltammetric Stripping Analysis. *Anal. Chem.* **1991**, *63*, 957–963.

(29) Baldo, M.-A.; Daniele, S.; Mazzocchin, G. A. Cyclic Voltammetry at Mercury Microelectrodes. Effects of Mercury Thickness and Scan Rate. *Electrochim. Acta* **1996**, *41*, 811–818.

(30) Alpuche-Aviles, M.; Baur, J. E.; Wipf, D. O. Imaging of Metal Ion Dissolution and Electrodeposition by Anodic Stripping Voltammetry−Scanning Electrochemical Microscopy. *Anal. Chem.* **2008**, *80*, 3612–3621.

(31) Danis, L.; Polcari, D.; Kwan, A.; Gateman, S. M.; Mauzeroll, J. Fabrication of Carbon, Gold, Platinum, Silver, and Mercury Ultramicroelectrodes with Controlled Geometry. *Anal. Chem.* **2015**, *87*, 2565–2569.

(32) Velmurugan, J.; Mirkin, M. V. Fabrication of Nanoelectrodes and Metal Clusters by Electrodeposition. *ChemPhysChem* **2010**, *11*, 3011–3017.

(33) Barton, Z. J.; Rodríguez-López, J. Cyclic Voltammetry Probe Approach Curves with Alkali Amalgams at Mercury Sphere-Cap Scanning Electrochemical Microscopy Probes. *Anal. Chem.* **2017**, *89*, 2708–2715.

(34) Amphlett, J. L.; Denuault, G. Scanning Electrochemical Microscopy (SECM): an Investigation of the Effects of Tip Geometry on Amperometric Tip Response. *J. Phys. Chem. B* **1998**, *102*, 9946–9951.

(35) Zhang, B.; Zhang, Y.; White, H. S. The Nanopore Electrode. *Anal. Chem.* **2004**, *76*, 6229–6238.

(36) Zhang, B.; Galusha, J.; Shiozawa, P. G.; Wang, G.; Bergren, A. J.; Jones, R. M.; White, R. J.; Ervin, E. N.; Cauley, C. C.; White, H. S. Bench-Top Method for Fabricating Glass-Sealed Nanodisk Electrodes, Glass Nanopore Electrodes, and Glass Nanopore Membranes of Controlled Size. *Anal. Chem.* **2007**, *79*, 4778–4787.

(37) Sun, P.; Mirkin, M. V. Scanning Electrochemical Microscopy with Slightly Recessed Nanotips. *Anal. Chem.* **2007**, *79*, 5809–5816.

(38) Bond, A. M.; Luscombe, D.; Oldham, K. B.; Zoski, C. G. A Comparison of the Chronoamperometric Response at Inlaid and Recessed Disc Microelectrodes. *J. Electroanal. Chem. Interfacial Electrochem.* **1988**, *249*, 1–14.

(39) Compton, R. G.; Eklund, J. C.; Marken, F.; Rebbitt, T. O.; Akkermans, R. P.; Waller, D. N. Dual Activation: Coupling Ultrasound to Electrochemistry—an Overview. *Electrochim. Acta* **1997**, *42*, 2919–2927.

(40) *Power Ultrasound in Electrochemistry*; Pollet, B. G., Ed.; John Wiley & Sons, Ltd: Chichester, UK, 2012.

(41) Lindsey, G.; Abercrombie, S.; Denuault, G.; Daniele, S.; De Faveri, E. Scanning Electrochemical Microscopy: Approach Curves for Sphere-Cap Scanning Electrochemical Microscopy Tips. *Anal. Chem.* **2007**, *79*, 2952–2956.

(42) Lefrou, C.; Cornut, R. Analytical Expressions for Quantitative Scanning Electrochemical Microscopy (SECM). *ChemPhysChem* **2010**, *11*, 547–556.

(43) Aoki, K.; Akimoto, K.; Tokuda, K.; Matsuda, H.; Osteryoung, J. Linear Sweep Voltammetry at Very Small Stationary Disk Electrodes. *J. Electroanal. Chem. Interfacial Electrochem.* **1984**, *171*, 219–230.

(44) Mahon, P. J.; Myland, J. C.; Oldham, K. B. A Fresh Approach to Voltammetric Modelling. *J. Electroanal. Chem.* **2002**, *537*, 1–5.

(45) Olmos, J. M.; Molina, A.; Laborda, E.; Martínez-Ortiz, F. Effects of Unequal Diffusion Coefficients and Coupled Chemical Equilibria on Square Wave Voltammetry at Disc and Hemispherical Microelectrodes. *Electrochim. Acta* **2015**, *176*, 1044–1053.

(46) Fawcett, W. R. Comparison of Solvent Effects in the Kinetics of Simple Electron-Transfer and Amalgam Formation Reactions. *Langmuir* **1989**, *5*, 661–671.

(47) Koper, M. T. M.; Schmickler, W. A Theory for Amalgam Forming Electrode Reactions. *J. Electroanal. Chem.* **1998**, *450*, 83–94.

(48) Bartlett, P. N.; Taylor, S. L. An Accurate Microdisc Simulation Model for Recessed Microdisc Electrodes. *J. Electroanal. Chem.* **1998**, *453*, 49–60.

(49) Alfred, L. C. R.; Oldham, K. B. Steady-State Currents at Sphere-Cap Microelectrodes and Electrodes of Related Geometry. *J. Phys. Chem.* **1996**, *100*, 2170–2177.

(50) Molina, A.; González, J.; Henstridge, M. C.; Compton, R. G. Voltammetry of Electrochemically Reversible Systems at Electrodes of Any Geometry: a General, Explicit Analytical Characterization. *J. Phys. Chem. C* **2011**, *115*, 4054–4062.

(51) Cornut, R.; Griveau, S.; Lefrou, C. Accuracy Study on Fitting Procedure of Kinetics SECM Feedback Experiments. *J. Electroanal. Chem.* **2010**, *650*, 55–61.

(52) Sánchez-Sánchez, C. M.; Rodríguez-López, J.; Bard, A. J. Scanning Electrochemical Microscopy. 60. Quantitative Calibration of the SECM Substrate Generation/Tip Collection Mode and Its Use for the Study of the Oxygen Reduction Mechanism. *Anal. Chem.* **2008**, *80*, 3254–3260.

(53) Rees, N. V.; Klymenko, O. V.; Coles, B. A.; Compton, R. G. Fast Scan Linear Sweep Voltammetry at a High-Speed Wall-Tube Electrode. *J. Electroanal. Chem.* **2003**, *557*, 99–107.

(54) Cornut, R.; Poirier, S.; Mauzeroll, J. Forced Convection During Feedback Approach Curve Measurements in Scanning Electrochemical Microscopy: Maximal Displacement Velocity with a Microdisk. *Anal. Chem.* **2012**, *84*, 3531–3537.

(55) Fulian, Q.; Fisher, A. C.; Denuault, G. Applications of the Boundary Element Method in

Electrochemistry: Scanning Electrochemical Microscopy. *J. Phys. Chem. B* **1999**, *103*, 4387–4392.

(56) Cornut, R.; Bhasin, A.; Lhenry, S.; Etienne, M.; Lefrou, C. Accurate and Simplified Consideration of the Probe Geometrical Defaults in Scanning Electrochemical Microscopy: Theoretical and Experimental Investigations. *Anal. Chem.* **2011**, *83*, 9669–9675.

(57) Combellas, C.; Fermigier, M.; Fuchs, A.; Kanoufi, F. Scanning Electrochemical Microscopy. Hydrodynamics Generated by the Motion of a Scanning Tip and Its Consequences on the Tip Current. *Anal. Chem.* **2005**, *77*, 7966–7975.

(58) Kuss, S.; Kuss, C.; Trinh, D.; Schougaard, S. B.; Mauzeroll, J. Forced Convection During Scanning Electrochemical Microscopy Imaging Over Living Cells: Effect of Topographies and Kinetics on the Microelectrode Current. *Electrochim. Acta* **2013**, *110*, 42–48.

CHAPTER 6

Detecting Potassium Ion Gradients at a Model Graphitic Interface

This chapter was published as an original research article in *Electrochimica Acta*:

Barton, Z. J.; Hui, J.; Schorr, N. B.; Rodríguez-López, J. Detecting Potassium Ion Gradients at a Model Graphitic Interface. *Electrochim. Acta*, **2017**, *241*, 98–105. DOI: 10.1016/j.electacta.2017.04.105

Jingshu Hui performed the substrate fabrication and patterning described in section 6.2.2, created and calibrated the Ag/Ag^+ reference electrode, and collected the substrate cyclic voltammetry data presented in Figure 6.5. Noah B. Schorr collected the scanning electron microscopy, Raman spectroscopy, and Raman imaging data presented in Figure 6.3 and Figure 6.4. The article is adapted and reprinted here with permission from the International Society of Electrochemistry, copyright 2017.

6.1 Abstract

Potassium ion batteries (KIBs) are gaining attention as attractive, low-cost alternatives to lithium ion batteries (LIBs). Emerging KIB materials are not yet fully understood, so *in situ* characterization techniques are being developed to address the similarities and differences to the operation of LIB materials, including aspects of interfacial ion transfer and solid electrolyte interphase (SEI) formation. Here, we introduce the use of Hg disc-well microelectrodes as probes in scanning electrochemical microscopy (SECM) for the detection of K^+ gradients on an operating graphitic material. Electrochemically controlled amalgamation and stripping reactions on these probes permit their accurate positioning near a conductive surface, and the detection of local concentration changes once the substrate is biased to intercalate K^+. K^+ reduction into the Hg phase follows a behavior similar to that of Li^+ and Na^+ and yields an electrochemical response that is used to evaluate local substrate reactivity. Using these probes *in situ*, we demonstrate the reversible intercalation of K^+ on a surface site of

patterned highly oriented pyrolytic graphite (HOPG), a model interface for carbonaceous KIB materials. Our method affords a direct measurement of localized K^+ fluxes, which are not resolvable through bulk electroanalytical techniques, thus making our approach potentially informative about reaction mechanisms for nascent KIB-based energy storage technologies (Figure 6.1).

6.2 Introduction

The field of portable energy storage is dominated by Li^+ batteries (LIBs), which operate by the reversible insertion and extraction of Li^+ at anode and cathode host materials.[1] Though LIBs meet present portable energy storage needs, the rising cost and material shortage of lithium sources pose challenges to the long-term sustainability of LIB technologies.[2,3] K-ion batteries (KIBs) are an attractive alternative to LIBs since potassium is ~1000 times more abundant than lithium in the Earth's crust.[4,5] In addition, the theoretical voltage limits for KIBs and LIBs are similar (-2.925 V *vs*. NHE for K/K^+ and -3.045 V *vs*. NHE for Li/Li^+),[6] so sustained technological developments may be able to bring commercially competitive KIBs to the market. Preliminary studies suggest that carbonaceous materials such as hard carbon,[7] graphite,[8-10] graphene oxide,[10] and nitrogen-doped graphene[11] may be good candidates for a KIB anode. Diversifying the materials pool for high performance energy storage requires a deeper understanding of the similarities and differences between LIBs and emerging ion insertion technologies. Building on our previous investigations of interfacial Li^+ fluxes[12] and ionic staging mechanisms in multi-layer graphene,[13] here we turn our attention to K^+ fluxes.

Scanned probe methods are often employed for surface investigations at energy storage materials, but few methods of *in situ* chemical imaging of ionic reactions at the battery–electrolyte interface exist.[14-17] Recently, we reported the use of Hg-based scanning electrochemical microscopy (SECM) probes for the detection of alkali ions *via* anodic stripping voltammetry.[18] In this technique, the reduction of the metal ion and subsequent diffusion of the metal into the Hg phase creates a steady-state amalgamation

current, which upon reversal of the potential scan direction yields a stripping peak. Both of these signals can be used for quantitative detection of differences in the local concentrations of various ions as a function of electrode activation, as well as for accurate positioning of the SECM probe. Furthermore, we recently reported the fabrication and stripping voltammetry of Hg disc-wells, which consist of a level pool of Hg confined to the glass-walled cavity before a recessed Pt microdisc.[19-21] These probes demonstrated their superior performance as SECM probes for the detection of Li^+ and Na^+, as compared to traditional Hg sphere-caps. The $K^+/K(Hg)$ redox pair shares similar electrochemical attributes with $Li^+/Li(Hg)$ and $Na^+/Na(Hg)$, so the same types of probes are able to detect this species.[22-24] Due to their chemical and mechanical robustness as well as their unique ability to directly access ion-specific information, Hg disc-wells enable SECM to pursue answers connecting chemical structures to their electrochemical performance in systems involving ionic gradients. Here, we demonstrate the measurement of ionic gradients on a model material for a KIB anode—highly oriented pyrolytic graphite (HOPG). While insertion of K^+ on this material is not ideal, the detection of ionic gradients over surface features upon activation is accurately tracked, independently from the activity measured at the substrate electrode. The application of SECM techniques for the chemical measurement of ion fluxes at KIB electrodes will enable further understanding of the impact of solid-electrolyte interphase (SEI) formation and electrode structure on the reactivity of emerging materials.

6.3 Experimental

6.3.1 Chemicals and Supplies

All chemicals were purchased as A.C.S. reagent grade or better and used as received without further purification. Nitric acid and water (ChromAr grade) were obtained from Avantor. Platinum wire (25 μm and 0.5 mm diameter) and silver wire (1 mm diameter) were obtained from Goodfellow. Ethylene carbonate (EC, anhydrous, 99%), mercury(II) nitrate monohydrate (≥99.99% trace metals basis),

potassium hexafluorophosphate (99.5%), propylene carbonate (PC, anhydrous, 99.7%), tetrabutylammonium hexafluorophosphate (NBu_4PF_6, 99.0%) and *N*,*N*,*N*′,*N*′-tetramethyl-*p*-phenylenediamine (TMPD, 99%) were obtained from Sigma-Aldrich. Tetramethylammonium nitrate (NMe_4NO_3) was obtained from Southwestern Analytical Chemicals.

Highly ordered pyrolytic graphic (HOPG, brand grade SPI-2) was purchased from SPI supplies. 3M™ copper conductive tape with a single conductive glue adhesive surface was purchased from Ted Pella, Inc. Microposit S1813 photoresist was purchased from MicroChem. AZ 917 MIF developer was purchased from AZ Electronic Materials. Ultra high purity (UHP) argon was obtained from Airgas.

6.3.2 Hg Disc-Well Electrode Fabrication

Hg disc-well probes were fabricated by etching Pt disc ultramicroelectrodes (UMEs), electrodepositing Hg in the cavity, and removing excess Hg with a flexible glass coverslip as previously published.[21] Specifically, Pt UMEs with a Pt radius (a_1) of 12.5 μm and a glass ratio ($R_G = a_2/a_1$, a_2 = total probe radius) smaller than 4 were etched in a solution of 30 v. % sat. $CaCl_2$ + 10 v. % HCl in H_2O for 40 s under ultrasonic agitation while applying a peak-to-peak voltage ($V_{p\text{-}p}$) of 2.70 V at 60 Hz with a variac. This gave an etched cylindrical cavity with a normalized depth ($H_2 = h_2/a_1$, h_2 = depth of cavity) of 1.1. Hg was deposited potentiostatically at +0.2 V *vs.* Ag/AgCl in 20 mM $Hg(NO_3)_2{\cdot}H_2O$ + 0.2 M NMe_4NO_3 and 0.5 v. % HNO_3 in H_2O until the deposition current reached 0.3 μA, indicating the growth of a Hg sphere-cap protruding from the overfilled cavity. The Hg deposit was then leveled and rinsed with H_2O to remove displaced Hg droplets, resulting in a Hg disc-well with a flat, mirror-like surface having a normalized height ($H_1 = h_1/a_1$, h_1 = Hg sphere-cap height) of 0 (Figure 6.2).

6.3.3 Substrate Fabrication and Patterning

Cu tape was used to mechanically exfoliate thin HOPG samples from a larger HOPG block. Following our previously published graphene patterning method,[13] the thin HOPG samples were treated with photolithography to create patterned windows to expose selected areas of the HOPG surface using a mask. The exposed HOPG was then etched by a Plasma Lab Freon/O_2 reactive ion etching (RIE) system with 37 mW RF energy under a pressure of 40 mTorr while flowing 20 sccm O_2 for 1 min. After RIE, the remaining photoresist was removed by rinsing with acetone and isopropanol. The resulting regular array of holes measured ~43 μm wide and ~1.4 μm deep (Figure 6.3). Neighboring holes were separated by 500 μm, measured from their centers.

6.3.4 *Ex Situ* Optical and Spectroscopic Measurements

Hg disc-well probe dimensions were verified though optical microscopy (Zeiss AxioLab.A1). In addition to optical microscopy, HOPG samples were characterized through scanning electron microscopy (SEM, Hitachi S-4800 high resolution SEM), Raman spectroscopy and imaging (Nanophoton Laser Raman Microscope RAMAN-11) (Figure 6.4).

6.3.5 Electrochemical Experiments

All electrochemical measurements were performed with a CHI 920D SECM under oxygen- and water-free conditions in an MBRAUN UniLab glovebox filled with UHP argon. All solutions were made in a PC and EC solvent mixture with 1:1 ratio (vol./vol.), which is hereafter referred to as PC-EC. The Teflon SECM cell was fitted with a patterned HOPG substrate (19.6 mm^2), a Pt wire counter electrode (CE), and a Ag wire quasi-reference electrode (QRE). Substrate CVs and CV-SECM experiments used a Ag/Ag^+ (0.1 M $AgNO_3$ in PC-EC) reference electrode (RE) instead of the Ag QRE to poise the cell potential. Potentials referenced against a 0.1 M Ag/Ag^+ RE (3.604 V *vs.* 0.1 M K/K^+) are reported *vs.* 0.1 M K/K^+ for clarity.

Prior to SECM investigations, the patterned HOPG electrode was cycled in 0.1 M KPF_6 in PC-EC for 6 cycles between 0.604 to 0.004 V *vs.* 0.1 M K/K^+ at 1 mV s^{-1} to form a stable SEI layer. In order to better observe K^+ intercalation and deintercalation processes, additional CVs with HOPG were acquired at 50 μV s^{-1} in 1 mM KPF_6 in PC-EC after SECM experiments (Figure 6.5).

A Hg disc-well UME performing TMPD oxidation in a solution of 2 mM TMPD and 0.1 M KPF_6 in PC-EC was used to collect an SECM feedback image (Figure 6.7) to find the approximate locations of etched holes. To avoid interference from oxidized TMPD generated at the CE, the cell was rinsed with PC and refilled with 1 mM KPF_6 in PC-EC. The Ag QRE was also swapped for a Ag/Ag^+ RE after the removal of TMPD from the cell. The same Hg disc-well probe was then approached to the substrate with a cyclic voltammetry probe scan surface (CV-PSS) in the Z direction (Figure 6.8). After reaching the HOPG surface, the probe was positioned directly over an etched hole and used to record a series of CVs with regular sequential incrementing (and then decrementing) of the substrate potential.

6.4 Results and Discussion

6.4.1 *Ex Situ* Optical and Spectroscopic Measurements

An SEM image of patterned HOPG shows a regular array of holes measuring ~43 μm in diameter and separated from their nearest neighbors by 500 μm (Figure 6.4A). The holes' size and center-to-center distance match with the designed pattern.

Raman spectra (Figure 6.4B) show the clear presence of a D band for etched holes but not for pristine HOPG. The D band corresponds to carbon ring "breathing" modes and is indicative of structural disorder, such as exposed graphitic edge planes.[25] In LIBs, uptake of Li^+ is greater at graphitic edge planes than at the basal plane,[26] so we expected to find similar ionic activity for K^+ in the present system. Following electrochemical cycling and SECM experiments, the D band remained nearly unchanged over un-etched areas but showed a marked increase over etched holes (Figure 6.4B). The

increase in D band intensity is consistent with the evolution of structural disorder expected from the repeated K^+ insertion and extraction. The localization of this increase in D band intensity to the etched holes (Figure 6.4C) suggests that exposed edge planes serve as primary sites for potassium ion intercalation.

6.4.2 Substrate Cycling and SEI Formation

The HOPG substrate was first cycled at 1 mV s^{-1} in 0.1 M KPF_6 in PC-EC for 6 cycles to form a stable SEI layer. Initial cycles showed broad, irreversible peaks that are likely attributable to solvent and electrolyte decomposition processes, such as those found in LIB systems (Figure 6.5A).[13,27,28] The intensity of these peaks diminished with cycling, eventually resulting in a clean background signal. Following SEI formation, cycling more slowly at 50 μV s^{-1} allowed the identification of K^+ intercalation behavior at $E < 0.54$ V (*vs.* K/K^+), in addition to various unknown processes from ~1.10 V to 0.54 V (*vs.* K/K^+), and a deintercalation event at 0.52 V (*vs.* K/K^+) on the return sweep (Figure 6.5B).

6.4.3 Identification of Region of Interest

A Hg disc-well UME (a_1 = 12.5 μm, R_G = 2.5) was positioned approximately one probe radius ($L = d/a_1 \sim 1$, d = tip–substrate gap) above the HOPG surface through a probe scan curve (PSC) in the Z direction using TMPD as the redox mediator and with the substrate left at open circuit. After rapidly imaging a large area to identify a region of interest (Figure 6.6), an area containing a single etched hole (Figure 6.7A) was slowly imaged at 2.5 μm s^{-1} (Figure 6.7B). This speed was selected to prevent distortions based on forced convective transport.[29] Initial SECM images exhibited negative feedback consistent with the insulating nature of SEIs observed for other alkali ions.[13] However, over time we observed a shift towards partial positive feedback. We believe this could be a result of some SEI degradation process or the incorporation of TMPD in the SEI. Though positive feedback is observed at all points in the image, even greater positive feedback occurs over the etched hole centered at [X, Y] =

[45 μm, 45 μm]. If the reactivity of the holes and the basal plane were equal, the SECM feedback current observed over holes would be less than over the basal plane due to the increased tip-substrate gap over holes. The possibility of electron transfer at the HOPG basal plane,[30] the susceptibility of HOPG to adventitious contaminants,[31] and the large number of exposed edge sites on this sample do not allow a straightforward quantification of the contributions from basal and edge planes. However, the observed increase in feedback current over the etched hole is supported by Raman spectra (Figure 6.4B), which suggest far greater planar disorder in the etched holes in comparison to the pristine basal plane, and is consistent with the increased electrochemical activity observed at electronic structure distortion sites in carbonaceous materials, such as graphene.[32-35]

6.4.4 Stripping-Based Approach to HOPG

After switching to a 1 mM KPF_6 solution in PC-EC, the Hg disc-well UME was re-approached to the origin in Figure 6.7 by recording stripping CVs between Z motor increments (Figure 6.8) with the HOPG left unbiased at its open circuit potential. Because ions are regularly stripped from the Hg probe, this method of approaching a surface avoids the risk of damaging the Hg probe by saturation of the amalgam phase. The amalgamation current (i_{amal}), peak stripping current (i_{strip}), and stripping charge (Q_{strip}) were each extracted from the CV-PAS dataset to give three CV-PACs.[18] Of these, Q_{strip} exhibited the least noise, which is consistent with the general insensitivity of integrated values to temporal fluctuations in a source signal. The negative feedback stripping charge CV-PAC was fit with an analytical model derived from COMSOL finite-element simulations[21] to obtain the final approach distance of L = 1.28 ± 0.02 ($\chi_{red}^2 = 4.0401 \times 10^{-5}$). Though smaller gaps are possible, wrinkles in the HOPG surface (Figure 6.4A) warranted caution to avoid mechanical damage to either the probe or the substrate. The final approach distance is consistent with the normalized timescale ($T_{amal} = D_{ox} \cdot \Delta E_t / (\nu \cdot a_1^2)$) of 1.9 ± 0.2,

for which the average Nernstian diffusion layer thickness (δ_N) is 7.7 ± 0.1 μm.[36] This timescale ensures that the depletion volume expanding from the SECM probe during amalgamation propagates far enough into solution to overlap with ionic gradients emanating from the substrate. The overlap between the probe and substrate diffusion fields is the source of informational probe signal perturbations. Negative feedback was observed for all three signals due to the increasingly hindered diffusion field with decreasing tip-substrate gap. The observation of positive feedback from TMPD redox signals and negative feedback from K(Hg) amalgamation and stripping signals demonstrates one of the key benefits of Hg disc-well SECM probes, namely, that amalgamation and stripping signals allow negative feedback SECM probe positioning over any substrate regardless of the substrate's electrical conductivity.[18] Furthermore, since stripping signals afford potential-based ionic specificity, Hg-based CV-SECM signals may provide accurate measurements even in concentrated solutions that are traditionally challenging for methods lacking this specificity, such as those based on resistance, conductance, or impedance.[16]

6.4.5 CVs with Substrate Competition

To show that Hg-based electrodes can directly probe changing ionic gradients, the Hg disc-well UME was positioned over unmodified HOPG at [X, Y] = [0 μm, 45 μm] and programmed to record a series of CVs with the substrate following a sequential staircase potential sweep. Scanning the potential at 0.2 V s^{-1} under the tested conditions gave T_{amal} = 2.4 ± 0.2. As the substrate potential increased (Figure 6.9A), activating K^+ intercalation, all three Hg disc-well signals decreased (Figure 6.9C) while the substrate current increased (Figure 6.9D). Then, as the substrate potential was stepped anodically to allow K^+ deintercalation (Figure 6.9B), the Hg disc-well signals increased in kind as the substrate current decreased, indicating the restoration of the local K^+ concentration. The total decrease in probe signal between inactive and fully active substrate potentials was 3.71 nA (56%) for i_{amal}, 17.6 nA (90%) for i_{strip}, and 3.29 nC (89%) for Q_{strip}. After testing over a pristine region of HOPG, the Hg disc-well UME was

positioned directly over an etched hole at [X, Y] = [45 μm, 45 μm] and made to repeat the same test sequence. As before, all three Hg disc-well signals decreased and then recovered in response to substrate activation then deactivation towards K^+ intercalation. The total decrease in probe signal between inactive and fully active substrate potentials was 2.06 nA (30%) for i_{amal}, 17.7 nA (77%) for i_{strip}, and 3.24 nC (77%) for Q_{strip}.

We hypothesize that the probe signal discrepancies, specifically, the larger changes in i_{strip} and Q_{strip} in comparison to i_{amal}, are due to cross-talk between the probe and the substrate in this low K^+ concentration regime.[37] Such low K^+ concentrations were used in order to safely access timescales allowing good ionic resolution and avoid saturating the ionic capacity of the thin HOPG sample but led to larger than ideal shared resistance between the two working electrodes. In the interest of avoiding co-intercalation phenomena,[38-40] no additional supporting electrolyte was present. i_{strip} and Q_{strip} are typically valuable for their ionic specificity and enhanced sensitivity due to pre-concentration of the amalgam phase, but the observed potential shifts compromised their usefulness in this particular system.

Nevertheless, i_{amal} remained a reliable metric of the local K^+ concentration since it reached a quasi-steady-state and does not depend on the accumulation of K^+ within the Hg probe over time. In both sites explored, the relatively stable i_{amal} signal for $E_{sub} \geq 0.5$ V suggests that the cathodic peaks observed in the HOPG voltammetry (Figure 6.5B) are not associated with K^+ uptake. It is reasonable to suspect that these peaks may be associated with changes in the SEI. $i_{amal}(E_{sub})$ is described well by a simple exponential function of the form $i_{amal} = A + B \cdot \exp(C \cdot E_{sub})$, where A, B, and C are freely varying constants, for both the activation ($\chi_{red}^2 = 1.62 \times 10^{-20}$ for pristine HOPG and $\chi_{red}^2 = 2.26 \times 10^{-21}$ for etched holes) and deactivation ($\chi_{red}^2 = 2.13 \times 10^{-20}$ for pristine HOPG and $\chi_{red}^2 = 2.26 \times 10^{-21}$ for etched holes) substrate potential sequences (Figure 6.10), which suggests that the Hg disc-well closely followed the

electrochemical uptake of K^+ by the substrate. Therefore, despite challenges unique to the system under study, these results demonstrate the ability of Hg disc-well SECM probes to track dynamic ionic fluxes at operating KIB interfaces.

Considering the enhanced positive feedback current in the SECM image (Figure 6.7B) and the pronounced D band in the Raman spectra (Figure 6.4B) over etched holes, we expected to observe a clear increase in K^+ uptake over etched holes in comparison to pristine sites due to the greater concentration of exposed edge planes at etched sites. Contrary to expectations, a greater proportional decrease in i_{amal} was observed over the pristine HOPG than over the etched hole. However, microscopic inspection of the pristine surface does indicate a large density of steps (Figure 6.7A), exposing edge sites at which the ionic flux could rival that of artificially-defective holes. Another possible explanation for the small differences observed between the pristine and hole sites is that the SEI formed on this KIB electrode strongly controls the flux of K^+, thus decreasing contrast between neighboring surface sites. Furthermore, the consistent i_{amal} registered at E_{sub} = 1.604 V, where the substrate is electrochemically inactive, is evidence that the bulk K^+ concentration was not significantly affected. Despite this, the average substrate current decreased with each cycle (Figure 6.9D and Figure 6.11). Therefore, we conclude that the substrate's activity towards K^+ uptake and release decreased with use and/or time. Regardless of the cause, this overall decrease in substrate activity was sufficiently large to obscure whatever differences in K^+ uptake and release may have been originally present over the pristine HOPG and etched holes. The decrease in K^+ uptake by the substrate with each cycle was also a contributing factor to the smaller distortions of i_{strip} and Q_{strip} when a test sequence was subsequently repeated at the same locations with a longer normalized timescale—obtained by increasing the overpotential and decreasing the potential scan rate (Figure 6.11).

While the measurement of K^+ fluxes at the activated KIB electrode–electrolyte interface was successful, this first exploration did not show significant differences in ionic uptake between two sites with different redox reactivity. Rather than a lack of contrast, the absence of meaningful differences at the two location types actually demonstrates the sensitivity of Hg disc-wells to local ionic fluxes, which can distinguish between various degrees of substrate uptake of a particular ionic species *in situ*. The probes accurately reported the changing ionic fluxes, but differences in K^+ uptake over pristine and etched regions were overwhelmed by the much larger impact of substrate aging. While HOPG is certainly not an ideal electrode material under the tested conditions, the methodology shown here might be useful to distinguish the different K^+-consuming processes that underlie the complex response observed on KIB electrodes.

6.5 Conclusions

We have used a novel electrochemical probe to obtain direct measurements of K^+ uptake by a representative graphitic anode material for KIBs. Our SECM investigations with a Hg disc-well UME revealed increased electronic conductivity as well as reversible K^+ intercalation and deintercalation over exposed HOPG edge planes. When positioned over an electrochemically active feature in HOPG, a Hg disc-well UME responded to activation of the substrate towards K^+ uptake. HOPG CVs confirmed the process under investigation was K^+ intercalation/deintercalation and not plating/stripping. However, the complex electrochemical response observed on the substrate electrode at potentials where the SEI is expected to form was chemically resolved by the probe, which did not identify a significant steady-state flux of K^+ towards the interface until potentials well into the expected intercalation range.

We compared the activity towards K^+ intercalation on two structurally different sites on the HOPG surface. Despite contrast in their Raman signatures, indicating a different degree of disorder, and differences in their redox reactivity as assessed by the use of the feedback mode of SECM, few

differences were detected on their K^+ flux activity. While HOPG is likely not a top candidate for KIBs, the new capabilities brought by these probes make them of interest to further understand the role of heterogeneities on ion insertion mechanisms in energy materials. Hg disc-well UMEs can acquire localized, chemically specific measurements of ionic flux over operating battery electrode materials. This information is inaccessible to existing analytical methods and will help inform the rational design of future alkali ion battery anodes and cathodes. CV-SECM imaging studies of multiple alkali ion intercalation and deintercalation processes at target energy storage materials are in progress and planned for future publications.

6.6 Acknowledgements

This material is based upon work supported by the National Science Foundation under Grant No. DMR-1611268 and the National Science Foundation Graduate Research Fellowship Program under Grant No. DGE-1144245. Any opinions, findings, and conclusions or recommendations expressed in this material are those of the authors and do not necessarily reflect the views of the National Science Foundation. J.R.-L. acknowledges support from an Alfred P. Sloan Foundation Fellowship. The authors also thank UIUC for generous start-up funds.

Sample characterization were carried out in part in the Frederick Seitz Materials Research Laboratory Central Facilities, University of Illinois. Sample preparation was carried out in part in the Micro and Nanotechnology Laboratory, University of Illinois. The authors thank Dr. Kenneth Hernández-Burgos for assistance with editing.

6.7 Figures

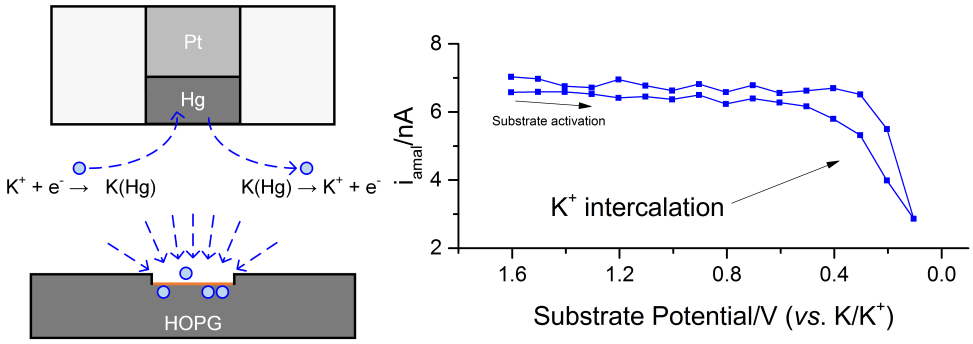

Figure 6.1. Table of contents graphic.

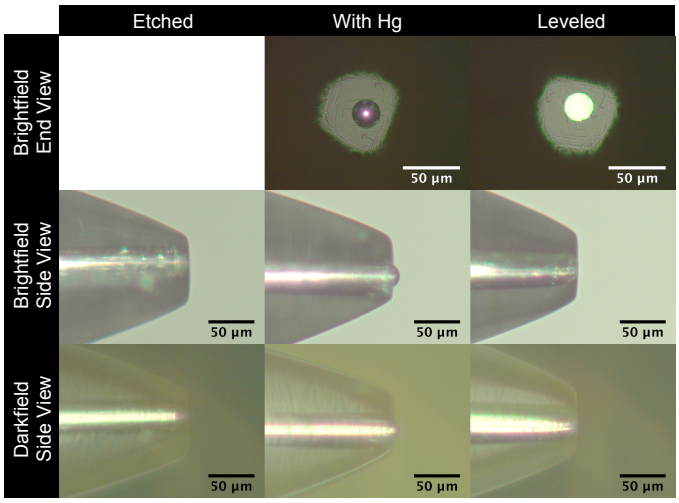

Figure 6.2. Hg Disc-Well Probe Fabrication Process. Electrochemical etching with sonication produces an evenly etched surface. Electrodeposition of Hg is terminated after over-filling the etched cavity. After leveling, the Hg disc-well is evenly filled and has a flat, mirror-like surface. The Hg disc-well shown here has a_1 = 12.5 µm, R_G = 2.5, H_1 = 0, and H_2 = 1.1.

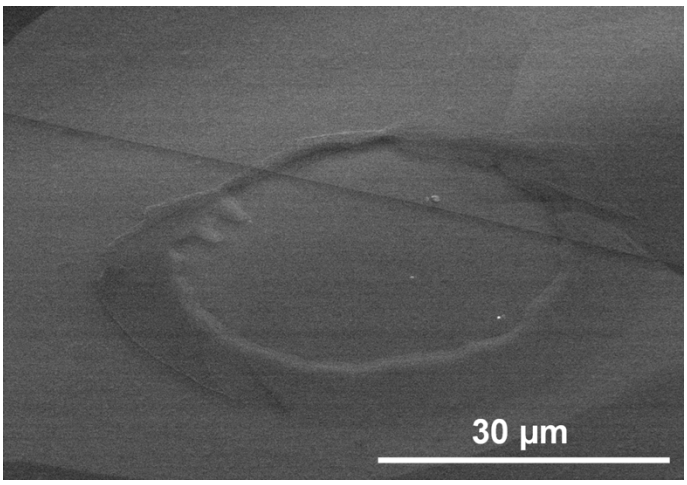

Figure 6.3. SEM Image of Etched Hole. The etched holes are ~1.4 µm deep. The tilt angle is 50°.

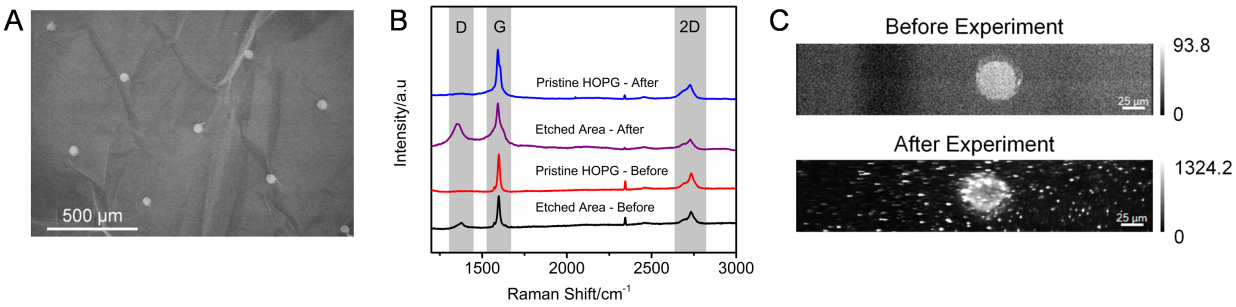

Figure 6.4. SEM and Raman Characterization of Patterned HOPG. (**A**) An SEM image shows the pattern etched holes on HOPG. The holes are ~43 µm wide, ~1.4 µm deep, and 500 µm from their nearest neighbors, measured from their centers. (**B**) Raman spectra before and after electrochemical experiments exhibit a D band signal only over the etched holes. (**C**) Raman mapping of the D band intensity before and after electrochemical experimentation shows an increase in D band signal limited to the etched holes.

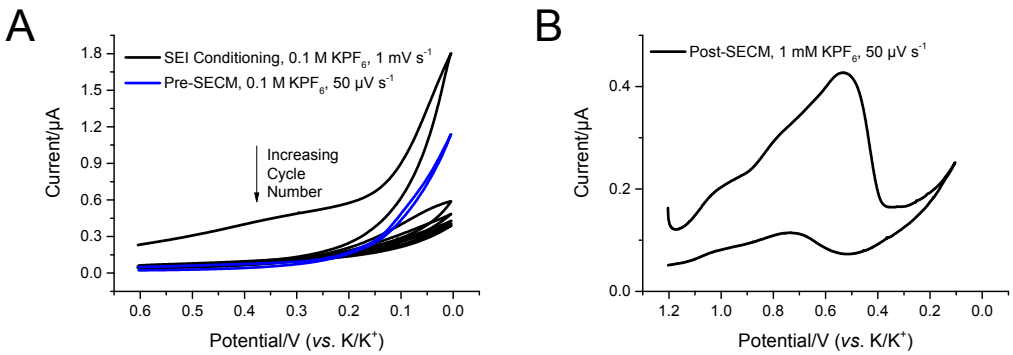

Figure 6.5. Cyclic Voltammetry of K^+ Intercalation and Deintercalation at Patterned HOPG. (**A**) Initially observed broad, irreversible peaks diminished with cycling number, eventually resulting in a clean, stable background signal. (**B**) After forming the SEI, a K-ion deintercalation process was observed at 0.52 V (*vs.* K/K^+).

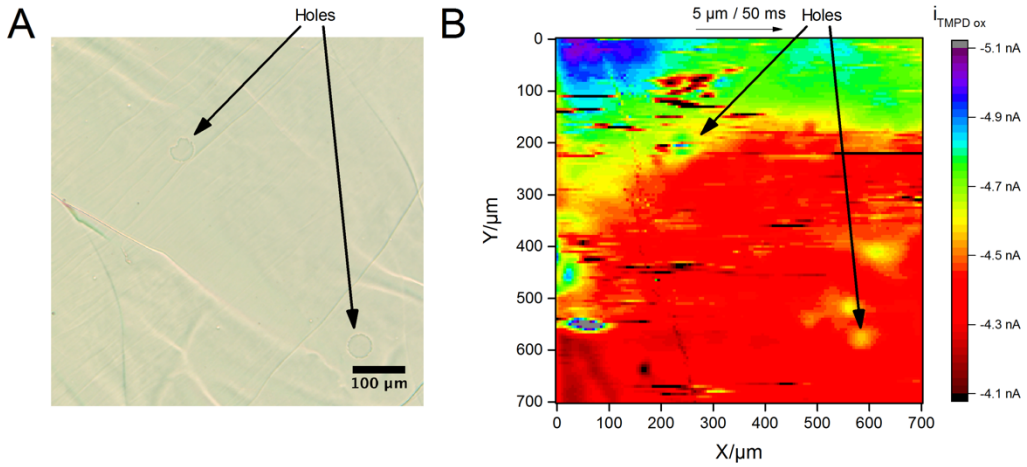

Figure 6.6. Overview of Region of Interest. (**A**) Photomicrograph of the region of interest. (**B**) SECM image with positive feedback from TMPD regeneration at the substrate. The SECM probe is the same Hg disc-well UME used in the main text. The hole at [X, Y] = [240 µm, 200 µm] is featured in Figure 6.7AB.

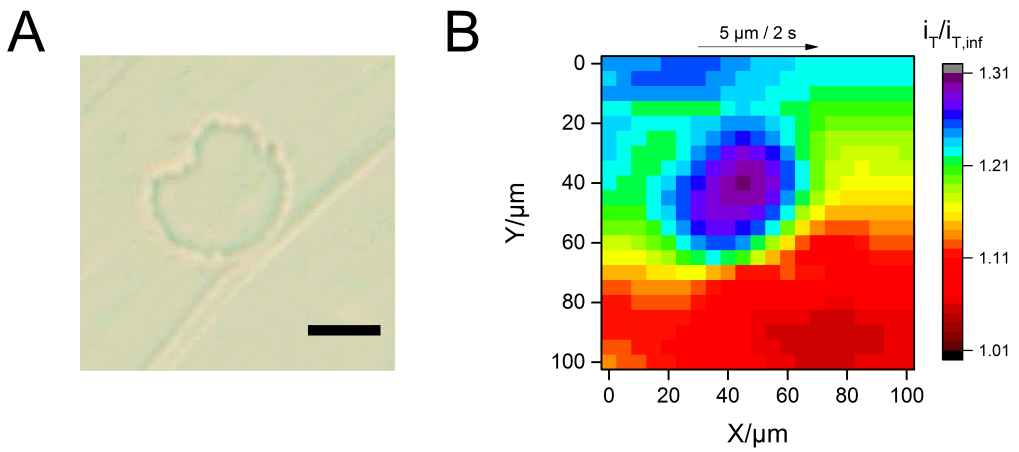

Figure 6.7. Identification of Etched Hole. (**A**) Optical micrograph of an etched hole in HOPG. The scale bar represents 25 µm. (**B**) SECM feedback image of the region shown in **A** taken with a Hg disc-well in 2 mM TMPD + 0.1 M KPF_6 in PC-EC.

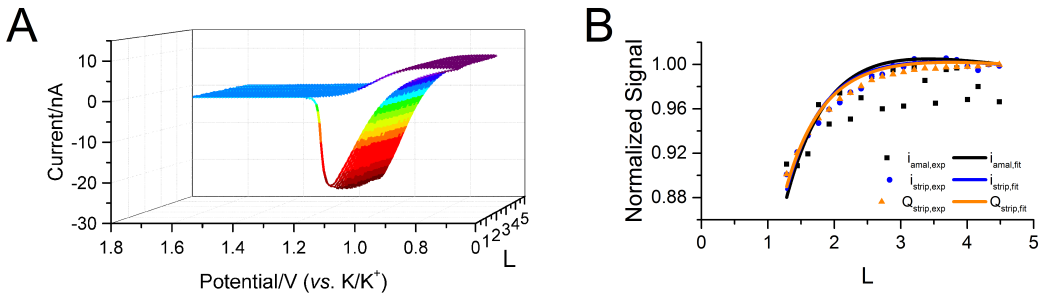

Figure 6.8. CV-SECM Stripping-Based Approach. (A) CV-PAS based on $K^+ + e^- \rightleftarrows K(Hg)$ ending with $L = 1.28 \pm 0.02$ at [X, Y] = [0 μm, 0 μm] in Figure 6.7B. **(B)** Extracted CV-PACs and fits based on COMSOL simulations. Key simulation conditions include: $a_1 = 12.5$ μm, $R_G = 2.5$, $H_1 = 0$, $H_2 = 1.1$, $C_{ox}^* = 1$ mol m^{-3}, $D_{K+,PC\text{-}EC} = 2 \times 10^{-10}$ m^2 s^{-1}, and $D_{K(Hg),Hg} = 7.9 \times 10^{-10}$ m^2 s^{-1}, $\Delta E = 0.295$ V, $\nu = 0.2$ V s^{-1}, $\alpha = 0.5$, and $k^o = 1 \times 10^{-2}$ m s^{-1}.

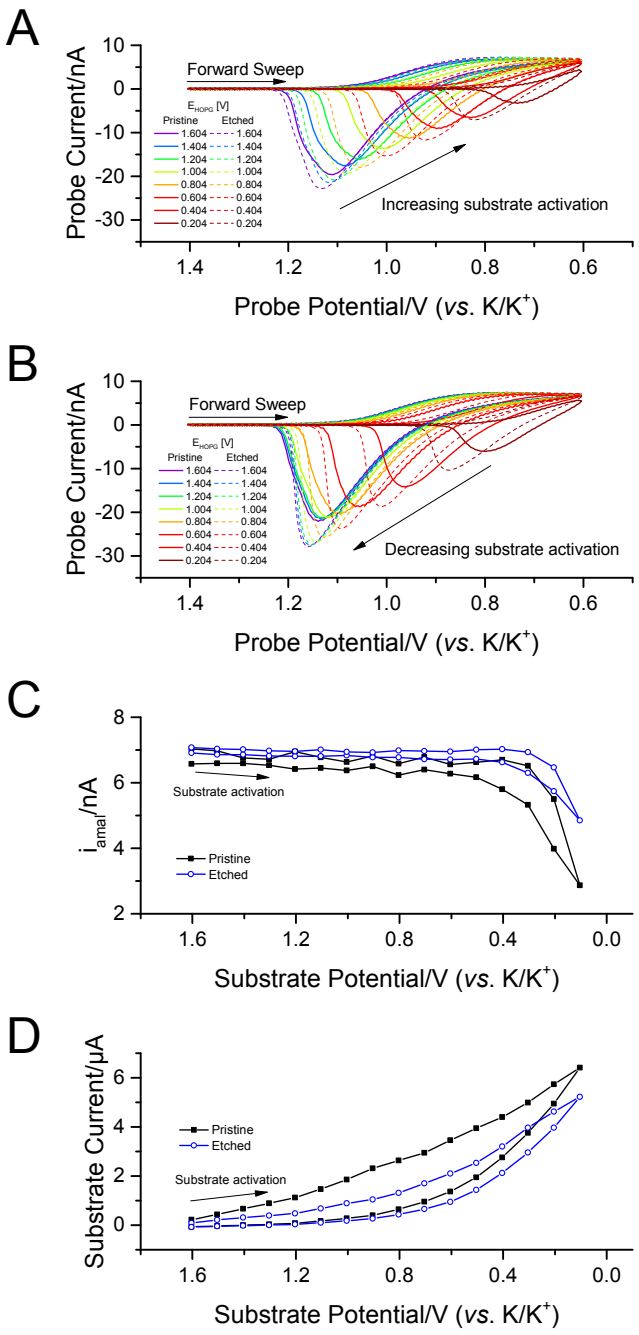

Figure 6.9. Competition for K^+ over Etched Hole. (**A**) Select Hg disc-well CVs taken with increasing substrate activation towards K^+ intercalation. $\nu = 0.2$ V s^{-1}, $T_{amal} = 2.4 \pm 0.2$, $\delta_N = 7.9 \pm 0.1$, and $w_N = 0.633 \pm 0.007$. (**B**) Select Hg disc-well CVs taken with decreasing substrate activation, giving way to K^+ deintercalation. (**C**) Hg disc-well amalgamation currents extracted from **A** and **B**. (**D**) Average chronoamperometric signal at the substrate at various activation potentials.

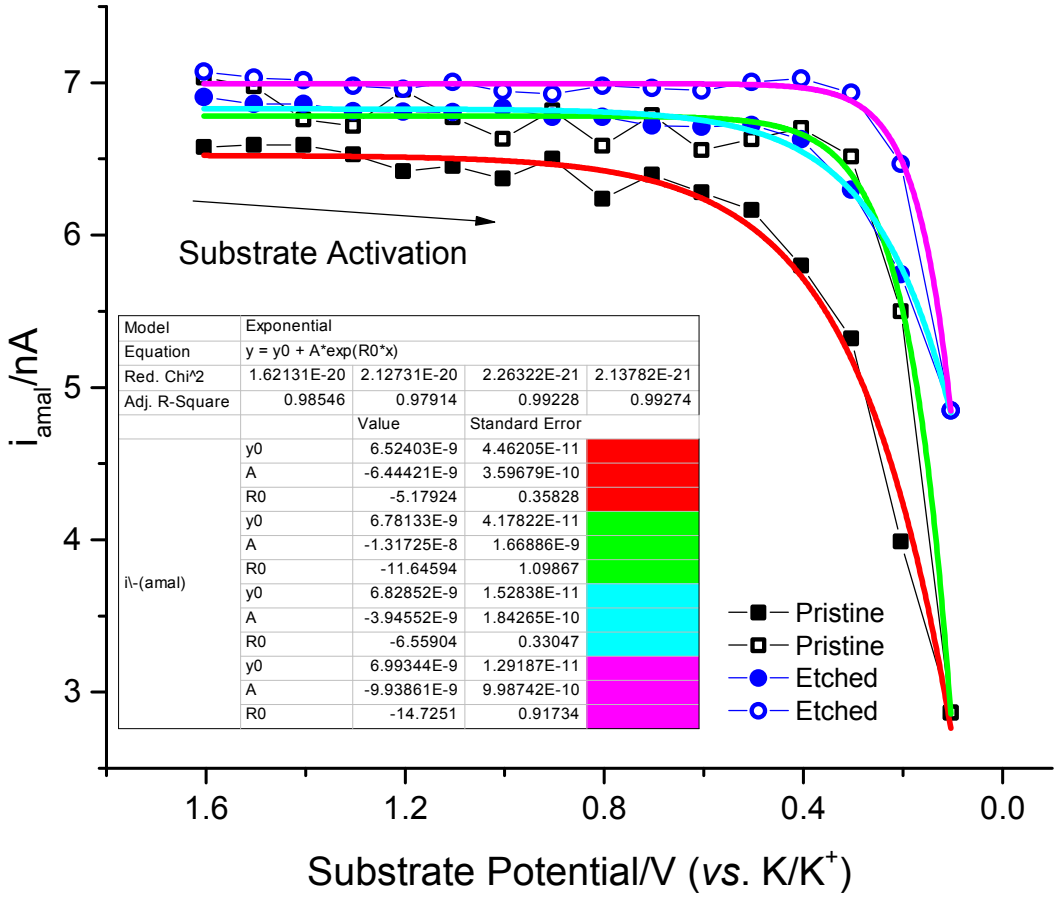

Figure 6.10. Exponential Fits of Hg Disc-Well Amalgamation Currents. These are fits of the data presented in Figure 6.9C in the main text.

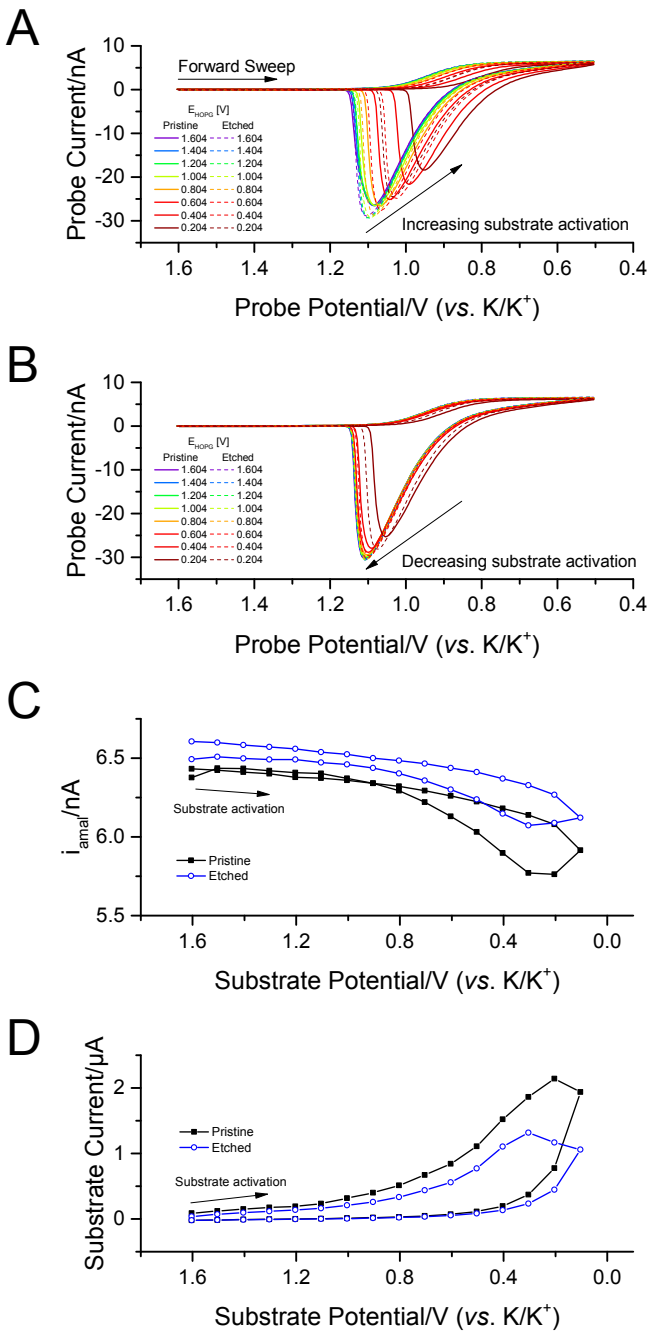

Figure 6.11. K^+ Competition at a Longer Timescale. (**A**) Select Hg disc-well CVs taken with increasing substrate activation towards K^+ intercalation. $\nu = 0.1$ V s^{-1}, $T_{amal} = 5.6 \pm 0.6$. All other parameters are identical to those used in Figure 6.9. (**B**) Select Hg disc-well CVs taken with decreasing substrate activation, giving way to K^+ deintercalation. (**C**) Hg disc-well amalgamation currents extracted from **A** and **B**. (**D**) Average chronoamperometric signal at the substrate at various activation potentials. Though the probe voltammetry benefits from the lengthened timescale, non-specific decreases in K^+ uptake by HOPG obscure information regarding spatial differences in ionic uptake. In other words, the probe is correctly tracking the local changes in K^+ concentration, but the overall passivation of HOPG dominates the signals and masks the smaller differences of interest.

6.8 References

(1) Etacheri, V.; Marom, R.; Elazari, R.; Salitra, G.; Aurbach, D. Challenges in the Development of Advanced Li-Ion Batteries: a Review. *Energy Environ. Sci.* **2011**, *4*, 3243–3262.

(2) Vikström, H.; Davidsson, S.; Höök, M. Lithium Availability and Future Production Outlooks. *Appl. Energy* **2013**, *110*, 252–266.

(3) Larcher, D.; Tarascon, J. M. Towards Greener and More Sustainable Batteries for Electrical Energy Storage. *Nat. Chem.* **2014**, *7*, 19–29.

(4) Taylor, S. R. Abundance of Chemical Elements in the Continental Crust: a New Table. *Geochim. Cosmochim. Acta* **1964**, *28*, 1273–1285.

(5) Xue, L.; Li, Y.; Gao, H.; Zhou, W.; Lü, X.; Kaveevivitchai, W.; Manthiram, A.; Goodenough, J. B. Low-Cost High-Energy Potassium Cathode. *J. Amer. Chem. Soc.* **2017**, *139*, 2164–2167.

(6) Bard, A. J.; Faulkner, L. R. *Electrochemical Methods: Fundamentals and Applications*; 2nd ed.; Wiley: New York, 2001.

(7) Vaalma, C.; Giffin, G. A.; Buchholz, D.; Passerini, S. Non-Aqueous K-Ion Battery Based on Layered $K_{0.3}MnO_2$ And Hard Carbon/Carbon Black. *J. Electrochem. Soc.* **2016**, *163*, A1295–A1299.

(8) Jian, Z.; Xing, Z.; Bommier, C.; Li, Z.; Ji, X. Hard Carbon Microspheres: Potassium-Ion Anode Versus Sodium-Ion Anode. *Adv. Energy Mater.* **2015**, *6*, 1501874–1501875.

(9) Jian, Z.; Luo, W.; Ji, X. Carbon Electrodes for K-Ion Batteries. *J. Amer. Chem. Soc.* **2015**, *137*, 11566–11569.

(10) Luo, W.; Wan, J.; Ozdemir, B.; Bao, W.; Chen, Y.; Dai, J.; Lin, H.; Xu, Y.; Gu, F.; Barone, V.; Hu, L. Potassium Ion Batteries with Graphitic Materials. *Nano Lett.* **2015**, *15*, 7671–7677.

(11) Share, K.; Cohn, A. P.; Carter, R.; Rogers, B.; Pint, C. L. Role of Nitrogen-Doped Graphene for Improved High-Capacity Potassium Ion Battery Anodes. *ACS Nano* **2016**, *10*, 9738–9744.

(12) Barton, Z. J.; Rodríguez-López, J. Lithium Ion Quantification Using Mercury Amalgams as *In Situ* Electrochemical Probes in Nonaqueous Media. *Anal. Chem.* **2014**, *86*, 10660–10667.

(13) Hui, J.; Burgess, M.; Zhang, J.; Rodríguez-López, J. Layer Number Dependence of Li^+ Intercalation on Few-Layer Graphene and Electrochemical Imaging of Its Solid–Electrolyte Interphase Evolution. *ACS Nano* **2016**, *10*, 4248–4257.

(14) Ventosa, E.; Schuhmann, W. Scanning Electrochemical Microscopy of Li-Ion Batteries. *Phys. Chem. Chem. Phys.* **2015**, *17*, 28441–28450.

(15) Schwager, P.; Bülter, H.; Plettenberg, I.; Wittstock, G. Review of Local in Situ Probing Techniques for the Interfaces of Lithium-Ion and Lithium-Oxygen Batteries. *Energy Technol.* **2016**, *4*, 1472–1485.

(16) Barton, Z. J.; Rodríguez-López, J. Emerging Scanning Probe Approaches to the Measurement of Ionic Reactivity at Energy Storage Materials. *Anal. Bioanal. Chem.* **2016**, *408*, 2707–2715.

(17) Danis, L.; Gateman, S. M.; Kuss, C.; Schougaard, S. B.; Mauzeroll, J. Nanoscale Measurements of Lithium-Ion-Battery Materials Using Scanning Probe Techniques. *ChemElectroChem* **2016**, *4*, 6–19.

(18) Barton, Z. J.; Rodríguez-López, J. Cyclic Voltammetry Probe Approach Curves with Alkali Amalgams at Mercury Sphere-Cap Scanning Electrochemical Microscopy Probes. *Anal. Chem.* **2017**, *89*, 2708–2715.

(19) Velmurugan, J.; Mirkin, M. V. Fabrication of Nanoelectrodes and Metal Clusters by Electrodeposition. *ChemPhysChem* **2010**, *11*, 3011–3017.

(20) Danis, L.; Polcari, D.; Kwan, A.; Gateman, S. M.; Mauzeroll, J. Fabrication of Carbon, Gold,

Platinum, Silver, and Mercury Ultramicroelectrodes with Controlled Geometry. *Anal. Chem.* **2015**, *87*, 2565–2569.

(21) Barton, Z. J.; Rodríguez-López, J. Fabrication and Demonstration of Mercury Disc-Well Probes for Stripping-Based Cyclic Voltammetry Scanning Electrochemical Microscopy. *Anal. Chem.* **2017**, *89*, 2716–2723.

(22) Hills, G. J.; Peter, L. M. Electrode Kinetics in Aprotic Media. *J. Electroanal. Chem. Interfacial Electrochem.* **1974**, *50*, 175–185.

(23) Koper, M. T. M.; Schmickler, W. A Theory for Amalgam Forming Electrode Reactions. *J. Electroanal. Chem.* **1998**, *450*, 83–94.

(24) Burgess, M.; Hernández-Burgos, K.; Cheng, K. J.; Moore, J. S.; Rodríguez-López, J. Impact of Electrolyte Composition on the Reactivity of a Redox Active Polymer Studied Through Surface Interrogation and Ion-Sensitive Scanning Electrochemical Microscopy. *Analyst* **2016**, *141*, 3842–3850.

(25) Ferrari, A. C.; Robertson, J. Interpretation of Raman Spectra of Disordered and Amorphous Carbon. *Phys. Rev. B* **2000**, *61*, 14095–14107.

(26) Yamada, Y.; Miyazaki, K.; Abe, T. Role of Edge Orientation in Kinetics of Electrochemical Intercalation of Lithium-Ion at Graphite. *Langmuir* **2010**, *26*, 14990–14994.

(27) Aurbach, D. Review of Selected Electrode–Solution Interactions Which Determine the Performance of Li and Li Ion Batteries. *J. Pow. Sour.* **2000**, *89*, 206–218.

(28) Norberg, N. S.; Lux, S. F.; Kostecki, R. Interfacial Side-Reactions at a $LiNi_{0.5}Mn_{1.5}O_4$ Electrode in Organic Carbonate-Based Electrolytes. *Electrochem. Commun.* **2013**, *34*, 29–32.

(29) Kuss, S.; Trinh, D.; Danis, L.; Mauzeroll, J. High-Speed Scanning Electrochemical Microscopy

Method for Substrate Kinetic Determination: Method and Theory. *Anal. Chem.* **2015**, *87*, 8096–8101.

(30) Patel, A. N.; Collignon, M. G.; O'Connell, M. A.; Hung, W. O. Y.; McKelvey, K.; Macpherson, J. V.; Unwin, P. R. A New View of Electrochemistry at Highly Oriented Pyrolytic Graphite. *J. Amer. Chem. Soc.* **2012**, *134*, 20117–20130.

(31) Nioradze, N.; Chen, R.; Kurapati, N.; Khvataeva-Domanov, A.; Mabic, S.; Amemiya, S. Organic Contamination of Highly Oriented Pyrolytic Graphite as Studied by Scanning Electrochemical Microscopy. *Anal. Chem.* **2015**, *87*, 4836–4843.

(32) Tan, C.; Rodríguez-López, J.; Parks, J. J.; Ritzert, N. L.; Ralph, D. C.; Abercrombie, S. Reactivity of Monolayer Chemical Vapor Deposited Graphene Imperfections Studied Using Scanning Electrochemical Microscopy. *ACS Nano* **2012**, *6*, 3070–3079.

(33) Zhong, J.-H.; Zhang, J.; Jin, X.; Liu, J.-Y.; Li, Q.; Li, M.-H.; Cai, W.; Wu, D.-Y.; Zhan, D.; Ren, B. Quantitative Correlation Between Defect Density and Heterogeneous Electron Transfer Rate of Single Layer Graphene. *J. Amer. Chem. Soc.* **2014**, *136*, 16609–16617.

(34) Unwin, P. R.; Güell, A. G.; Zhang, G. Nanoscale Electrochemistry of Sp^2 Carbon Materials: From Graphite and Graphene to Carbon Nanotubes. *Acc. Chem. Res.* **2016**, *49*, 2041–2048.

(35) Hui, J.; Zhou, X.; Bhargava, R.; Chinderle, A.; Zhang, J.; Rodríguez-López, J. Kinetic Modulation of Outer-Sphere Electron Transfer Reactions on Graphene Electrode with a Sub-Surface Metal Substrate. *Electrochim. Acta* **2016**, *211*, 1016–1023.

(36) Molina, A.; González, J.; Henstridge, M. C.; Compton, R. G. Analytical Expressions for Transient Diffusion Layer Thicknesses at Non Uniformly Accessible Electrodes. *Electrochim. Acta* **2011**, *56*, 4589–4594.

(37) Trinh, D.; Maisonhaute, E.; Vivier, V. Electrical Cross-Talk in Transient Mode of Scanning

Electrochemical Microscopy. *Electrochem. Commun.* **2012**, *16*, 49–52.

(38) Kim, H.; Yoon, G.; Lim, K.; Kang, K. A Comparative Study of Graphite Electrodes Using the Co-Intercalation Phenomenon for Rechargeable Li, Na and K Batteries. *Chem. Commun.* **2016**, *52*, 12618–12621.

(39) Ri, G.-C.; Yu, C.-J.; Kim, J.-S.; Hong, S.-N.; Jong, U.-G.; Ri, M.-H. First-Principles Study of Ternary Graphite Compounds Cointercalated with Alkali Atoms (Li, Na, and K) and Alkylamines Towards Alkali Ion Battery Applications. *J. Pow. Sour.* **2016**, *324*, 758–765.

(40) Cohn, A. P.; Muralidharan, N.; Carter, R.; Share, K.; Oakes, L.; Pint, C. L. Durable Potassium Ion Battery Electrodes From High-Rate Cointercalation Into Graphitic Carbons. *J. Mater. Chem. A* **2016**, *4*, 14954–14959.

CHAPTER 7

Ongoing Work and Future Prospects

This chapter contains as yet unpublished data obtained in collaboration with Jingshu Hui, Zachary T. Gossage, Matthew L. Kromer, and Michael J. Counihan under the direction of Prof. Joaquín Rodríguez-López at the University of Illinois. Jingshu Hui provided exfoliated HOPG samples coated with Parylene C for section 7.4. Zachary T. Gossage performed cyclic voltammetry of vanadium oxide particles and related substrates in section 7.5. Matthew L. Kromer sintered vanadium oxide particles and characterized them through X-ray diffraction (XRD) for section 7.5. Michael J. Counihan performed electron beam physical vapor deposition (EBPVD) to provide Pt films on which to dropcast the vanadium oxide particles for section 7.5.

7.1 Abstract

The tools and strategies resulting from this research effort allow direct, unambiguous quantification of ionic fluxes in non-aqueous systems. These developments are continuing to open new avenues of inquiry for energy storage materials and may be adapted to bear fruit in other areas of electrochemical research as well.

7.2 Introduction

This body of work has pioneered Hg-based SECM of alkali ions and produced time-resolved SECM techniques, mathematical tools for extracting meaningful information from these techniques, and a reproducible protocol for fabricating a novel electrochemical sensor.[1-3] These electroanalytical tools have already found application in the detection of K^+ uptake at HOPG,[4] and presently unpublished work extends to Na^+ and K^+ uptake over partially insulated HOPG as well as Li^+ uptake over vanadium oxide particles.

7.3 Spatial Resolution

CV-SECM methods are facilitating further experiments at energy storage interfaces. A recent example of Hg-based positioning over activated highly oriented pyrolytic graphite (HOPG) is provided as Figure 7.1. In brief, a Hg disc-well UME (a_1 = 12.6 μm, R_G = 2.4, H_2 = 1.0) was connected as the primary working electrode in a cell containing 1 mM TMPD, 1 mM $NaClO_4$, and 0.5 M NBu_4ClO_4 in PC. The secondary working electrode was a exfoliated HOPG sample, and a Pt wire and Ag wire fulfilled the roles of counter electrode and quasi-reference electrode, respectively. The probe was first approached to L_f = 0.610 ± 0.001 at 0.24 μm s^{-1} (40 nm per 166.7 ms) while poised at E_{tip} = +0.4 V (*vs.* Ag QRE) to continuously oxidize TMPD over un-insulated HOPG poised at E_{sub} = -0.3 V (*vs.* Ag QRE) to regenerate TMPD from its oxidized state. The probe was then retracted 150 μm and made to execute a CV-PSS in Z at T_{amal} = 8.0 ± 0.4 ($T_{amal} = D_{M+}\eta/(a_1^2\nu)$ with $D_{M+} = 2.0 \times 10^{-10}$ m^2 s^{-1},[5] η = 0.64 V, a_1 = 12.6 μm, and ν = 0.1 V s^{-1}), ending 2 μm closer to the substrate than before at L_f = 0.451. Importantly, the Hg-based amalgamation and stripping signals exhibit pure negative feedback despite positive feedback of an organic redox mediator. Combined with the controlled diffusional timescale of CV-based SECM methods, this fact enables precise and accurate probe positioning without any *a priori* knowledge of surface chemistry. Because scanned probe signals are distance-dependent, this new ability is essential for ongoing and future studies of energy storage materials, since the electronic properties and spatial dimensions of the SEI fluctuate during battery cycling.

7.4 Ionic Resolution

In addition to improving the spatial resolution and chemical versatility of Hg-based SECM probes, CV-SECM methods are being used to monitor changing ionic fluxes with chemical specificity. Our recent paper[4] showed that only the amalgamation signal is usable in CV-SECM data taken with the

substrate activated to intercalate alkali ions in dilute conditions without supporting electrolyte. Additionally, we found that the basal plane of HOPG is not innocent under activation for K^+ insertion, so differences in reactivity can be obscured or conflated with changes in topography under such conditions. Therefore, recent work has been done to establish measurements of distance, electronic reactivity, and ionic activity over partially insulated HOPG, which offers more clearly defined regions of low and high ionic uptake than bare HOPG does.

A CV-SECM experiment monitoring K^+ insertion over partially insulated HOPG with high ionic strength is provided in Figure 7.2. These preliminary results demonstrate spatial agreement between co-localized measurements of electronic and ionic reactivity over a model carbon anode material. Furthermore, stationary point measurements of the potential-dependent uptake of K^+ at the substrate demonstrate greater change in ionic flux with the Hg probe positioned over a known electronically conducting region than over a known insulating region. The consistent substrate response to activation supports the hypothesis that K^+ may insert reversibly into HOPG under the tested conditions. CV-SECM performed with Hg-based probes accesses this ionic information directly and quantitatively. The removal of ambiguity is a powerful asset when conclusions must otherwise be reached by indirect, inconclusive postulation.

7.5 Future Electrode Material Candidates

The sensing platform of Hg-based probes and associated time-resolved SECM measurement strategies will continue to prove their worth as new material candidates emerge in the search for better Li-ion batteries and viable Na-ion or K-ion batteries.[6,7] In the negative side, synergistic effects may allow layered materials to escape the present dominance of carbon anodes.[8] In the positive side, we have begun working with readily accessible materials, such as vanadium-based particles annealed on an indium tin oxide (ITO) support (Figure 7.3A). Our initial studies of these particles may have unintentionally

benefitted from crystalline phase stabilization by titanium doping of the vanadium oxide lattice,[9] so we have also tried supporting the vanadium-based particles on Pt films deposited on silicon wafer (Figure 7.3B). Vanadium is not a particularly promising material for consumer energy storage applications, however, so we are also considering new materials, such as Prussian blue inks, which have recently garnered interest as dimensionally stable cathodes for Na-ion and K-ion batteries.[10,11]

7.6 Future Analytical Developments

Myriad opportunities lie ahead for Hg-based probes and CV-SECM. Perhaps the soonest development will be to capitalize on *in situ* Raman spectroscopy and imaging methods. Raman spectroscopy has only recently been applied as an *in situ* tool for studying surface chemistry and ion insertion dynamics,[12-19] so the possibility of hyphenating it with other techniques during battery operation is only now becoming a reality. Considering the case of graphitic anode materials, the combination of hyperspectral CV-SECM data with spatially resolved Raman maps of D, G, and 2D peak positions, intensities, and intensity ratios could reveal new connections between redox reactivity, ionic flux, and the interfacial electronic structure at a scale that is relevant to the heterogeneities driving battery operation.[20-22]

In addition to addressing questions in energy storage, Hg-based probes and CV-SECM experiments may also aid scanning probe studies of metal and mineral corrosion processes[23-30] or biological systems[31-36] through the addition of ionically specific information. Though biofouling and parasitic corrosion processes often present insuperable barriers to chemical sensors in these environments, Hg-based probes afford unique strategies to circumvent compromising phenomena. One possibility is to fabricate a theta-barrel pipette, making a Hg disc-well in one barrel and a fluorous electrolyte phase in the other. Measurements of distance and ionic reactivity could then be handled by the Hg side while measurements of redox activity could be carried out through the electron-transfer/ion-transfer mode of

SECM.[37] Having an immiscible liquid phase may also enable single-particle titration experiments in which a discrete amount of Li^+ (or other ion) is introduced from liquid-containing side and the fraction taken up and later released by an active particle quantified by the Hg disc-well side in a manner similar to previously published methods in electrocatalysis.[38] Titrations of various particle sizes and compositions may unmask new relationships between phase transitions and domain sizes. These and other hybrid experimental designs are imminently possible and offer new roads to understanding key steps in concerted electron transfer and ion transfer processes.

Hg-based CV-SECM excels in obtaining ion-specific information at surfaces generating fluxes of metal ions. This has been leveraged to isolate contributions to the formation and aging of the SEI from the overall response of an operating battery electrode as well as to study potential-dependent ionic reactivity of local hot spots. The probes and strategies pioneered by this research effort have already made paths to new insights and hold the potential to revolutionize the electoanalytical toolbox for addressing fundamental questions at operating energy storage material interfaces.

7.7 Figures

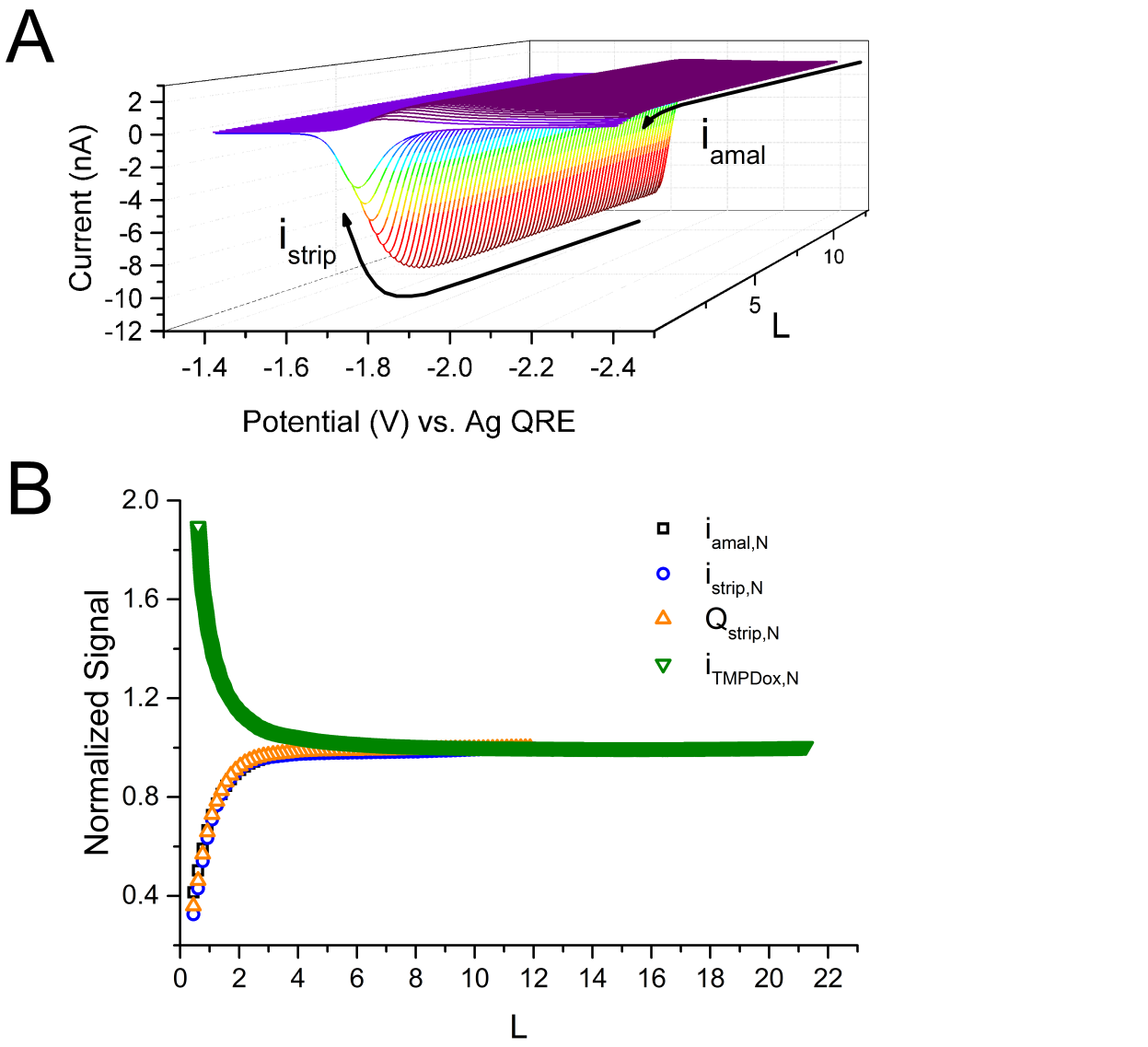

Figure 7.1. Cyclic voltammetry probe scan surfaces (CV-PSSs) allow precise and accurate SECM probe positioning over any substrate, even if the electronic reactivity of the substrate interface fluctuates. (**A**) A Na(Hg) CV-PSS taken with a Hg disc-well UME (a_1 = 12.6 µm, R_G = 2.4, H_2 = 1.0) at T_{amal} = 8.0 ± 0.4 provides pure negative feedback over electrified HOPG. L_f = 0.451. (**B**) The extracted cyclic voltammetry probe scan curves (CV-PSSs) are free from kinetic complications, convective distortions, and parasitic side-reactions. A potentiostatic probe scan curve (PSC) based on TMPD oxidation at the SECM probe exhibits positive feedback, which is not ideal for positioning, especially when the substrate's surface reactivity is neither homogeneous nor static. The cell contains 1 mM TMPD, 1 mM $NaClO_4$, and 0.5 M NBu_4ClO_4 in PC.

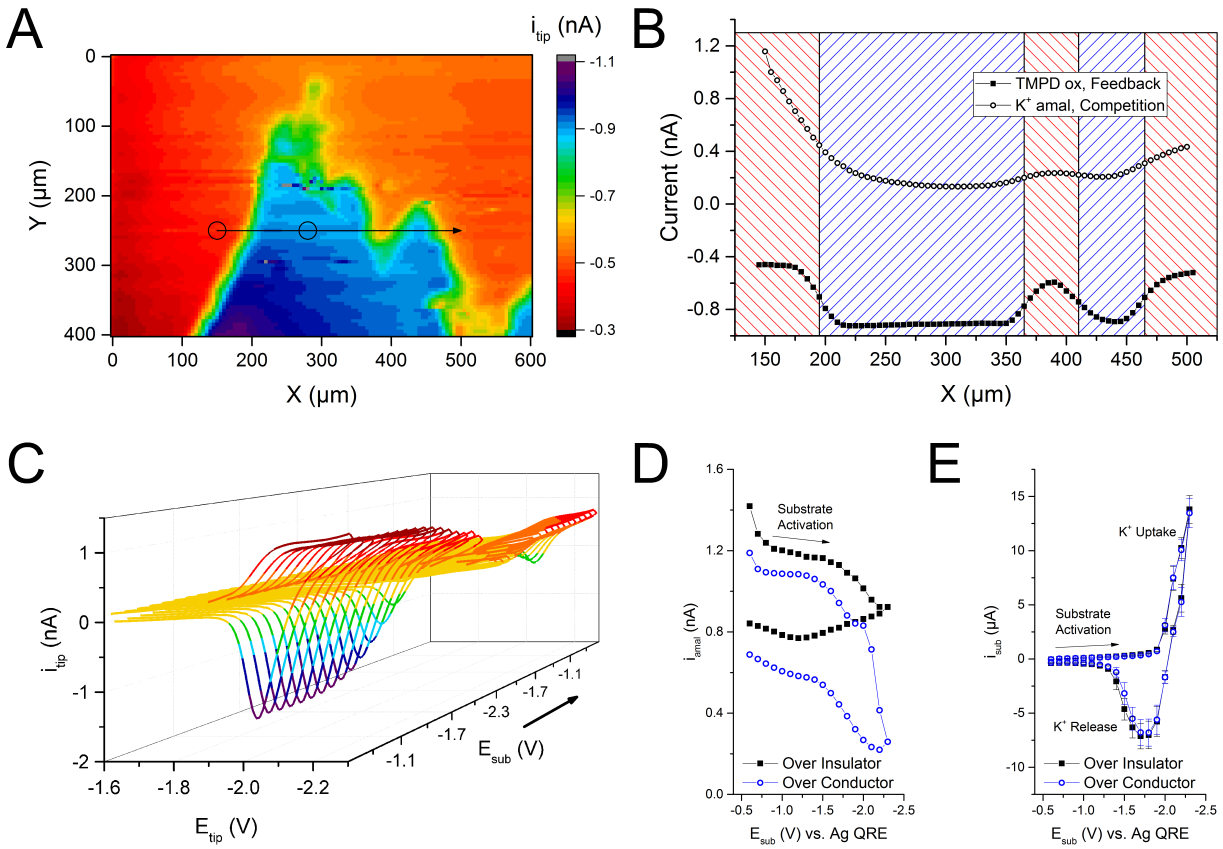

Figure 7.2. CV-SECM resolves differences in ionic reactivity with chemical specificity. (**A**) A potentiostatic map of electronic conductivity over HOPG partially insulated by Parylene C. The map was acquired by a Hg disc-well UME (a_1 = 12.5 μm, R_G = 3.1, H_2 = 0.4) operating in the feedback mode (E_{tip} = +0.4 V and E_{sub} = -0.6 V) while rastering in +X at 100 μm s^{-1} (5 μm per 50 ms). L_f ~ 0.6. (**B**) Amalgamation current at a Hg disc-well competing for K^+ (ν = 0.2 V s^{-1}) over an HOPG anode (E_{sub} = -2.2 V) partially insulated with a coating of Parylene C. The studied region is indicated by a black arrow in panel **A**. The corresponding TMPD oxidation signal is extracted from panel **A** and presented as filled squares. The initial decrease in amalgamation current is tied not only to changes in local reactivity but also to the timescale of the substrate establishing a stable concentration gradient. Insulating Parylene C and conductive HOPG regions are indicated by red declining diagonals and blue inclining diagonals, respectively. (**C**) Probe CV response during a triangular staircase sweep of E_{sub} while positioned over a region of exposed HOPG at [X, Y] = [280 μm, 250 μm], as indicated in panel **A**. The amalgamation and stripping signals do not recover fully due to the slower timescale of K^+ deinsertion in the tested system. (**D**) The K^+ amalgamation currents extracted from identical tests performed at [X, Y] = [150 μm, 250 μm] and [X, Y] = [280 μm, 250 μm], indicated by black circles in panel **A**, demonstrate a greater local decrease in K^+ concentration over HOPG than over insulating Parylene C. (**E**) The average substrate current during triangular staircase potential sweeps is consistent over time, indicating chemical reversibility and suggesting no substantial surface degradation. The cell contains 0.5 mM TMPD, 0.5 mM $KClO_4$, and 0.5 M NBu_4ClO_4 in PC. All potentials are given *vs.* Ag QRE.

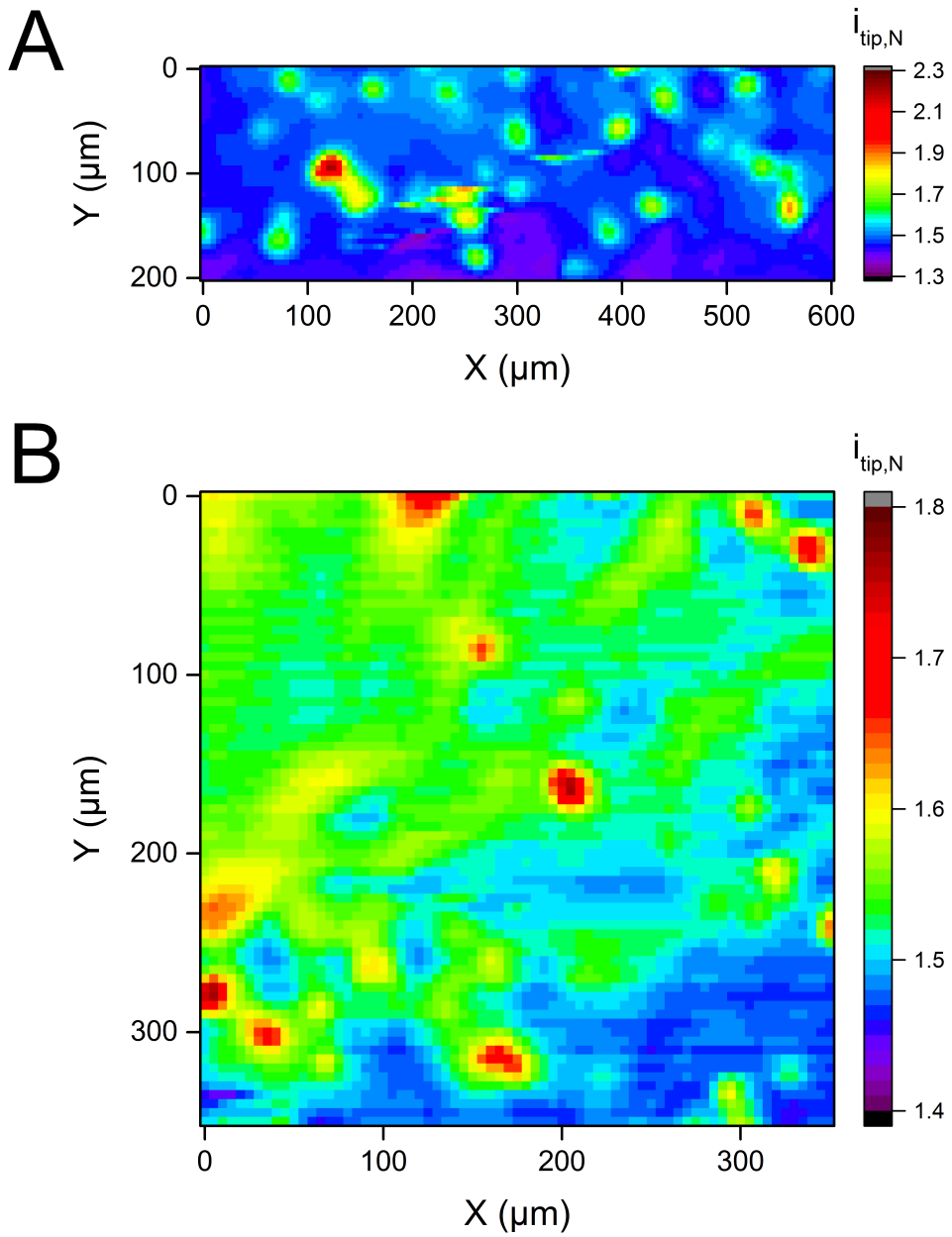

Figure 7.3. (**A**) A potentiostatic map of electronic conductivity over vanadium oxide particles supported on indium tin oxide (ITO). The map was acquired by a Hg disc-well (a_1 = 12.55 µm, R_G = 3.7, H_2 = 0.7) operating in the feedback mode (E_{tip} = +0.3 V, E_{sub} = -0.6 V) while rastering in +X at 50 µm s^{-1} (5 µm per 100 ms). The probe current has been normalized by its value under steady-state conditions in bulk solution: -1.253 nA. L_f = 0.6740 ± 0.0001. The cell contains 1 mM TMPD, 1 mM $LiClO_4$, and 0.5 M NBu_4ClO_4 in PC. (**B**) A potentiostatic map of electronic conductivity over vanadium oxide particles supported on Pt. The map was acquired by a Hg disc-well (a_1 = 12.5 µm, R_G = 3.7, H_2 = 0.6) operating in the feedback mode (E_{tip} = +0.4 V, E_{sub} = -0.4 V) while rastering in +X at 100 µm s^{-1} (5 µm per 50 ms). The probe current has been normalized by its value under steady-state conditions in bulk solution: -1.59639 nA. L_f = 0.532 ± 0.002. The cell contains 1 mM TMPD, 1 mM $LiClO_4$, and 0.5 M NBu_4ClO_4 in PC:EC (1:1 vol.). All potentials are given *vs.* Ag QRE.

7.8 References

(1) Barton, Z. J.; Rodríguez-López, J. Lithium Ion Quantification Using Mercury Amalgams as *In Situ* Electrochemical Probes in Nonaqueous Media. *Anal. Chem.* **2014**, *86*, 10660–10667.

(2) Barton, Z. J.; Rodríguez-López, J. Cyclic Voltammetry Probe Approach Curves with Alkali Amalgams at Mercury Sphere-Cap Scanning Electrochemical Microscopy Probes. *Anal. Chem.* **2017**, *89*, 2708–2715.

(3) Barton, Z. J.; Rodríguez-López, J. Fabrication and Demonstration of Mercury Disc-Well Probes for Stripping-Based Cyclic Voltammetry Scanning Electrochemical Microscopy. *Anal. Chem.* **2017**, *89*, 2716–2723.

(4) Barton, Z. J.; Hui, J.; Schorr, N. B.; Rodríguez-López, J. Detecting Potassium Ion Gradients at a Model Graphitic Interface. *Electrochim. Acta* **2017**, *241*, 98–105.

(5) Hills, G. J.; Peter, L. M. Electrode Kinetics in Aprotic Media. *J. Electroanal. Chem. Interfacial Electrochem.* **1974**, *50*, 175–185.

(6) Zhao, Y.; Wang, L. P.; Sougrati, M. T.; Feng, Z.; Leconte, Y.; Fisher, A.; Srinivasan, M.; Xu, Z. A Review on Design Strategies for Carbon Based Metal Oxides and Sulfides Nanocomposites for High Performance Li and Na Ion Battery Anodes. *Adv. Energy Mater.* **2016**, *451*, 1601424–1601470.

(7) Cui, J.; Yao, S.; Kim, J.-K. Recent Progress in Rational Design of Anode Materials for High-Performance Na-Ion Batteries. *Energy Storage Materials* **2017**, *7*, 64–114.

(8) Subramaniyam, C. M.; Deshmukh, K. A.; Tai, Z.; Mahmood, N.; Deshmukh, A. D.; Goodenough, J. B.; Dou, S. X.; Liu, H. K. 2D Layered Graphitic Carbon Nitride Sandwiched with Reduced Graphene Oxide as Nanoarchitectured Anode for Highly Stable Lithium-Ion Battery. *Electrochim. Acta* **2017**, *237*, 69–77.

(9) Armer, C. F.; Lübke, M.; Reddy, M. V.; Darr, J. A.; Li, X.; Lowe, A. Phase Change Effect on the Structural and Electrochemical Behaviour of Pure and Doped Vanadium Pentoxide as Positive Electrodes for Lithium Ion Batteries. *J. Pow. Sour.* **2017**, *353*, 40–50.

(10) Lu, Y.; Wang, L.; Cheng, J.; Goodenough, J. B. Prussian Blue: a New Framework of Electrode Materials for Sodium Batteries. *Chem. Commun.* **2012**, *48*, 6544–3.

(11) Xiao, P.; Song, J.; Wang, L.; Goodenough, J. B.; Henkelman, G. Theoretical Study of the Structural Evolution of a $Na_2FeMn(CN)_6$ Cathode Upon Na Intercalation. *Chem. Mater.* **2015**, *27*, 3763–3768.

(12) Lei, J.; McLarnon, F.; Kostecki, R. In Situ Raman Microscopy of Individual $LiNi_{0.8}Co_{0.15}Al_{0.05}O_2$ Particles in a Li-Ion Battery Composite Cathode. *J. Phys. Chem. B* **2005**, *109*, 952–957.

(13) Baddour-Hadjean, R.; Pereira-Ramos, J.-P. Raman Microspectrometry Applied to the Study of Electrode Materials for Lithium Batteries. *Chem. Rev.* **2010**, *110*, 1278–1319.

(14) Nanda, J.; Remillard, J.; O'Neill, A.; Bernardi, D.; Ro, T.; Nietering, K. E.; Go, J.-Y.; Miller, T. J. Local State-of-Charge Mapping of Lithium-Ion Battery Electrodes. *Adv. Funct. Mater.* **2011**, *21*, 3282–3290.

(15) Sole, C.; Drewett, N. E.; Hardwick, L. J. *In Situ* Raman Study of Lithium-Ion Intercalation Into Microcrystalline Graphite. *Faraday Discuss.* **2014**, *172*, 223–237.

(16) Share, K.; Cohn, A. P.; Carter, R. E.; Pint, C. L. Mechanism of Potassium Ion Intercalation Staging in Few Layered Graphene From in Situ Raman Spectroscopy. *Nanoscale* **2016**, *8*, 16435–16439.

(17) Cohn, A. P.; Muralidharan, N.; Carter, R.; Share, K.; Oakes, L.; Pint, C. L. Durable Potassium

Ion Battery Electrodes From High-Rate Cointercalation Into Graphitic Carbons. *J. Mater. Chem. A* **2016**, *4*, 14954–14959.

(18) Zou, J.; Sole, C.; Drewett, N. E.; Velický, M.; Hardwick, L. J. In Situ Study of Li Intercalation Into Highly Crystalline Graphitic Flakes of Varying Thicknesses. *J. Phys. Chem. Lett.* **2016**, *7*, 4291–4296.

(19) Fang, S.; Yan, M.; Hamers, R. J. Cell Design and Image Analysis for in Situ Raman Mapping of Inhomogeneous State-of-Charge Profiles in Lithium-Ion Batteries. *J. Pow. Sour.* **2017**, *352*, 18–25.

(20) Das, A.; Pisana, S.; Chakraborty, B.; Piscanec, S.; Saha, S. K.; Waghmare, U. V.; Novoselov, K. S.; Krishnamurthy, H. R.; Geim, A. K.; Ferrari, A. C.; Sood, A. K. Monitoring Dopants by Raman Scattering in an Electrochemically Top-Gated Graphene Transistor. *Nat. Nanotechnol.* **2008**, *3*, 210–215.

(21) Harris, S. J.; Lu, P. Effects of Inhomogeneities—Nanoscale to Mesoscale—on the Durability of Li-Ion Batteries. *J. Phys. Chem. C* **2013**, *117*, 6481–6492.

(22) Etienne, M.; Dossot, M.; Grausem, J.; Herzog, G. Combined Raman Microspectrometer and Shearforce Regulated SECM for Corrosion and Self-Healing Analysis. *Anal. Chem.* **2014**, *86*, 11203–11210.

(23) Macpherson, J. V.; Unwin, P. R.; Hillier, A. C.; Bard, A. J. In-Situ Imaging of Ionic Crystal Dissolution Using an Integrated Electrochemical/AFM Probe. *J. Amer. Chem. Soc.* **1996**, *118*, 6445–6452.

(24) Pust, S. E.; Maier, W.; Wittstock, G. Investigation of Localized Catalytic and Electrocatalytic Processes and Corrosion Reactions with Scanning Electrochemical Microscopy (SECM). *Z. Phys. Chem.* **2008**, *222*, 1463–1517.

(25) Santana, J. J.; Pähler, M.; Schuhmann, W.; Souto, R. M. Investigation of Copper Corrosion Inhibition with Frequency-Dependent Alternating-Current Scanning Electrochemical Microscopy. *ChemPlusChem* **2012**, *77*, 707–712.

(26) Peruffo, M.; Mbogoro, M. M.; Edwards, M. A.; Unwin, P. R. Holistic Approach to Dissolution Kinetics: Linking Direction-Specific Microscopic Fluxes, Local Mass Transport Effects and Global Macroscopic Rates From Gypsum Etch Pit Analysis. *Phys. Chem. Chem. Phys.* **2013**, *15*, 1956–1965.

(27) Kuznetsov, V.; Maljusch, A.; Souto, R. M.; Bandarenka, A. S.; Schuhmann, W. Characterisation of Localised Corrosion Processes Using Scanning Electrochemical Impedance Microscopy. *Electrochem. Commun.* **2014**, *44*, 38–41.

(28) Dauphin-Ducharme, P.; Asmussen, R. M.; Shoesmith, D. W.; Mauzeroll, J. *In-Situ* Mg^{2+} Release Monitored During Magnesium Alloy Corrosion. *J. Electroanal. Chem.* **2015**, *736*, 61–68.

(29) Danis, L.; Gateman, S. M.; Snowden, M. E.; Halalay, I. C.; Howe, J. Y.; Mauzeroll, J. Anodic Stripping Voltammetry at Nanoelectrodes: Trapping of Mn^{2+} By Crown Ethers. *Electrochim. Acta* **2015**, *162*, 169–175.

(30) Bülter, H.; Denuault, G.; Mátéfi-Tempfli, S.; Mátéfi-Tempfli, M.; Dosche, C.; Wittstock, G. Electrochemical Analysis of Nanostructured Iron Oxides Using Cyclic Voltammetry and Scanning Electrochemical Microscopy. *Electrochim. Acta* **2016**, *222*, 1326–1334.

(31) Scott, E. R.; White, H. S.; Phipps, J. B. Iontophoretic Transport Through Porous Membranes Using Scanning Electrochemical Microscopy: Application to in Vitro Studies of Ion Fluxes Through Skin. *Anal. Chem.* **1993**, *65*, 1537–1545.

(32) Novak, P.; Li, C.; Shevchuk, A. I.; Stepanyan, R.; Caldwell, M.; Hughes, S.; Smart, T. G.; Gorelik, J.; Ostanin, V. P.; Lab, M. J.; Moss, G. W. J.; Frolenkov, G. I.; Klenerman, D.; Korchev,

Y. E. Nanoscale Live-Cell Imaging Using Hopping Probe Ion Conductance Microscopy. *Nat. Methods* **2009**, *6*, 279–281.

(33) Shen, M.; Ishimatsu, R.; Kim, J.; Amemiya, S. Quantitative Imaging of Ion Transport Through Single Nanopores by High-Resolution Scanning Electrochemical Microscopy. *J. Amer. Chem. Soc.* **2012**, *134*, 9856–9859.

(34) Chen, C.-C.; Zhou, Y.; Morris, C. A.; Hou, J.; Baker, L. A. Scanning Ion Conductance Microscopy Measurement of Paracellular Channel Conductance in Tight Junctions. *Anal. Chem.* **2013**, *85*, 3621–3628.

(35) Yamada, H.; Haraguchi, D.; Yasunaga, K. Fabrication and Characterization of a K^+-Selective Nanoelectrode and Simultaneous Imaging of Topography and Local K^+ Flux Using Scanning Electrochemical Microscopy. *Anal. Chem.* **2014**, *86*, 8547–8552.

(36) Perry, D.; Paulose Nadappuram, B.; Momotenko, D.; Voyias, P. D.; Page, A.; Tripathi, G.; Frenguelli, B. G.; Unwin, P. R. Surface Charge Visualization at Viable Living Cells. *J. Amer. Chem. Soc.* **2016**, *138*, 3152–3160.

(37) Oleinick, A.; Yu, Y.; Svir, I.; Mirkin, M. V.; Amatore, C. Theory and Simulations for the Electron-Transfer/Ion-Transfer Mode of Scanning Electrochemical Microscopy in the Presence or Absence of Homogenous Kinetics. *ChemElectroChem* **2016**, *4*, 287–295.

(38) Lin, C.-L.; Rodríguez-López, J.; Bard, A. J. Micropipet Delivery–Substrate Collection Mode of Scanning Electrochemical Microscopy for the Imaging of Electrochemical Reactions and the Screening of Methanol Oxidation Electrocatalysts. *Anal. Chem.* **2009**, *81*, 8868–8877.

APPENDIX A

COMSOL Multiphysics Model Summary

A.1 Global Definitions

Salient global parameters are provided in Table A.1. These include distances defined in terms of the electrode radius for defining domains and boundaries in a flexible way, experimentally adjustable electrochemical parameters, diffusion coefficients and heterogeneous rate constants, and forward and reverse rates assuming the Butler–Volmer formalism of electron-transfer kinetics. Cyclic voltammograms are executed through a globally defined piecewise function:

$$E_{app} = pw1(t) = \begin{cases} E_{ox} - \nu t, & 0 < t \leq t_{sw} \\ E_{ox} - 2\nu t_{sw} + \nu t, & t_{sw} < t \leq 2t_{sw} \end{cases} \quad (1)$$

The piecewise function is defined with periodic (rather than constant) extrapolation to prevent discontinuities. The electrochemical response to this applied potential is defined with the Butler–Volmer formalism of electron-transfer kinetics:

$$k_f = k^o \exp\left(-\alpha n f\left(E_{app} - E^o\right)\right) \quad (2)$$

$$k_b = k^o \exp\left((1-\alpha) n f\left(E_{app} - E^o\right)\right) \quad (3)$$

A.2 Geometry

A 2-dimensional axisymmetric geometry is built for Hg sphere-caps (Figure A.1A) or for Hg disc-wells (Figure A.1B) with distances defined in the global parameters.

A.3 Physics

A.3.1 Two Nodes

A unique physics node describing the transport of diluted species is defined for each of the two domains. In both domains, deactivating convection and electric field effects leads to mass transport being governed by diffusion:

$$\frac{\partial c_i}{\partial t} + \nabla \cdot (-D_i \nabla c_i) = R_i \quad (4)$$

$$\mathbf{N}_i = -D_i \nabla c_i \quad (5)$$

Using two separate physics nodes allows the user to define oxidized species (i = Na^+, K^+, Li^+) only in the solution domain and reduced species (i = Na(Hg), K(Hg), Li(Hg)) only in the Hg domain. The alternative is to define a single shared physics node for both domains, which then requires the assignment of non-zero diffusion coefficients for insoluble species—oxidized species in the Hg domain and reduced species in the solution domain. This leads to a buildup of oxidized species at mesh points inside the Hg domain and adjacent to the Hg–solution interface, which distorts the calculated current and does not reflect reality. This issue is avoided by defining two separate physics nodes.

A.3.2 Solution Domain Boundaries

Zero-flux conditions are defined at the glass–solution interface around the probe body:

$$-\boldsymbol{n} \cdot \boldsymbol{N}_i = -D_i \nabla c_i \quad (6)$$

Open boundary conditions are defined at the limits of the simulated solution volume:

$$\begin{cases} -n \cdot D_i \nabla c_i = 0, & \mathbf{n} \cdot \mathbf{u} \geq 0 \\ c_i = c_{0,i}, & \mathbf{n} \cdot \mathbf{u} < 0 \end{cases} \quad (7)$$

The uppermost solution domain boundary (opposite the Hg-based probe) is designated either as an open boundary to simulate conditions in bulk solution or as a zero-flux boundary to simulate a stripping-based approach to a substrate. Lastly, a general inward flux is defined at the Hg–solution interface:

$$-\boldsymbol{n} \cdot \mathbf{N}_i = N_{0,i} \quad (8)$$

$$N_{0,ox} = -k_f n_{ox} + k_b n_{red} \quad (9)$$

A.3.3 Hg Domain Boundaries

Zero-flux conditions are defined at the glass–Hg interface:

$$-\boldsymbol{n} \cdot \boldsymbol{N}_i = -D_i \nabla c_i \quad (10)$$

A general inward flux is defined at the Hg–solution interface:

$$-\boldsymbol{n} \cdot \mathbf{N}_i = N_{0,i} \tag{11}$$

$$N_{0,red} = -\left(-k_f n_{ox} + k_b n_{red}\right) \tag{12}$$

A.4 Mesh

Both domains share a free triangular mesh with maximum element size of 50 μm, minimum element size of 100 pm, curvature factor of 0.3, a resolution of 5 for narrow regions, and a maximum element growth rate of 1.3. This mesh is modified by an advancing front distribution with 420 elements defined at the Hg–solution interface and a single domain refinement for the Hg domain (Figure A.2). These refinements of the mesh increase the required computation time but are essential for accurately capturing sudden changes in ionic flux during anodic stripping voltammetry.

A.5 Probes

The applied potential is recorded by a global variable probe of E_{app}. The internal concentration of reduced metal species is monitored by a domain probe of *red* in the Hg domain. The surface concentration of metal ions is obtained by a boundary probe of *ox* at Hg–solution interface. The current registered at the Hg-based electrode is calculated by a boundary probe at the Hg–solution interface:

$$i = 2\pi r F \cdot (\text{chds. bndFlux\_ox}) \tag{13}$$

A.6 Study

A time-dependent study is solved by PARDISO for $0 \le t \le 2 \cdot t_{sw}$ with a timestep of t_{int}. The 2-dimensional concentration plot and all probe plots are set to update with each completed timestep while solving (Figure A.3). Within the study, nested parametric sweeps of initial bulk ion concentrations, potential scan rate, tip–substrate gap size, probe dimensions, and other parameters enable rapid testing of a wide variety of conditions without the need for further user input while solving.

A.6 Data Export

Probe data for each solution is cleared from the report table before the next run. This data may be saved by including an Export Table node under the Job node, but this node does not exist until the simulation has been run at least once.

A.7 Figures and Table

Name	Expression	Description
r1	12.5e-6 [m]	Hg drop basal radius
r2	3*r1	Total tip radius
h1	1*r1	Hg cap height
h2	1.2*r1	Depth of Hg well
area	pi*(r1^2 + h1^2)	Surface area of Hg
reff	area/(2*(pi*area - pi^2*r1^2)^0.5)	Radius of circle giving rise to correct sphere-cap
zp	10*r1	Length in Z of probe sheath
wcell	40*r1	Side length of cell
d	30*r1	Inital Z-position
dstop	h1 + 0.1*r1	Smallest allowable tip-substrate gap
nu	0.01 [V/s]	Potential scan rate
Eint	5e-3 [V]	Potential sampling interval
tint	Eint/nu	Time sampling interval
t	0 [s]	Time, a floating parameter that is reset for each parametric sweep
Eox	0.35 [V]	Oxidative potential limit
Ered	-0.4 [V]	Reductive potential limit
tsw	abs(Eox - Ered)/nu	Time elapsed for each linear potential sweep
Eapp	pw1(t)	Potential applied at the probe tip
F	96485.3 [C/mol]	Faraday's constant
R	8.3144598 [J*K^ - 1*mol^ - 1]	Universal Gas Constant
T	273.15 + 25 [K]	Temperature
f	F/(R*T)	F/RT
oxa0	0.5 [mol/m^3]	Initial Na+ concentration (in mM)
aa	0.5	Electron transfer coefficient (symmetry factor) for Na(Hg)
na	1	Moles of electrons per mole of reactant
E0a	0 [V]	Standard reduction potential for Na(Hg) formation
k0a	1 [cm/s]	Apparent rate constant for Na(+) + e(-) --> Na(Hg)
kfa	k0a*exp(-aa*na*f*(Eapp - E0a))	Forward, Na amalgamation
kba	k0a*exp((1 - aa)*na*f*(Eapp - E0a))	Backward, Na stripping
Doxa	2e-6 [cm^2/s]	Na+ diffusion in solution
Dreda	8.4e-6 [cm^2/s]	Na diffusion in Hg
oxb0	0.5 [mol/m^3]	Initial Li+ concentration (in mM)
ab	0.7	Electron transfer coefficient (symmetry factor) for Li(Hg)
nb	1	Moles of electrons per mole of reactant
E0b	-0.12 [V]	Standard reduction potential for Li(Hg) formation
k0b	2.2e-2 [cm/s]	Apparent rate constant for Li(+) + e(-) --> Li(Hg)
kfb	k0b*exp(-ab*nb*f*(Eapp - E0b))	Forward, Li amalgamation
kbb	k0b*exp((1 - ab)*nb*f*(Eapp - E0b))	Backward, Li amalgamation
Doxb	1.7e-6 [cm^2/s]	Li+ diffusion in solution
Dredb	9.2e-6 [cm^2/s]	Li diffusion in Hg

Table A.1. Globally defined parameters in the COMSOL model.

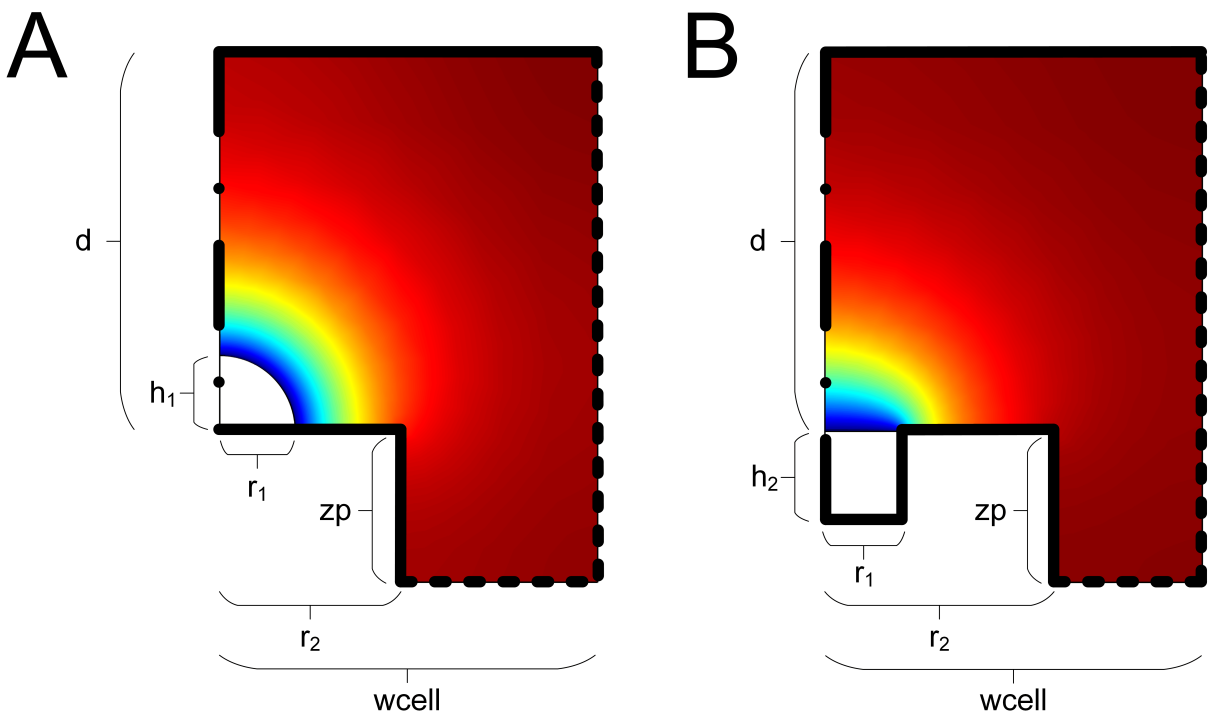

Figure A.1. Geometry and boundaries for (**A**) a Hg sphere-cap and (**B**) a Hg disc-well. The Hg sphere-cap is created by truncating a circle centered at $[r, z] = [0, zp + h_1 - r_{\text{eff}}]$ with radius r_{eff}.

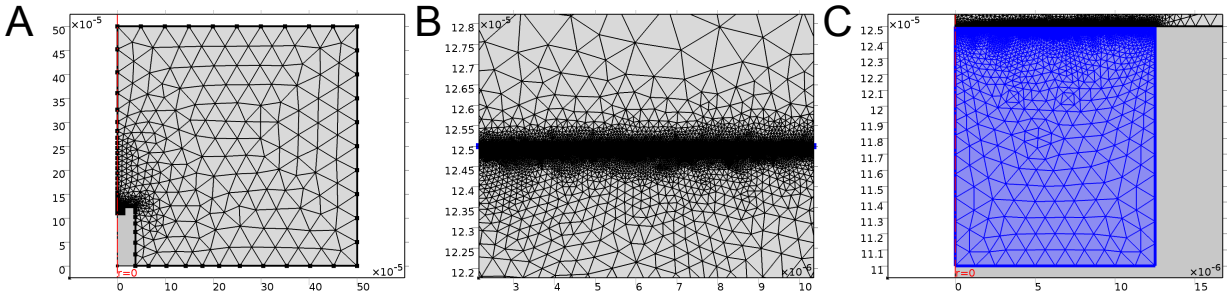

Figure A.2. (**A**) Overview of modified free triangular mesh. (**B**) Advancing front refinement at the Hg–solution interface. (**C**) Single refinement of the Hg domain.

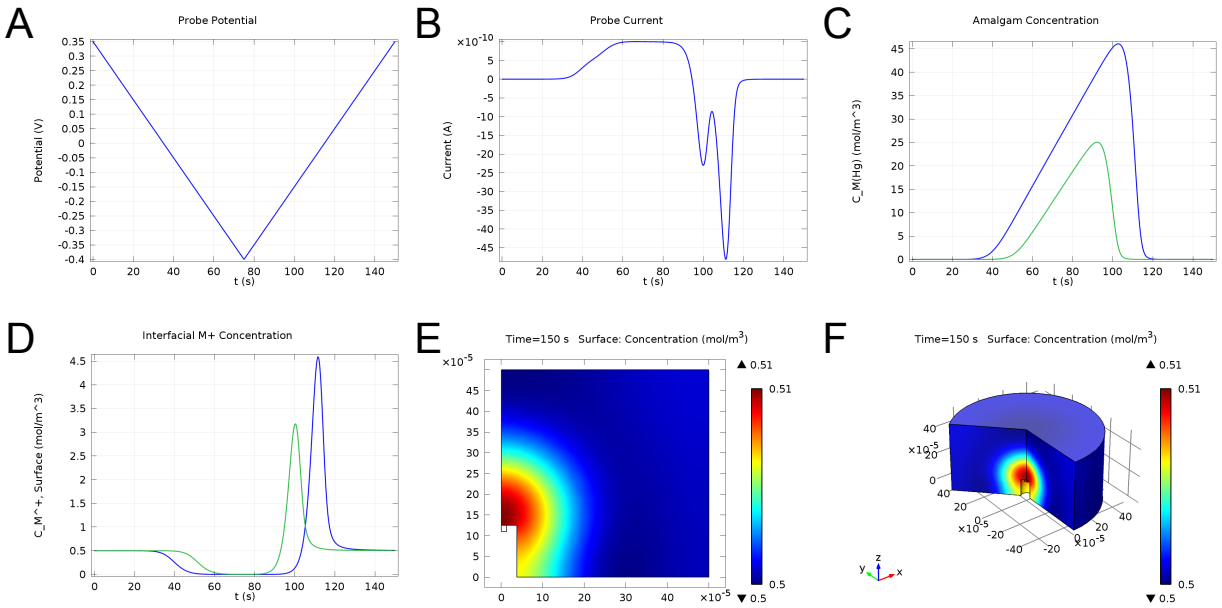

Figure A.3. Plots of (**A**) probe potential, (**B**) probe current, (**C**) amalgam concentration, (**D**) interfacial analyte ion concentration, and (**E**) 2-dimensional *oxa* concentration update while solving. (**F**) A 3-dimensional plot of *oxa* concentration is available after solving.